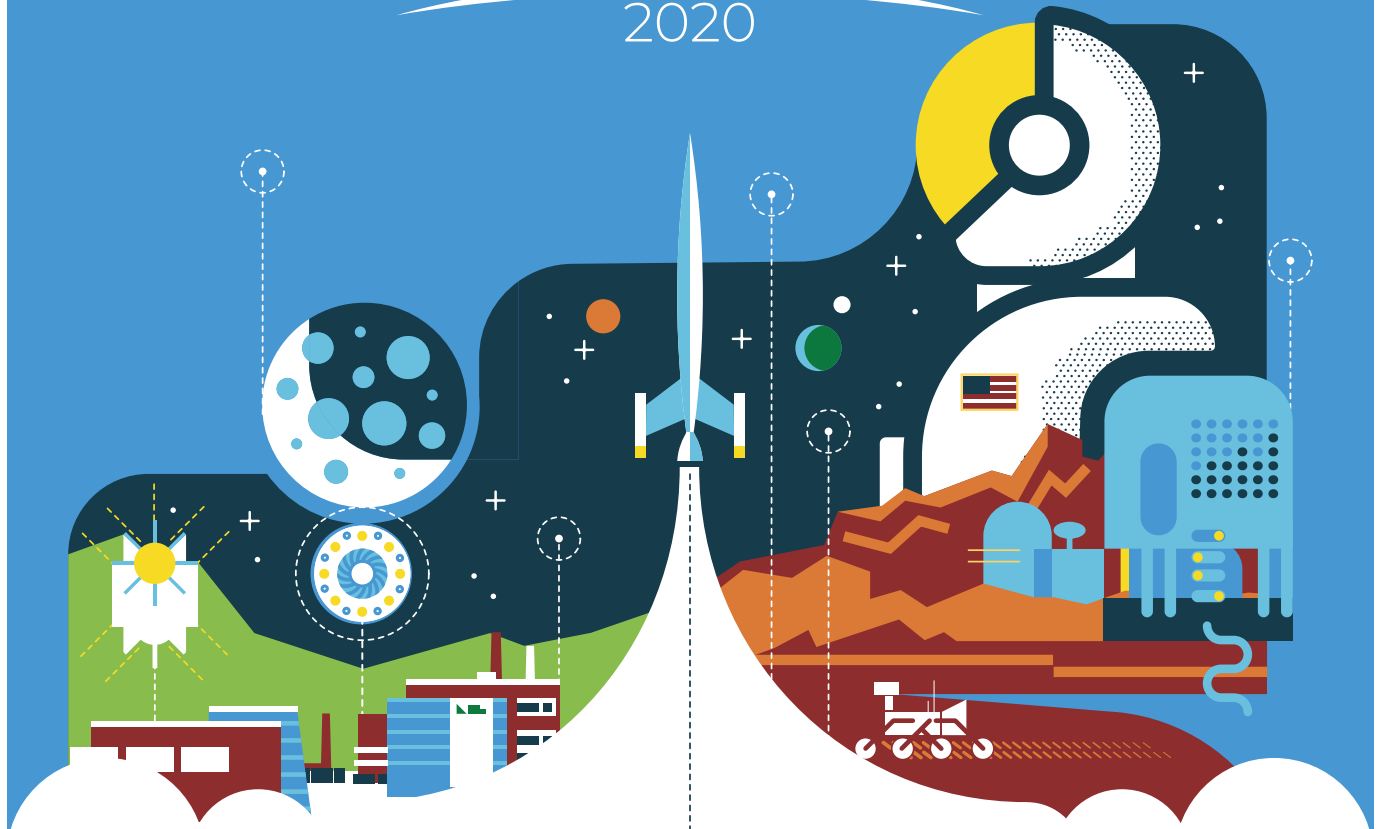


# NETS

2020



**CONFERENCE  
PROCEEDINGS**

**NUCLEAR and  
EMERGING  
TECHNOLOGIES for  
SPACE**

Knoxville, TN 2020, April 6th – 9th

## **Track 1: Radioisotopes and Power Conversion Systems**

**Technical Track Chair: Michael Smith**

Author	Title
Ambrosi, Richard M.	European Radioisotope Power Systems Programme: Recent Updates
Ambrosi, Richard M.	A Concept Study on Advanced Radioisotope Solid Solutions and Mixed Oxide Fuel Forms for Future Space Nuclear Power Systems
Armstrong, Megan	Cassini Lightweight Radioisotope Heater Unit Characterization and Surveillance
Breedlove, Jeffrey J.	Turbo-Brayton Converter for Radioisotope Power Systems
Caillat, T.	An Update on the Development of Skutterudite-Based Thermoelectric Technology for Integration Into a Potential Enhanced Multi-Mission Radioisotope Thermoelectric Generator
Campbell, Catherine	Progress on Alternative Solvent Extraction Flowsheet for Separating Plutonium From Neptunium
Carver, F. A.	238-Plutonium Dioxide Fuel Fabrication Multiple Processing Cerium Dioxide Replication and Particle Size Analysis
Cheu, Darrell	Modeling Chemical Reactions and Diffusion in a MMRTG Plutonium Pellet
Cheu, Darrell	Overview of the Betavoltaic Development at Perdue University
Collins, Josh	Sunpower Robust Stirling Converter (SRSC) Phase II Overview
Colvin, Emory	Optimization of Plutonium-238 Production in the Advanced Test Reactor
DePaoli, David	Chemical Processing in Plutonium-238 Supply Program - Status After Campaign 4
Gogolski, Jarrod	Using N,N-Dihexylhexanamide for Plutonium-238 Purification
Hong, Jintae	Development of Engineering Qualification Model of a Small ETG for Launch Environmental Test
Izon, Stephen	Risk-Informed Life Test Modeling Framework - Development Overview
Kramer, Daniel P.	Preliminary Testing of Commercially Available Silicon Germanium Based Thermoelectric Modules
Lee, Young H.	Icy and Ocean World Exploration Enabled by Radioisotope Power Systems
Mesalam, R.	A Facile Polymeric Templating Route Towards Fabricating RTG and RHU Vent Hole Filters
Romano, Catherine	Measurement of the Integral Capture and Fission Cross Sections of 238Np
Sadegaski, Luke R.	Spectroscopic and Multivariate Analysis Development in Support of the Plutonium-238 Supply Program
Schifer, Nicholas A.	Stirling Converter Extended Testing in Support of Dynamic RPS Maturation
Valentin, Francisco I.	Development of a Novel Miniature Power Converter for Low-Power Radioisotope Heat Sources: Numerical and Experimental Results
Venkatasubramanian, Rama	Bipolar Couple Assembled Module (BCAM) Design for Scalable and Rugged Architecture for TEG Applications
Venkatasubramanian, Rama	Advancements in Low-Temperature, Mid-Temperature, and High-Temperature Heat-To-Electric Conversion Devices
Watkinson, E. J.	Americium-Based Oxide and Pt-Rh Alloys Compatibility/Interaction Tests in the Context of European Space Radioisotope Power Systems
Whiting, Christofer E.	Proposed Standard for Extrapolating Limited RTG Performance Data to Establish Behavior Trends and a Lifetime Performance Prediction
Whiting, Christofer E.	Empirical Analysis of the MMRTG Qualification Unit Operated at a Low Thermal Inventory
Wilson, Scott	Converter Development for Dynamic Radioisotope Power Systems

## EUROPEAN RADIOISOTOPE POWER SYSTEMS PROGRAMME: RECENT UPDATES

Richard M. Ambrosi<sup>1</sup>, Alessandra Barco<sup>1</sup>, Ramy Mesalam<sup>1</sup>, Emily Jane Watkinson<sup>1</sup>, Chris Bicknell<sup>1</sup>, Tony Crawford<sup>1</sup>, Keith Stephenson<sup>2</sup>, Hugo Williams<sup>3</sup>, Colin Stroud<sup>4</sup>, Robert Slater<sup>4</sup>, Kevin Simpson<sup>5</sup>, Richard Tuley<sup>5</sup>, Marie-Claire Perkinson<sup>6</sup>

<sup>1</sup>University of Leicester, School of Physics & Astronomy, University Rd, Leicester, Leicestershire, LE1 7RH, UK

<sup>2</sup>European Space Agency, ESTEC TEC-EP, Keplerlaan 1, 2201AZ Noordwijk, The Netherlands

<sup>3</sup>University of Leicester, School of Engineering, University Rd, Leicester, Leicestershire, LE1 7RH, UK

<sup>4</sup>Lockheed Martin UK, Reddings Wood, Amptill, Bedford MK45 2HD, UK

<sup>5</sup>European Thermodynamics Ltd, 8 Priory Business Park, Kibworth, Leicestershire, LE8 0RX, UK

<sup>6</sup>Airbus, Gunnels Wood Rd, Stevenage, SG1 2AS, UK

Primary Author Contact Information: +44(0)1162231812, [rma8@leicester.ac.uk](mailto:rma8@leicester.ac.uk)

*Radioisotope power systems have transformed our ability to explore the solar system for almost seven decades. Most missions have utilized <sup>238</sup>Pu as the radioisotope of choice to generate electrical power and to produce heat for the operation and thermal management of space craft systems. In Europe, for the past decade, <sup>241</sup>Am has been selected for radioisotope power system (RPS) research programs. This paper provides an update of how the European RPS technology solutions, in the form of radioisotope heater units (RHU) and radioisotope thermoelectric generators (RTG), are developing and evolving by providing a snapshot of some of the most recent results from the program.*

### I. INTRODUCTION

Radioisotope power systems are an enabling technology for space science and exploration missions with a heritage spanning almost seven decades. To date the focus has been utilization of these systems to provide electrical power and heat for spacecraft to survive the most challenging environments in the solar system. Looking forward, and given the increased interest in targeting new destinations in the solar system, radioisotope power could potentially play an increasing role in a new class of future missions. The renewed interest in the Moon and having a permanent human presence on the lunar surface will require diverse and complementary thermal and electrical power sources to provide the right mix of baseline and variable power for a complex cislunar and deep space exploration economy. Science missions to the ice giant planets and icy moons will require innovative probe and power solutions to make these missions viable. The radioisotope that has been the workhorse for space missions to date has been <sup>238</sup>Pu-based ceramic fuels for both US and Russian RPS technologies. More recently the European Space Agency (ESA) has been developing RPS technologies focused on utilizing the heat from <sup>241</sup>Am-based ceramic fuels. These radioisotopes have the characteristics of relatively long half lives i.e. 88 years for <sup>238</sup>Pu and 432 years for <sup>241</sup>Am.

The ESA RPS program consists of the development of both radioisotope thermoelectric generators (RTGs) and heater units (RHUs). The former is based on a 200 W<sub>th</sub>, 10 W<sub>e</sub> architecture (Ref. 1) with the ability to scale the electrical power output from 10 W<sub>e</sub> to 50 W<sub>e</sub> by using each 10 W<sub>e</sub> RTG system as the module or building block (Ref. 1). The specific power is roughly 1 W<sub>e</sub>/kg. The RHU is a 3 W<sub>th</sub> system with a specific thermal power of 15 W<sub>th</sub>/kg.

A detailed summary of the European RPS developments between 2009 and 2019 is provided in detail by Ambrosi et al (Ref. 1).

### II. AMERICIUM-BASED RADIOISOTOPE FUELS

The production of <sup>241</sup>Am for the ESA RPS program is outlined in detail by Sarsfield et al. (Ref. 2, Ref. 3) and Vigier et al. (Ref. 4). The former (Ref. 2, Ref. 3) focus on the method of extraction of <sup>241</sup>Am from the reprocessed separated civil plutonium fuel stored in the U.K. and the consolidation of pure <sup>241</sup>Am<sub>2</sub>O<sub>3</sub>. The latter focuses on the fuel form and how the addition of uranium (at the 15% actinide content level) in a solid solution with <sup>241</sup>Am results in a stable fuel matrix. This fuel matrix has remained in a consolidated pellet-like geometry for several years to date. The most recent ESA RTG system is designed to work with either pure <sup>241</sup>Am<sub>2</sub>O<sub>3</sub> or a fuel that is a solid solution of <sup>241</sup>Am and uranium. The fuel for the European RTG is likely to take the form of a stack of discs rather than single pellets. The work by Vigier et al. (Ref. 4) provides a baseline for the European RHUs and RTGs. More recently the fuels research has migrated to compatibility testing with platinum-based cladding materials as well as measurement of He outgassing, both of which are also presented at this conference by Watkinson et al.

### III. PLATINUM CLADDING

The baseline cladding material for both the RHU and RTG fuel is platinum-20%rhodium and the architecture of the two cladding structures are similar, with dimensional values being the key differences as shown in Figure 1. In both cases the wall thickness values are 2 mm, the frit vent

arrangements are identical, the frit activation and clad sealing structures are the same.

The authors have also successfully welded and sealed Pt-20%Rh cladding structures as well as Pt-30%Rh structures and developed an etching method for the analysis of welds. This is shown in Figure 2. At present, frit vent development is ongoing with promising results that are outlined in a paper by Mesalam at this conference.

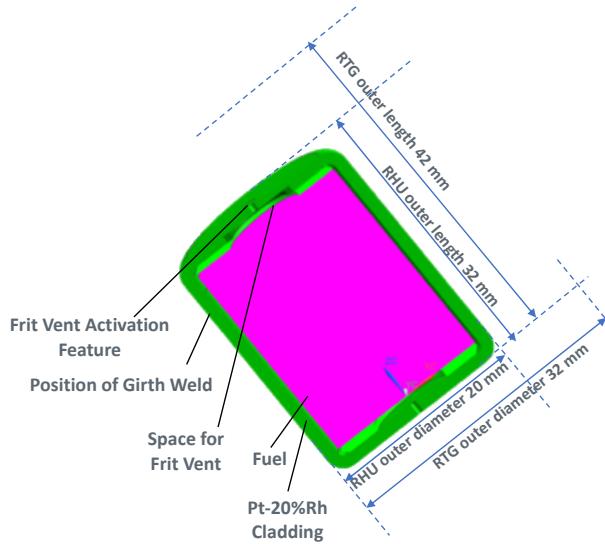


**Fig. 1.** Cladding structures for RHU and RTG heat sources. The primary differences are the dimensional values. Cladding structures are based on Pt-20%Rh cladding, these are threaded and welded. Each clad incorporates the same frit vent technology. The dimensions of the RHU and RTG clads are shown.



**Fig. 2.** Welding, sectioning and etching of welded structures. The top image on the left shows some small test pieces that were welded and then sectioned and etched. The

etched sections are shown in the micrographs below. The top image on the right shows a welded clad. The welding was done in house at the University of Leicester.

#### IV. HEAT SOURCE GEOMETRIES

Heat source geometries for RHU and RTG are shown in Figure 3. In both cases the same carbon-carbon composite aeroshell material is used. The aeroshells are composed of a SEPCARB® (Ref. 5) carbon-carbon composite material. SEPCARB® composites are composed of carbon fibers and a carbon matrix bonding the fibers together. A chemical vapor infiltration process, produces a homogeneous matrix that has an even load distribution and is highly resistant to heat. The distribution and combination of these characteristics render this 3D composite material light, resistant to thermal shock and mechanically stable to temperatures in excess of 3000 K. In addition to the common use of aeroshell materials, the insulation layer between the cladding structure and the aeroshell is a carbon felt. This insulation is used in both the RTG and RHU. One feature that has only recently been added to the RTG heat source, are chamfers that will induce tumbling of the heat source during re-entry to reduce the rate of ablation of the aeroshell and also distribute the mechanical stresses across the aeroshell. These features are shown in Figure 3.

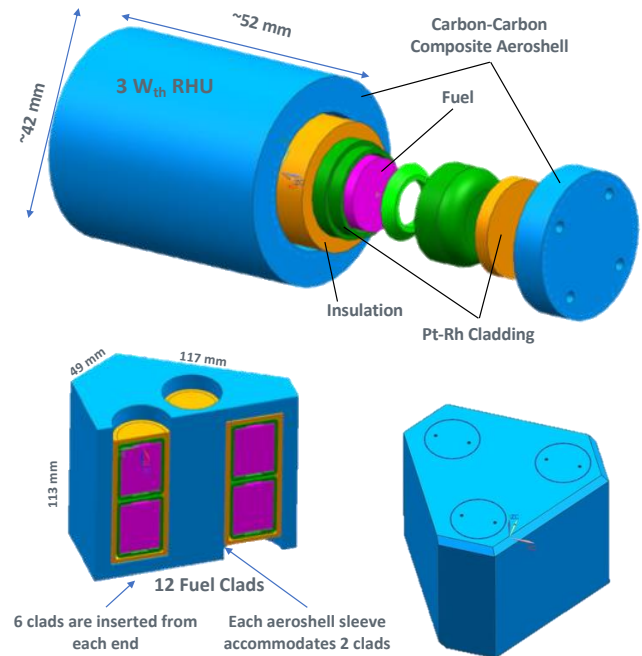


**Fig. 3.** (Top) The cylindrical RHU system producing 3 W<sub>th</sub>. (Bottom) The six sided RTG heat source generating 200 W<sub>th</sub>. The image also shows the additional chamfers added in the most recent design as shown in the bottom right figure on the top right hand edge and continuing on the two short sides adjacent to it.

## V. RTG SYSTEM

The RTG system has evolved over the past 10 years from a design with the fuel on axis to a design with a distributed fuel in a heat source shown in Figure 3. The evolution in design is shown in Figure 4. The radiator area has recently been increased in size with capacity to grow it further and this is shown in Figure 4. A full thermal and mechanical analysis has been carried out and further design refinements are planned in the coming year.

RTG test results are summarized in Ref. 1 and these are therefore not duplicated here. The headline results are that specific power values are at the 1 W<sub>e</sub>/kg and would unlikely exceed 1.5 W<sub>e</sub>/kg. Conversion efficiencies are around 5% at system level and that scaling from 10 W<sub>e</sub> to 50 W<sub>e</sub> of electrical power will be done by using the 10 W<sub>e</sub> RTG unit as the building block.

### V.A. Automated Production of Thermoelectric Generators

The thermoelectric converters for the RTG system are bismuth telluride based. Thermoelectric generators that operate between 220°C and room temperature are well-suited to americium-based RPS (Ref. 1). The program has focused on establishing the complete end-to-end production capability in the UK, from producing the thermoelectric materials from the constituent elements, using appropriate materials processing and consolidation methods, through to segmentation into unicouples and module production. This approach is summarized in Figure 5. Several generations of modules have been produced. Previously the baseline was a 40 mm x 40 mm module which had 161 couples, each with a 1.2 mm x 1.2 mm cross section and a height of 6 mm. More recently, in order to produce modules with greater homogeneity in performance and exercise greater control of the properties of the modules from batch to batch, the UK team migrated to an automated production method. This included an optimization of the module geometry step to ensure automation of the manufacturing was possible without impacting too negatively on overall system level performance. The result was modules with 127 x 127 couples, 1.2 x 1.2 x 5 mm<sup>3</sup> for the unicouples and improvements in contact resistance values. These devices are shown in Figure 5.

## VI. RHU SYSTEM

The RHU system has not changed significantly from the design described in Refs. 1 and 2, with the exception of the standardization of the cladding design features as described in Section III. Figure 3 shows an external view of the RHU.

## VII. RE-ENTRY HEATING AND IMPACT TESTING

More recently, re-entry heating modelling was iterated to focus on the effect of tumbling on the thermomechanical

stresses and predicted recession levels in both RHU and RTG heat sources. Tables 1 and 2 outline some of the results from this modelling.

### VII.B. Laser Heating of RHU system

In order to simulate the re-entry heating and the propagation of heat through an RHU structure a fully assembled structural model of the RHU, with fuel mass dummy, welded clad, carbon-bonded-carbon-fiber insulation (CBCF) insulation layer and outer carbon-carbon aeroshell was subjected to a laser heating experiment. The re-entry profile chosen was that associated with a re-entry angle of 11° as this was an extreme heating case. The test was carried out at the Laser Hardened Materials Evaluation Laboratory (LHMEL) at Wright-Patterson Air Force Base in Ohio. Figure 6 shows a radiograph of RHU during the test and the heating test. The results are shown in Figure 6 where the external temperature exceeded 4000°C and the inner core increased from room temperature to around 200°C with a time lag of several tens of seconds. The increase in fuel simulant temperature occurred when the system was in the cooling phase. Adding an offset to account for nominal fuel operating temperatures of 300°C (also shown in Figure 9) still gives a margin of between 1000°C and 1200°C between the peak temperature under these re-entry conditions and critical temperatures identified for americium based RPS as shown by Ambrosi et al (Ref. 1).

### VII.C. Impact Testing & High Strain-Rate of Cladding Materials and Impact of RHU System

The RHU subjected to re-entry heating was also subjected to impact on ground to simulate the entire re-entry process. This impact test on concrete as a target, was carried out at the Ariane Group facilities in Vert-Le-Petit, France, near Paris. The cladding structure in the RHU survived an impact velocity of 150 m/s about 3 times the predicted impact velocity for an RHU. The RHU external aeroshell absorbed much of the impact and fractured. The RHU clad was then subjected to a further impact again at a velocity around 150 m/s and survived intact. This impact campaign was the second utilizing Pt-Rh cladding structures to determine the resilience of these structures to various impact conditions. Detailed dynamic models are currently being developed by co-author (A. Barco), which will appear in the literature later this year.

This impact work is complemented by high-strain-rate testing of Pt-30%Rh, Pt-20%Rh and Pt-10%Rh as a function of temperature to obtain a full set of data and models for cladding behavior that will feed into the dynamic models.

The preliminary data from the high-strain-rate testing will be presented at this conference by Watkinson et al.

Some images from these test campaigns are shown in Figure 7.

**TABLE I.** Results from complete re-entry model RTG heat source tumbling at rotation frequency of 10 Hz. Numbers in brackets are the velocity aligned values i.e. with the heat source not tumbling.

Parameter	Comet Return (CR)	Shallow Re-entry (SE)
Initial Velocity (km.s <sup>-1</sup> )/Flight Angle (deg)	12.1/-11.1	11/-6.5
Peak Convective Heat Flux (MWm <sup>-2</sup> )	40*	16*
Altitude at Peak Convective Heat Flux (m)	43*	66*
Conv. Heat Load (MJm <sup>-2</sup> )	230 (714)	164 (1281)
Peak Surface Temp. (K)	3989 (4449)	2500 (3760)
Predicted Recession (mm)	1.1 (4.2)	1.3 (4.3)
Ground Impact Vel. (ms <sup>-1</sup> )	111*	111*

\*No change.

**TABLE II.** Results from complete re-entry model RHU heat source tumbling at rotation frequency of 10 Hz. Numbers in brackets are the velocity aligned values.

Parameter	Comet Return (CR)	Shallow Re-entry (SE)
Initial Velocity (km.s <sup>-1</sup> )/Flight Angle (deg)	12.1/-11.1	11/-6.5
Peak Convective Heat Flux (MWm <sup>-2</sup> )	24*	14*
Altitude at Peak Convective Heat Flux (m)	62*	66*
Conv. Heat Load (MJm <sup>-2</sup> )	95 (277)	164 (555)
Peak Surface Temp. (K)	2978 (3790)	2761 (3565)
Predicted Recession (mm)	0.4 (1.2)	0.9 (2.4)
Ground Impact Vel. (ms <sup>-1</sup> )	50.5*	50.5*

\*No change.

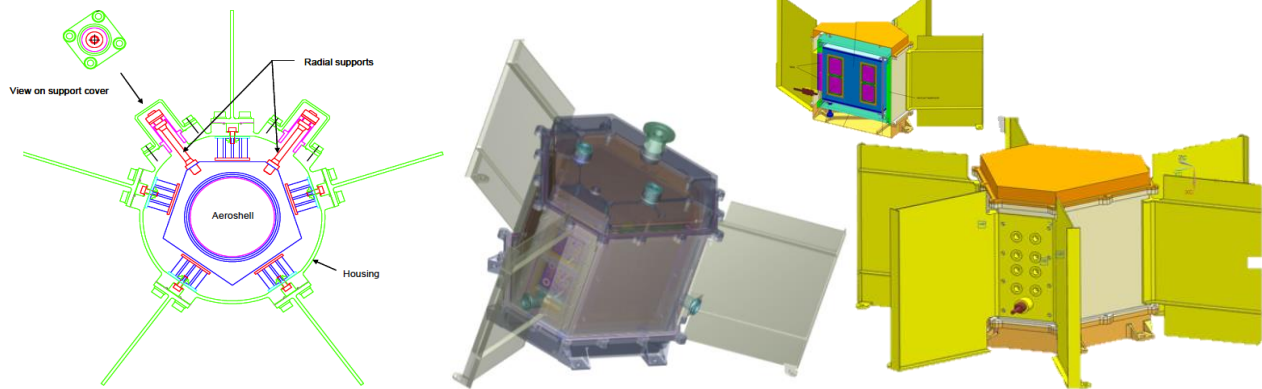


**Fig. 4.** (Left) RTG design with fuel on axis. (Middle) The six sided 200 W<sub>th</sub> RTG heat source shaping the RTG system level design. (Right) The most recent design based around the 200 W<sub>th</sub> heat source with 12 clads and a larger radiator area.

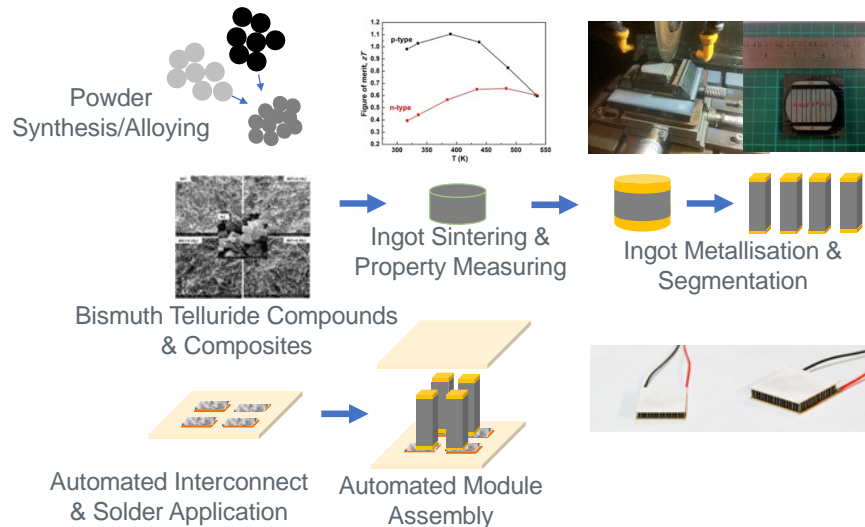


**Fig. 5.** The production of thermoelectric generators established end-to-end with the most recent development including the automated production of modules as shown in the image. The first modules produced in this way were received in late 2019.

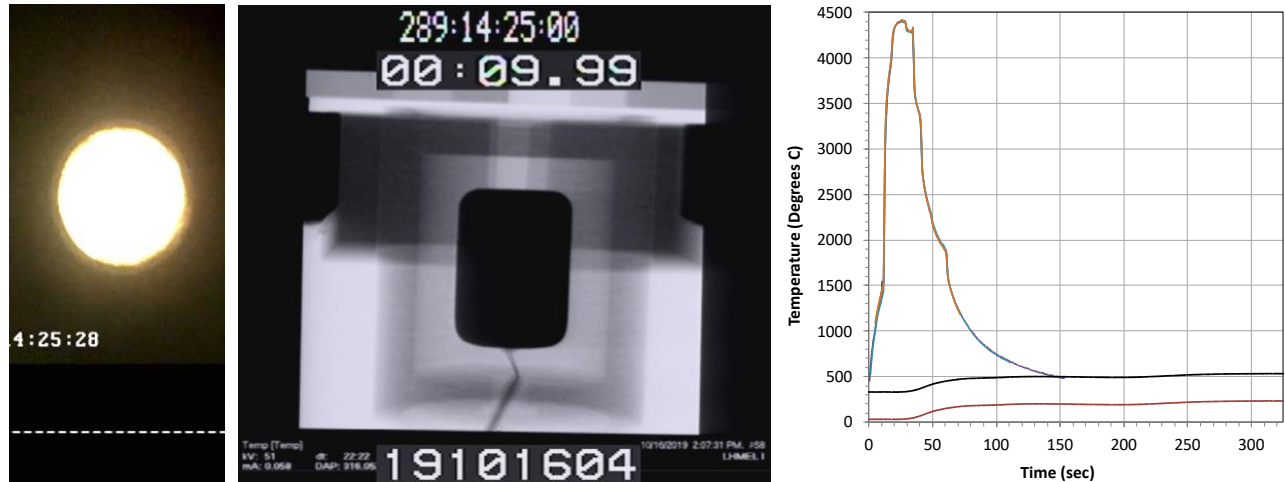


**Fig. 6.** (Left) Image of a structural thermal model of an RHU exposed to a re-entry heating experiment. (Middle) X-ray image of the RHU during the heating experiment. (Right) Heating profile showing the time lag between the outer surface and inner core (red line). The black line considers the fuel operating temperature which would add an offset of a few hundred degrees.

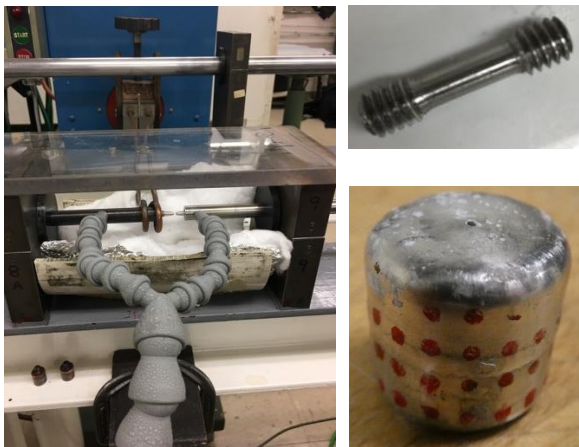


**Fig. 7.** (Left and top right) High strain rate testing versus temperature and samples used in the testing. (Bottom right) Welded RHU clad survives impact testing.

## VIII. CONCLUSIONS

The paper provides an update of the development of European RTG and RHU systems and also should be read as an extension of the summary provided by Ambrosi et al. (Ref. 1). The project is currently at a point where a number of active research activities are running in parallel to mature both RHU and RTG heat sources to TRL5 and the results of these will be appearing in the literature in coming months. The program continues to reduce risk across all of the key areas of: fuel, containment and thermoelectric conversion at reasonable pace. The current plan to have a launch-ready RHU by 2026 as a first step in European RPS development is still on track.

## ACKNOWLEDGMENTS

The University of Leicester is funded by the European Space Agency. The authors would like to thank the UK Space Agency and acknowledge the ongoing collaboration with National Nuclear Laboratory (UK) Ariane Group (France) and Thales Alenia Space (UK).

## REFERENCES

1. R. M AMBROSI, H. WILLIAMS, E J WATKINSON, et al., *European Radioisotope Thermoelectric Generators (RTGs) and Radioisotope Heater Units (RHUs) for Space Science and Exploration*, Space Science Reviews, **215:55** (2019) <https://doi.org/10.1007/s11214-019-0623-9> .
2. M. SARSFIELD, C. CAMPBELL, C. CARRIGAN et al., E3S Web Conf. **16**, 05003 (2017) <https://doi.org/10.1051/e3sconf/20171605003> .
3. M. SARSFIELD, J. BROWN, C. CAMPBELL et al., *Progress in Nuclear Energy*, **106**, 396–416 (2018) <https://doi.org/10.1016/j.pnucene.2018.02.008> .
4. J-F. VIGIER, D. FREIS, P. PÖML et al., *Inorganic Chemistry* **578**, 4317–4327 (2018) <https://doi.org/10.1021/acs.inorgchem.7b03148> .
5. M. LACOSTE, A. LACOMBE, P. JOYEZ, et al., *Carbon/Carbon extendible Nozzles*, Acta Astronautica, **50**, 6, p. 357 (2002).

## A CONCEPT STUDY ON ADVANCED RADIOISOTOPE SOLID SOLUTIONS AND MIXED OXIDE FUEL FORMS FOR FUTURE SPACE NUCLEAR POWER SYSTEMS

Richard M. Ambrosi<sup>1</sup>, Daniel P. Kramer<sup>2</sup>, Emily Jane Watkinson<sup>1</sup>, Ramy Mesalam<sup>1</sup>, Alessandra Barco<sup>1</sup>

<sup>1</sup>University of Leicester, School of Physics and Astronomy, Space Research Centre, University Rd, Leicester, Leicestershire, LE1 7RH, United Kingdom

<sup>2</sup>University of Dayton, 300 College Park, Dayton, Ohio, OH 45469, USA

Primary Author Contact Information: +44(0)1162231812, [rma8@leicester.ac.uk](mailto:rma8@leicester.ac.uk)

Radioisotope power systems have transformed our ability to explore the solar system. Radioisotope power systems (RPS) have been in existence for almost seven decades. Most missions have utilized <sup>238</sup>Pu as the radioisotope of choice to generate electrical power and to produce heat for the operation and thermal management of spacecraft systems. In Europe, for the past decade, <sup>241</sup>Am has been selected for radioisotope power system research programs. This paper hypothesizes that the inclusion of small quantities of relatively short-lived radioisotopes such as <sup>232</sup>U and <sup>244</sup>Cm, particularly when dealing with long-lived radioisotope <sup>241</sup>Am, could have implications for future RPS designs. This paper focuses on the thermal output implications and impact on system level design. The authors recognize that the selection of any new or modified radioisotope heat source material will require extensive research on fuel form stability, the radiological impact, cost of production, containment and launch safety considerations.

### I. INTRODUCTION

Radioisotope power systems are an enabling technology for space science and exploration missions with a heritage spanning almost seven decades. To date, the focus has been on the utilization of these systems to provide electrical power and heat for spacecraft to survive the most challenging environments in the solar system. Looking forward, and given the increased interest in targeting new destinations in the solar system, radioisotope power could potentially play an increasing role in a new class of future missions. The renewed interest in the Moon and having a permanent human presence on the lunar surface will require both thermal and electrical power sources of varying output and type to provide the right mix of baseline and variable power for a complex lunar ecosystem to flourish. Science missions to the ice giant planets and icy moons will require innovative probe and power solutions to make these missions viable. Some of these missions may require previously unexploited heat source radioisotopes such as <sup>232</sup>U and/or <sup>244</sup>Cm (Refs. 1, 2).

The radioisotope that has been the workhorse for space missions to date is <sup>238</sup>Pu in the form of ceramic oxide fuels for both US and Russian RPS technologies. More recently,

the European Space Agency (ESA) has been developing RPS technologies focused on utilizing the heat from <sup>241</sup>Am-based ceramic fuels. These radioisotopes have relatively long half-lives i.e. 88 years for <sup>238</sup>Pu and 432 years for <sup>241</sup>Am.

The hypotheses outlined in this paper focus on scenarios where the inclusion of small amounts of other shorter-lived radioisotopes and their daughters, specifically <sup>232</sup>U and <sup>244</sup>Cm could play an important role in augmenting the thermal performance of longer-lived radioisotopes like <sup>238</sup>Pu and <sup>241</sup>Am. The change in the thermal output could consequently have an impact on system level RPS design and end of life mission level performance.

Table I provides the detailed characteristics of various radioisotopes under consideration and these are compared to both <sup>238</sup>Pu and <sup>241</sup>Am. Figure 1 shows the thermal output for the same radioisotopes in Table I as a function of time over a 35-year period. The time period is chosen to reflect a whole range of missions including missions to the most remote regions or beyond the edge of the solar system. Taking into consideration that the Voyager 1 mission reached interstellar space in 2012 about 35 years after launch in 1977. The 35-year period is therefore chosen as a unifying point in time that does not exclude a possible future mission beyond the edge of the solar system. This time period is used in the calculations and figures below.

**TABLE I.** Comparison of the thermal power output properties and half-lives of various radioisotopes.

Radioisotope	Half Life (years)	Thermal Output (W/g)
Uranium-232 <sup>a</sup>	68.9	0.6 <sup>c</sup> (4.4 <sup>d</sup> )
Thorium-228 <sup>b</sup>	1.91	165 <sup>c</sup>
Curium-244	18.1	2.5
Plutonium-238	87.7	0.5
Americium-241	432.6	0.1

<sup>a</sup> Uranium-232 decays to thorium-228.

<sup>b</sup> Thorium-228 decay series consists of short-lived radionuclides.

<sup>c</sup> Peak power output for Th-228 and for U-232 at time t=0 for the radioisotopes taken in isolation.

<sup>d</sup> After t=10 years the peak power resulting from the decay of U-232 and buildup of Th-228

## II. EUROPEAN RPS SYSTEMS

The ESA RPS program is targeting both radioisotope thermoelectric generators (RTG) and heater units (RHU). While RTG heat sources are designed to generate 200 W<sub>th</sub>, and 10 W<sub>e</sub> (Ref. 3), the RTGs are also scalable to produce electrical power outputs up to 50 W<sub>e</sub> (Ref. 3). The specific power of RTGs is roughly 1 W/kg. The RHU is a 3 W<sub>th</sub> system with a specific thermal power of 15 W/kg.

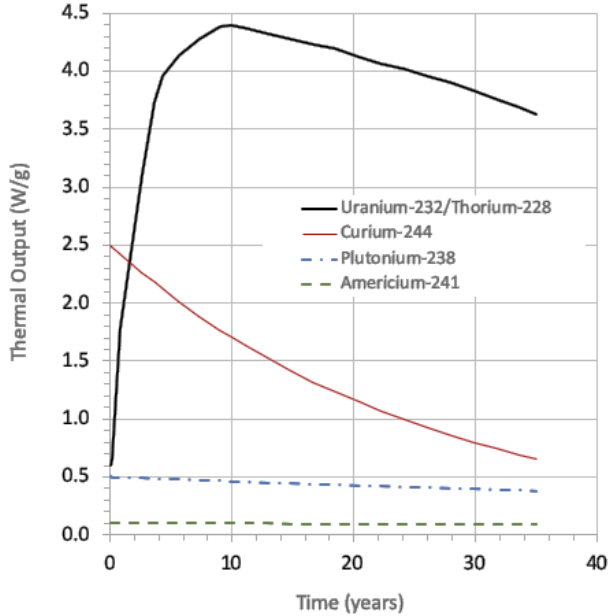


Fig. 1. Thermal power output versus time for the radioisotopes listed in Table I.

## III. AMERICIUM-BASED RADIOISOTOPE FUELS

The production of <sup>241</sup>Am for the ESA RPS program is outlined in detail by Sarsfield et al. (Ref. 4, Ref. 5) and Vigier et al. (Ref. 6). The former (Ref. 4, Ref. 5) focus on the method of extraction of <sup>241</sup>Am from the reprocessed separated civil plutonium fuel stored in the UK and the consolidation of pure <sup>241</sup>Am<sub>2</sub>O<sub>3</sub>. The latter focuses on the fuel form and how the addition of uranium (at the 15% level of actinide content) in a solid solution with <sup>241</sup>Am results in a stable fuel matrix. This fuel matrix has remained in a consolidated pellet-like geometry for several years to date. The most recent ESA RTG system is designed to work with either pure <sup>241</sup>Am<sub>2</sub>O<sub>3</sub> or a fuel that is a solid solution of <sup>241</sup>Am and uranium. The details of the ESA RTG development work are described by Ambrosi et al. (Ref. 3). These papers highlight that the fuel for the European RTG is likely to take the form of a stack of discs rather than single pellets.

Assuming that the same stabilizing effect can be achieved by utilizing <sup>232</sup>U at the 15% level in a solid solution with <sup>241</sup>Am, the thermal output and system level implications of this fuel can be analyzed further.

The second assumption that is considered, is that a mixed oxide fuel form could be created between <sup>241</sup>Am<sub>2</sub>O<sub>3</sub> and <sup>244</sup>Cm<sub>2</sub>O<sub>3</sub>, or that in a stack of fuel discs, <sup>244</sup>Cm<sub>2</sub>O<sub>3</sub>, could be interspersed with the <sup>241</sup>Am based fuel. In this case, the thermal output and system level implications of this fuel can be analyzed further. Again, the assumption is that 15% of the mass of the fuel is curium-based.

### III.A. Thermal characteristics of the <sup>232</sup>U-based solid solution with <sup>241</sup>Am and implications for European RPS

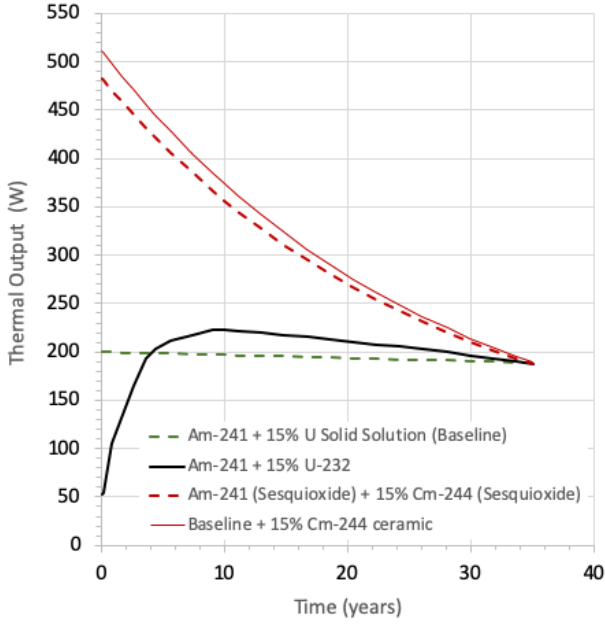
The thermal output of a solid solution between <sup>232</sup>U and <sup>241</sup>Am is enhanced by the ingrowth of <sup>228</sup>Th, which has a very short half-life. The <sup>232</sup>U is limited to 15% by mass and an assumption is made that the <sup>232</sup>U can be produced efficiently and the solid solution produced close to launch. Taking these assumptions into consideration, the thermal output grows and peaks about 10 years after launch as shown in Figure 1.

Given that the baseline thermal power output at launch for a 10 W<sub>e</sub> European RTG is 200 W<sub>th</sub>, the calculated end of life thermal power output is approximately 189 W<sub>th</sub> after 35 years. Using this 35-year point as a common end of life mission point in time, the beginning of life power output and mass of the alternative option of a solid solution of <sup>241</sup>Am and <sup>232</sup>U can be determined. Figure 2 provides a visual representation of this calculation. In this specific case, a thermal output at launch of 53 W<sub>th</sub> will peaking at 223 W<sub>th</sub>, 10 years after launch and will reach a similar an end of life power output of 189 W<sub>th</sub> thermal.

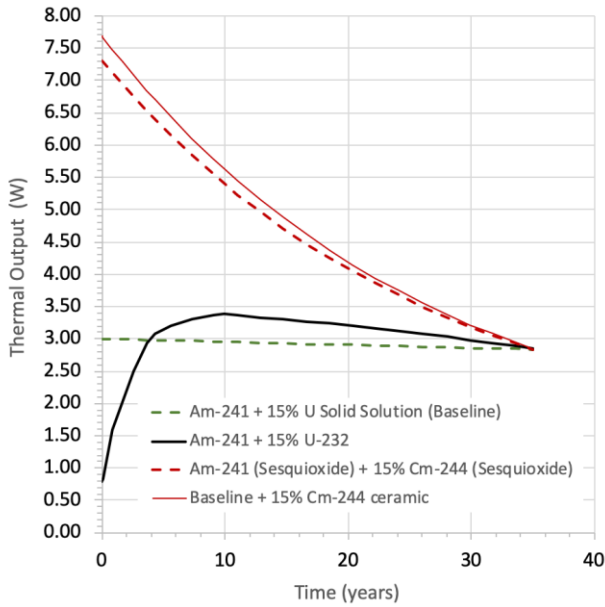
As shown in Table II, the mass of the fuel reduces by 87% from 2400 g to 302 g to produce the same end-of-life power at a unifying point of 35 years post launch. This would have a significant impact on the volume and specific power of the RTG system. For the 3 W<sub>th</sub> RHU, the thermal power at launch is 0.8 W<sub>th</sub> peaking at 3.4 W<sub>th</sub> 10 years after launch. This is shown in Figure 3. The mass reduction is from 36 g to 4.6 g of material and this is shown in Table III.

TABLE II. Mass of radioisotope at beginning of life required to generate the same power output at end of life as shown in Figure 2 for a European RTG. Comparison is made with the baseline of the mass of <sup>241</sup>Am based ceramic fuel required for a 200 W<sub>th</sub> heat source.

Radioisotope	Mass (g)
<sup>241</sup> Am + 15% <sup>232</sup> U	302
<sup>241</sup> Am + 15% <sup>244</sup> Cm (Both Sesquioxides)	1056
Baseline + 15% <sup>244</sup> Cm Ceramic	1150
<sup>241</sup> Am + 15% U Solid Solution (Baseline)	2400



**Fig. 2.** Thermal power output versus time for the radioisotopes listed in Table I. The nominal 200 W<sub>th</sub> thermal power output is for the European RTG heat source.



**Fig. 3.** Thermal power output versus time for the radioisotopes listed in Table I. The nominal 3 W<sub>th</sub> power output is for the European RHU.

### III.B. Thermal characteristics of the <sup>244</sup>Cm and <sup>241</sup>Am mixed ceramic fuel and implications for European RPS

The thermal output of a mixed oxide fuel of <sup>244</sup>Cm and <sup>241</sup>Am is enhanced by exploiting the greater specific thermal power of <sup>244</sup>Cm. The <sup>244</sup>Cm is also limited to 15% by mass in this instance. An assumption is made that the

<sup>244</sup>Cm can be produced efficiently and the mixed oxide produced close to launch. Taking these assumptions into consideration, the thermal output starts at a much higher baseline level as shown in Figure 1.

Given that the baseline thermal power output at launch for a 10 W<sub>e</sub> European RTG is 200 W<sub>th</sub>, the calculated end of life thermal power output is approximately 189 W<sub>th</sub> after 35 years. Using this 35-year point as a common end of life mission point in time, the beginning of life power output and mass of the alternative option of a solid solution of <sup>241</sup>Am and <sup>244</sup>Cm can be determined. Figure 2 provides a visual representation of this calculation. In this specific case, the thermal output at launch is around 500 W<sub>th</sub> and an end of life power output of 189 W<sub>th</sub> is achieved. As shown in Table II, the mass of the fuel reduces by around 50% from 2400 g to around 1100 g.

This would have a significant impact on the volume and specific power of the RTG system. For the 3 W<sub>th</sub> RHU, the thermal power at launch is around 7.5 W<sub>th</sub> dropping to around 3 W<sub>th</sub> after 35 years. This is shown in Figure 3. The mass reduction is from 36 g to approximately 16.5 g of material. This is shown in Table III. A number of past studies support the feasibility of this concept and in particular the production of Am and Cm compounds with Cm levels close to the 15% value outlined in this paper (Refs. 7 and 8). In Ref 8, an Am-Cm compound was produced via oxalate precipitation and calcination and also welded the resulting pellet into a Pt-based containment structure.

**TABLE III.** Mass of radioisotope at beginning of life required to generate the same power output at end of life as shown in Figure 3 for a European RHU. Comparison is made with the baseline of the mass of <sup>241</sup>Am based ceramic fuel required for a 3 W<sub>th</sub> heat source.

Radioisotope	Mass (g)
<sup>241</sup> Am + 15% <sup>232</sup> U	4.6
<sup>241</sup> Am + 15% <sup>244</sup> Cm (Both Sesquioxides)	15.9
Baseline + 15% <sup>244</sup> Cm Ceramic	17.3
<sup>241</sup> Am + 15% U Solid Solution (Baseline)	36.0

### IV. PLUTONIUM-BASED MIXED CERAMIC RADIOISOTOPE FUELS

Previous discussions centered on the potential advantages of employing both a short (<sup>232</sup>U or <sup>244</sup>Cm) and a long half-life radioisotope (<sup>241</sup>Am) in a predominantly <sup>241</sup>Am mixed oxide pellet. During the evaluation, it became increasingly apparent that the same general concept could also be applied in a mixed oxide fuel pellet consisting primarily of <sup>238</sup>Pu (“long” half-life) and a quantity of a shorter half-life radioisotope such as <sup>244</sup>Cm.

The processing details of a mixed  $^{238}\text{Pu}$ - $^{244}\text{Cm}$  oxide fuel form is outside the margins of this research. However, previous work associated with materials aging studies have shown that mixed  $^{238}\text{PuO}_2$ - $^{244}\text{Cm}_2\text{O}_3$  compacts have been fabricated (Ref. 9). As a part of these studies, the crystalline phases present (referring to the oxide and not just the actinide) include up to 10 mole percent  $^{244}\text{Cm}_2\text{O}_3$  and 90 mole percent  $^{238}\text{PuO}_2$  specimens sintered at 1300 °C for 6 hours followed by a second thermal segment of 1300 °C for 2 hours. The results demonstrated that the two oxides form a solid solution.

Another study discusses curium vaporization results obtained on a small sintered pellet that was originally fabricated using  $^{244}\text{Cm}_2\text{O}_3$  feed material (Ref. 10). The actual vaporization experiments were performed on samples obtained from the pellet after ~26 years of storage. At that time, due to the decay of the  $^{244}\text{Cm}$ , the pellet was actually a mixed curia-plutonium oxide with actinide stoichiometry to be ( $^{244}\text{Cm}_{0.76}$ ,  $^{240}\text{Pu}_{1.24}$ ).

Both of the studies briefly discussed above indicate the feasibility of the fabrication of  $^{238}\text{Pu}$ - $^{244}\text{Cm}$  mixed oxide compacts. Other ceramic processing and materials compatibility studies show that up to 10 g  $^{244}\text{Cm}_2\text{O}_3$  stand-alone ceramic pellets have also been fabricated (Refs 11, 12). Thus, future RTG designers who may wish to employ a long half-life and a short half-life radioisotope ( $^{238}\text{Pu}$  and/or  $^{244}\text{Cm}$ ) containing heat sources could conceivably consider employing a mixed oxide or a two independent pellets fuel form.

#### IV.A. Background Discussion on the General Characteristics of a GPHS-RTG

Figure 4 shows a cutaway of a GPHS-RTG (General Purpose Heat Source Radioisotope Thermoelectric Generator) employed to power several U.S. space missions launched in the 1989-2006 timeframe including; Galileo/Jupiter, Cassini/Saturn, Ulysses and New Horizons/Pluto (Ref 13). GPHS-RTGs were designed with 18 GPHS modules (eleven are exposed in the figure). Each of the GPHS modules contain four 151 g  $^{238}\text{PuO}_2$  ceramic pellets that each produce at beginning of life 62.5  $\text{W}_{\text{th}}$  of thermal heat. Thus, each of the 18 GPHS modules yields 250  $\text{W}_{\text{th}}$  or a total GPHS-RTG thermal output of 4500  $\text{W}_{\text{th}}$ . This particular RTG design utilized SiGe based thermoelectric couple with a thermal to electrical conversion rate of 7%; thus producing 310  $\text{W}_e$  of power at Beginning of Life (BOL).

#### IV.B. Conceptual Application of Employing $^{244}\text{Cm}$ to Enhance the Performance of a $^{238}\text{PuO}_2$ Mixed Fueled Step 2 GPHS-RTG

In the design and development of an RTG, the prime focus is the safe confinement of the radioactive fuel under all mission environment/conditions. Since the original design of the GPHS modules for GPHS-RTGs, a newer

slightly more dimensionally robust Step 2 GPHS design is being utilized in the latest generation RTG; MMRTG (Multi-Mission RTG) (Ref 14). If Step 2 GPHS modules were employed in the older GPHS-RTG design, the result will be that only 16 modules will fit within the housing. Resulting in a total thermal output of only 4000  $\text{W}_{\text{th}}$  with a correspondingly lower power output of only 275  $\text{W}_e$  BOL.

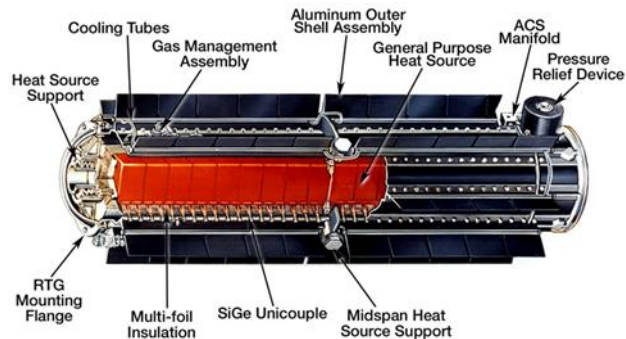


Fig. 4. Cutaway of a GPHS-RTG showing a portion of the GPHS modules (Ref 13).

As an example, it is interesting to speculate on how the application of a small quantity of  $^{244}\text{Cm}_2\text{O}_3$  could be employed to increase the thermal output of a conceptual Step 2 GPHS-RTG back to its original thermal design of 4500  $\text{W}_{\text{th}}$ . A Step 2 GPHS-RTG would contain 16 modules, so each module would need to emit 281.25  $\text{W}_{\text{th}}$  at BOL to obtain the total thermal output of a legacy GPHS-RTG of 4500  $\text{W}_{\text{th}}$ . Each of the 16 modules in a Step 2 GPHS-RTG will still contain four mainly  $^{238}\text{PuO}_2$  fuel pellets. Each Step 2 GPHS-RTG pellet will need to emit 70.3  $\text{W}_{\text{th}}$ . Since a standard  $^{238}\text{PuO}_2$  fuel pellet emits only 62.5  $\text{W}_{\text{th}}$ , the thermal output of each Step 2 pellet would need to be enhanced by at least 7.8  $\text{W}_{\text{th}}$ . The question then becomes how much  $^{244}\text{Cm}_2\text{O}_3$  would need to be “added” to a  $^{238}\text{PuO}_2$  pellet to enhance its thermal output by 7.8  $\text{W}_{\text{th}}$ . Table II adapted from the literature presents some of the properties of  $^{244}\text{Cm}_2\text{O}_3$  (Ref 15). Density and power density values at 88% theoretical density in Table IV are shown.

TABLE IV. Reported properties of  $^{244}\text{Cm}_2\text{O}_3$  (Ref 15).

Property	Value
Density (100% Theoretical Density)	11.7 $\text{g}/\text{cm}^3$
Density (88% T.D.)	10.3 $\text{g}/\text{cm}^3$
Melting Point	2250°C
Specific Power of $^{244}\text{Cm}$	2.3 $\text{W}_{\text{th}}/\text{g}^*$
Specific Power of $^{244}\text{Cm}_2\text{O}_3$	2.1 $\text{W}_{\text{th}}/\text{g}^*$
Power Density ( $^{244}\text{Cm}_2\text{O}_3$ -88% T.D.)	21.6 $\text{W}_{\text{th}}/\text{cm}^3^*$

\* Two year old fuel as per Figure 1.

Employing the information presented in Table IV, it can be calculated that a 0.36  $\text{cm}^3$  sintered  $^{244}\text{Cm}_2\text{O}_3$  pellet (88% T.D.) fabricated using two-year old material would yield 7.8  $\text{W}_{\text{th}}$ . Since it is highly desirable to maintain the exact pellet dimensions of the current  $^{238}\text{PuO}_2$  fuel pellets, this suggests that a corresponding volume of 0.36  $\text{cm}^3$  of

$^{238}\text{PuO}_2$  needs to be “subtracted” from the current volume of a  $^{238}\text{PuO}_2$  pellet. Removing this amount of  $^{238}\text{PuO}_2$  will reduce the pellet’s thermal output by  $1.5 W_{\text{th}}$ ; considering that fuel pellets are 2.7 cm in diameter x 2.7 cm in height, are 151 g, and have a thermal output of  $62.5 W_{\text{th}}$ . To compensate for the reduced thermal output of the “subtracted”  $^{238}\text{PuO}_2$  material, the volume of a sintered  $^{244}\text{Cm}_2\text{O}_3$  pellet would need to be slightly increased by  $0.08 \text{ cm}^3$  for a total of  $0.44 \text{ cm}^3$ . The authors accept that the accuracy of the calculation is at the few % level. The authors also accept that a more accurate approach would be to use a conversion of the values to a W per mole to determine the convergence point of the mole fraction of Cm and the desired thermal output.

A  $0.44 \text{ cm}^3$  sintered 88% T.D.  $^{244}\text{Cm}_2\text{O}_3$  pellet would have a mass of 4.5 g.

As previously discussed, it is conceptually feasible to “add”  $^{244}\text{Cm}_2\text{O}_3$  to a  $^{238}\text{PuO}_2$  pellet in two ways; 1) mixing a specific ratio of the two oxide powders to make a mixed oxide pellet, or 2) placing a separate small volume sintered  $^{244}\text{Cm}_2\text{O}_3$  pellet into a  $^{238}\text{PuO}_2$  pellet. Figure 5 presents one conceptual concept for obtaining such a dual  $^{244}\text{Cm}_2\text{O}_3$ - $^{238}\text{PuO}_2$  fuel pellet configuration. In this example, “half” replica alumina fuel pellets were pressed with a center indent and then sintered (Figure 5, left). Figure 5 (center) shows a simulated  $^{244}\text{Cm}_2\text{O}_3$  pellet of the needed geometry to yield the required additional thermal heat positioned in a half replica pellet’s indent. In this example, the simulated  $^{244}\text{Cm}_2\text{O}_3$  ceramic pellet has been welded within a cladding of molybdenum (represented by the small metal component). This is only presented as a concept to create a clean interface between the Cm-based thermal component of the pellet and the Pu-based component of the fuel pellet. Other approaches of directly inserting the ceramic Cm pellet in the indent could be considered.

The feasibility of fabricating  $^{244}\text{Cm}_2\text{O}_3$  pellets has been demonstrated by researchers at Oak Ridge National Laboratory (ORNL) in the 1970s. DiStefano and Lin discuss the ceramic processing of  $^{244}\text{Cm}_2\text{O}_3$  pellets employing curium-244 powder, obtained mainly from Savannah River Laboratory (Aiken, South Carolina) (Ref. 11). The curium-244 metal powder was 95 wt.% isotopic and it was first oxidized via calcining at  $1335^\circ\text{C}$  into  $^{244}\text{Cm}_2\text{O}_3$  powder. This powder was employed in the fabrication of ceramic pellets using a vacuum hot press. The hot press temperature was  $1445^\circ\text{C}$  utilizing a one-hour soak. Another reference related to the then current  $^{244}\text{Cm}_2\text{O}_3$  program at ORNL discusses pellets of up to 10 g in weight (Ref. 12). Each of the larger 10 g sintered cerium oxide pellets may have had a thermal output up to  $24 W_{\text{th}}$ .

Molybdenum is identified as a possible candidate cladding material for  $^{244}\text{Cm}_2\text{O}_3$  since: a) high temperature long term tests at ORNL in the 1970s demonstrated that  $^{244}\text{Cm}_2\text{O}_3$  and molybdenum have very good compatibility,

and b) the Pioneer and Viking missions successfully employed a  $^{238}\text{PuO}_2/\text{Mo}$  cermet fuel (Refs. 11 and 16). Figure 5 (right) presents an assembly of two ceramic processed half pellets with an internal simulated clad  $^{244}\text{Cm}_2\text{O}_3$  pellet. Once stacked, an assembly of this type could be welded within an iridium cladding similar to a RTG fuel clad.

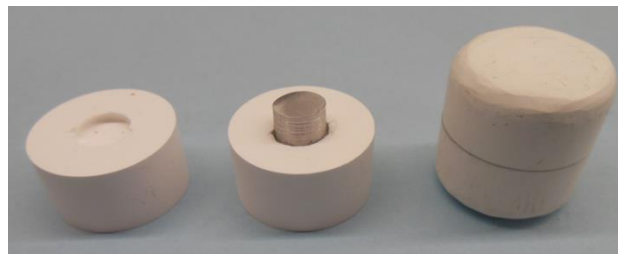


**Fig 5.** (left) Conceptual indented sintered half fuel pellet, (center) a simulated and molybdenum clad  $^{244}\text{Cm}_2\text{O}_3$  pellet positioned in the half fuel pellet’s indent, and (right) assembled dual fuel pellet 2.6 cm diameter by 2.6 cm in height.

## II. CONCLUSIONS

The paper outlines hypotheses regarding the utilization of relatively higher activity and shorter half-life radioisotopes such as  $^{232}\text{U}$  and  $^{244}\text{Cm}$  to boost the thermal power output of longer-lived radioisotopes  $^{241}\text{Am}$  and  $^{238}\text{Pu}$ . The implications are reduced mass at RTG and RHU system level in the case of European  $^{241}\text{Am}$  based RPS. The paper theorizes that the utilization of  $^{232}\text{U}$  and  $^{244}\text{Cm}$  in manageable small quantities at the 15% level.

A first-order conceptual application of  $^{244}\text{Cm}$  to enhance the operating performance of the legacy GPHS-RTG is discussed. The utilization of the dimensionally larger Step 2 GPHS modules would result in a  $>10\%$  decrease in thermal and electrical power for a mission. The study theorizes that the addition of a second  $^{244}\text{Cm}$ -based pellet within a  $^{238}\text{PuO}_2$  fuel pellet would compensate for the  $>10\%$  reduction in thermal power output. This would enable the GPHS-RTG performance criteria to be maintained.

The authors recognize that there are many questions to address as part of any practical implementation of the concepts presented, but this work does outline the potential benefits of exploring how solid solutions or mixed oxide fuels could enhance the operating performance of future RPS technologies and missions.

## ACKNOWLEDGMENTS

The authors would like to thank Steven Goodrich at the University of Dayton. The University of Leicester is funded by the European Space Agency.

## REFERENCES

1. D. P. KRAMER, C. E. WHITING, C. D. BARKLAY, R.M. AMBROSI, “Nuclear Heat Source Considerations for an Icy Moon Exploration Subsurface Probe,” *Proceedings of the Nuclear Emerging Technologies for Space (NETS2019)*, Richland WA, February 2019.
2. D. P. KRAMER, R. M. AMBROSI, C. E. WHITING, C. D. BARKLAY, and E. J. WATKINSON, “Curium-244 as a Potential Thermal and Electrical Power Source for an Icy Moon Subsurface Probe,” *Proceedings of the European Space Power Conference (ESPC2019)*, Juan-Les-Pins, France, September-October, 2019.
3. R. M AMBROSI, H. WILLIAMS, E J WATKINSON, et al., *European Radioisotope Thermoelectric Generators (RTGs) and Radioisotope Heater Units (RHUs) for Space Science and Exploration*, *Space Science Reviews*, **215:55** (2019)  
<https://doi.org/10.1007/s11214-019-0623-9>
4. M. SANSFIELD, C. CAMPBELL, C. CARRIGAN et al., E3S Web Conf. **16**, 05003 (2017)  
<https://doi.org/10.1051/e3sconf/20171605003> .
5. M. SANSFIELD, J. BROWN, C. CAMPBELL et al., *Progress in Nuclear Energy*, **106**, 396–416 (2018)  
<https://doi.org/10.1016/j.pnucene.2018.02.008> .
6. J-F. VIGIER, D. FREIS P. PÖML et al., *Inorganic Chemistry* **578**, 4317–4327 (2018)  
<https://doi.org/10.1021/acs.inorgchem.7b03148> .
7. P. E. RAISON, R. G. HAIRE, *Structural investigation of the pseudo-ternary system  $AmO_2$ – $Cm_2O_3$ – $ZrO_2$  as potential materials for transmutation*, *Journal of Nuclear Materials*, **320**, 31-35 (2003).
8. W. MÜLLER, F. MAINO, J.-C. TOUSSAINT, *The Isolation of Americium and Curium from Irradiated  $^{241}Am$  Targets*, JRC Report EUR 4232 e (1969).
9. E. Lamb, “ORNL Isotopic Power Fuels Quarterly Report for Period Ending September 30, 1971,” ORNL-4750, Oak Ridge National Laboratory, Oak Ridge TN, December, 1971.
10. J.P. HIERNAUT and C. RONCHI, “Curium Vaporization from  $(Cm,Pu)_2O_3$  and from Irradiated Oxide Fuel: Mass Spectrometric Measurement,” *Journal of Nuclear Materials*, **334** 133-138, (2004). DOI:10.1015/j.jnucmat.2004.05.009
11. J. DiSTEFANO and K. LIN, “Compatibility of Curium Oxide with Refractory Metals at 1650°C and 1850°C,” ORNL-4773, Oak Ridge National Laboratory, Oak Ridge TN, April 1972.
12. P. ANGELINI and R. McHENRY, “Helium Release from  $^{244}Cm_2O_3$ ,” ORNL-4785, Oak Ridge National Laboratory, Oak Ridge TN, November 1973.
13. <http://spaceflight101.com/newhorizons/spacecraft-overview/>
14. D.R. PANTANO and D.H. HILL, “Thermal Analysis of Step 2 GPHS for Next Generation Radioisotope Power Source Missions,” *Space Technology and Applications International Forum-STAIF 2005*, Albuquerque NM, CP746, p. 827-834, American Institute of Physics (2005).
15. J. POSEY, “Curium-244 Isotopic Power Fuel-Chemical Recovery from Commercial Reactor Fuels,” Conf-730602—1, Isotopes Development Center, Oak Ridge National Laboratory, Oak Ridge TN, January 1973.
16. J. A. ANGELO JR. and D. BUDEN, *Space Nuclear Power*, pp. 133-157, Orbit Book Company, Inc., Malabar, Florida (1985).

## CASSINI LIGHTWEIGHT RADIOISOTOPE HEATER UNIT CHARACTERIZATION AND SURVEILLANCE

Megan Armstrong<sup>1</sup>, Thomas Ricketts<sup>1</sup>

<sup>1</sup>Los Alamos National Laboratory, Los Alamos, NM, 87545

Primary Author Contact Information: 505-665-2695 [armstrong@lanl.gov](mailto:armstrong@lanl.gov)

The Cassini mission was a collaborative effort between the National Aeronautics and Space Administration (NASA), the European Space Agency, and the Italian Space Agency. This mission was launched in 1997 and was used to examine Saturn, Saturn's rings, Titan (One of Saturn's moons), Icy Satellites, and Saturn's Magnetosphere. Cassini's official mission was completed in 2008, but NASA continued to use Cassini until September 2018. The mission was ended by sending Cassini into Saturn's atmosphere causing it to disintegrate.

Cassini provided more data during its 21 years of flight than it was designed to collect. This effort was supported by Los Alamos National Laboratory's (LANL) nuclear materials technology space program. LANL as the designer of the LWRHU worked with other Laboratories to provide Cassini with Lightweight Radioisotope Heater Unit (LWRHU) and General Purpose Heat Source (GPHS) fueled clads. During the production of the LWRHUs, 180 units were made and 59 of them still remain at LANL. After being stored for 25 years, there is a renewed interest in using the LWRHUs for new applications. LANL recently performed an inspection and characterization of these units to understand their current condition.

### I. INTRODUCTION

A Lightweight Radioisotope Heater Unit (LWRHU) is an assembly containing an encapsulated hot-pressed Heat Source Plutonium Dioxide (HS-PuO<sub>2</sub>) fuel pellet. The rest of the assembly, the graphite insulator and the aeroshell body made of fine weave pierce fabric (FWPF), were made to contain the fuel pellet and protect it from the various potential environments that the LWRHU may face. These environments are the launch, launch abort, and Earth reentry.

LANL has stored the remaining Cassini LWRHUs since 1995. These LWRHUs were designed in the 1980s and fabrication started in the mid-1990s. Out of the 59 LWRHUs at LANL, 44 of them have their Certificate of Inspection (CoI), designating them flight quality. Flight quality units are approved for use during NASA missions.

The rest are considered Engineering Use Only (EUO). In order to validate the quality of the existing LWRHU inventory at LANL, several inspections and non-destructive tests have recently been performed.

Out of the existing LWRHU inventory in storage, nine units were selected for evaluation. Four of them are Flight Quality and the other five are classified as Engineering Use Only.

### LIGHT-WEIGHT RADIOISOTOPE HEATER UNIT (LWRHU)

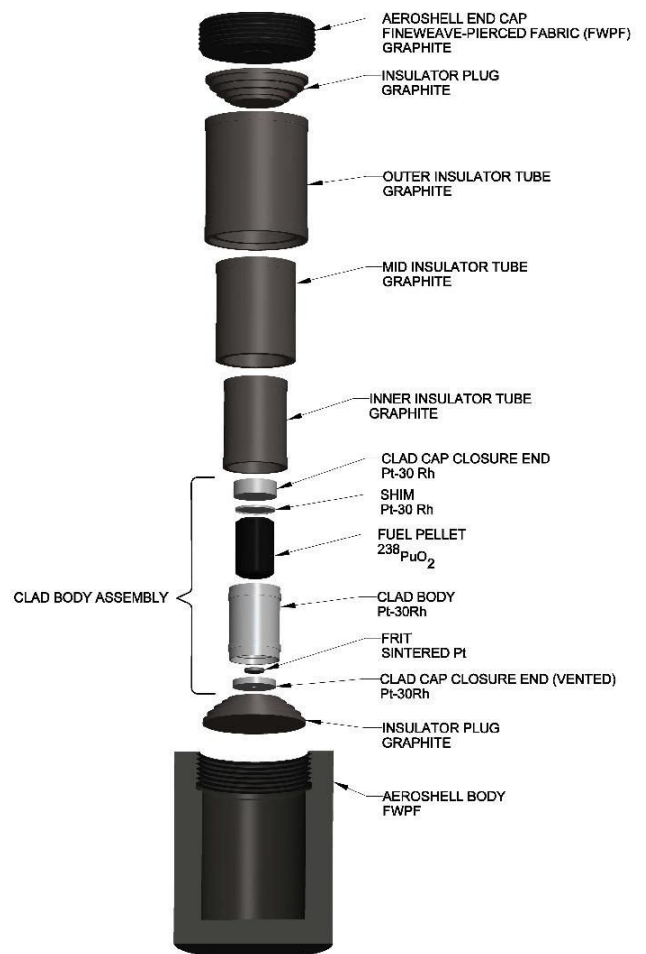


Fig. 1. The LWRHU assembly exploded view.

## II. EVALUATION

Using non-destructive techniques, the initial evaluation of the selected LWRHUs was to ensure the integrity of the assembly after 25 years of storage. It is important to ensure that there were no unexpected reactions between the HS-PuO<sub>2</sub> and the cladding material, no apparent breach in cladding containment/vent and that the graphitic components have maintained their integrity.

### II.A. Aeroshell Inspection

The primary inspection of the LWRHUs' aeroshells consisted of a visual inspection and a radiological smear.

#### II.A.1. Visual Inspection

The visual inspection looked for any anomalies in the graphite aeroshell such as chips, cracks, discoloration, and graphite imperfections that could have resulted during storage. There were no anomalies reported in any of the units' aeroshells. In figure 2, the Flight Quality LWRHUs can be seen.

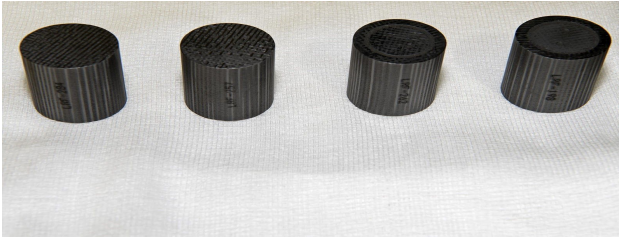


Fig. 2. Flight Quality LWRHUs during visual inspection.

#### II.A.2. Radiological Smear

The radiological smear was conducted by using a cotton smear and thoroughly wiping the outside of the unit's aeroshell. Then using a calibrated Eberline Alpha Scintillation Counter SAC-4 to measure any alpha activity from the aeroshell. Each unit resulted with no detectable activity indicating there was no removable contamination.

### II.B. Dose and Calorimetry

#### II.B.1. Dose Readings

The dose (gamma and neutron) measurements were taken of each of the nine LWRHUs at contact and 30 cm. These measurements can be seen in Table I. The measurements were taken to verify that the LWRHU dose was still low and no reaction occurred that might have caused an unexpected increase in dose. Too high of a dose rate can be harmful to spacecraft components that the LWRHU is used to heat, so it is important that the fuel capsule maintains a low dose rate.

The gamma results were obtained using a Thermo Scientific Model RO-20, portable air ionization chamber

instrument. The neutron results were obtained using an E-600/Neutron Rem Detector (NRD) Ball Survey Meter. It should be noted that even though the location of dose measurements was carefully selected to reduce background impacts, working in a nuclear facility, slight variation in the dose results are not unexpected.

TABLE I. Dose Readings of the LWRHUs

Flight Quality	Gamma/ Neutron	Contact/30cm mRem/hr
LRF-284	γ	1.3/0.2
	η	0.5/0.25
LRF-198	γ	1.0/0.1
	η	0.5/0.25
LRF-257	γ	1.1/0.2
	η	0.5/0.25
LRF-262	γ	1.2/0.2
	η	0.9/0.25
Engineering Use Only		
LRF-278	γ	1.0/0.1
	η	0.5/0.25
LRF-302	γ	1.2/0.1
	η	0.3/0.25
LRF-296	γ	1.4/0.2
	η	0.5/0.25
LRF-298	γ	1.2/0.2
	η	0.9/0.25
LRF-307	γ	1.7/0.2
	η	0.9/0.25

#### II.B.2. Calorimetry Results

The LWRHUs were designed so that they would supply approximately 1 thermal watt for the first 7 years of use. In September of 1995, the wattage of each LWRHU was measured and recorded. Due to delayed production approval, a few of the LWRHUs were measured in October 1998. Since it has been 25 years, the thermal wattage has naturally decreased due to the decay of the plutonium-238. Using the following equation an estimated wattage was determined.

$$W = W_i * e^{(-\ln(2) * (\frac{Decay\ Period}{Pu^{238}\ Half\ Life}))} \quad (1)$$

Calorimetry was used to measure the current output wattage of each unit identified for the surveillance activities. This was compared to the estimated output wattage to ensure that there were no anomalies noted. The measured watts, estimated (calculated) watts, and the new measured watts for each of the nine LWRHUs can be seen in table II.

**TABLE II.** Calorimetry Readings of the LWRHUs

Flight Quality	Measured Watts (September 1995)	Calculated Watts (October 1, 2019)	New Measured Watts (September/October 2019)
LRF-284	1.052	0.87	0.870
LRF-198	1.049	0.867	0.866
LRF-257	1.049	0.867	0.869
LRF-262	1.049	0.868	0.868
Engineering Use Only			
LRF-278	1.048	0.867	0.867
LRF-302	1.025*	0.869	0.872
LRF-296	1.024*	0.868	0.867
LRF-298	1.025*	0.869	0.870
LRF-307	1.025*	0.869	0.869

**Note:** \*Watts were measured in October 1998

When comparing the measured wattage to the calculated wattages, there are no anomalies. All measured wattages were within  $\pm 0.003$  watts of the calculated values.

### III. GEOMETRY

#### III.A. Computerized Tomography

Computerized Tomography (CT) is a non-destructive test that uses a 150 kV microfocus x-ray system to examine the LWRHU assembly. The goal of using the CT technique was to examine the graphite components (insulator tubes and aeroshell) for any potential anomalies. In addition, a shadow-graph of each fueled clad was obtained to ensure cladding integrity and to evaluate for possible cladding distention. One example of this can be seen in Figure 3. With the density difference between the graphite and the HS-PuO<sub>2</sub> fuel pellet and the cladding an evaluation can be made as to the integrity of the Pt-30Rh cladding. Also, whether or not a breach occurred and if any fuel may have escaped the cladding over the years.

Figure 3 below shows the CT scans of one of the selected LWRHUs. The images show the ends of the aeroshell, the graphite insulator layers, and the fuel clad body. Each layer of the assembly was examined for anomalies.

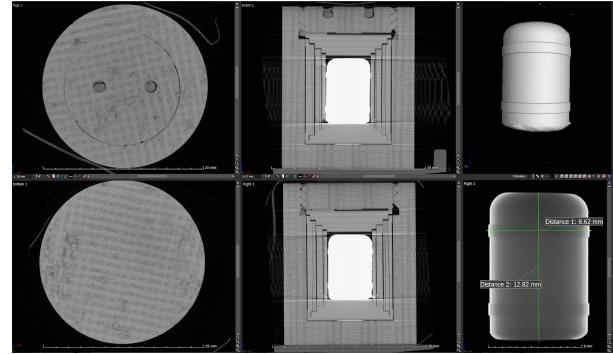


**Fig. 3.** The CT scan results of the LFR-284 unit.

**TABLE III.** CT Measurements Results

Flight Quality	Diameter of Fueled Clad (mm)	Length of Fueled Clad (mm)
LRF-284	8.62	12.82
LRF-198	8.57	12.84
LRF-257	8.54	12.80
LRF-262	8.55	12.80
Engineering Use Only		
LRF-278	8.56	12.80
LRF-302	8.60	12.82
LRF-296	8.60	12.77
LRF-298	8.58	12.81
LRF-307	8.59	12.81

The geometry of the cladding allows the fuel clad to have a maximum diameter of 8.65mm and a length of 12.85 mm. Since the fuel pellet fabrication is a difficult process, getting precise sizes on each unit is not feasible. All the LWRHUs above meet that requirement. The results concluded that there were no anomalous conditions in any fuel clad or graphite for all nine LWRHUs.

#### III.B. Digital Radiography

Digital radiographs using 3.5 MeV X-ray were taken of each LWRHU. This was used to examine integrity and possible distention in the fueled clads. In addition, the cladding wall thickness and the physical condition of the fuel pellet were examined. The diameter and length of the fueled clad were also measured. These values validated the measurements from the CT scans in Table III.

Figure 4 is an example of one of the DR scans taken of the selected LWRHUs. The scans of the nine LWRHUs concluded that there were no cladding concerns of

dimensional issues or distention. All wall thickness measurements were consistent, this indicates that no thinning or degradation has occurred during storage.

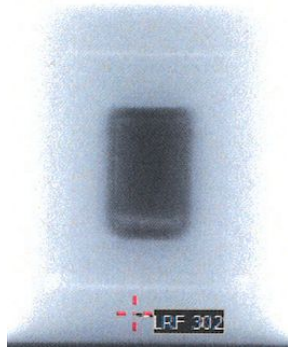


**Fig. 4.** The DR scan of LRF-302's entire assembly.

Figure 5 is an example of a scan that indicates cracking of the fuel pellet within the cladding.

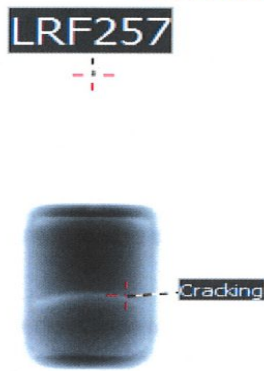


**Fig. 5.** DR scan of LRF-257's fueled clad.

In Table IV, the results of all nine digital radiographs can be seen. Minimal fuel cracking was determined on the number of cracks found in a fueled clad. One to two cracks was determined to be considered minimal cracking. The side wall thinning was also reported in Table IV.

**TABLE IV.** DR Inspection Results

Flight Quality	Fuel Clad Condition	Side Wall Thinning
LRF-284	Minimal Fuel cracking	No Thinning visible
LRF-198	Minimal Fuel cracking	No Thinning visible
LRF-257	Minimal Fuel cracking	No Thinning visible
LRF-262	Minimal Fuel cracking	No Thinning visible
Engineering Use Only		
LRF-278	Minimal Fuel cracking	No Thinning visible
LRF-302	No Fuel cracking	No Thinning visible
LRF-296	No Fuel cracking	No Thinning visible
LRF-298	Minimal Fuel cracking	No Thinning visible
LRF-307	No Fuel cracking	No Thinning visible

#### IV. CONCLUSIONS

After non-destructive testing and examination of the selected nine LWRHUs from storage, it is apparent that they are still in excellent condition. Each of the nine assemblies appear to be intact with no anomalies, signs of loss containment, cladding distention, or side wall thinning of the fuel pellet encapsulation. The fuel pellets showed signs of minimal cracking. In no cases, were there signs that the cladding encapsulation had lost its integrity and HS-PuO<sub>2</sub> fuel had escaped.

The thermal output of each unit was as expected to be after 25 years. This characterization provides valuable information on the current inventory's condition and ageing behavior for potential users.

#### ACKNOWLEDGMENTS

I would like to thank both of my mentors Jackie Lopez-Barlow and Stacey Eaton for the opportunity to work with them and all the guidance they have given me. I would also like to thank Tom Ricketts for his technical assistance and characterization data for this report. The technical expertise of Timothy Ickes who performed and interpreted the CT and DR measurements is greatly appreciated.

#### REFERENCES

1. G.H. Rinehart, "Lightweight Radioisotope Heater Unit (LWRHU) Production for the Cassini Mission,"

Los Alamos National Laboratory report  
LA-13143-MS (May 1996)

2. R. E. Tate, "The Light Weight Radioisotope Heater Unit (LWRHU): A Technical Description of the Reference Design," Los Alamos National Laboratory report, LA-9078-MS (January 1982)

## TURBO-BRAYTON CONVERTER FOR RADIOISOTOPE POWER SYSTEMS

Jeffrey J. Breedlove<sup>1</sup>, Thomas M. Conboy<sup>1</sup>, and Mark V. Zagarola<sup>1</sup>

<sup>1</sup>Creare LLC, 16 Great Hollow Road, Hanover, NH 03755

Jeffrey J. Breedlove: 603-643-3800, [jfb@creare.com](mailto:jfb@creare.com)

Creare has teamed with Aerojet Rocketdyne, West Coast Solutions, Sest Incorporated, and the University of New Mexico Institute for Space and Nuclear Power Studies (UNM ISNPS) to develop a turbo-Brayton power converter for future National Aeronautics and Space Administration (NASA) missions that use radioisotope heat sources. NASA has considered the closed Brayton cycle attractive for space since the 1960s, and Creare has developed miniature Brayton technology for over 40 years. Key characteristics include high specific power, high efficiency, long-life operation without wear, undetectable vibration, and flexible packaging. Detailed design results indicate a 300 We-class converter with a turbine inlet temperature of 730°C will have a thermal-to-electric conversion efficiency of nearly 25% and a specific power greater than 20 We/kg.

### I. INTRODUCTION

Future NASA space missions require advanced systems to convert thermal energy into electric power for long durations. Closed-loop Brayton converters are attractive for these applications because they enable high reliability, long life, and high specific power. They also consist of discrete components that can be packaged to fit optimally with other subsystems, and their continuous gas flow can communicate directly with remote heat sources and heat rejection surfaces without heavy conductive links or intermediate flow loops.

Prior closed Brayton cycle work at Creare has focused on cryogenic refrigerators for spaceflight applications. This experience provides critical expertise, which is now being leveraged to develop power converters for space. The resulting technology is readily scalable for power levels from tens of watts to hundreds of kilowatts and beyond. Potential near-term NASA applications include Radioisotope Power System (RPS) devices, “Kilopower” reactor concepts, Nuclear Electric Propulsion (NEP), and Surface Power missions.

Creare, Aerojet Rocketdyne, West Coast Solutions, UNM ISNPS, and Sest form a complementary team. Creare is designing, fabricating, and testing the converter; Aerojet Rocketdyne is performing system integration activities; and West Coast Solutions is designing spaceflight power conversion and control electronics. Earlier in the program, UNM ISNPS evaluated the thermal performance of the heat source assembly, and

Sest assessed converter reliability and robustness. The combined efforts of our team enable design and development of a prototype converter with a path to a complete generator system that is practical and attractive for future space missions.

### II. TECHNOLOGY DESCRIPTION

Figure 1 is a schematic representation of a closed-loop Brayton converter. In this configuration, the compressor pressurizes the cycle gas and forces it to pass through the system in a continuous loop of steady flow. The temperature of the cycle gas increases as it flows through the recuperator and the hot interface heat exchanger. The hot, high-pressure gas then produces mechanical power as it expands through the turbine. The turbine exhaust stream transfers most of its heat to the high-pressure flow stream via the recuperator. The pre-cooler then transfers waste heat to the heat rejection system before the gas is re-pressurized. The compressor impeller and turbine impeller are attached to a common shaft with a permanent-magnet alternator between them. As a result, the mechanical power produced by the turbine drives the compressor directly, and excess shaft power generates electric power via the alternator. The power conversion electronics transform the high-frequency, three-phase, alternator output into regulated DC power for general use. A heat rejection system transfers waste heat from the pre-cooler, turbomachine housing, and electronics to space via radiator surfaces.

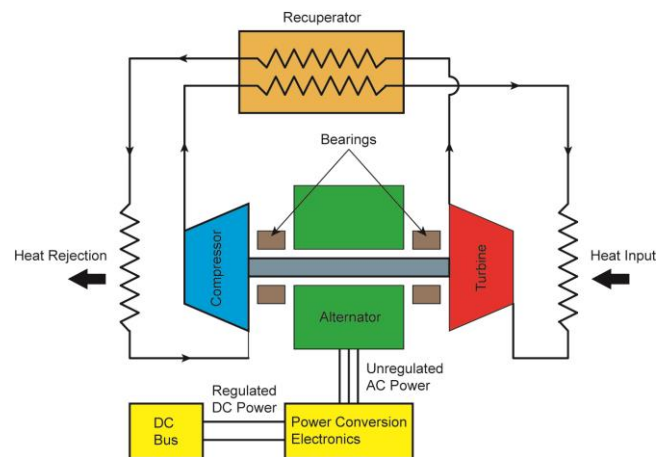


Fig 1. Schematic for closed-loop Brayton converter.

The only moving part in the converter is a miniature turbomachine rotor. Hydrodynamic gas bearings and clearance seals eliminate mechanical contact between moving surfaces. This lack of contact permits high rotational speeds, which is important for high efficiency and specific power; and it also enables extremely long maintenance free life. Creare has performed several reliability and endurance tests, including a 14 year life test and over 10,000 start/stop cycles with no maintenance, wear, or performance degradation.<sup>1</sup>

### III. HERITAGE

The converter builds on proven technology for miniature turbo Brayton systems Creare has developed for long duration space missions. These systems have satisfied rigorous NASA and Department of Defense requirements for reliability, endurance, vibration emittance, space launch tolerance, electromagnetic interference and susceptibility, and environmental cycling.<sup>1,2</sup> One such system is a turbo Brayton cryocooler that operated on the Hubble Space Telescope for over 6.5 years without maintenance or performance degradation while meeting all mission requirements.<sup>3</sup> Subsequently, Creare made significant improvements in manufacturing,<sup>4</sup> and is continuing advanced component and system development for several emerging applications.<sup>5,6</sup> Creare began applying turbo Brayton technology toward the development of miniature power converters for NASA in 2001,<sup>7,8</sup> and this work is continuing today. These projects have demonstrated fundamental technologies required at the sizes, power levels, temperatures, and rotational speeds needed for radioisotope power system converters.

### IV. TURBOMACHINE

A single turbomachine assembly contains the turbine, alternator, and compressor. It has a hot end and cold end, joined together by relatively thin metal features. These thin features provide adequate structural rigidity for mechanical loads while minimizing conductive heat transfer. The compressor, alternator, and bearings are located at the cold end of the assembly. The rotor shaft extends from the cold end to the hot end, where the turbine is located. The turbine is the only major component at the hot end of the assembly.

The turbomachine includes a small high-speed rotor with a mass of only 39 grams. The rotor has a compressor impeller and a turbine impeller attached to a common shaft, and a permanent magnet is installed inside the hollow shaft to provide the rotating magnetic field for the alternator. The impeller diameters are 19 mm (0.75 inch), and the shaft diameter is 9.53 mm (0.375 inch). Figure 2 is a photograph of the compressor impeller (left) and turbine impeller (right).

The turbomachine is designed to operate during launch, consistent with RPS program requirements. Prior

Creare Brayton systems have completed vibration qualification testing and spaceflight launches. Most notably, the Creare cryocooler on the Hubble Space Telescope endured qualification testing, two launches, and one landing. Several other programs have also conducted vibration tests with Creare turbomachines. However, none of these tests were performed while the turbomachines were operating because none of the applications required operation during launch. Consequently, extensive dynamic CFD analyses have been completed to assess rotordynamic operation during launch, and a risk-reduction test will be performed with a representative rotor assembly to corroborate the results.



Fig 2. Compressor impeller (left) and turbine impeller (right).

### V. RECUPERATOR

The recuperator is a micro tube heat exchanger with counter current flow. It is an advanced adaptation of traditional shell and tube technology commonly used for industrial heat exchangers. The RPS embodiment is significantly lighter and smaller than conventional shell and tube heat exchangers and plate fin units with the same performance characteristics. High performance is achieved by utilizing thousands of very small tubes. Small length scales enable extremely high heat transfer area per unit volume without the need for secondary surfaces (i.e., fins). The result is very high heat transfer density with very low pressure losses. Longitudinal conduction from the hot end to the cold end is also very low, which is important when high thermal effectiveness is desired.

The RPS recuperator is very similar to five units Creare recently built for a turbo-Brayton refrigerator to enable cryogenic propellant storage in space for NASA missions.<sup>9</sup> The cryocooler version passed NASA GEVS launch vibration qualification testing, and analyses indicate the RPS version has greater design margin.

The recuperator is an all-welded stainless steel assembly. There are no braze joints. The tubes are 304 stainless steel (UNS S30400), and all of the other components are 316L stainless steel (UNS S31603). Stainless steel has acceptable strength and creep resistance for the specified operating conditions. The predicted stress in the micro tubes is only 8.9 MPa

(1,300 psi) due to their small diameter. Stresses in the outer shell and headers are greater because of their larger sizes; however, material thicknesses in these areas have been specified to achieve acceptable creep life with desired reliability.

Creare developed the micro tube heat exchanger technology and associated manufacturing processes collaboratively with Mezzo Technologies Incorporated and Edare Incorporated. Several units have been built, and the required fabrication processes have been demonstrated. The supply chain, manufacturing process, and quality control are well established and have demonstrated consistently high quality. Figure 3 is a photograph of the recuperator built for the RPS prototype converter.



**Fig 3.** Recuperator for RPS prototype converter.

## VI. LIFE AND RELIABILITY

Long life with high reliability is critical for spaceflight power systems. Consequently, Sest was recruited to conduct an objective life and reliability assessment with assistance from Creare. The results from this work formed the basis for further independent review currently being conducted by a Risk-Informed Life Testing (RILT) team led by the Johns Hopkins University Applied Physics Laboratory.

Long life is straightforward to achieve since there is no lubrication or sliding contact during operation, and axisymmetric rotation produces negligible reciprocating forces to initiate fatigue. The life-limiting factor for the converter is centrifugal creep of the turbine rotor. Although high temperature and high speed are desired to maximize efficiency and specific power, both factors are limited to maintain centrifugal creep growth within acceptable limits. Detailed finite element analyses indicate that the RPS life goal of 20 years of operation time (3 years of ground storage and 17 years of operation in space) can be achieved with a turbine inlet temperature of 730°C, using Inconel 718 (UNS N07718) for the turbine impeller. However, creep tests with samples from the selected material lot are required to validate these predictions.

## VII. GENERATOR SYSTEM CONCEPT

Creare and Aerojet Rocketdyne worked together to develop a conceptual design for a generator system with a

spaceflight configuration. A key requirement is that the assembly must fit within the USA/9904/B(U)F-85 Radioisotope Thermoelectric Generator (RTG) Transportation System (RTGTS). The resulting design is very similar to the design Rockwell International Corporation (forerunner to Aerojet Rocketdyne) developed previously for the 500 We Dynamic Isotope Power System (DIPS) for the JPL Mariner Mark 2 spacecraft.<sup>10</sup> Figure 4 shows two Creare converters integrated with two electronics assemblies, six General Purpose Heat Source (GPHS) Step 2 modules, and a heat rejection system. This configuration enables both converters to operate at approximately half power, or one converter to operate at full power. The two converters are hermetically isolated from each other with independent gas charges, so they do not interact directly with each other.

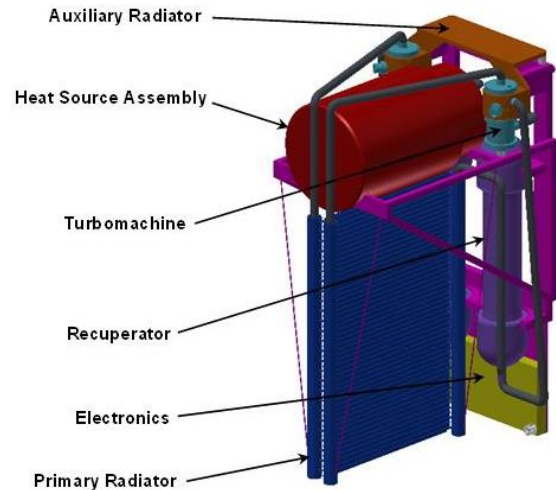


**Fig 4.** Baseline design for generator system.

Figure 5 illustrates an alternative power system design that replaces the planar radiator in our baseline configuration with a curved radiator. Although the curved radiator increases system mass, it is attractive because its larger surface area reduces the compressor inlet temperature to improve power conversion efficiency. The planar radiator discharges heat from both of its surfaces, with a total area of 0.80 m<sup>2</sup>; while we have assumed single-sided heat transfer for the curved radiator, with a total effective area of 1.19 m<sup>2</sup>. The primary drawback associated with the curved radiator is that it requires more fabrication development effort.

We predicted the performance of our power system for nine potential missions identified by NASA. The prototype converter we are developing is expected to produce 337 W of AC electric power with a turbine inlet temperature of 730°C and a compressor inlet temperature of 100°C. The corresponding thermal to electric conversion efficiency is 24.9%, and the power density is 20.4 W/kg. At the generator-system level, our baseline

design has an overall conversion efficiency of 21.3% and a specific power of 2.40 W/kg for reference operating conditions with a 4 K vacuum environment, while the alternative design with the curved radiator is at 26.7% and 2.60 W/kg for the same conditions. In both systems, the two converters and electronics modules are cross-connected to provide full power when either converter and/or either controller fail completely.

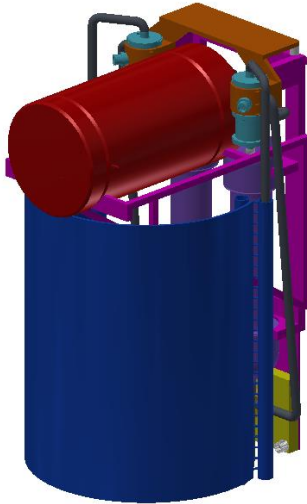


**Fig 5.** Alternative design for generator system.

### VIII. STATUS AND PLANS

We have completed detailed design activities for the converter assembly, and we are now fabricating a prototype unit for laboratory testing. Component fabrication is presently under way, and converter assembly is expected to be complete in June 2020. Operation and performance tests will then follow.

### IX. CONCLUSIONS

Creare and its partners are developing a turbo Brayton power converter to support future NASA RPS missions. This converter leverages extensive closed Brayton cycle technology developed at Creare over several decades with emphasis on cryogenic refrigerators for long-life spaceflight applications. This technology is now being adapted to create a converter that is designed to produce 337 W of electric power with a predicted thermal to electric conversion efficiency of 24.9% and a predicted specific power of 20.4 W/kg.

### ACKNOWLEDGMENTS

The information presented in this paper is based upon work supported by the National Aeronautics and Space Administration under Contract Number 80GRC17C0028.

### REFERENCES

1. J. J. BREEDLOVE, M. V. ZAGAROLA, G. F. NELLIS, J. A. GIBBON, F. X. DOLAN and W. L. SWIFT, Life and Reliability Characteristics of Turbo

- Brayton Coolers, pp. 489-498, R. G. ROSS, JR., Ed., Kluwer Academic/Plenum Publishers, New York, NY (2001).
2. F. X. DOLAN, W. L. SWIFT, LT. B. J. TOMLINSON, A. GILBERT and J. BRUNING, A Single Stage Reverse Brayton Cryocooler: Performance and Endurance Tests on the Engineering Model, pp. 465-474, Plenum Press, New York (1997).
3. W. L. SWIFT, F. X. DOLAN and M. V. ZAGAROLA, The NICMOS Cooling System – 5 Years of Successful On Orbit Operation, pp. 799-806, Trans Cryogenic Engineering Conference – CEC, 52, AIP Conference Proceedings, 985 (2008).
4. M. V. ZAGAROLA, J. J. BREEDLOVE, C. S. KIRKCONNELL, J. T. RUSSO and T. CHIANG, Demonstration of a Two Stage Turbo Brayton Cryocooler for Space Applications, pp. 461-469, S. D. MILLER and R. G. ROSS, JR., ICC Press (2008).
5. J. J. BREEDLOVE, K. J. CRAGIN and M. V. ZAGAROLA, Testing of a Two Stage 10 K Turbo Brayton Cryocooler for Space Applications, S. D. MILLER and R. G. ROSS, JR., ICC Press (2014).
6. M. V. ZAGAROLA, J. J. BREEDLOVE and K. J. CRAGIN, Demonstration of a High Capacity Cryocooler for Zero Boil Off Cryogen Storage in Space, International Cryocooler Conference 17, Los Angeles, CA (9-12 July 2012).
7. L. S. MASON, Realistic Specific Power Expectations for Advanced Radioisotope Power Systems, 4th International Energy Conversion Engineering Conference and Exhibit (IECEC), Paper AIAA 2006 4193, San Diego, CA (2006).
8. M. ZAGAROLA, M. G. IZENSON, J. BREEDLOVE, G. M. O’CONNOR, A. C. KETCHUM, R. L. JETLEY and J. K. SIMONS, An Advanced Turbo Brayton Converter for Radioisotope Power Systems, pp. 632-640, Space Technology and Applications International Forum—STAIF 2005, Publ. AIP Conf Proc 746, American Institute of Physics, Melville, NY (2005).
9. D. DESERRANNO, M. V. ZAGAROLA, D. CRAIG, R. GAREHAN, T. GIGLIO, J. SMITH, J. K. SANDERS and M. DAY, Performance Testing of a High Effectiveness Recuperator for High Capacity Turbo-Brayton Cryocoolers, 19th International Cryocooler Conference (ICC 19), San Diego, CA (2016).
10. OTTING, W., NASA [National Aeronautics and Space Administration] low power DIPS [Dynamic Isotope Power System] conceptual design study; Final report. United States: N. p., 1990. DOI: 10.2172/721000

## AN UPDATE ON THE DEVELOPMENT OF SKUTTERUDITE-BASED THERMOELECTRIC TECHNOLOGY FOR INTEGRATION INTO A POTENTIAL ENHANCED MULTI-MISSION RADIOISOTOPE THERMOELECTRIC GENERATOR (eMMRTG)

T. Caillat<sup>1\*</sup>, S. Pinkowski<sup>1</sup>, I. Chi<sup>1</sup>, C. -K. Huang<sup>1</sup>, K. Smith<sup>1</sup>, K. Yu<sup>1</sup>, J. Paik<sup>1</sup>, P. Gogna<sup>1</sup>, B. Phan<sup>1</sup>, E. Heian<sup>1</sup>, T. Holgate<sup>2</sup>, Y. Song<sup>2</sup>, J. VanderVeer<sup>2</sup>, R. Bennett<sup>2</sup>, S. Keyser<sup>2</sup>, P. Frye<sup>3</sup>, K. Wefers<sup>3</sup>, M. Hoffmann<sup>4</sup>, and M. Deminico<sup>4</sup>

<sup>1</sup>Jet Propulsion Laboratory/California Institute of Technology MS 277-207, 4800 Oak Grove Drive, Pasadena CA, 91107

<sup>2</sup>Teledyne Energy Systems, Inc., 10707 Gilroy Road, Hunt Valley, MD 21301

<sup>3</sup>Aerojet Rocketdyne, 8900 De Soto Ave, Canoga Park, CA 91304

<sup>4</sup>NASA Glenn Research Center, 21000 Brookpark Rd, Cleveland, OH 44135

\*Phone: 818-354-0407 e-mail: [thierry.caillat@jpl.nasa.gov](mailto:thierry.caillat@jpl.nasa.gov)

The concept of the enhanced Multi-Mission Radioisotope Thermoelectric Generator (eMMRTG) was first proposed in 2013. It is based on retrofitting the flight-proven MMRTG that uses PbTe/TAGS thermoelectric couples with higher-efficiency thermoelectric couples based on skutterudite (SKD) materials developed at the Jet Propulsion Laboratory (JPL) while keeping the balance of the system virtually unchanged. A multi-organization team composed of Teledyne Energy Systems, Inc., Aerojet Rocketdyne, the Idaho National Laboratory, NASA Glenn Research Center, and the Jet Propulsion Laboratory have collaborated over the last several years to develop and mature the SKD-based thermoelectric converter technology and to establish the potential of the eMMRTG to deliver a minimum of 77 We after 17 years of operation (i.e. 3 years under storage conditions and 14 years of operation). Several iterations of SKD couple development have been completed with evolving configurations to achieve a more robust design that could be manufactured with a sufficient yield and with the potential to achieve the eMMRTG life performance goals. This paper will briefly describe the eMMRTG concept, report on the most recent life performance test data for the couples, and discuss the potential of the latest iteration of SKD couples to meet the 77We power output goal at 17 years.

### I. Introduction

The flight-proven MMRTG is composed of sixteen, 48-couple modules composed of PbTe/TAGS thermoelectric couples packaged in fibrous insulation and is operated under inert gas in an hermetically sealed environment that contains O<sub>2</sub> and H<sub>2</sub> getters. The MMRTG is currently powering the Mars Curiosity rover, will power the next Mars M2020 rover and was selected for the Dragonfly spacecraft. The eMMRTG is nearly identical except for new, upgraded 48-couple modules.

The module along with other potential changes for the eMMRTG are illustrated in Figure 1. The first change would be to replace PbTe/TAGS-based couples with more efficient, higher temperature capable (i.e. increase in hot-junction temperature from 535°C to 600°C) skutterudite (SKD)-based couples. The second change is to replace the fibrous insulation used in the MMRTG 48-couple thermoelectric modules with SiO<sub>2</sub>-based aerogel. The third change is a modification to the liner inner surface finish to maintain an acceptable temperature and structural integrity for key system components. Figure 1 illustrates the three changes being considered.

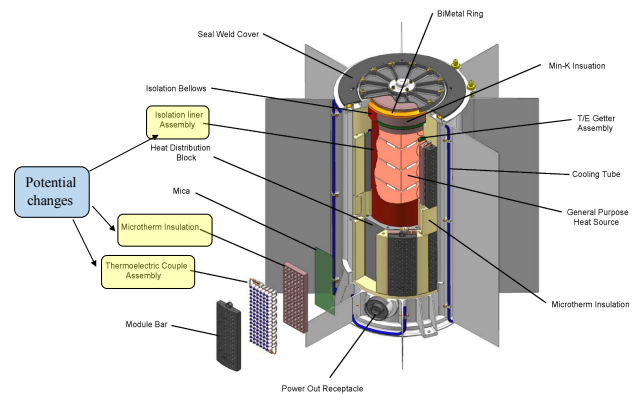


**Fig. 1.** Changes under consideration for the potential eMMRTG

One of the key performance requirements for the eMMRTG is its End-Of-Design-Life (EODL) capacity to produce at least 77 We of power output after 17 years, 3 years of storage and 14 years of operation, at the following conditions:  $T_{fr} = 157^{\circ}\text{C}$ ,  $Q_{BOL} = 1952 \text{ W}$ , and  $V_{load} = 34 \text{ V}$  ( $T_{fr}$  being the fin root temperature for the eMMRTG,  $Q_{BOL}$  the PuO<sub>2</sub> fuel inventory at beginning of life, and  $V_{load}$  the eMMRTG operating load voltage). The

approach chosen to verify this requirement relies on a combination of life test data for the thermoelectric couples/devices and a physics-based life performance prediction model used to generate the  $\geq 17$  year-life performance prediction.

This paper will present and discuss the couple life test data acquired to date for the latest SKD-based couple configuration and the current 17-year life performance prediction best estimate.

## II. Couple manufacturing and life test data

Over the course of the last several years, the project team has conducted several couple development cycles including fabrication and testing to arrive at the current configuration that has the potential to address some of the key degradation mechanisms identified for the earlier configurations. These SKD-based couples are illustrated in Figure 2. In collaboration with the Jet Propulsion Laboratory (JPL), Teledyne Energy Systems, Inc. (TESI) has demonstrated that they can manufacture these couples with a sufficient yield to support the potential production of a full eMMRTG unit within a similar timeframe that a typical MMRTG unit is produced. Beginning-of-life (BOL) performance test for these couples have shown that their power output are within a few percent of the predicted values.



**Fig. 2.** TESI-produced SKD-based couples with latest configuration

Figures 3-5 show the n-leg life test data (open circuit voltage (EOC), internal resistance (Ri) and peak power) for a number of couples produced and tested by TESI. The test temperatures are 550°C, 575°C, and 600°C. 550°C is approximately the hot-junction temperatures at which the couples would operate at BOL at the following conditions:  $T_{fr} = 157^\circ\text{C}$ ,  $Q_{BOL} = 1952 \text{ W}$ , and  $V_{load} = 34 \text{ V}$ . These are the operating conditions at which the 17-year 77We requirement needs to be met. Testing is also conducted at higher temperatures to assess the degradation at these temperatures. The couples are

designed never to operate at hot-junction exceeding 600°C. Up to about 11,000 hours of life test data have been acquired to date. Figures 6-8 show the same data for p-legs.

Performance of the n-legs, that produce about 2/3 of the couple power, is generally more stable than the performance of the p-legs. For n-legs, the performance is rather stable at 550°C (that corresponds to the BOL hot-junction temperature at which the EODL requirement needs to be met) but also at higher temperatures. For p-legs, the degradation over time is more pronounced and clearly shows a temperature dependence, with higher degradation at higher temperatures. The degradation rate appears to be higher initially but is decreasing significantly over the last several thousand hours. This is similar to RTGs that have been flown whether they use SiGe or PbTe/TAGS thermoelectric materials.

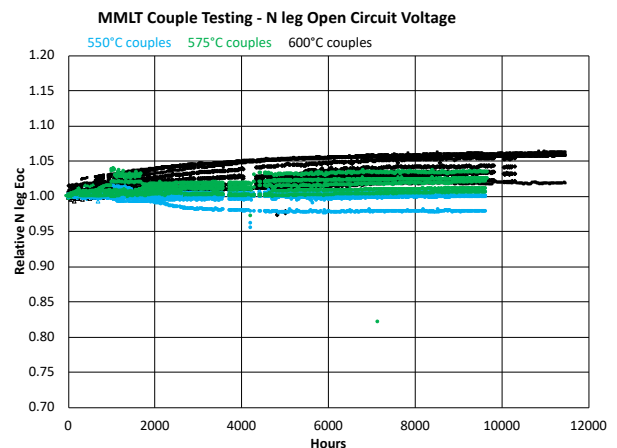


**Fig. 3.** Relative n-leg open circuit voltage (Eoc) as function of time for multiple SKD-based couples at 550, 575, and 600°C

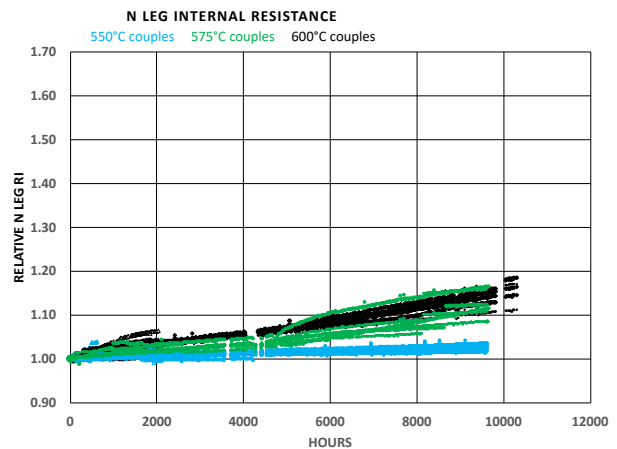


**Fig. 4.** Relative n-leg internal resistance (Ri) as function of time for multiple SKD-based couples at 550, 575, and 600°C

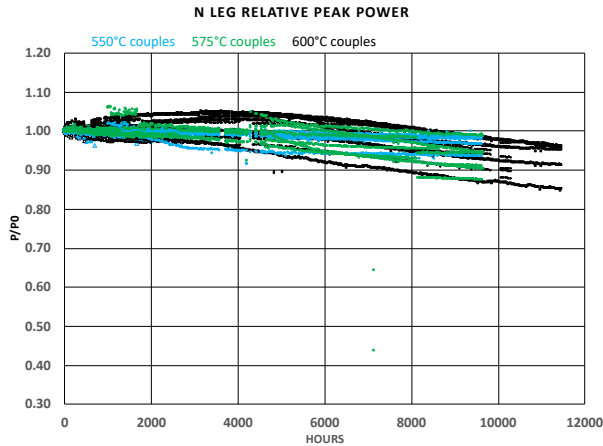


**Fig. 5.** Relative n-leg peak power as function of time for multiple SKD-based couples at 550, 575, and 600°C

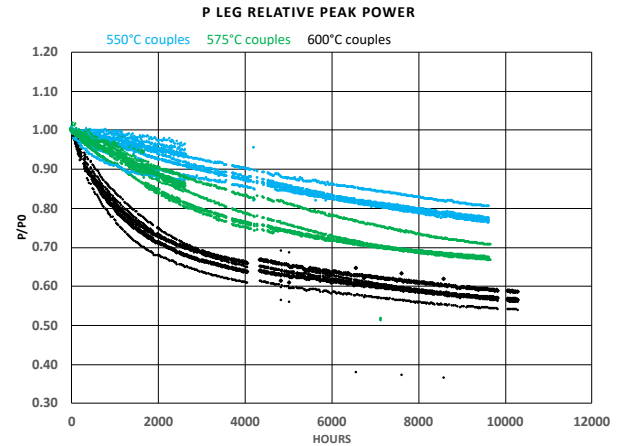


**Fig. 8.** Relative p-leg peak power as function of time for multiple SKD-based couples at 550, 575, and 600°C

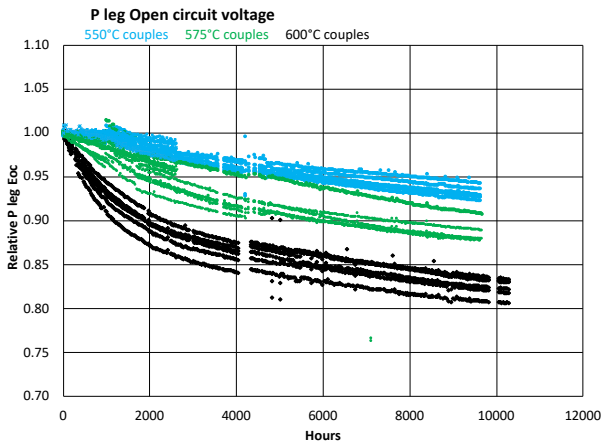


**Fig. 6.** Relative p-leg open circuit voltage as function of time for multiple SKD-based couples at 550, 575, and 600°C

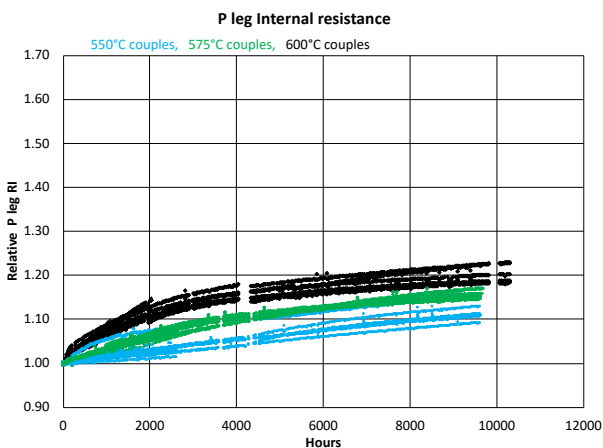


**Fig. 7.** Relative p-leg internal resistance ( $R_i$ ) as function of time for multiple SKD-based couples at 550, 575, and 600°C

Up to 2 years of SKD TE property life testing have been conducted to date and the results show that TE properties of SKDs remain unchanged over time at temperatures ranging from 550 to 640°C. Destructive Physical Analysis (DPA) of several couples tested at temperatures ranging from 550 to 600°C and for different durations have shown that the key degradation mechanism controlling the degradation of the p-legs, and to a much lesser extent of the n-legs, is the degradation of the couple hot-side interfaces between the SKD materials and the metallization adjacent to them. The degradation of these interfaces lead to an increase in the Electrical Contact Resistance (ECR) and Thermal Contact Resistance (TCR) at these interfaces that explain the decrease in open circuit voltage observed for the p-legs over time and the increase in internal resistance for the same p-legs.

It is therefore necessary to quantify the ECR and TCR variations over time and temperature to best predict the degradation over time and, in turn, the predicted eMMRTG power output over time. This is accomplished by both extracting the ECR and TCR values from couple life test data and developing extrapolation models based on couple DPA results and couple test data. The DPA results inform when the degradation associated with the chemical reaction at the hot-side interfaces will be completed and the degradation will level off. The ECR and TCR model will be refined as more DPA data is generated and more test data becomes available.

Figure 9 shows the current best eMMRTG power output prediction estimate based on current ECR and TCR best estimates for n- and p-legs. The prediction assumes 3 years of storage followed by 14 years of operation. Black curves are EODL eMMRTG power output with  $Q_{BOL} = 1952$  W,  $V_{load} = 34$  V, and  $T_{fr} = 157^\circ\text{C}$ . Blue is actual test data (1,000-hour increments) and red is extrapolated data

(10,000-hour increments). The current best 17-year eMMRTG power output estimate is 85We (requirement is 77We).

As previously mentioned, the confidence in the prediction will increase as more DPA and test data become available and the uncertainty associated with the various degradation models (e.g. ECR and TCR) is reduced. A relatively large number of couples remain on test and DPA is scheduled to produce the input needed to refine these models.

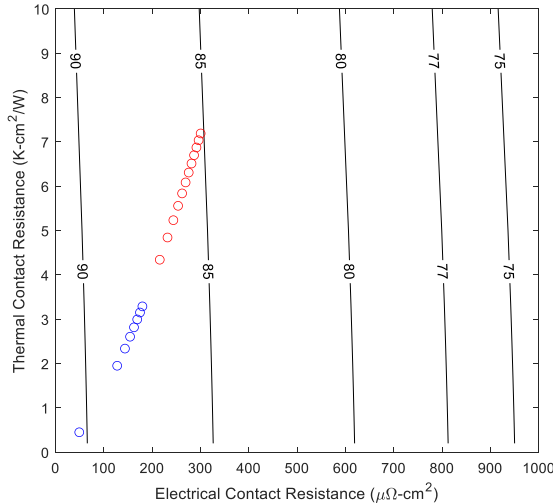


**Fig. 9.** The current eMMRTG 17-year power output prediction best estimate is 85We. The prediction assumes 3 years of storage followed by 14 years of operation. Black curves are EODL eMMRTG power output with  $Q_{BOL} = 1952 \text{ W}$ ,  $V_{load} = 34 \text{ V}$ , and  $T_{fr} = 157^\circ\text{C}$ . Blue is actual test data (1,000-hour increments) and red is extrapolated data (10,000-hour increments).

## II. CONCLUSIONS

The eMMRTG has the potential to provide a significant EODL power output increase over the MMRTG. The current eMMRTG 17-year power output prediction best estimate is 85We. Testing is continuing for a number of SKD-based couples to provide the input to the physics-based life performance prediction model and increase confidence in the EODL predictions.

## ACKNOWLEDGMENTS

This research was carried out, in part, at the Jet Propulsion Laboratory, California Institute of Technology, under a contract with the National Aeronautics and Space Administration.

Reference herein to any specific commercial product, process, or service by trade name, trademark,

manufacturer, or otherwise, does not constitute or imply its endorsement by the United States Government or the Jet Propulsion Laboratory, California Institute of Technology.

## REFERENCES

“An Update on the development of Skutterudite-Based Thermoelectric Technology for Integration into a Potential Enhanced Multi-Mission Radioisotope Thermoelectric Generator (eMMRTG)”, 2020 Deep Space Power Conference

“A Status Update on the eMMRTG Project”, 2019 IEEE Aerospace Conference

“Analysis of Raw Materials Sourcing and the Implications for the Performance of Skutterudite Couples in Multi-Mission Radioisotope Thermoelectric Generators”; Journal of Electronic Materials volume, Sept 2019

“Fabrication and Life Testing of Advanced Skutterudite-Based Unicouples for a Proposed Enhanced Multi-Mission Radioisotope Thermoelectric Generator”, Materials Research Society, Nov 27, 2018

“Skutterudite-Based Thermoelectric Technology for Integration into a Proposed eMMRTG: An Update”; Nuclear and Emerging Technologies, Feb 2017

“Advanced Skutterudite Unicouples for a Proposed Enhanced MMRTG”; Nuclear and Emerging Technologies, Feb 2017

## PROGRESS ON AN ALTERNATIVE SOLVENT EXTRACTION FLOWSHEET FOR SEPARATING PLUTONIUM FROM NEPTUNIUM

Catherine Campbell<sup>1</sup>, Michael Carrott<sup>1</sup>, Chris Maher<sup>1</sup>, Chris Mason<sup>1</sup>, Rebecca Sanderson<sup>1</sup>, Mark Sarsfield<sup>1</sup>, Robin Taylor<sup>1</sup>, Tim Tinsley<sup>1</sup>, Daniel Whittaker<sup>1</sup>, Dave Woodhead<sup>1</sup>

<sup>1</sup>National Nuclear Laboratory, Sellafield, Seascale, Cumbria, CA20 1PG, UK

+44 (0)1946 779259; email [mark.sarsfield@uknnl.com](mailto:mark.sarsfield@uknnl.com)

*The production of <sup>238</sup>Pu, to the specifications required for space flight, requires the separation of plutonium from neptunium and a range of fission products. The valuable neptunium is then recycled into targets for further irradiation. At Oak Ridge National Laboratory (ORNL) a solvent extraction process has been developed to separate neptunium using sodium nitrite to control the neptunium oxidation state in the neptunium strip section. This results in a neptunium product contaminated with sodium, which needs to be removed prior to recycling. NNL in the UK have developed a separation process that results in a sodium free neptunium product with very low levels of plutonium contamination thereby reducing the number of purification steps and thus simplifying the process.*

### I. Introduction

In the UK, a strategy of reprocessing spent nuclear fuel has led to a detailed understanding of solvent extraction technology to separate uranium and plutonium from highly radioactive fission products using the well-established Plutonium Uranium Redox Extraction (PUREX) process. One of the troublesome elements in PUREX is neptunium, which can be distributed throughout the various products and waste streams because of the complicated oxidation/reduction chemistry. Such behaviour requires the use of additional purification cycles to remove neptunium from the uranium and plutonium products; at considerable cost and increased volumes of waste. Over the last two decades NNL and others have compiled a large body of experimental data to help understand the kinetics and thermodynamics of neptunium speciation under conditions of relevance to the PUREX process (Ref 1 and refs therein).

This expertise has recently been applied to the issue of separating neptunium from plutonium in the production of <sup>238</sup>Pu heat source material at the ORNL hotcell facility (Ref 2 and 3). Targets of <sup>237</sup>Np are irradiated in the High Flux Isotope Reactor (HFIR) resulting in <sup>238</sup>Pu, unreacted <sup>237</sup>Np and fission products. A solvent extraction process is used whereby all of the neptunium and plutonium are extracted and separated from radioactive fission products. Neptunium is selectively recovered from the solvent

leaving the plutonium, which is then stripped separately from the solvent. The neptunium is then purified and recycled into new targets for <sup>238</sup>Pu production and the plutonium product is further purified before fabrication into heat source pellets.

While this process has been demonstrated successfully on irradiated neptunium target materials, the stripping reagent for the separation of neptunium adds sodium to the neptunium product, which needs to be removed using ion exchange columns. NNL have proposed an alternative flowsheet that will provide a pure neptunium product, without any sodium, by taking advantage of the difference in the kinetics of reduction between Pu(IV) and Np(VI) using hydroxylamine nitrate (HAN). Selectively reducing Np(VI) to the less extractable Np(V) while avoiding the formation of the poorly extractable Pu(III) provides an efficient separation of neptunium from plutonium.

This presentation will detail some of the experimental work that has been performed to underpin this flowsheet and detail the chemical modelling results used to guide the flowsheet design. The flowsheet chemical models will be discussed together with some preliminary results from a flowsheet trial using a lab-scale centrifugal contactor cascade.

### II. Defining the flowsheet

The main premise behind the alternative flowsheet design is the difference in reactivity between neptunium and plutonium with hydroxylamine nitrate (HAN). Studies have shown that the rate of Pu(IV) reduction is strongly dependent on the inverse concentration of the acidity (Ref 4) while Np(VI) is readily reduced in a short period of time at 1M HNO<sub>3</sub> (Ref 5). However, there are many competing reactions that can play a role in the routing of neptunium and plutonium and to understand the most influential the following reactions were included in the process model:

- a) Reduction of Pu(IV) by HAN
- b) Reduction of Np(VI) by HAN
- c) Reduction of Np(V) by HAN
- d) Oxidation of Np(V) by HNO<sub>2</sub>

- e) Reduction of Np(VI) by HNO<sub>2</sub>
- f) Reduction of Pu(IV) by Np(IV)
- g) Oxidation of Pu(III) by Np(V)
- h) Oxidation of Pu(III) by Np(VI)
- i) Np(V) disproportionation
- j) Np(IV) / Np(VI) reaction (re-proportionation)
- k) HAN / HNO<sub>2</sub> reaction
- l) Radiolysis of HNO<sub>3</sub> to produce HNO<sub>2</sub>
- m) Organic phase Pu(III) oxidation by HNO<sub>2</sub>
- n) Organic phase Np(V) oxidation by HNO<sub>2</sub>.

A number of flowsheet iterations were simulated, with the final version shown in Figure 1, as the following points became evident:

i) There will always be some residual amount of Pu(III) generated at the HAN inlet (stage 5) that will follow the aqueous stream towards the neptunium product (stage 20). To counter this, the acidity at stage 13 is increased to promote the re-oxidation of Pu(III) and extraction of the resultant Pu(IV).

ii) There is a fast reaction between Np(VI) and Pu(III) that acts as a barrier to plutonium following the neptunium product so the solvent:aqueous ratio was optimized to promote this reaction.

iii) There will always be some Np(IV) produced from the disproportionation of Np(V) and the reduction of Np(V) by HAN.

This last point is difficult to avoid and will always result in some neptunium contamination in the plutonium product in stage 1, although this is also true for the flowsheet currently in use at ORNL with the neptunium removed by ion exchange in downstream steps. The focus of the present work was, therefore, on the production of a pure neptunium product that could be fabricated back into targets for irradiation and further <sup>238</sup>Pu production.

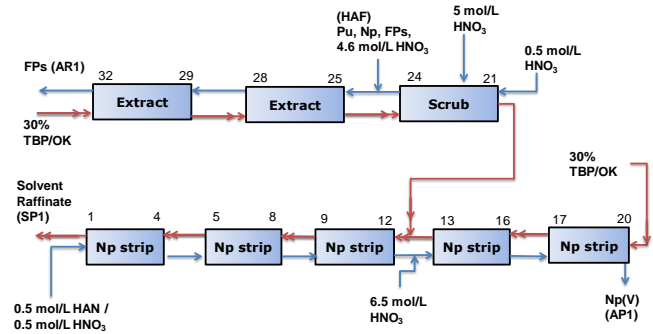


**Fig. 1.** Final version of the flowsheet tested experimentally using centrifugal contactors.

The removal of plutonium from the solvent using HAN at low acidity is well proven (Ref 5 and 6) and was not the focus of this study. Instead the available contactors were used to demonstrate the neptunium strip section of the flowsheet. The flowsheet trial was run for 6 hours with the active feed and the neptunium product (AP1) was monitored using a scanning vis/NIR spectrophotometer and the plutonium product (SP1) was monitored using a UV/vis diode array spectrophotometer. Both products demonstrated steady state before the end of the feed. At the end of the trial, aqueous and organic samples from each stage were taken for analysis by gamma and alpha spectrometry.

### III. Results

Table I shows the concentrations of neptunium, plutonium and acidity in the feed and products. Most of the neptunium (~97%) and nearly all of the plutonium (~99.8%) is extracted.

**TABLE I.** Concentrations of Np, Pu and HNO<sub>3</sub> in the feeds and products of the flowsheet test in Fig. 1.

Feed/ Product	[Np] (g/L)	[Pu] (g/L)	[HNO <sub>3</sub> ] (mol/L)
HAF	29.3	5.4	4.55
AR1	0.68 (3±0.2%)	0.007 (0.2±0.03%)	4.00
AP1	49.2 (85±21%)	0.012 (0.1±0.01%)	1.75
SP1	2.72 (15±3%)	3.92 (111±22%)	0.19

*Note: the % mass values are relative to the total mass fed in to the system, accounting for flowrates. The large error in some values is due to the uncertainty in the measured flowrates. % mass <sup>238</sup>Pu/Pu = 0.24%.*

#### III.A. Neptunium routing

The small amount of neptunium routed to the AR1 stream is expected due to a small amount of reduction of the Np(VI) to Np(V) at the feed stage. Recovery of this neptunium (3%) may still be possible by increasing the temperature in the scrub and feed stages (Ref 3 and 7), although this capability was not available in this study. Of the neptunium that is extracted, 85% is recovered while 15% remains in the solvent following the plutonium product. This amount is much higher than that predicted by the model and the reasons for this are, at present, unclear. Closer examination of the UV/vis/NIR spectra, recorded five days after the flowsheet trial was completed, shows little sign of Np(IV) in the plutonium product and this is consistent with the in-line analysis observed on the day of the flowsheet trial.

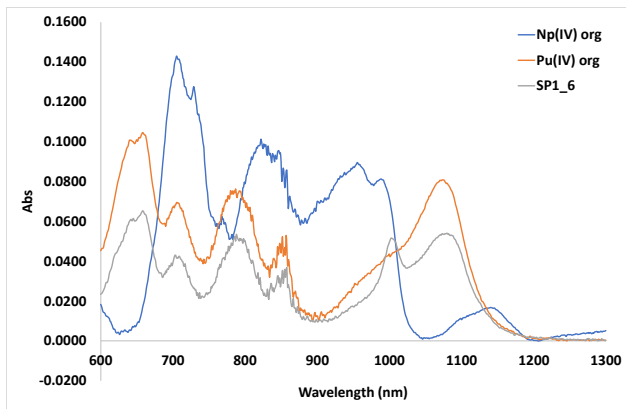


**Fig. 2.** UV/vis/NIR spectra of the plutonium loaded solvent product (SP1) compared to pure Np(IV) and Pu(IV) in 30% TBP/OK.

The plutonium loaded solvent product (SP1) spectrum closely aligns with that of Pu(IV), albeit with an additional absorption at 1000 nm. There is no evidence of significant amounts of Np(IV) or Np(VI) in the vis/NIR spectrum and the broad peak expected for the latter around 1150 nm in 30% TBP overlaps with that of Pu(IV). It is possible that the 1000 nm peak is related to Np(V) in the organic phase, which is unusual as Np(V) would be expected to be readily stripped from the solvent given its very low distribution coefficient in 30% TBP. One possible explanation is the presence of a Np(V)-Pu(IV) cation-cation complex forming which has been demonstrated to occur in the Np(V)-U(IV)-30% TBP/OK system (Ref 8). Further studies on this hypothesis are ongoing.

### III.B. Plutonium routing

The amount of plutonium in the aqueous phase decreases gradually from stages 1 to 12 and then drops sharply from stages 13 to 20 as the aqueous phase meets the fresh solvent fed into stage 20 (Figure 3).

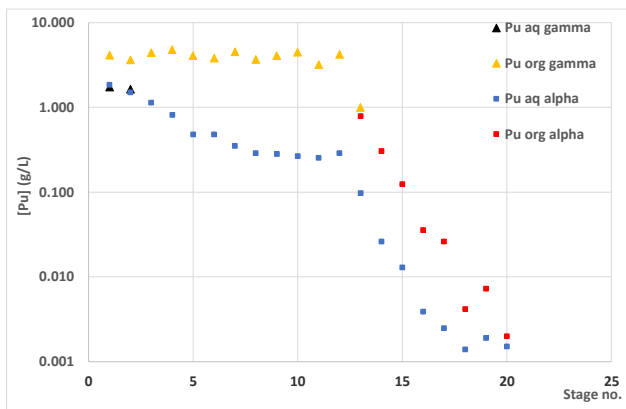


**Fig. 3.** Plutonium concentration profile across the neptunium strip section for the aqueous and organic phases.

There is an inconsistency in the plutonium concentrations measured in the neptunium product (AP1) (taken throughout the rig trial) and the profile concentrations measured at the end. The AP1 samples contain ~200 ppm Pu with respect to Np levels while the profile values contain ~30 ppm Pu with respect to Np. It is not clear why this discrepancy exists although it may be due to cross contamination on the outlet tube of the AP1 product line. With a target of < 100 ppm Pu with respect to Np the profile samples suggest that this can be met – provided cross contamination can be avoided on the actual process line at ORNL.

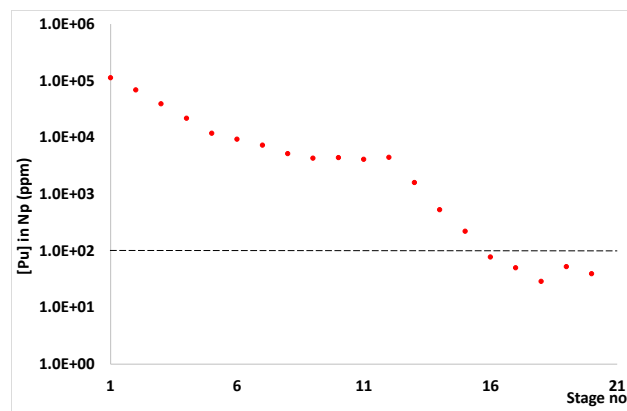


**Fig. 4.** The concentration of plutonium in ppm (or µg/gNp) showing the specification requirement for the neptunium product (black dotted line).

## IV. CONCLUSIONS

$^{238}\text{Pu}$  production requires separation from  $^{237}\text{Np}$  and this can be achieved by solvent extraction with control of the neptunium and plutonium oxidation states. Neptunium and plutonium are extracted as Np(VI) and Pu(IV), respectively. Using hydroxylamine nitrate (HAN) as the reductant and controlling the acidity, we can create the conditions where Np(VI) is selectively reduced to the less extractable Np(V) while leaving Pu(IV) in the solvent phase. This is a salt free reduction providing a pure neptunium product that can be directly recycled into new targets for  $^{238}\text{Pu}$  production.

The amount of neptunium in the plutonium loaded solvent is unusually high and may be a result of cation-cation complex formation between the oxo ligands of Np(V) and the Pu(IV) ion. This flowsheet also needs to be tested using  $^{238}\text{Pu}$  rather than civil grade plutonium.

## ACKNOWLEDGMENTS

The authors are grateful to NNL for internal research funding under the Advanced Recycle and Isotope Separations (ARIS) core science theme and to ORNL for providing the neptunium.

## REFERENCES

1. R.J. TAYLOR, C.R. GREGSON, M.J. CARROTT, C. MASON, M.J. SARSFIELD, "Progress towards the full recovery of neptunium in an advanced PUREX process", *Solvent Ext. Ion Exch.*, **31**, 442 (2013).
2. D. W. DEPAOLI, D. E. BENKER. L. H. DELMAU, S. R. SHERMAN, F. D. RILEY, P. D. BAILEY, E. D. COLLINS and R. M. WHAM, "Process Development for Plutonium-238 Production at Oak Ridge National Laboratory," Nuclear and Emerging Technologies for Space, American Nuclear Society Topical Meeting, Richland, WA, February 25 – February 28, (2019).
3. D. W. DEPAOLI, D. E. BENKER. L. H. DELMAU, E. D. COLLINS and R. M. WHAM, "Progress in Chemical Processing for Production of Plutonium-238 from Irradiated Neptunium Oxide Cermet Targets," NETS 2018—Nuclear and Emerging Technologies for Space, Las Vegas, NV, Feb. 26–March 1, 2018, on CD-ROM, American Nuclear Society, LaGrange Park, IL (2018).
4. G. S. BARNEY, "A Kinetic Study of the Reaction of Plutonium(IV) With Hydroxylamine", *J. Inorg. Nucl. Chem.*, **38**, 1677 (1976).
5. V.S. KOLTUNOV, R.J. TAYLOR, S.M. BARANOV, E.A. MEZHOV and I. MAY, "The Reduction of Plutonium (IV) and Neptunium (VI) Ions by N,N-ethyl (hydroxyethyl) Hydroxylamine in Nitric Acid", *Radiochim. Acta* **86**, 115 (1999).
6. J. BROWN, C. CAMPBELL, C. CARRIGAN, M. CARROTT, K. GREENOUGH, C. MAHER, B. MCLUCKIE, C. MASON, C. GREGSON, T. GRIFFITHS, J. HOLT, M. SARSFIELD, K. STEPHENSON, R. TAYLOR, T. TINSLEY, "Americium and Plutonium Purification by Extraction (the AMPPEX process): Development of a new method to separate <sup>241</sup>Am from aged plutonium dioxide for use in space power systems," *Progress in Nuclear Energy*, **106**, 396 ( 2018).
7. H. CHEN, R.J. TAYLOR, M. JOBSON, D.A. WOODHEAD, C. BOXALL, A.J. MASTERS and S. EDWARDS, "Simulation of Neptunium Extraction in an Advanced PUREX Process—Model Improvement", *Solvent Extraction and Ion Exchange*, **35**, 1 (2017).
8. M.J. SARSFIELD, R.J. TAYLOR, C.J. MAHER, "Neptunium(V) disproportionation and cation–cation interactions in TBP/kerosene solvent". *Radiochim. Acta* **95**, 677 (2007).

## 238-PLUTONIUM DIOXIDE FUEL FABRICATION MULTIPLE PROCESSING CERIUM DIOXIDE REPLICATION AND PARTICLE SIZE ANALYSIS

F.A Carver, C. Piatt and N. R. Wozniak

Los Alamos National Laboratory, Los Alamos, NM, 87545

(505)-412-8621, [fcarver@lanl.gov](mailto:fcarver@lanl.gov)

*During 238-plutonium dioxide,  $^{238}\text{PuO}_2$ , ceramic processing, quality assurance sample analysis determined deficiencies in Pu isotopics for numerous fuel lots. In an attempt to mix and ensure homogeneity within operating parameters, fuel lots were combined and subjected to a second round of processing. This new processing method was a result of an attempt at combining multiple processed fuel lots and reprocessing through the fuel fabrication flow sheet a second time, referred to as 'twice processed'. During twice processing, the  $^{238}\text{PuO}_2$  exhibited a noticeable difference in production handling behavior. In order to study the resultant production lots, a simulant material was selected. Historically,  $\text{CeO}_2$  has been utilized as a surrogate due to the limited and expensive nature associated with  $^{238}\text{PuO}_2$ . The twice processed  $^{238}\text{PuO}_2$  production process was replicated here with  $\text{CeO}_2$  to gain a better understanding and analyze the effects of twice processed fuel fabrication processing. The resultant material was by comparing  $\text{CeO}_2$  direct handling effects in relation to  $^{238}\text{PuO}_2$  production and  $\text{CeO}_2$  particle size analysis throughout both single and twice processing rounds.*

### I. BACKGROUND

Historically, radioisotope power sources used in deep space missions and explorations have been powered through the utilization of the alpha decay inherent in  $^{238}\text{Pu}$  and the Seebeck effect (Ref. 1-3). The Pu used for these missions undergoes processing to create a ceramic,  $\text{PuO}_2$  pellet, producing ~0.5 thermal watts per gram of material (Ref. 1-7). After initial production or recovery of the isotope itself, aqueous processing purifies the oxide for subsequent fuels processing procedures; including granule, grog and pellet creation during fuels processing and fabrication efforts at Los Alamos National Laboratory, LANL, before encapsulation (Ref. 5-7). The end LANL result is an iridium clad, pellet producing ~62.5 thermal watts.

After initial production and purification of the isotopically enriched Pu, the  $^{238}\text{PuO}_2$  is subjected to processing steps designed to produce a repeatable fuel lot for subsequent grog creation; known as fuel fabrication and processing. The grog itself, is a combination of high fired and low fired fuel lots in specified proportions to ensure ceramic pellet formation during hot press and sintering activities. The process consists of, first, creating

the desired fuel lot from aqueous processing, then ball milling the lot to achieve homogeneous particle size. After which, a 'slugging and screening' operation is performed by first cold pressing portions of the total fuel lot and followed by forcibly screening through various sieves to achieve known, repeatable granule sizes. After which, a 'S1' sample is collected for analysis and process quality assurance, detailed in Table 1.

TABLE I. Process Sample Descriptions.

Sample	Purpose	Method Name
S1	Thorium and $^{234}\text{U}$ isotopic analysis	Pu Assay, Radiochemistry
S2	Trace chemical analysis	DC ARC
S3	Pu isotopics, $^{241}\text{Am}$ , $^{237}\text{Np}$ analysis	Gamma FRAM
S3	Neutron Emission Rate	
S3	Calorimetry	

From there, the fuel lot is seasoned at elevated temperatures under  $\text{H}_2^{16}\text{O}$  saturated, flowing argon to ensure proper stoichiometry and neutron emission rate in the final product. It is during this process that the lot undergoes grain growth, sintering mechanisms and  $^{16}\text{O}$  exchange, forming an agglomerated mass. The post-fired lot is then carefully broken up during screening and worked through a sieve stack to ensure repeatable particle size. The remaining samples, 'S2' and 'S3', are then taken from the bulk fuel lot for further analysis and quality assurance, also detailed in Table 1. All particles free falling through the last sieve are used for production. A visual representation of the fuel fabrication process flow is shown below in Figure 1.

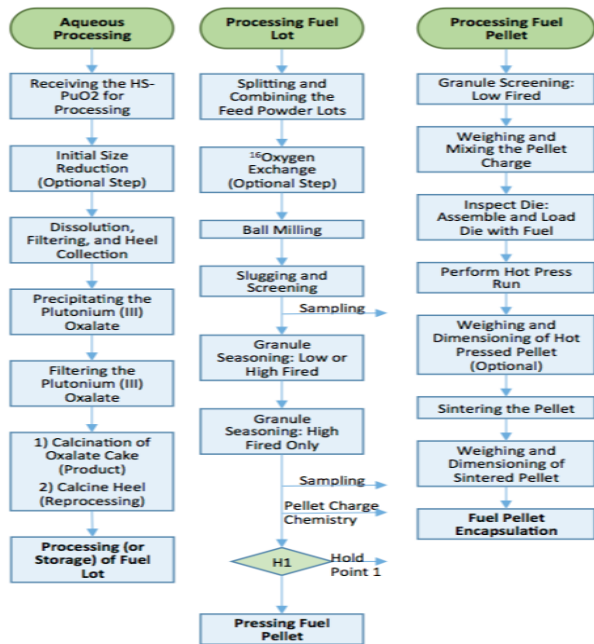


Fig. 1. Fuel fabrication process flow diagram.

## II. $^{238}\text{PuO}_2$ PRODUCTION OBSERVATIONS

Upon completion of sample analysis during processing  $^{238}\text{PuO}_2$  fuel lots, it was determined that several lots fell short of the ‘S3’ Pu isotopic analysis requirements. In order to combat this problem, while continuing to move forward with processing, an attempt at blending the isotopically low lots with isotopically high lots was selected as a path forward. No such process has been utilized to ensure a homogenous mixture after firing of multiple, production lots. The fuel lots were split equally and reprocessed through the flow sheet, observable in Figure 1, as opposed to reprocessing the fuel lots through aqueous processing a second time. This complete reprocessing is referred to as ‘twice processed fuel lots’. By mixing and reprocessing single processed fuel lots, in theory, the ball mill process would serve to homogenize and break down the already formed granules for reconstruction and subsequent seasoning. By doing so, the new, twice processed fuel lots would meet the specifications for continued production without the lost time and process losses associated with reprocessing through aqueous processing.

After the combined and redistributed material into fuel lots underwent ball milling, the observed processing behavior and characteristics of the fuel differed significantly from past experience. While operators unloaded the fuel from the ball mill jar and began slugging and screening operations, abnormal behavior of the fuel was noted. Normally, the ‘slug and screen’ pellets compacted via press require notable force on the top sieve

to break apart the ceramic pellet through the sieve stack. In the reprocessing of the twice processed fuel lot, however, the pellets crumbled during the initial screen. Additionally, the broken pellets, now granules, passed through the remaining sieves with relative ease. After twice processed slugging and screening operations, the granules underwent twice processed high fire furnace operations. This subsequent twice processed fuel lots left the post fired agglomerated granules in a significantly more rigid and unyielding mass than previously encountered during post high fire screening operations. It proved immensely difficult to both remove the amassed granules from the platinum boat and screen them through the appropriate sieves. It was noted that throughout this screening, that once the granules were forcefully freed from the mass they had a strong tendency to either break apart as noticeably and unusually fine particles or remain as compact, buoyant particles. These buoyant particles could be seen ‘bouncing’ off the sieves as all stages of screening occurred. Ultimately, after all samples analysis were received, the twice processed mixing plan served its intention, as all of the ‘S3’ samples passed isotopic analysis. However, this was met with significant production fuel losses and considerable changes in observed fuel characteristics and behavior.

## III. $\text{CeO}_2$ SIMULANT RESULTS

To better quantify and investigate loss mitigation techniques from these abnormal occurrences,  $\text{CeO}_2$  powder was prepared using the same processing steps as the twice processed fuel lots.  $\text{CeO}_2$  has been used as a surrogate for  $^{238}\text{PuO}_2$  experiments previously to combat both the immense cost and potential negative health effects (Ref. 8-11). Surrogate  $\text{CeO}_2$  ( $\text{CeO}_2$  99.99%, Alfa Aesar, Ward Hill, USA) was prepared in a non-radioactive lab to the same processing parameters and steps detailed above and in Figure 1, in an attempt to replicate and quantify the particle size (Camsizer X2, Horiba) and abnormal particle behavior observed by the  $^{238}\text{PuO}_2$  during production and to gain enhanced assurance for  $\text{CeO}_2$  as a surrogate material.

Replicating the  $^{238}\text{PuO}_2$  with  $\text{CeO}_2$  yielded very similar conditions as presented during production. Even without alpha radiation and heat generation inherent with  $^{238}\text{PuO}_2$ , the twice processed  $\text{CeO}_2$  still exhibited very similar qualities during processing, such as crumbling pellets during slugging and screening and increased force during post high fire screening. Very few deviations from processing characteristics were identified during simulant reproduction. With the increased confidence in simulant processing reproduction, samples throughout the processing stages were collected and underwent particle size analysis to understand how the particles differed from single to twice processing. All particle size analysis results presented here are the smallest chord length

observed on the particle throughout the sample analysis, referred to as xc-min, due to the particles smallest chord length having the ability to pass through the sieve during operations. Figure 2 below highlights the differences between single processed, high fired and twice processed, high fired CeO<sub>2</sub>.

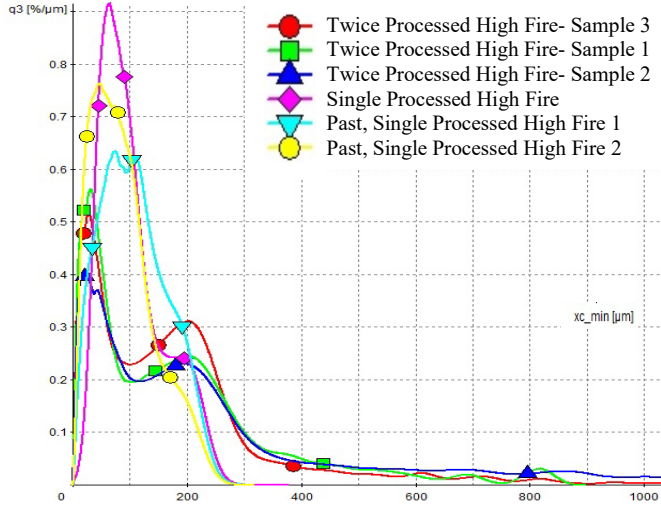


**Fig. 2.** Single and twice processed, high fire particle size analysis.

Historically, single processed, high fired CeO<sub>2</sub> exhibits a single peak centered just below 100μm, as seen in Figure 2. However, the twice processed, high fired material displays two peaks, centered around 50μm and 200μm. From particles of a similar, equal size with all particles under 300μm, to two distinct peaks with larger quantities of particles dispersed above 300μm, this bimodal shift indicates a significant particle size shift as a result of reprocessing. With a notable difference in particle size distribution, it helps support the observable differences in material behavior.

To account for the behavior of the larger particles observed in twice processed fuel lots, it was hypothesized that the larger portion of fine particles, peak <100μm, absorbed the water in the ambient environment to create the appearance of particles larger than the sieving process allowed. As done previously, the fuel lot was refired for 1hour at 350°C and rescreened in an effort to reduce the observed agglomerations directly before particle size analysis (Ref. 11). The results of this effort can be seen below in Figure 3.

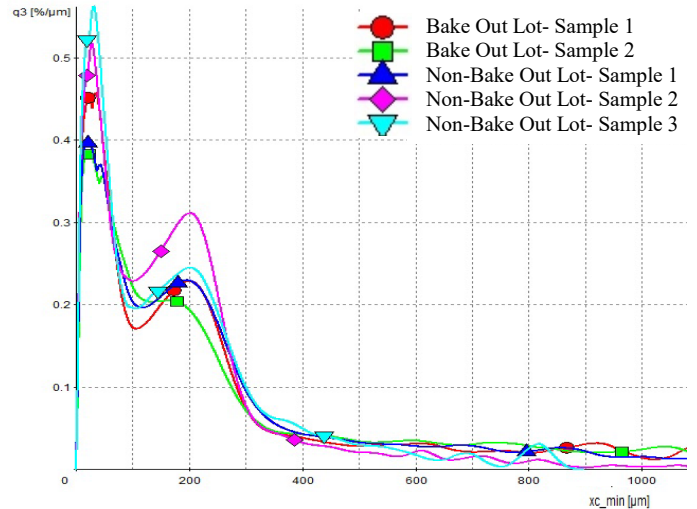


**Fig. 3.** Non-baked out in comparison to baked out at 350°C for 1 hour and screening of twice processed, high fire.

No noticeable improvement in redistributing or preventing the larger particles from agglomerating post bake out and screening was observed. Further analysis and sampling is necessary in order to determine the mechanism promoting the phenomena after the particles free fall through the smaller sieve.

#### IV. CONCLUSIONS

CeO<sub>2</sub> surrogate studies suggest that by undergoing ball mill and subsequent screenings and high firing operations twice, the granules were sintered to a higher density than normally observed. These denser granules were a result of the combination of cumulative over-milling with multiple sintering, high fire, operations. After the initial processing, both the <sup>238</sup>PuO<sub>2</sub> with CeO<sub>2</sub> were presintered, high fire granules; serving as the higher density, low surface energetic component of the grog mixture. By undergoing reprocessing, the milling stage served to break down the already dense granules further, leading to noticeably smaller and unreactive material to be pressed during granule formation. This is evident from the inability for pellets to adhere during the slugging and screening process. It is reasonable to assume this process step did not serve its purpose of larger, homogenized granule formation without proper, observable ceramic pellet formation. Going into sintering operations, the relative decrease in granule size led to an increase in sinterability during the second round of high fire operations (Ref. 12). Therefore, post high fire screening was made increasingly difficult by the high degree of sintering the additional round of processing generated. Consequently, two rounds of processing is not recommended for pellet creation due to the increased

potential for microcracking during hot press attributed to the heightened density particles produced (Ref. 12).

Though further refinement in agglomeration efforts for second round processing/high fire agglomerations is necessary to understand the interaction mechanisms of the heightened density CeO<sub>2</sub>, the results and observations presented help to promote enhanced confidence in the ability of CeO<sub>2</sub> to reproduce production characteristics. Useful as a tool for further development and to predict with increased reliance the impact of subtle changes in process parameters. By doing so, this has the capability to assess and avoid changes which negatively impact production with an increased degree of reliability.

#### ACKNOWLEDGMENTS

This research is funded by Radioisotope Power Systems Program at Los Alamos National Laboratory.

#### REFERENCES

1. G.L. BENNETT, J.J. LOMBARDO, R.J. HEMLER, G. SILVERMAN, C.W. WHITMORE et al., "Mission of Daring: The General-Purpose Heat Source Radioisotope Thermoelectric Generator." *4th International Energy Conversion Engineering Conference and Exhibit (IECEC)*, 26 June 2006.
2. R.A. BROCKMAN, D.P. KRAMER, C.D. BARKLAY, D. CAIRNS-GALLIMORE, J.L. BROWN et al., "Modeling of Selected Ceramic Processing Parameters Employed in the Fabrication of <sup>238</sup>PuO<sub>2</sub> Fuel Pellets." *Physics Procedia*, Vol. No. 20, p. No. 397–403, 2011.
3. T.K. KEENAN, R.A. KENT, and R.W. ZOCHER, "The Relationship of Fabrication Parameters to Selected Properties of <sup>238</sup>PuO<sub>2</sub> Radioisotopic Fuels I. Dimensional Changes, Stoichiometries, and Microstructural Features." *LA-5622-MS*, May 1974.
4. D.T. RANKIN, J.W. CONSDON, J.T. LIVINGSTON and N.D. DUNCAN, "Ceramic Fuel Pellets for Isotopic Heat Sources." *Nuclear Division of the American Ceramic Society*, San Francisco, 26 October 1980.
5. R.A. KENT, "LASL Fabrication Flowsheet for GPHS Fuel Pellets." LASL, *LA-7972-MS*, August 1979.
6. T.D. RANKIN, W.R. KANNE JR, M.R. LOUTHAN JR., D.F. BICKFORD, and J.W. CONGDON. "Production of Pu-238 Oxide Fuel for Space Exploration." *WSRC-MS-2000-00061*, p. No. 179–186.
7. B. MARK, S. FRANK, P. LESSING, D.F. BICKFORD, R. CANNON et al., "Evaluation of Aqueous and Powder Processing Techniques for Production of Pu-238-Fueled General Purpose Heat Sources." *Idaho National Laboratory*, June 2008.
8. I.S. GOLOVNIN, "Properties of Plutonium Dioxide as a Nuclear Fuel." *Atomic Energy*, Vol. No. 89, No. 2, p. No. 627–637, 2000.
9. T.K. KEENAN, R.A. KENT, R.N.R. MULFORD and M.W. SHUPE, "Data Sheets for PPO Radioisotopic Fuel." *LA-5160-MS*, December 1973.
10. R.J.M. KONINGS, L.R. MORSS, and J. FUGER, "Chapter Nineteen: Thermodynamic Properties of Actinides and Actinide Compounds." p. No. 2113–2224.
11. F.A. CARVER, H.M. MILENSKI, M.J. WILKIN and A.J. PARKISON, "Particle Size Analysis of Cerium Dioxide Surrogate Material as a Simulant for Plutonium-238 Dioxide Fuels Processing", *Nuclear and Emerging Technologies for Space, American Nuclear Society Topical Meeting (NETs)*, 25 February 2019.
12. P.K. SMITH, D.F. BICKFORD and T. RANKIN, "Reproducible Fabrication of PuO<sub>2</sub> Fuel." *Savannah River Laboratory*, 5 April 1977.

**MODELING CHEMICAL REACTIONS AND DIFFUSION IN A MMRTG PLUTONIUM PELLET**

Darrell Cheu<sup>1</sup>, Kevin Judd<sup>2</sup>, Joseph Hafen<sup>3</sup>, Andrew Lesh<sup>4</sup>, Quinn Killian<sup>5</sup>, Alex Perry<sup>1</sup>, Cole Nielsen<sup>1</sup>, and Steve Herring<sup>6</sup>

<sup>1</sup>Purdue University, West Lafayette, IN, 47907, [dcheu@purdue.edu](mailto:dcheu@purdue.edu)

<sup>2</sup>North Carolina State University, Raleigh, NC 27695

<sup>3</sup>University of Idaho, Moscow, ID 83844

<sup>4</sup>Stanford University, Stanford, CA 94305

<sup>5</sup>University of Michigan, Ann Arbor, MI 48109

<sup>6</sup>Center for Space Nuclear Research, Universities Space Research Association, Idaho Falls, ID 83402, [jherring@usra.edu](mailto:jherring@usra.edu)

Long-term chemical reactions in an MMRTG Plutonia pellet were simulated in a COMSOL Multiphysics environment. The plutonia pellet’s production of oxygen through reduction was implemented in COMSOL with the Bessman-Lindemer model. In addition, the puffing of oxygen through the frit vent and the consumption of oxygen by the GIS through additional chemical reactions were included in COMSOL. Simulation results showed that the pellet reached chemical equilibrium within the first minute and achieved minimal reduction with a substoichiometry of  $40 \times 10^{-9}$ .

**I. INTRODUCTION**

Plutonium-238 (<sup>238</sup>Pu) is an effective power supply in the multi-mission radioisotope thermoelectric generator (MMRTG), which is a long-term power source for unmanned spacecraft. Unlike previous research which focused on modeling oxygen and helium behavior from the plutonium-238 fuel pellet separately,<sup>1</sup> this study combines the helium and oxygen production with their chemical reactions in the gas space of the MMRTG simultaneously within a COMSOL Multiphysics environment. The results generated by this model will prove useful for understanding the long-term chemistry that takes place inside MMRTGs and improve their design for future missions

**I.A. MMRTG**

Radioisotope thermoelectric generators (RTGs) have been used for long-term space applications since the early 1960s, beginning with the US Transit satellite system. RTGs were used throughout the space race, primarily as power and heat sources for Earth observation satellites and the Apollo Lunar Surface Experiment Packages. The technology has since been used on several interplanetary missions such as Pioneer, Voyager, Galileo, Ulysses, Cassini, and New Horizons. The MMRTG was first used with the Curiosity rover in 2011 as an evolution of these older power systems and is planned for use on future NASA missions in the 2020s. RTGs generate electricity through the Seebeck effect by heating one end of a thermocouple with the decay heat from <sup>238</sup>Pu and using space or extraterrestrial environment as a heat sink. These devices are best suited for missions where solar panels are

ineffective due to a lack of solar energy. Isotopes with long half-lives that emit only alpha particles, such as <sup>238</sup>Pu, are ideal heat sources because they provide sufficient power for the extended length of interplanetary space missions. An MMRTG can produce at least 110 watts of electrical power at launch and has an operation lifetime of up to 14 years, making them suitable for a wide array of missions with minimal situational modification.

**II. PHYSICAL PROCESSES**

**II.A. Thermal Power and Helium Behavior**

The radioactive decay of plutonium-238, detailed in Eq. 1, in the plutonia pellet results in the production of heat and helium.

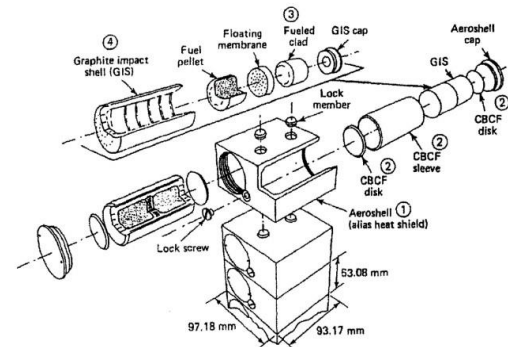
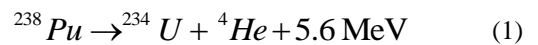


**Figure 1: PuO<sub>2</sub> Pellets Housed in GPHS**



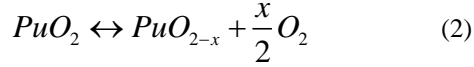
Each alpha decay produces a helium nucleus in the plutonia grains. Helium diffuses along the plutonia grain boundaries to the connected porous network in the plutonia pellet before exiting through the frit vent in the iridium cladding. This prevents helium bubble adsorption and swelling from occurring inside of the pellet. Since helium is chemically inert, it does not react with any other gasses or components in the MMRTG.

In addition to the helium atom, each decay also releases approximately 5.6 MeV of thermal energy. Each

pellet has an initial thermal flux of  $4.95 \times 10^6 \text{ W/m}^2$  at launch and decays at the same rate as the plutonium-238.

## II.B. Oxygen Behavior

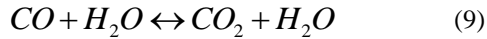
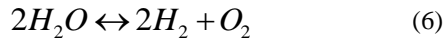
The plutonia in the fuel pellet undergoes oxidation-reduction reactions to produce or absorb oxygen. Due to a lack of oxygen, the plutonia will reduce and result in the production of free  $\text{O}_2$  molecules and substoichiometric  $\text{PuO}_2$  in Eq. 2. In the presence of oxygen, Eq. 2 can reverse as the plutonia can absorb oxygen and re-oxidize.



Like helium, the oxygen is produced in the plutonia grain and diffuses out of the grain boundary, into the connected porous network and exits through the iridium frit vent. Oxygen does not form into bubbles inside of the pellet and is assumed to freely flow.

## II.C. Chemical Reactions

In addition to the increase of oxygen and helium, secondary chemical reactions, found in Equations 3-9, can impact the effectiveness of the MMRTG. Their equilibrium compositions affect the pressure inside the GIS. The secondary oxidation reactions are represented in Eqs. 3 through 9. Species are in the gas phase unless otherwise indicated.



The oxidation of surface carbon via Eq. 3 at the surface of the GIS is the primary mechanism of oxygen removal from the MMRTG. This reaction combined with the remaining chemical reactions result in the plutonia reducing due to the constant removal of  $\text{O}_2$  from the MMRTG.

During the manufacturing process and storage, the atmosphere within the MMRTG is predominantly argon to limit chemical reactions listed in Eq. 3 through 9 and

oxygen to prevent plutonia reduction and maintain its stoichiometry.

## II.D. Modeling in COMSOL

Modeling of the pellet was performed in a COMSOL 5.4 environment with 2-D axisymmetric geometry built in CATIA v5. Five built-in physics modules were utilized in the simulation: chemistry, surface reactions, laminar flow, transport of diluted species, and heat transfer. A fine mesh was built over the geometry and the simulation was ran over this time step.

## II.E. Geometry

A 2-D asymmetric model in Figure 2 was used instead of a 3-D model to save computational resources. Area 1 is the fuel pellet, area 3 is the iridium clad, section 5 is the GIS. Areas 2 and 4 are fluid spaces between components and area 6 is the frit vent within the iridium clad.

The fuel pellet was modeled as a porous media with 14% porosity while the iridium clad and GIS are modeled as solids. Even though the frit vent is a 50% porous medium, it is modeled as an air gap due to the high permeability of gasses flowing through that component.

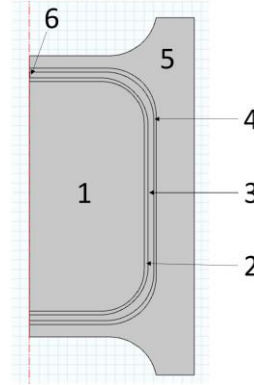


**Figure 2:** 2D Asymmetric Model of Fuel Pellet in COMSOL

## II.F. Gas Transport

For all gas transport, transport mechanisms were assumed to be diffusion with no convection or adsorption and dispersion of bubbles. This was performed within the Transport of Species module in COMSOL.

Diffusion of oxygen from the pores to the grain boundary was determined using the diffusion coefficients in Eq. 10, where  $D$  is the diffusion coefficient in  $\text{m}^2/\text{s}$ ,  $T$  is the absolute temperature in Kelvin and  $p_{\text{O}_2}$  is the partial pressure of oxygen in atm.<sup>2</sup>

$$D = 7.48 \times 10^{-3} \exp\left(-\frac{48100}{T}\right) P_{O_2}^{-\frac{1}{2}} + 3.43 \times 10^{-4} \exp\left(-\frac{28300}{T}\right) P_{O_2}^{-\frac{1}{6}} \quad (10)$$

Not all of the gases can be released from the pores in a single time step. Gas release from the pores was modeled similarly to Booth's gas release model in Eq. 11 where  $f$  is the mass fraction of gas released,  $D$  is the diffusion coefficient through the pores,  $t$  is the time step and  $a$  is the effective radius of the pore.<sup>3</sup>

$$f = 1 - \frac{6}{\pi^2} \sum_{n=1}^{\infty} \exp\left(\frac{-n^2 \pi^2 D t}{a^2}\right) \quad (11)$$

Gas transport through the interconnected pores, the frit vent and in the spaces between components were treated as binary gas mixtures. Since argon is the dominant gas by orders of magnitude due to backfilling, it is treated as the primary solvent for all cases and individual gases are treated as the solute. The binary gas mixtures of gas A and gas B were modeled with the Chapman and Enskog model in Eq. 12, where  $D_{AB}$  is the diffusion coefficient in cm<sup>2</sup>/s,  $T$  is absolute temperature in Kelvin,  $M_A$  is the molecular mass of gas A,  $p$  is pressure in atm,  $\sigma_{AB}$  is the collision parameter in Å and  $\Omega_{AB}$  is the collision integral.<sup>6</sup>

$$D_{AB} = 1.858 \times 10^{-3} \frac{\sqrt{T^3 (1/M_A + 1/M_B)}}{p \sigma_{AB}^2 \Omega_{AB}} \quad (12)$$

## II.G. Oxygen Production

Unlike the other reactions in the MMRTG, the reaction kinetics for oxygen production are poorly understood due to the difficulty in opening plutonia pellet from the iridium cladding during storage. Studies on plutonia reduction have generally been limited to determining thermodynamic equilibrium. The Bessman-Lindemer model described in Eq. 13 is used since it takes into account both the oxygen potential the plutonia is exposed to and the substoichiometric state of the plutonia. The first line of Eq. 13 describes the thermodynamic equilibrium of stoichiometric plutonia through gibbs free energy while the remainder of the equation take into account the substoichiometric states.  $R$  is the universal gas constant in J/(mol\*K),  $T$  is the absolute temperature in Kelvin,  $N_1$  and  $N_2$  are the mole fractions of oxygen potentials the pellet is exposed to and substoichiometric plutonia respectively and  $P_{O_2}$  is the partial pressure of all oxygen potentials.

$$\begin{aligned} RT \ln P_{O_2} &= -915500 + 241.9T \\ &+ 4RT \ln N_2 - 3RT \ln N_1 + \\ &(41510 + 30.2T)[4N_1(-2N_2 + N_1 + 2N_2(N_2 - N_1)) \\ &- 3N_2[2N_1 - N_2 - 2N_1(N_1 - N_2)]] \end{aligned} \quad (13)$$

Initial substoichiometric states were used to find the partial pressure of oxygen within the pellet using Eq. 13.<sup>4</sup> While oxygen diffuses through the plutonia pores, a new equilibrium substoichiometric state is determined based on the remaining oxygen present in the plutonia pellet. In most programs, a root solver would be used to solve for the substoichiometric states in Eq. 13. However, COMSOL does not have a user-accessible root solver so a fitted function developed by Komeno, described in Eq. 14 was used instead,<sup>5</sup> where  $x$  is the substoichiometric state seen in Eq. 2.

$$\begin{aligned} x^{-2} &= \left(163000 \exp\left(\frac{-376000}{RT}\right) P_{O_2}^{-\frac{1}{2}}\right)^{-2} \\ &+ \left(\left(66200 \exp\left(\frac{-445000}{RT}\right)\right)^{\frac{1}{2}} P_{O_2}^{-\frac{1}{4}}\right)^{-2} \end{aligned} \quad (14)$$

## II.H. Secondary Chemical Reaction Kinetics

COMSOL required reaction rates to calculate equilibrium values. When reaction rates could not be directly input, COMSOL calculated reaction rates based from user-input Arrhenius Equation constants taken from the NIST Chemical Kinetics Online Database. This allowed for the forward and backward rate constants to be derived from the Arrhenius expression for each subreaction that comprised the seven main reactions.

The subreactions, each comprising an elementary step of an overall reaction, each have their own set of Arrhenius parameters and rate constants. The resulting rate constants were compared for each step, both in the forwards and backwards directions. The subreaction with the smallest rate constant in each direction was then considered the forward or backward rate determining step of the reaction mechanism. Using this approximation, the rate constants for the selected rate determining steps were input as the forward and backward rate constants for each overall reaction, which are temperature dependent.

Any of the variables found using these methods was input into COMSOL's chemical reaction module within the Arrhenius parameter section.

## III. RESULTS

### III.A. Chemical Kinetics

The chemistry within the pellet equilibrates in the first minute. To confirm this, the simulation was repeated time steps split into two distinct sections. The first section takes place within the first minute, the time step was set to be a second to observe the chemistry reaching equilibrium. The next section lasts for the remainder of the simulation where the time step was set to be an hour and lasts for the year to observe the maintained equilibrium and to save on computational resources.

The main driver of all the chemical reactions is the oxygen production from the plutonia and its reaction with the GIS. This can be seen in Figure 3 where the total oxygen concentration increases as the production rate is significantly higher than the reaction outside of the pellet, especially due to the limiting volume gases can pass through in the frit vent. Figure 4 shows the frit vent (area 6) in further detail where there is an increase in oxygen concentration inside of the pellet compared to outside of it, which confirms that the pellet does "puff" oxygen out.

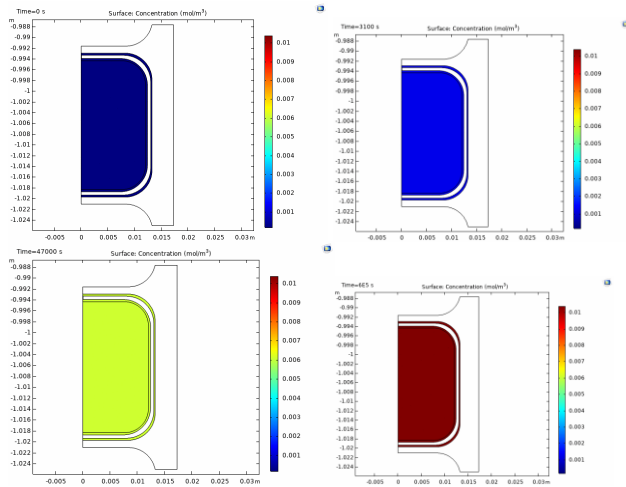


**Figure 3:** O<sub>2</sub> Concentration in Plutonia Pellet at 0s, 3100s, 4700s, and 60000 s

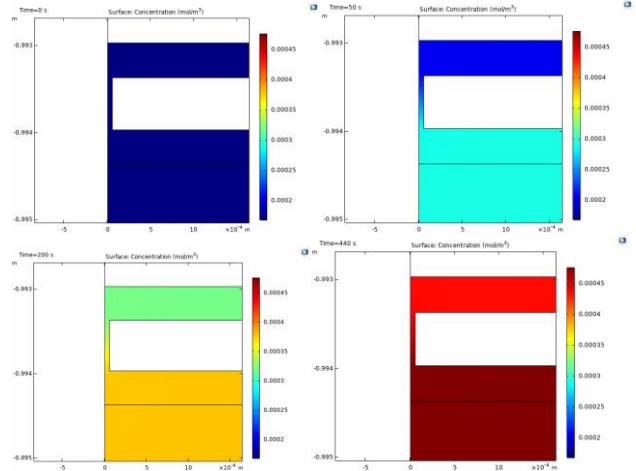


**Figure 4:** O<sub>2</sub> Concentration in Frit Vent of Plutonia Pellet at 0s, 50s, 200s and 440s

### III.B. Substoichiometry

The substoichiometry of the plutonia did not drastically change as expected, especially compared to past work such as Whiting's study where the CeO<sub>2</sub> surrogate substoichiometry  $x$  increased up to 0.25(Ref. 7) and the previous CSNR study that estimated the maximum substoichiometry to be 0.12 (Ref. 1). In this simulation, the substoichiometry only reached a maximum of  $40 \times 10^{-9}$ .

In the middle of the pellet, the substoichiometry over time was plotted in Figure 5. As expected, the pellet released oxygen at a logarithmic rate until it reached an equilibrium with the oxygen surrounding it.

This phenomenon can be seen in the 2D cut of the pellet in Figure 6 where the center of the pellet has a higher substoichiometry compared to the exterior. This is due to the increase in oxygen concentration, especially near the frit vent, that re-oxidizes the plutonia.

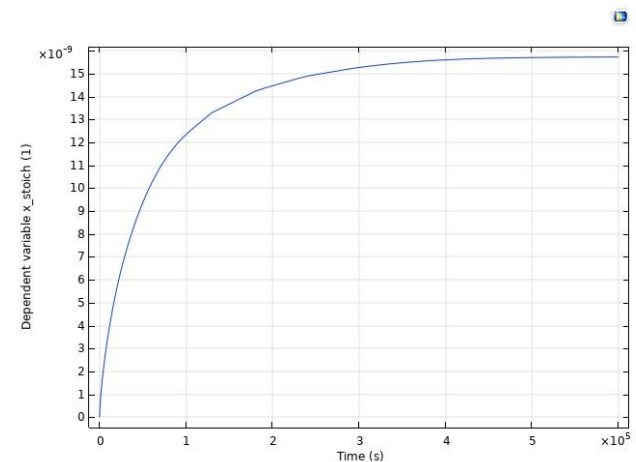


**Figure 5:** Substoichiometry of Plutonia Pellet

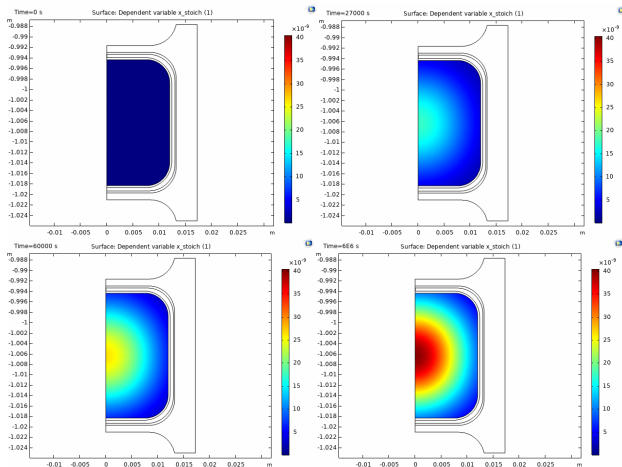


**Figure 6:** Substoichiometry of Plutonia Pellet at 0s, 27000s, 60000s, and 600000 s

### III.C. Temperature

To confirm that the simulation ran correctly, certain temperature boundary conditions were used as checks. Figure 7 shows the pellet core temperature around 1300 K, dropping down to 1000 K at the GIS, similar to physical measurements, and confirming that this module of the simulation ran correctly.

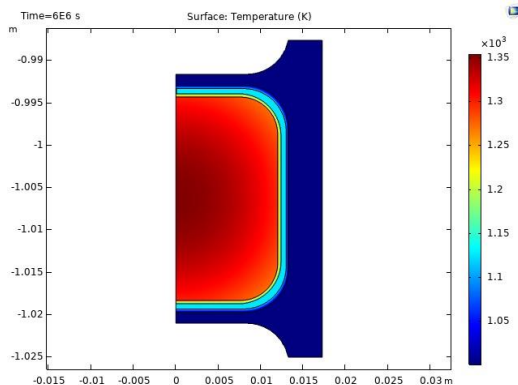


**Figure 7:** Temperature Distribution in Pellet

### ACKNOWLEDGMENTS

We would like to thank Dr. Brad Kirkwood of Idaho National Laboratory (INL) for assisting with modeling the plutonia reduction, and Dr. Jing Zhou of INL for assisting with understanding the chemical reactions. All authors were funded through the Center for Space Nuclear Research under the Universities Space Research Association.

### REFERENCES

1. K. DANI, L. HAWKINS, W. CHAN, T. TROUNG, A. GODFREY, and S. HERRING, "MODELING HELIUM AND OXYGEN BEHAVIOR OF A PLUTONIA PELLET IN AN

MMRTG," in "Nuclear and Emerging Technologies for Space," American Nuclear Society, Richland, WA (2019).

2. M. KATO, T. UCHIDA, and T. SUNAOSHI, "Measurement of oxygen chemical diffusion in  $\text{PuO}_{2-x}$  and analysis of oxygen diffusion in  $\text{PuO}_{2-x}$  and  $(\text{Pu,U})\text{O}_{2-x}$ ," *physica status solidi (c)*, 10, 2, 189–192 (feb 2013).
3. A. H. BOOTH, "A METHOD OF CALCULATING FISSION GAS DIFFUSION FROM UO FUEL 2 AND ITS APPLICATION TO THE X-2-f LOOP TEST CRDC-72!" Tech. rep. (1957).
4. T. M. BESMANN and T. B. LINDEMÉR, "IMPROVEMENT IN THE CHEMICAL THERMODYNAMIC REPRESENTATION OF  $(\text{PuO}_{2-x})$  AND  $(\text{U}_{1-z}\text{Pu}_z\text{O}_w)$ " (1986).
5. A. KOMENO et al., "Oxygen potentials of  $\text{PuO}_{2-x}$ ," *Mater. Res. Soc. Symp. Proc.* **1444** (2012); <https://doi.org/10.1557/opl.2012.1162>.
6. F. B. PIDDUCK, S. CHAPMAN, and T. G. COWLING, "The Mathematical Theory of Non-Uniform Gases," *Math. Gaz.* (1939); <https://doi.org/10.2307/3607024.C>.
7. E. WHITING, H. KNACHEL, E. J. WATKINSON, and R. M. AMBROSI, "Validating a model to predict the chemistry of the fuel used in radioisotope power systems," in "IEEE Aerospace Conference Proceedings," IEEE (mar 2017), pp. 1–9.

## OVERVIEW OF BETAVOLTAIC DEVELOPMENT AT PURDUE UNIVERSITY

Darrell Cheu<sup>1</sup>, Thomas Adams<sup>2</sup>, and Shripad Revankar<sup>1</sup>

<sup>1</sup>Purdue University, 516 Northwestern Ave, Room 4025, West Lafayette, IN, 47907; [dcheu@purdue.edu](mailto:dcheu@purdue.edu)

<sup>2</sup>Naval Surface Warfare Center-Crane Division, Crane, IN, 47522

Betavoltaic cells are nuclear power sources similar to a photovoltaic cell where a beta source irradiates a semiconductor p-n junction which generates current. Betavoltaic development at Purdue University has been performed in conjunction with City Labs Inc. to evaluate and improve the NanoTritium™ cell and are summarized in this paper. Hydrogen loaded solid state films were evaluated to determine the best techniques and choice of film to hold tritium. NanoTritium™ cells were thermally stress tested to withstand temperature swings and performance were accurately predicted with models used for photovoltaic cells.

### I. Introduction

Betavoltaics are direct conversion nuclear power sources that are ideal for long uninterrupted, small power applications. Betavoltaics last longer than the 4-5 year lifespan of chemical batteries of similar size and can operate at a wider temperature range (traditionally 5-45°C). Ideal applications of betavoltaics include medical implants and remote micro sensors.

At Purdue University, work is done in conjunction with City Labs Inc. on the NanoTritium™ betavoltaic cell. The NanoTritium™ cell uses a loaded titanium tritide film to irradiate a gallium-arsenide p-n junction to generate power in the nanowatt range. To date, the NanoTritium™ cell is the only betavoltaic to be issued a general license by the Nuclear Regulatory Commission, allowing for the user to operate it without the need for a radiation license or training.<sup>1</sup> This paper summarizes the work done at Purdue University to assist in the development of the NanoTritium™ cell.

#### I.A. Theory of Operation

Betavoltaics operate similarly to photovoltaic cells where the incident particle generates electron-hole pairs (EHPs) in the semiconductor p-n junction, visualized in Figure 1. Holes are accelerated to the p-side while electrons are accelerated to the n-side. Once the load is connected, the electrons travel through the load and return to the p-side, generating current.

Since beta particles have thousand times more energy than photons (5.7 keV vs 2-4 eV), thousands more EHPs can be generated, increasing the power output.

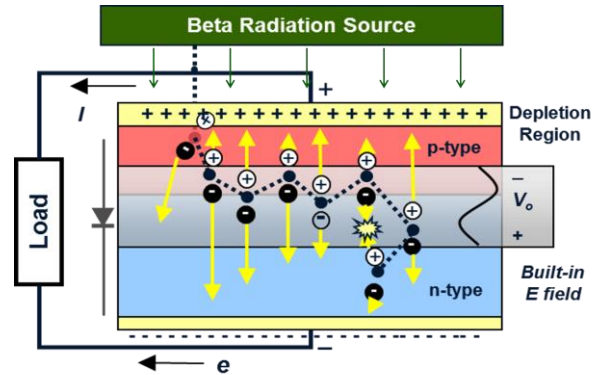


Figure 1: Betavoltaic Operation<sup>2</sup>

#### I.A.1. Beta Source Selection

The main limiting factor in beta source selection is the endpoint energy. Since the displacement energy for most semiconductors is 300 keV(Ref. 2), the beta endpoint energy must be below it to prevent semiconductor damage over the device’s lifetime. This and radioisotope half-life limits beta source selection to tritium, nickel-63 and promethium-147, with their properties listed in Table 1.

Tritium is the most commonly studied and utilized source due to its widespread commercial availability from CANDU reactors. Even though using nickel-63 and promethium-147 would have a higher energy density and easier mode of storage, they are not used due to lack of availability since nickel-63 is generated via neutron activation and promethium-147 is a fission product from light water reactors.

Table 1: Sources for Betavoltaic Devices<sup>3</sup>

Source	$E_{avg}$ [keV]	$E_{max}$ [keV]	Half-Life [yrs]
Tritium	5.7	18.6	12.3
Nickel-63	17.6	66.7	101.2
Promethium-147	65.1	224	2.6

## II. Experimental Work

### II.A. Hydrogen Film Loading

Since tritium is a gas, finding an appropriate storage medium is a challenge. Instead of storing tritium gas in

vials, it can be loaded into a solid substrate instead to minimize leakage and mitigate physical damage while maximizing beta particle interaction with the semiconductor p-n junction.

Behavior of thin films during loading is evaluated in the test setup in Figure 2, with focus on the total amount of hydrogen absorbed by the films, as shown in Figure 3.

Research at Purdue University has led to the development of palladium films to be used as tritium storage for future designs of the NanoTritium™ cell.

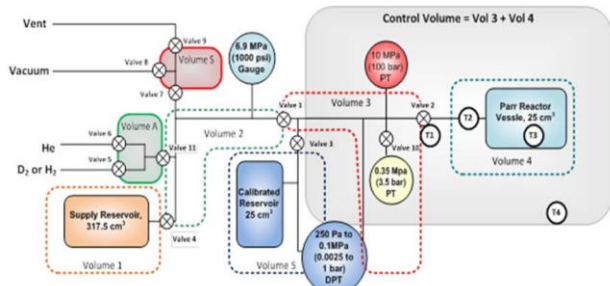


Figure 2: Hydrogen Loading System Schematic<sup>4</sup>

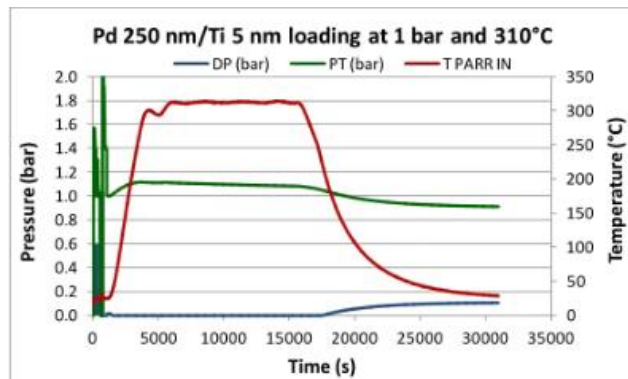


Figure 3: Sample Hydrogen Absorption Experiment<sup>4</sup>

**II.B. Thermal Cycling and Testing**

Betavoltaics must be able to withstand extreme environments, especially in remote areas where maintenance is impossible. Unlike chemical batteries, betavoltaics can operate from a range of -50°C up to 150°C (Ref. 1). Thermal evaluations were performed in the experimental setup in Figure 4 with various temperature profiles, ranging from steady temperature buildup to severe temperature drops, to ensure that the betavoltaic cell is continuously operating at its appropriate power after multiple cycles.

In Figure 5, a NanoTritium™ cell was cycled between 75°C and -40°C, with the betavoltaic cell producing the predicted voltage and withstanding any thermal stresses acting upon it, demonstrating the durability of the cell.

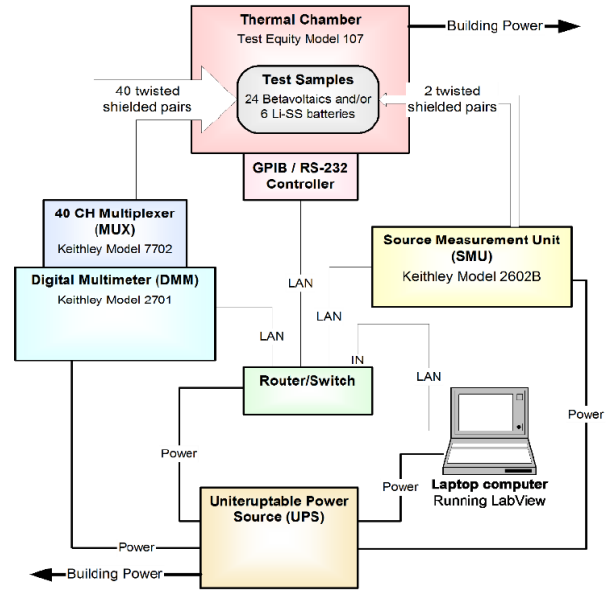


Figure 4: Temperature Chamber System Schematic<sup>5</sup>

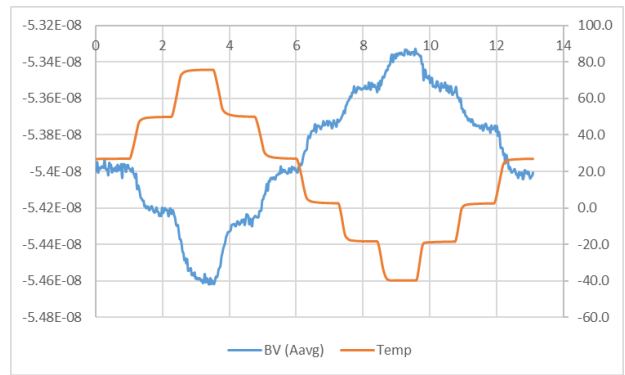


Figure 5: Sample Temperature Cycle<sup>6</sup>

**III. Modeling Work**

**III.A. Monte Carlo Simulation**

*III.A.1. Self-Shield Effects*

Since betas can be stopped effectively by a piece of paper, self-shielding losses are a significant factor in choice of film for tritium loading. To find a desired thickness of titanium tritide foil, MCNP6 simulations were performed, resulting in Figure 6.

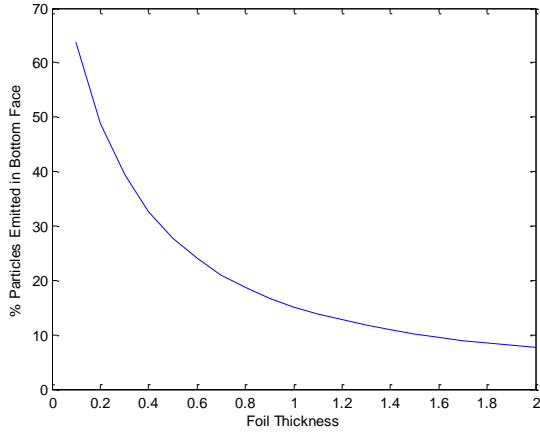


**Figure 6:** Particles Emitted by Titanium Tritide Film<sup>5</sup>

The energy spectrum emitted by the film in Figure 7 shows the high energy betas decelerated down while low energy betas get absorbed within the film. This affects the required thickness of the semiconductor p-n junction to collect EHPs.

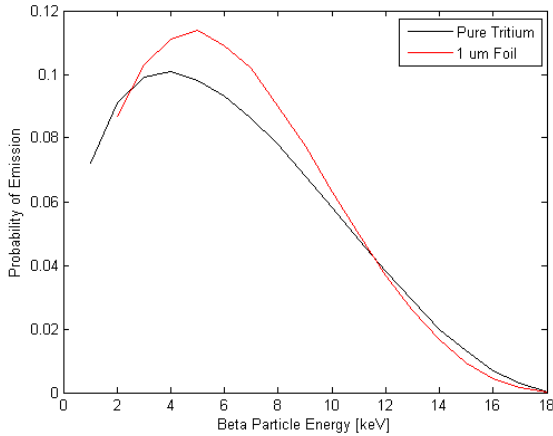


**Figure 7:** Self-Shielded Spectrum Emitted by 1 μm Titanium Tritide Foil<sup>5</sup>

### III.A.2. Absorption Coefficients

Assuming that beta particles are absorbed uniformly across the semiconductor cross-section, the only parameter that needs to be determined is the depth of absorption, which factors into the collection efficiency and desired thickness of the semiconductor p-n junction.

MCNP6 simulations were performed and compared to the traditional Katz-Penfold estimation in Eq. 1 (Ref. 6). Two conditions were used to determine absorption depth: the thickness where 99% of a beta particle's energy was absorbed or the thickness where enough energy remained to generate one EHP.

$$R = \frac{0.412E^{1.265-0.0954\ln(E)}}{\rho} \quad (1)$$

In Figure 8, both conditions in MCNP6 showed a larger absorption depth than analytically predicted, with 18 keV betas penetrating 4 μm in the substrate compared to the analytical prediction of 1 μm. This is due to the Katz-Penfold estimation predicting when 1/e of the penetrating beta's energy is deposited into a substrate.

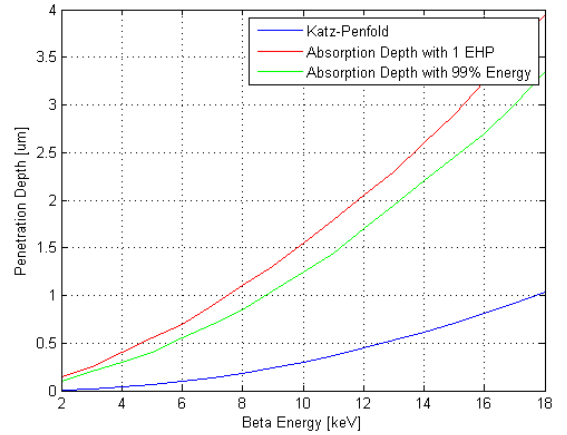


**Figure 8:** Absorption Depth of Beta Particles in GaAs<sup>5</sup>

### III.B. Electric Performance

Since betavoltaics operate similarly to photovoltaic cells, they also utilize the Shockley-Diode model in Eq. 2 (Refs. 5, 8).

$$I = I_0 \left[ \exp\left(\frac{qV}{nkT}\right) - 1 \right] - I_R \quad (2)$$

Dark current  $I_0$  flows opposite the output diode current  $I$  and is a function of the semiconductor. High dark currents indicate that the semiconductor traps and recombines EHPs, preventing EHPs from being collected which lowers  $I$ . Recombination can be determined from semiconductor properties in Eq. 3, such as intrinsic carrier concentration  $n_i$ , diffusion coefficients  $D_n$  and  $D_p$ , and diffusion length  $L_n$  and  $L_p$ , and measured semiconductor properties of doping concentrations  $N_d$  and  $N_a$ .

$$I_0 = qAn_i^2 \left( \frac{D_n}{L_n N_d} + \frac{D_p}{L_p N_a} \right) \quad (3)$$

Since the semiconductor wafers are significantly smaller than those used in photovoltaic cells, there are going to be significantly higher defects and parasitic resistances that need to be considered. Eq. 2 expands to Eq. 4, which is used to predict the betavoltaic's I-V curve with great accuracy seen in Figure 9.

$$I = I_0 \left[ \exp \left( \frac{q(V + IR_s)}{nkT} \right) - 1 \right] + \frac{V + IR_s}{R_{sh}} - I_R \quad (4)$$

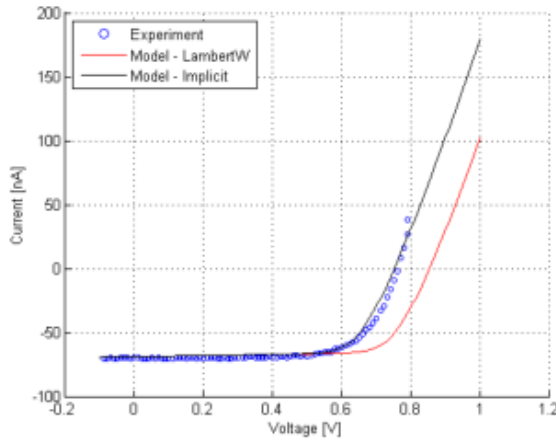


**Figure 9:** Comparison of Predicted and Measured Betavoltaic IV Curve<sup>5</sup>

## CONCLUSIONS

Research on betavoltaics at Purdue University have improved the quality and performance of the NanoTritium™ cell. Palladium films were evaluated as an improved substrate alternative to titanium films to store tritium. The NanoTritium™ cell's ruggedness or durability was also tested under multiple temperature cycles. Simulations were also performed for parametric studies on film thickness for tritium storage and semiconductor thickness to optimize power output. In addition, modeling work at Purdue University was the first to characterize and accurately model betavoltaics.

## ACKNOWLEDGMENTS

The authors would like to thank Dr. Peter Cabauy and City Labs Inc. for providing the NanoTritium cells, Naval Surface Warfare Center, Crane Division for assistance with the equipment used and Purdue Radiological and Environmental Management for allowing use of their facilities.

## REFERENCES

1. "P200 Series Extended-Life Models P200 Series Performance Characteristics Betavoltaic Power Decay" (2017).

2. L. OLSEN, P. CABAUY, and B. J. ELKIND, "Betavoltaic Power Sources," *Phys. Today*, December, 35 (2012).
3. E. M. BAUM, KNOLLS ATOMIC POWER LABORATORY., and BECHTEL MARINE PROPULSION CORPORATION., *Nuclides and isotopes : chart of the nuclides.*, KAPL (2010).
4. T. E. ADAMS, "Hydrogen Loading System Development and Evaluation Of Tritiated Substrates To Optimize Performance In Tritium Based Betavoltaics," Purdue University (2014).
5. D. S. CHEU, "Modeling and Parameter Characterization of a Betavoltaic Cell," Purdue University (2018).
6. "Temperature Characterization Test Plan for the City Labs Betavoltaic," Cambridge, Massachusetts.
7. L. KATZ and A. S. PENFOLD, "Range-Energy Relations for Electrons and the Determination of Beta-Ray End-Point Energies by Absorption," *Rev. Mod. Phys.* **24** 1, 28, American Physical Society (1952); <https://doi.org/10.1103/RevModPhys.24.28>.
8. W. SHOCKLEY, "The Theory of p-n Junctions in Semiconductors and p-n Junction Transistors," *Bell Syst. Tech. J.* **28** 3, 435 (1949); <https://doi.org/10.1002/j.1538-7305.1949.tb03645.x>.

## SUNPOWER ROBUST STIRLING CONVERTOR (SRSC) PHASE II OVERVIEW

Josh Collins<sup>1</sup>, John Stanley<sup>2</sup>, Gary Wood<sup>3</sup>

<sup>1</sup> 2005 East State Street, Ste 104, Athens OH 45710. 740-566-1108, [Josh.Collins@ametek.com](mailto:Josh.Collins@ametek.com)

<sup>2</sup> 2005 East State Street, Ste 104, Athens OH 45710. 740-594-2221 (1035), [John.Stanley@ametek.com](mailto:John.Stanley@ametek.com)

<sup>3</sup> 2005 East State Street, Ste 104, Athens OH 45710. 740-594-2221 (1109), [Gary.Wood@ametek.com](mailto:Gary.Wood@ametek.com)

*In July 2018, after successful completion of Phase I, NASA GRC awarded the Sunpower and Aerojet Rocketdyne team Phase II of a development contract under NASA's ROSES 2016 Announcement of Opportunity. The contract is in support of the Radioisotope Power Systems (RPS) office's goal of developing a robust, dynamic convertor that will enable potential future 200W – 500W RPS generators and flight missions. Sunpower's convertor – the Sunpower Robust Stirling Convertor (SRSC) – implements improvements in robustness over the heritage ASC-E3 design that were identified in the Phase I design. New project requirements for potential RPS missions have been added including high reject temperature operation, tolerance of unloaded operation, constant acceleration vibration environment, and high efficiency across a wide range of operating conditions while maintaining requirements for long life (20yrs). Based on a modular design to provide flexibility of output power and redundancy, the SRSC will enable a range of generators from 100W to 500W. This paper will focus on the accomplishments of the SRSC Phase II project including concept generator design and convertor fabrication, testing, and performance.*

### I. Project Overview

#### I.A. Phase II Project Scope

Phase II, which started in mid-2018, includes hardware as well as soft deliverables. Hardware deliverables include two flanged prototype convertors and a separate gas bearing test rig. Phase II soft deliverables include a conceptual generator design, an updated FMECA, a Flight Maturation Plan, a convertor Test Plan, Risk Management, analyses, and support of NASA GRC test plans.

#### I.B. Project Team

Sunpower and Aerojet Rocketdyne (AR) comprise the SRSC project team. Sunpower serves as prime contractor while AR serves as a subcontractor to Sunpower.

Sunpower has significant Free-Piston Stirling Engine (FPSE) expertise, including analysis, design, fabrication and testing, Sunpower has extensive free-piston machine controls experience based on convertor, cryocooler and linear compressor development. Sunpower also brings its Advanced Stirling Convertor (ASC) development experience. For this phase, Sunpower is tasked with:

- Convertor design, analysis, fabrication, and testing

- Convertor performance and compliance predictions
- Program management and reporting.

AR brings its reliability expertise, system integration expertise, RPS and aerospace experience, and extensive materials expertise. Aerojet Rocketdyne tasks include:

- Leading concept generator design and trades
- Analysis of robustness and reliability (FMECA)
- Development of a Flight Maturation Plan
- Advising on system-level considerations such as integration, controls, thermal and structural analysis

#### I.C. Project Schedule and deliverables

The Phase II PoP is currently 21 months, running from July 2018 to March 2020. It is anticipated that the contract will be extended into the 2<sup>nd</sup> quarter of 2020 based on overall program conditions.

Hardware deliverables in Phase II consist of two non-hermetic SRSC prototypes. The prototype SRSC-01 is shown in Figure 1.

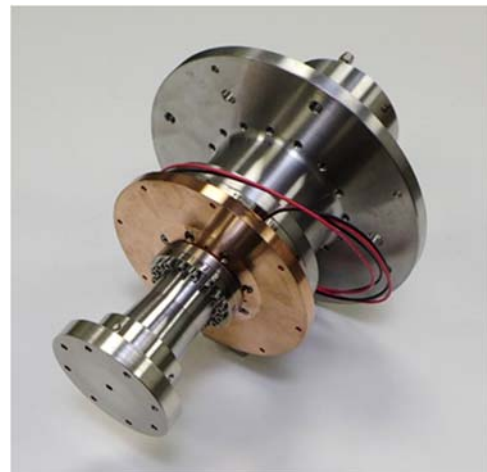


Figure 1 - SRSC prototype

Design changes and drawing updates were the focus of the first 3 months of Phase II. Hardware procurement, fabrication and processing began in October 2018. Sunpower completed test cell preparation in early 2019. The first operation of convertors were Sept 13, 2019 and Jan 8, 2020 respectively. Deliveries are tentatively planned for May and July. Onsite, post-delivery support will be provided early in Phase III. Production milestones are presented in the Table 1.

Table 1- SRSC production milestones

Soft deliverables have focused on incorporating design changes identified in the Phase I design review, production

Milestone	SRSC1	SRSC2
Component fab complete	Jul 2019	Dec 2019
Front-end assembly	Aug 2019	Jan 2020
1st operation	Sep 2019	Feb 2020
High-Temperature operation	Oct 2019	Feb 2020
Unloaded operation	Oct 2019	Feb 2020
Burn-in testing	Dec 2019	Apr 2020
Final Performance test	Jun 2020	Apr 2020
Hardware Acceptance Review	Jul 2020	Apr 2020
Delivery to NASA GRC	Jul 2020	May 2020

planning and documentation, test data delivery, development of a concept generator design and routine meetings and reporting. Additional data deliverables include updated FMECA, Flight Maturation plan, hardware photographs, and risk register.

**II. SRSC Overview**

The SRSC is a similar power level and overall physical envelope as the ASC. It includes robustness enhancements derived from lessons learned during ASC development. It also includes changes made to meet new project requirements such as a 5g lateral load requirement and unloaded operation for 10 seconds without damage. The reject temperature capability has also been increased. Overall, the SRSC design fully addresses the new robustness requirements while providing an output power of ~64W (~20% output power trade compared to ASC).

Key physical and operating characteristics are presented in the following two tables.

Table 2 - SRSC physical and operating characteristics

Physical Characteristics (Flight)	
Mass	2.0kg - Convertor only 3.4kg - Convertor, CSAF, incl. external
Outer Diameter	127mm
Overall Length	237mm
Physical Characteristics (Flanged)	
Mass	7.2 kg - Includes flanges
Outer Diameter	127mm 182mm - Test mounting flange
Overall Length	265mm
Nominal Operating Point (BOL, Low Heat)	
Head temperature	680 - 720C
Reject Temperature	100C
Alternator Temperature	110C
GPHS heat	244W
Insulation loss	20.6W
Convertort Heat Input	223.4W
PV Power	74.1W
Alternator losses	10.5W
Net Output Power	63.7W
Conversion Efficiency	29%

**II.B. SRSC Design Change Implementation**

Design changes incorporated into the SRSC were made for four criteria – responding to new project requirements, increasing robustness, increasing reliability, or increasing manufacturability. Key changes are listed in the following table along with which criteria is addressed.

*II.B.1. Robust Regenerator*

Sunpower is currently studying regenerator designs which will ensure no debris are released during operation. Indications are that debris observed in previous regenerator designs were related to fabrication, cleaning and installation processes. The baseline regenerator production method will follow Sunpower’s proprietary cryocooler regenerator production method and will be tailored as necessary. The cleaning method, if it is necessary, will also be tailored for the SRSC. Sunpower has also independently researched a wrapped regenerator design as a fall back plan.

*II.B.2. Bumper and piston centering*

A key NASA requirement in the DRPS project is survival of 10 seconds of unloaded operation with no long-term loss of function or capability. Two mechanical features implemented in the SRSC design are known first-contact surfaces (bumpers) between the moving components and the structure, and mechanical axial piston centering. Figure 2 shows a side view of the bumper and piston assembly. Bumper surfaces are fabricated for flat, face-to-face contact and the material was selected such that no debris is generated during contact. A planar spring provides mechanical, axial piston centering. The mechanical spring’s sole function is to eliminate the startup procedure which previously required DC current to center the piston prior to operation.

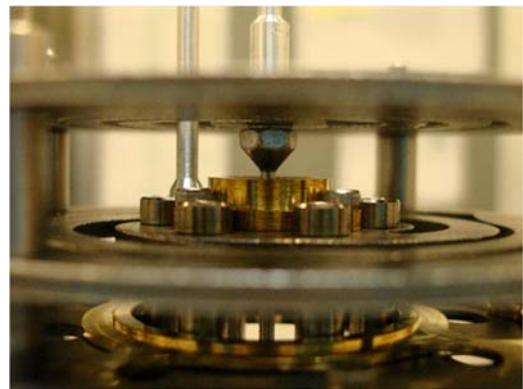


Figure 2 - Bumper and piston assembly

*II.B.3. Loss of Load Tolerant (LLT) Features*

In addition to mechanical bumpers, Sunpower has developed a pneumatic method of contact avoidance during unloaded operation. Sunpower’s patented design (patent 20180112625) is named the Loss of Load Tolerant (LLT) design. When the electrical load is removed, the

SRSC piston amplitude grows instantaneously and uncontrolled as the cycle attempts to dissipate all of the thermodynamic energy. The cycle operates, detuned, at its natural frequency rather than the design point. The LLT engages as the piston amplitude grows to causing collisions with the displacer.

LLT operation has been demonstrated in SRSC-01 and SRSC-02 on multiple occasions. LLT testing will be included in, at least, two production steps – once with practice running parts (Shakedown 1 testing) and once with production running parts (Shakedown 2 or later). For SRSC-01 and SRSC-02 the first operation of LLT occurred during the Design Verification step, during which converters are iteratively progressed through operating conditions to characterize performance prior to beginning the production test sequence. LLT in Design Verification or Shakedown 1 testing may be eliminated in future builds.

The Figure 3 presents sample test data from Shakedown 2 LLT testing. Note, piston motion remains sinusoidal and does not come into contact with the in-stop nor the out-stop. Non-contact operation has been verified through post-operation inspection.

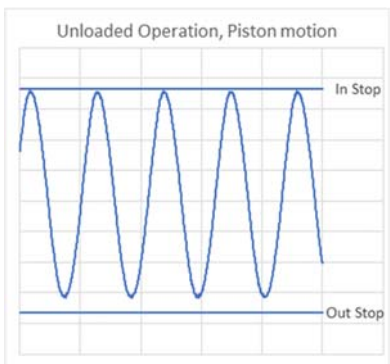


Figure 3 - Piston motion during LLT operation

#### II.B.4. Cylinder mounting and material change

The installed ASC cylinder geometry was found to be sensitive to the torque applied to the mounting clamp. Because of this, the SRSC design utilizes an improved mounting technique found in U.S Patent 20180306140 which minimizes distortion to the cylinder caused by mounting torque, charge pressure, or thermal expansions.

Additionally, the required elevated temperature operation raises concerns of issues due to materials' thermal expansion mismatch. With the new reject temperature requirement of 175°C, the engine cylinder and piston material have been changed to titanium, which is the same material as the magnet can. This removes concerns with any difference in thermal expansion between materials. The SRSC prototypes have demonstrated no sign of sensitivity to cycling and hours-long exposure to max required reject temperatures.

#### II.B.5. Increased Gas Bearing Capacity

A new, 5g lateral load requirement is imposed on the SRSC project which is greater than heritage projects and requires design modification to accommodate. To address this requirement, the displacer rod diameter was increased so that its gas bearings have a larger support area. Additionally, we increased the number of gas bearing pads. These design changes do require a modest trade in output power and efficiency due to increased pumping losses. Sunpower will further quantify and correlate gas bearing capacity using the test rig shown in Figure 4.

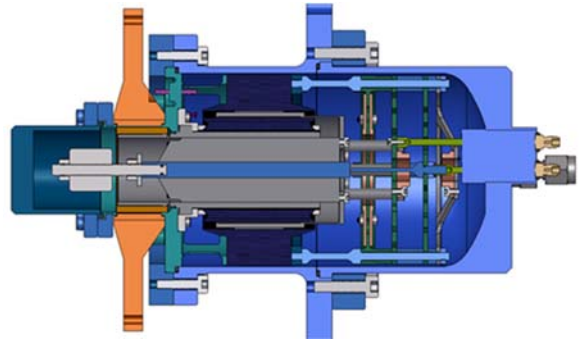


Figure 4 – Gas bearing test rig

#### II.B.6. Gas bearing check valve and filter

Sunpower converter designs incorporate gas bearings on the moving components. Gas bearings simplify converter mechanical design as well as reduce assembly difficulty. The use of gas bearings also largely reduces the number of single point failures in the converter. There are concerns within the RPS community that gas bearings could be compromised by debris in the working space. Though isolated, there have been instances of compromised gas bearings due to debris entering the gas bearing system and preventing the check valve from sealing properly. Two features have been added to the SRSC design to make the gas bearing system robust to debris. First, a redundant check valve (in series) has been added. Second, a filter has been added to the inlet of the gas bearing system (Figure 5) to prevent debris from entering the system. These modifications require three cascading failures by multiple pieces of debris entering the



Figure 5 – Gas bearing system entrance filter

gas bearing system and navigating a tortuous path to compromise the gas bearings.

*II.B.7. Encapsulated magnet can*

During the ASC-E3 program, two convertors were unintentionally driven to severe collisions during offsite testing. The high-impact, driven collisions caused permanent deformation to the magnet can assembly, and ultimately led to convertor failure.

Phase II SRSC design modifications targeted increasing the magnet can assembly robustness to contact. The design (shown in Figure 6) incorporates a thin, split sleeve to cover the magnets, ribs at each end of the magnets, thicker magnet can structure, and a thicker magnet can hub. The thin, split sleeve prevents direct contact between laminations and sintered magnets. The thicker magnet can, ribs, and thicker hub result in a stiffer assembly that is more robust against collisions. The alternator running clearances have also been increased.

Two additional design changes include changing magnet material to meet elevated reject temperature requirements and posts on the out end of the magnet can for assembly with the piston spring.



Figure 6 – SRSC magnet can assembly

*II.B.8. Heater head material change*

Previous convertor designs selected MarM for the heater head material due to its high temperature strength capabilities. However, MarM had drawbacks including material availability, long lead times, limited material property data, low yield, and extensive/costly processing. Resulting from a Phase I trade study, AR recommended Haynes 230 alloy based on their extensive experience with it. Haynes is superior to MarM in material availability, material property data, weldability, cost, machinability, and yield. Haynes has a slightly lower operating temperature when designing for >20 years life.

Figure 7 shows two completed heater heads. Of the four processed assemblies, three production worthy heater heads were produced. Production time, cost, and yield of Haynes 230 heater heads have demonstrated significant improvement over MarM.



Figure 7 – SRSC heater heads

**II.C. SRSC Performance Predictions**

The point of departure design – ASC-E3 - convertors all produced slightly over 40 percent thermal to electrical conversion efficiency. New requirements levied on the SRSC, namely 175°C reject temperature, increased lateral acceleration loads, design changes to increase robustness, and a lower nominal operating temperature for the heater head have combined to reduce overall convertor efficiency by approximately 10 percentage points compared to the heritage ASC convertor design. The projected efficiency of the SRSC is 29% which exceeds both the required efficiency of 24% and the programmatic goal of 28%. This efficiency remains essentially constant over the 17-year mission requirement. The first SRSC prototype has demonstrated 65.5W<sub>e</sub> output at a calculated 29.4% efficiency at the design point. At high reject, the SRSC has demonstrated 54.3W<sub>e</sub> and 24.3% efficiency. The following table presents demonstrated SRSC projected performance.

Table 3 – SRSC performance predictions

	Head Temp (C)	Reject Temp (C)	Heat In (W <sub>th</sub> )	Output Power (W <sub>e</sub> )	Eff (%)	Eff Reqt (Goal) (%)	Specific Power (W <sub>e</sub> /kg)
Nominal	720	100	223	63.7	28.6%	24 (28)	31.9
125C Reject	720	125	223	63.3	28.4%		31.7
High Reject	720	175	223	52.1	23.4%		26.1
2/3 Heat Input	720	100	149	41.1	27.6%		20.6
1/2 Heat Input	720	100	112	28.7	25.6%	20	14.4

**II.D. Concept generator design**

Aerojet Rocketdyne developed a conceptual design for a RPS generator based upon the SRSC. NASA instructed AR to focus on a generator design utilizing four GPHS. The concept generator incorporates a total of six SRSC convertors arranged in three opposing pairs (50% redundancy). Convertor pairs are synchronized for vibration cancellation. The overall dimensions of the design are 271cm diameter (fin tip) and 154cm in height. The design is shown in Figure 8.

Key requirements of the design include:

- 17-year design life
- ≥ 2 W<sub>e</sub>/kg specific power (DC output to spacecraft)
- ≥ 20% thermal to electric conversion efficiency

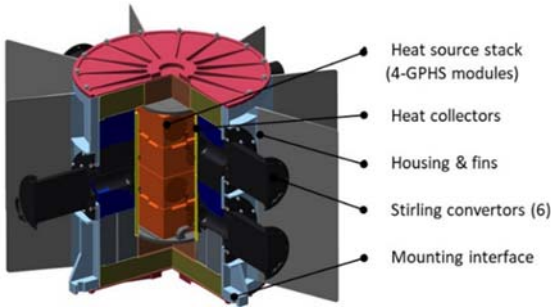


Figure 8 – Concept generator design

- Operable in Lunar, Mars, Titan, Europa, Triton, and Enceladus environments
- Compatible with DOE existing 9904 shipping cask

The Table 4 presents the generator design performance at the reference condition and in various operational environments.

Table 5 - Concept generator predicted performance

Concept Generator Design Performance	
Heat input	1000 W
Head Temperature	720°C
Reject Temperature	104°C
Power out of converters	274 W <sub>ac</sub>
Controller efficiency (allocation)	87%
Power out, generator	238 W <sub>dc</sub>
Mass (excludes controller)	49.3 kg
Specific power	3.5 W <sub>dc</sub> /kg
Generator efficiency	24%

	Reference	VGA	Lunar	Mars	Europa	Enceladus	Triton
Q in	1000	1000	1000	1000	1000	1000	1000
T Hot, converter	720	720	720	720	720	720	720
T Cold, converter	103	129	163	125	104	104	103
Power out, W ac	274	260	242	247	274	274	274
Efficiency	27%	26%	24%	25%	27%	27%	27%
Controller efficiency	87%	87%	87%	87%	87%	87%	87%
Power out, W dc	238	226	210	215	238	238	238
Generator efficiency	24%	23%	21%	22%	24%	24%	24%

### III. CONCLUSIONS

Sunpower’s SRSC design offers improvements in robustness, reliability, and manufacturability based on lessons learned from the point of departure design – the ASC-E3. The SRSC is expected to be compliant with all program requirements and goals as shown in the Table 5. Both SRSC prototypes have demonstrated successful implementation of the design changes and, based on test data, are projected to meet requirements.

In terms of new project requirements, the most difficult to attain are unloaded operation, high reject temperature operation, and increased static acceleration loading. Both SRSC prototypes have demonstrated unloaded operation and high reject temperature operation multiple times successfully.

The Sunpower, Aerojet Rocketdyne team is entering the final months of Phase II performance. Sunpower’s primary focus at this time is completing and delivering

Table 4 - SRSC predicted compliance with requirements

Category	Requirement	Goal	Current Estimate
T/E conversion efficiency	≥ 24% at Trej ≥ 100C	≥ 28% at Trej ≥ 100C	29%
Partial power op	≥ 20% efficiency at half power		27%
Head operating temp	< 1000C		Th = 720C
Reject operating temp	≥ 100C to meet efficiency req't		Demonstrated
	Operation 20 - 175C		Demonstrated
Loss of load	10 second loss of load at full power, no power loss		Demonstrated
Prototype instrumentation	Direct measurement of Th, Tr, alternator, Xp, Xd		Demonstrated
Specific power	> 20W/kg (converter only)		~33 W/kg
Design life	20 years continuous operation		Compliant
Power output	Enables 200-500W generator		Compliant
Start-stop cycles	Capable of min 150 cycles		Compliant
Launch vibration	Survive, no long-term power loss		Compliant
Static acceleration	Static and random vbe exposure, no long-term power loss		Compliant
Performance degradation		Power degradation < 0.5%/yr	Compliant
Thermal energy input	Accept heat from GPHS		Compliant
Atmospheres	Earth, argon, vacuum, Mars, Titan		Compliant
Radiation environment		No power loss after 300krad exposure	Compliant
EMI		DC magnetic field	Compliant
Autonomy		No set point adjustments during launch	Compliant
		No set point adjustments during static accel	Compliant
Transmitted forces	< 10N transmitted to spacecraft		Compliant
Size	Generator fits DOE cask		Compliant
Manufacturability		Utilize proven MFG methods	Compliant
Flight instrumentation		No sensors required for mission	Compliant

prototype hardware to NASA GRC. Both prototypes have operated and demonstrated compliance with key requirements. Convertors are expected to be delivered in April and July 2020.

Aerojet Rocketdyne’s concept generator design focused on using four GPHS modules. However, it is designed for scalability to meet larger output powers. To include redundancy and meet power requirements, the generator is based on six SRSC convertors oriented in opposed, synchronized pairs. Predicted performance for the generator meets project requirements. If one considers the Phase II generator concept as a module, it also fits in line with RPS goals of enabling missions with power needs of 100W – 500W. The generator concept design is scalable and modular which makes the SRSC generator flexible to meet a wide range of mission power outputs and redundancy requirements.

### ACKNOWLEDGMENTS

The authors wish to acknowledge NASA’s Radioisotope Power Systems program office and NASA Glenn Research Center’s project and SRL teams for their continued support of the SRSC team and dynamic space power. The authors also wish to recognize Bill Otting and the technical team at Aerojet Rocketdyne and the technical team at Sunpower for their continued excellence in performance, technical innovation, and collaboration.



## II. PAST WORK

Previous work<sup>5</sup> from the Center for Space Nuclear Research (CSNR) considered the use of targets placed in the ATR's "I" lattice positions. These targets were assumed to be of the same design as those currently in use at HFIR. The model did not incorporate design limitations related to safety or the baskets used to hold targets in place. The use of HFIR targets underutilized the active core length of the ATR, showing potential for <sup>238</sup>Pu production increase with a longer target length. The absence of basket design constraints overestimated the number of target rods that could be placed in each lattice position.

Prior to the CSNR investigation, ATR production capacity was estimated based on work by INL's Bruce Schnitzler<sup>6,7</sup>. Schnitzler's work assumed shorter reactor operations cycles and higher power, fewer limitations on target placement, and higher acceptable levels of <sup>236</sup>Pu content. That work was accomplished using a software module linking the ORIGEN module of SCALE and MCNP. As this was developed for significantly older versions of both codes and is no longer in use, this is not a reasonable computational approach to take for our current analyses.

## III. METHODS

A Serpent<sup>8</sup> model of the ATR was used to evaluate the target composition over time. The burn card performs activation, depletion, and decay analyses in specified time steps and was used to calculate the final target composition.

Table I shows the parameters and goals used to constrain our analysis. Target construction varied in length and volume percent NpO<sub>2</sub> in the pellets. Our goals were production of at least 1500 g PuO<sub>2</sub> per year, minimizing the concentration of <sup>236</sup>Pu in the final PuO<sub>2</sub>, maximizing the amount of <sup>237</sup>Np converted into <sup>238</sup>Pu, and maximizing the assay of isotope <sup>238</sup>Pu in the total plutonium produced.

**TABLE I.** Analysis Parameters and Goals

Parameter	Goal/Limit
Target Length	40 inch MAX
NpO <sub>2</sub> Concentration	30 vol% MAX
<sup>238</sup> Pu Mass	1500 g/year
<sup>236</sup> Pu Concentration	2 ppm MAX
<sup>238</sup> Pu Conversion	10% MIN
<sup>238</sup> Pu Assay	87% MIN

In order to develop a fuller understanding of trends, target length and NpO<sub>2</sub> concentration were varied beyond these set limits.

ATR operating parameters were assumed to be 100 MW operating power with 62 days spent at power followed

by a 60 day cool down period. INL design specifications require targets to be surrounded by a water channel, an aluminum basket, and an outer water channel within the irradiation position.

An additional model was generated to explore the impact of a sleeve of moderator around the target in order to soften the flux spectrum experienced by the target.

## IV. RESULTS

In all irradiation positions, an increase in NpO<sub>2</sub> pellet concentration resulted in increased <sup>238</sup>Pu production and <sup>238</sup>Pu assay. However, it also increased <sup>236</sup>Pu concentration and decreased conversion ratio. Figures 3 and 4 show this behavior for the combined large and medium I positions. The quantitative impact of these varies between positions based on flux magnitude and spectrum.

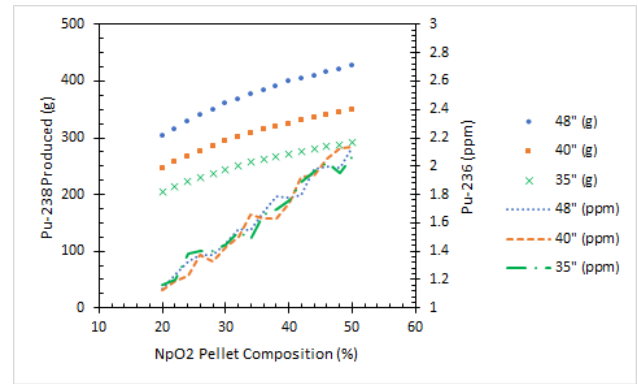


**Fig. 3.** Annual <sup>238</sup>Pu yield and <sup>236</sup>Pu concentration at different pellet compositions and target lengths in large and medium I positions.

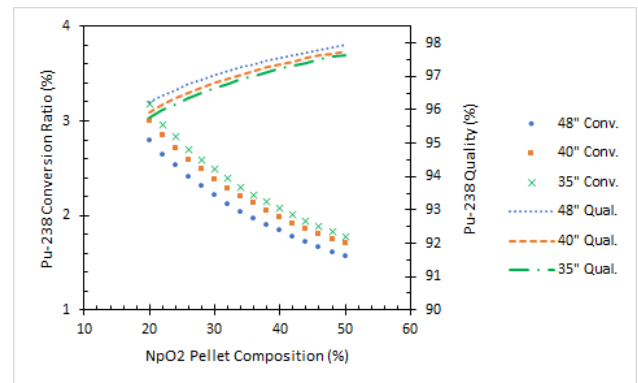


**Fig. 4.** Annual <sup>238</sup>Pu quality (assay) and conversion ratio at different pellet compositions and target lengths in large and medium I positions.

Figures 5-8 show the four irradiation position groupings in comparison to each other over the course of three full-power cycles. The results combine all targets in each group (e.g., "Med/Large I" includes the sum of all targets in all medium and large I positions).

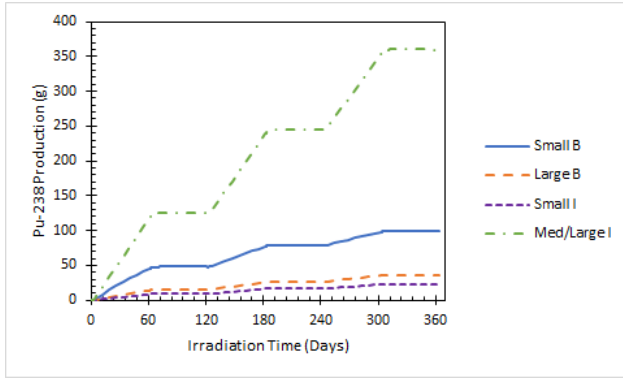


**Fig. 5.**  $^{238}\text{Pu}$  production over time in various ATR positions (48" rod, 30%  $\text{NpO}_2$ ).

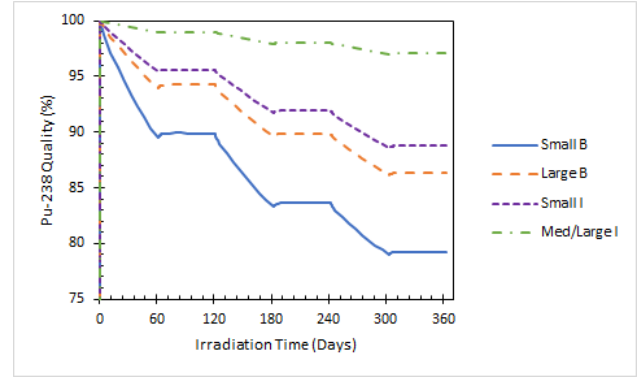


**Fig. 8.** Plutonium assay over time in various test positions (48" rod, 30%  $\text{NpO}_2$ ).

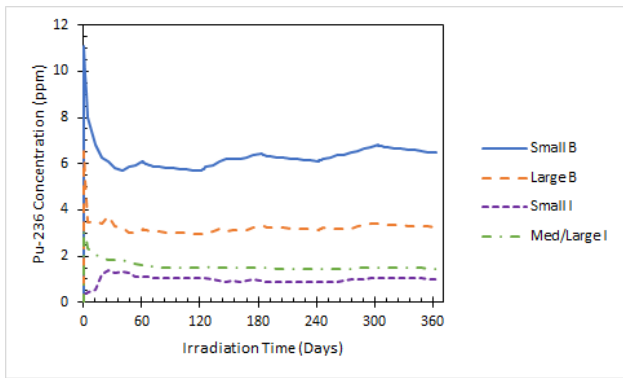


**Fig. 6.**  $^{236}\text{Pu}$  concentrations over time in various test positions (48" rod, 30%  $\text{NpO}_2$ ).

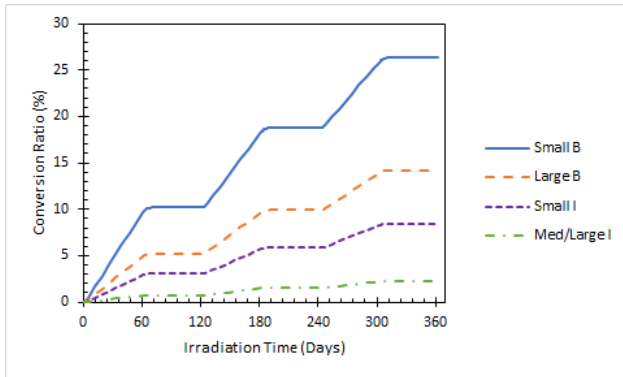


**Fig. 7.**  $^{238}\text{Pu}$  conversion ratio over time in various test positions (48" rod, 30%  $\text{NpO}_2$ ).

The quantity of  $^{238}\text{Pu}$  produced per position is tied strongly to the amount of  $^{237}\text{Np}$  irradiated. Although this is obvious, in the case of comparing the production in different experimental positions it obscures the impact of the increased costs of target construction and processing. Figure 8 provides an overview of production per irradiation position (Figures 3-8 show results for all irradiation positions of a given type, while Figures 9 and 10 show the production for a single position), showing the large and medium I positions as very attractive options for  $^{238}\text{Pu}$  production. However, Figure 10 shows that the difference in production per target is significant. The cost and capacity of the ORNL facilities to process the targets post-irradiation become a significant factor in the feasibility of achieving that production quantity in the large and medium I positions. Their production potential is due entirely to their ability to hold a large number of targets.

The addition of a graphite sleeve had little significant impact. Although  $^{238}\text{Pu}$  production increased, and in some positions other factors improved, the improvement was minimal and unlikely to be worth the added complications in target fabrication and qualification. Other potential moderating materials were disregarded due to difficulty in implementing the construction of such a sleeve.

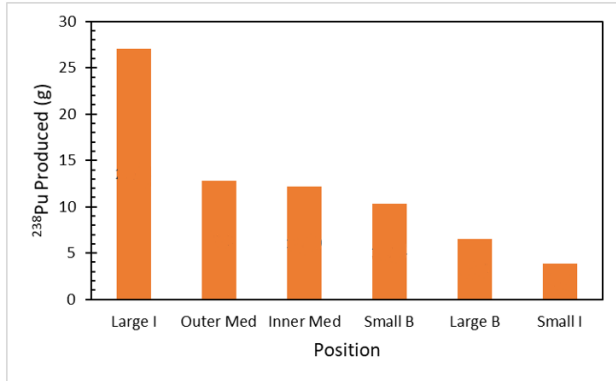


**Fig. 9.** <sup>238</sup>Pu production per position per year (48'' rod, 30% NpO<sub>2</sub>).

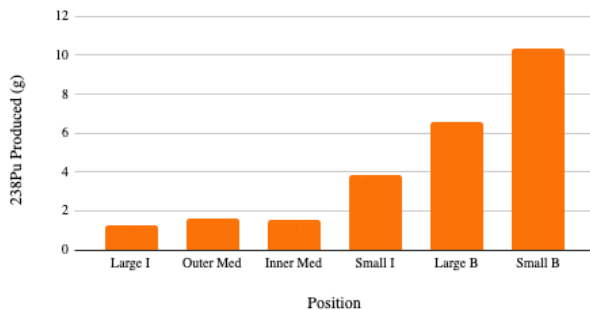


**Fig. 10.** <sup>238</sup>Pu production per target in each position per year (48'' rod, 30% NpO<sub>2</sub>).

## V. CONCLUSIONS

In keeping with previous studies, the most important parameter predicting <sup>238</sup>Pu production capacity is the amount of <sup>237</sup>Np being irradiated. Unlike previous work, this study explores the impact of several additional parameters on production capacity as well as other important characteristics of the end product that must be taken into consideration.

A balance must be found between <sup>236</sup>Pu production and plutonium assay and the conversion rate. In order to address the <sup>236</sup>Pu concentration, an additional step will be necessary after a delay of several years to allow for decay to nuclides (such as <sup>232</sup>U) that can be separated from the rest of the plutonium chemically. Meeting a 2 ppm limit on <sup>236</sup>Pu concentration would preclude use of higher-flux lattice positions and significantly impact the final plutonium assay.

## VI. FUTURE WORK

Additional irradiation positions with high flux must be evaluated. Although the I positions are attractive when considering assay, <sup>236</sup>Pu concentration, and <sup>238</sup>Pu production, that comes at the cost of a large number of

targets that must then be shipped to Oak Ridge and processed. The allowable concentration of <sup>236</sup>Pu must be reassessed from the current 2 ppm limit.

Analysis of target design could also provide benefits, but would involve careful consideration of the capabilities of existing target production, transport, and processing facilities. In this case, changes in target radius were not considered, nor were non-cylindrical geometries.

## ACKNOWLEDGMENTS

A special thanks to Dr. Herring from CSNR; Brian Gross, Doug Crawford, and Mark DeHart from INL; and Jaakko Leppänen from VTT for their support of this project.

Previous CSNR project members have made invaluable contributions to this research: Ashoak Nagarajan, Dominik Fritz, Grace Marcantel, Lucas Beveridge, Joshua Rhodes, Tyler Gates, and John Kuczek.

This research made use of the resources of the High Performance Computing Center at Idaho National Laboratory, which is supported by the Office of Nuclear Energy of the U.S. Department of Energy and the Nuclear Science User Facilities under Contract No. DEAC0705ID14517.

## REFERENCES

1. "SPACE EXPLORATION: DOE Could Improve Planning and Communication Related to Plutonium-238 and Radioisotope Power Systems Production Challenges," Tech. Rep. GAO-17-673, United States Government Accountability Office, (Sep. 2017).
2. C. R. DAILY and J. L. DUFFEE, "Design Optimization Studies for NpO<sub>2</sub> Targets Irradiated in the High Flux Isotope Reactor," presented at Nuclear and Emerging Technologies for Space 2019 American Nuclear Society Topl. Mtg., Richland, WA, February 25-28, 2019.
3. "Chart of the Nuclides," Nuclear Data Center, Brookhaven National Laboratory, 2019.
4. "FY 2009 Advanced Test Reactor National Scientific User Facility User's Guide," Tech. Rep. INL/EXT-08-14709, Idaho National Laboratory, (2009).
5. E. COLVIN, J. H. RHODES, G. A. MARCANTEL, T. KAJIHARA, J. T. GATES, J. J. KUCZEK, L. B. BEVERIDGE, A. N. NAGARAJAN, and D. A. FRITZ, "Optimization of Plutonium-238 Production in the Advanced Test Reactor for Radioisotope Thermoelectric Generators in Deep Space Exploration Applications," presented at Nuclear and Emerging Technologies for Space 2019 American Nuclear Society Topl. Mtg., Richland, WA, February 25-28, 2019.

6. B. G. SCHNITZLER, "INEL Advanced Test Reactor Plutonium-238 Production Feasibility Assessment," *AIP Conf. Proc.*, Albuquerque, NM, January 10-14, Vol. 271, p.143-151, AIP (1993).
7. B. SCHNITZLER, "Plutonium-238 production in the Idaho National Laboratory Advanced Test Reactor," Tech. Rep. INL/LTD-11-21461, United States Department of Energy, (2011).
8. J. LEPPÄNEN et al., "The Serpent Monte Carlo code: Status, development and applications in 2013," *Annals of Nuclear Energy*, **82**, 142–150 (2015).

## CHEMICAL PROCESSING IN PLUTONIUM-238 SUPPLY PROGRAM—STATUS AFTER CAMPAIGN 4

David DePaoli, Dennis Benker, Lætitia Delmau, Porter Bailey, Steven Sherman, Frank Riley, Kristian Myhre, Emory Collins, and Robert Wham

Oak Ridge National Laboratory, Oak Ridge, Tennessee, 37831-6423  
(865) 574-6817, [depaolidw@ornl.gov](mailto:depaolidw@ornl.gov)

*Continued progress is being made in development of processes for production of  $^{238}\text{Pu}$  at Oak Ridge National Laboratory for NASA. During the past year, the processes to prepare source material for target fabrication were advanced and matured into routine operations. All processes from dissolution of irradiated targets through to plutonium purification and conversion to oxide product were performed at a batch size suitable for full-scale production, representing important steps in the transition to full-scale production.*

### I. INTRODUCTION

Oak Ridge National Laboratory (ORNL) has restarted domestic production of  $^{238}\text{Pu}$  for use in space power applications. This mission involves producing neptunium targets for irradiation in Department of Energy research reactors, processing the irradiated targets to produce heat-source plutonium oxide (HS-PuO<sub>2</sub>) product, and shipping the product to Los Alamos National Laboratory. NASA and Department of Energy plans for constant-rate production of  $^{238}\text{Pu}$  heat sources<sup>1</sup> require increasing ORNL production of HS-PuO<sub>2</sub> to a full-scale production average of 1.5 kg/year by 2025.

Chemical processing is a key element of the overall production process. Primary requirements of the chemical processes are a) to supply Np that can be converted into neptunium oxide cermet pellets for inclusion in targets that are compliant with the Experiment Authorization Bases Document for irradiation in the High Flux Isotope Reactor (HFIR) and b) to recover plutonium from irradiated targets to produce HS-PuO<sub>2</sub> meeting General-Purpose Heat Source (GPHS) specifications.

A simplified diagram of chemical processes is shown in Figure 1. Neptunium oxide (NpO<sub>2</sub>) source material is dissolved in nitric acid and treated for removal of Th and Pa-233, the decay daughter of Np-237. That solution is processed using modified direct denitration into NpO<sub>2</sub>. The oxide is mixed with aluminum powder and formed into cermet pellets, which are assembled into targets for irradiation. The irradiated targets are dissolved in a two-step process: the aluminum cladding and aluminum from the cermet pellets are dissolved in caustic nitrate solution and then the remaining oxide is dissolved in nitric acid. In the primary separation step, bulk Np and Pu are separated

from each other and from fission products. Solvent extraction has been used for primary separations in ORNL processing. The Pu stream is further purified by anion exchange, then converted to oxide by loading onto cation exchange resin and calcining. The Np stream is further purified and recycled for target fabrication. Anion exchange is the baseline process for Np purification.

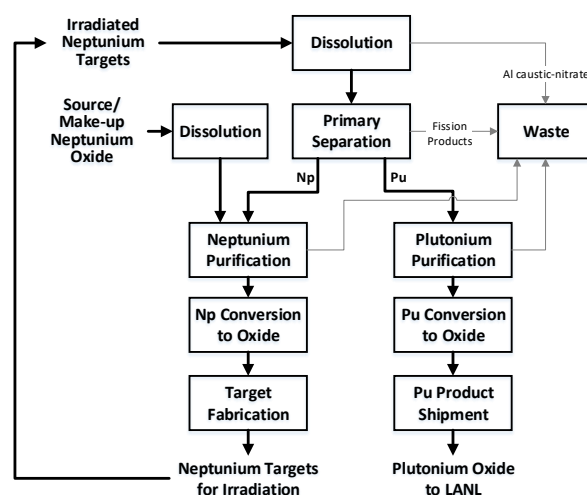


**Fig. 1.** Simplified depiction of chemical processing for  $^{238}\text{Pu}$  production.

At NETS 2019, we reported<sup>2</sup> results of the third processing campaign with irradiated targets (Campaign 3), which produced ~250 g of HS-PuO<sub>2</sub> meeting  $^{238}\text{Pu}$  content and GPHS impurity specifications. Demonstrating the capability to produce suitable product from irradiated neptunium targets was a significant milestone for the program; the remaining challenge is to scale up and mature the processes to achieve and maintain full-scale production. Significant processing experience has been gained since NETS 2019. Enough Np was supplied to produce approximately 190 targets and a batch of 63 irradiated targets was processed during Campaign 4 to produce HS-PuO<sub>2</sub>. This summary describes the chemical processing activities conducted during the past year, presents an evaluation of the current status of process maturity, and discusses prospects for future development.

## II. PROCESSING SUMMARY

### II.A. Neptunium Supply

Approximately 4.5 kg of  $\text{NpO}_2$  was dissolved, treated, and processed in 2019 into  $\text{NpO}_2$ -Al cermet targets. The remainder of the  $>6$  kg of Np processed in 2019 was recycled Np. Several technical challenges were overcome in developing an efficient and integrated process for the oxide.

The  $\text{NpO}_2$  source/make-up material was recovered several years ago at Savannah River Site. Dissolution of the oxide in nitric acid must proceed at a reasonable rate and generate a product solution suitable for subsequent cation exchange treatment for removal of Th, Pu, and impurities in the  $\text{NpO}_2$  as well as in-grown Pa-233. Operating conditions have been optimized by adjusting the amount of acid used in the batch process to enable full dissolution of oxide batches in less than a day and have resulted in an acceptable acid-to-Np ratio in the product solution.

Cation exchange treatment for removal of Th, Pu, and Pa from Np solution is conceptually straightforward. The Np is converted to the Np(V) oxidation state by addition of hydrogen peroxide, and the solution is passed through a cation exchange column. Thorium, plutonium, and protactinium are preferentially retained on the resin and the column effluent is collected as a clean and sufficiently concentrated Np product solution. Treatment of 23 batches of Np has demonstrated that excellent Th, Pu, and Pa removal may be obtained under conditions where the Np(IV) and Np(VI) concentrations are minimized and the acid and Np concentrations are not too high. Operations technicians have successfully and routinely conducted these steps without direct guidance from development staff.

### II.B Irradiated Target Processing

Campaign 4 demonstrated efficient and scaled-up processes for conversion of irradiated targets into HS- $\text{PuO}_2$  and Np for recycling into new cermet targets. Successes in the campaign include the demonstration of a more efficient approach for target dissolution and operation of scaled-up ion exchange processes.

A total of 63 aluminum-clad targets containing 20 vol%  $\text{NpO}_2$ -Al cermet pellets that had been irradiated for 3 HFIR cycles were processed through caustic nitrate dissolution steps for removal of aluminum, followed by dissolution of the actinide oxides in nitric acid. The caustic dissolution was conducted using an approach designed to reduce processing time and overall waste volume. Rather than proceeding with the entire dissolution sequence (a caustic decladding step, followed by a caustic pellet digest, vessel flushes, and acid dissolution) for each of the three 21-target batches, the decladding steps were conducted sequentially, followed

by a single caustic digest on the remaining pellet material from 63 targets and a single acid dissolution. The approach eliminated six process steps and reduced the volume of caustic waste by eliminating two volumes of caustic digest solution and two caustic heel flushes. The volume of caustic waste generated during the campaign was reduced by 25% to a value within the operating volume of the waste tank. Another important benefit of this dissolution approach was a significant reduction in actinide concentration in the caustic solution.

The primary separation of Pu in Campaign 4 was a Pu-selective solvent extraction run using a tributyl phosphate (TBP) solvent. Hydraulics of the two-phase flow in both mixer-settler banks was excellent throughout the run. Accumulation of solids in the organic phase of the settlers was not detectable in the coextraction bank. This improvement in operations compared to Campaign 3 may be related to the addition of a filtration step on the feed solution. Online spectrophotometry enabled real-time monitoring of Pu and Np concentrations in the stages of the mixer-settler banks. Excellent recovery of Pu was achieved, resulting in a level of 33 ppm of  $^{238}\text{Pu}$  relative to Np in the raffinate stream containing Np and fission products. This run demonstrated the potential for adding hydroxylamine nitrate to the scrub solution in the coextraction bank for selective Np reduction to lower the amount of Np in the product stream.

Plutonium anion exchange, which was introduced into the flowsheet in Campaign 3, was used again in Campaign 4 for removal of P, Th, and most of the remaining Np. Column size was scaled up by 50% for this campaign to match capacity with the subsequent cation exchange step. Online spectroscopic monitoring was conducted throughout the runs. Ultraviolet-visible spectroscopy was used to monitor feed adjustment and to provide information for routing the effluent solution based on relative concentrations of Np and Pu. Acceptable removal of Th and Np was achieved.

The  $\text{PuO}_2$  product was generated by loading the Pu product solutions from anion exchange onto cation exchange resin and calcining the loaded resin. The column and furnace for this step were scaled up by a factor of 3 from Campaign 3. A total of approximately 175 g of HS- $\text{PuO}_2$  was generated from the first three runs of the campaign. A remaining amount of Pu from Campaign 4 equivalent to approximately 70 g of oxide is available for future purification and conversion to oxide. Good oxide purity was indicated by calorimetry of the products. Impurity analyses of the product oxide are pending.

Scaled-up processing produced a reduction in the number of process operations by greater than a factor of 2 compared to Campaign 3; this is a significant step

towards the needed reduction in campaign duration to meet production goals in the future.

Recycled Np from Campaign 4 has been treated in several ways to evaluate process alternatives. Solvent extraction using TBP for fission product removal, followed by anion exchange for phosphorus removal is the current baseline for recycle Np processing. Phosphorus removal is of concern, as P above a few hundred parts per million in NpO<sub>2</sub> have resulted in physical changes (expansion, cracking) of NpO<sub>2</sub>-Al cermet pellets during heat treatment. Anion exchange may not be optimal for full-scale production because of lower throughput (approximately 400 g Np per day maximum rate) and high nitric acid usage (approximately 40 mol of acid per target). A combination of alternative steps was tested—multistage, countercurrent contacting of the Np stream generated by fission product removal by solvent extraction, followed by cation exchange treatment for removal of Pa, Pu, and Th under feed conditions adjusted to remove complexed P. The phosphorus concentration was reduced somewhat; however, conditions that result in sufficiently low phosphorus in the treated solutions have not yet been obtained.

### III. PROCESS MATURITY

The current state of maturity of process steps is summarized in Figure 2. This figure, which presents a color-coded qualitative measure of process maturity, indicates significant progress during the past year.

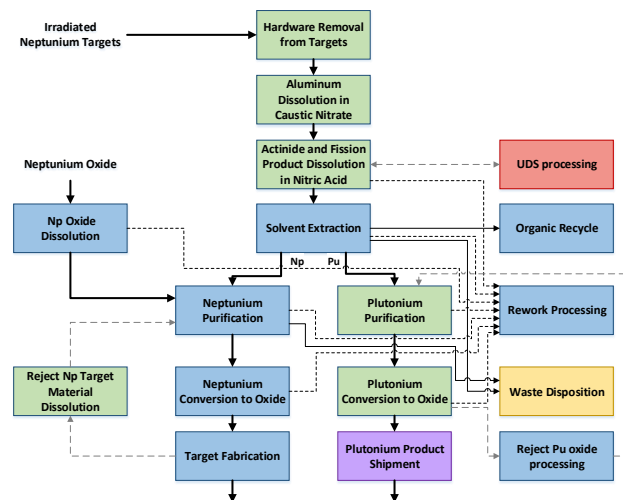


**Fig. 2.** Maturity of chemical processing steps in <sup>238</sup>Pu Supply Program. Red—concept only, no testing to date. Yellow—partial progress, significant technical issues to address. Purple—positive progress, options identified to address issues. Blue—demonstrated, scale-up and/or

efficiency issues remain. Green—suitable for full-scale production.

Neptunium oxide dissolution and cation exchange treatment for target fabrication have been demonstrated, and the remaining step is to acquire permanent equipment for scaled-up processing.

Conversion of Np to oxide, pellet production, and target fabrication have been demonstrated at approximately half the rate required for full-scale production. A second pellet press system with an increased processing rate was designed and is expected to be operational later this year. Capability to process reject cermet pellets and targets to recover the Np appears to be suitable for full-scale production.

With demonstration of a more efficient dissolution approach in Campaign 4, the first three steps of irradiated target processing—hardware removal, caustic dissolution, and acid dissolution—are suitable for full-scale production.

Undissolved solids processing for recovery of Pu and Np has not been tested. A relatively small amount of undissolved solids were observed after dissolution of targets irradiated for two HFIR cycles, while significantly more solids were collected after dissolution of three-cycle targets. Measurements on the undissolved solids collected from Campaign 3 indicate a relatively small amount of <sup>238</sup>Pu.

Two TBP-based solvent extraction options have been demonstrated that can produce suitable Pu product—a single-cycle co-decontamination of Pu and Np with selective Np stripping by nitrite addition and a two-step process of selective Pu extraction that is followed by a second cycle of Np extraction and stripping. The main efficiency issue presented by these options is the P present in the aqueous Np and Pu products from the breakdown of TBP in the solvent. A single batch of TBP solvent has been successfully regenerated and reused for seven solvent extraction processing runs from Campaign 2 through Campaign 4, with make-up solvent accounting for approximately 25% of the total volume added at the start of Campaign 4.

Plutonium purification and conversion to oxide product by anion exchange followed by cation exchange resin loading and calcination have been demonstrated at a scale suitable for full-scale production. Installation of a system for transferring HS-PuO<sub>2</sub> out of the processing hot cells and into shipping containers is in progress. Electrochemical dissolution of PuO<sub>2</sub> has been translated from laboratory testing<sup>3</sup> into a hot-cell system capable of dissolving batches of off-specification product at the scale of tens of grams.

Positive progress has been made in waste disposition, but this topic remains a challenge needing continued focus. Batch extraction with di-(2-ethylhexyl) phosphoric acid (HDEHP) has been demonstrated for removal of  $^{238}\text{Pu}$  from the combined acidic streams for management of transuranics in liquid waste. Techniques for solidification of the HDEHP solvent, as well as spent TBP solvent, have been tested; the potential suitability of those waste forms for disposition at the Waste Isolation Pilot Plant is under review. Laboratory tests have been conducted with monosodium titanate for removal of  $^{238}\text{Pu}$  from caustic waste; hot cell tests on Campaign 3 and Campaign 4 caustic solutions will be conducted during the first quarter of 2020.

#### IV. PATH FORWARD

Upcoming efforts will focus on improving process efficiency to increase the achievable production rate. One major efficiency issue is related to phosphorus in the recycle Np stream. Testing continues with a goal of identifying a minor alteration of the flowsheet to remove phosphorus from recycle Np without anion exchange by adjusting the cation exchange process used for Pa removal on each batch of Np solution used for target fabrication. However, if phosphorus cannot be removed efficiently through a minor alteration, an efficient alternative may be to eliminate phosphorus from the flowsheet. Initial experimentation has been conducted toward consideration of replacing TBP in the solvent extraction step by monoamide extractants.

Waste disposition will continue to influence production. Waste minimization efforts described above will continue. Possible alternatives to HDEHP extraction for TRU removal from aqueous waste will also be tested.

Two campaigns of irradiated target processing are scheduled to be conducted in 2020. Campaigns 5 and 6 will process batches of 63 targets irradiated for 2 HFIR cycles. Those campaigns will be conducted with a focus on efficient operations. Identified process improvements will be tested, and scheduling will seek opportunities for parallel operations.

#### ACKNOWLEDGMENTS

Funding for this program is provided by the Science Mission Directorate of the National Aeronautics and Space Administration through the US Department of Energy, Office of Nuclear Energy. This work used resources at the High Flux Isotope Reactor, a Department of Energy Office of Science User Facility operated by Oak Ridge National Laboratory.

Progress in this effort is made possible through the dedication and hard work of many individuals in multiple organizations. Other contributors from Oak Ridge

National Laboratory include Mindee Albright, Paul Benny, Caleb Browning, Patrick Burgess, Doug Canaan, Don Caverly, Fred Chattin, Jimmy Christopher Jr., Jason Cook, Jordan Couch, Jeff Delashmitt, Cory Dryman, Miting Du, Sergio Dukes, Nelson Fauls, Jon Garrison, Michael Green, Joseph Guy, Laura Harvey, Steven Hinds, Jessica Hobby, Riley Hunley, Rodney Hunt, Tom Hylton, Chris Jensen, Josh Langley, Samuel Lawson, Brian Lester, Catherine Mattus, Howard Meadows, Marty Milburn, Kristian Myhre, Charles Nevius, Brian Oakley, Steve Owens, James Parfitt, Kaara Patton, Curt Porter, Ben Roach, Luke Sadergaski, Larry Sawyer, Logan Skjei, Allen Smith, Rob Smith, Phillip Snyder, Gerald Sullivan, Paul Taylor, Robin Taylor, Brad Tinker, Ray Vedder, Matt Walker, Roger Weaver, Gary West, Chris Wightman, and Ken Wilson.

#### REFERENCES

1. R. M. WHAM, G. B. ULRICH, J. C. LOPEZ-BARLOW, S. G. JOHNSON, "Constant Rate Production: DOE Approach to Meeting NASA Needs for Radioisotope Power Systems for Nuclear-Enabled Launches," *American Journal of Aerospace Engineering*, **5**, 2, 63 (2018).
2. D. W. DEPAOLI, D. E. BENKER, L. H. DELMAU, S. R. SHERMAN, F. D. RILEY, P. D. BAILEY, E. D. COLLINS and R. M. WHAM, "Process Development for Plutonium-238 Production at Oak Ridge National Laboratory," Nuclear and Emerging Technologies for Space, American Nuclear Society Topical Meeting, Richland, WA, February 25–28, 2019, available online at <http://anstd.ans.org/>.
3. K. G. MYHRE, M. E. WOODS, A. J. UNGER, P. D. BENNY, D. E. BENKER, E. D. COLLINS, L. H. DELMAU, D. W. DEPAOLI, F. D. RILEY, and R. M. WHAM, "Initial Testing of Mediated Electrochemical Oxidation for Inclusion in the Plutonium-238 Production Program, Nuclear and Emerging Technologies for Space, American Nuclear Society Topical Meeting, Richland, WA, February 25–28, 2019, available online at <http://anstd.ans.org/>.

## USING *N,N*-DIHEXYLHEXANAMIDE FOR PLUTONIUM-238 PURIFICATION

Jarrold Gogolski<sup>1</sup> and Mark Jensen<sup>1</sup>

<sup>1</sup>Colorado School of Mines, 1500 Illinois St, Golden, CO, 80401

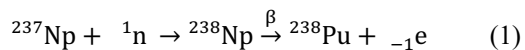
303-273-2785, [mjensen@mines.edu](mailto:mjensen@mines.edu)

*To meet the demand for heat sources to efficiently power radioisotope generators, plutonium-238 is being synthesized from neptunium-237. The two elements are then purified using tri-butyl phosphate (TBP). The quest for cleaner alternatives to TBP suggests an alternate group of extractants, the *N,N*-dialkylamides. While there are many compounds within this group, this study focuses on *N,N*-dihexylhexanamide, which shows promise for a selective separation of <sup>237</sup>Np and <sup>238</sup>Pu.*

### I. INTRODUCTION

The energy from exothermic chemical reactions has been used to provide energy for spacecraft since the 1950s (Ref. 1). While this represents a reliable energy source for spacecraft, chemical fuels have limited utility for space exploration. Long-range spacecraft or multi-decade missions would have to be refueled to remain operational. This energy constraint can be circumvented by using the nuclear energy from radioactive decay.

Even though the decay of all radionuclides emits some energy, there are only a few radionuclides that can be used to efficiently generate electrical power, such as plutonium-238 (<sup>238</sup>Pu) or americium-241. The United States has used <sup>238</sup>Pu for decades to provide thermal energy in devices otherwise referred to as radioisotope thermoelectric generators (RTGs) for spacecraft. Unfortunately, only minuscule amounts of <sup>238</sup>Pu are created in nuclear reactors that fission <sup>235</sup>U using thermal neutrons. Therefore, the primary method<sup>2</sup> for making <sup>238</sup>Pu is the transmutation of <sup>237</sup>Np via the reaction shown in Equation 1.



While the thermal neutron capture cross section of <sup>237</sup>Np is reasonably high at 170 barns,<sup>3</sup> the <sup>238</sup>Np and <sup>238</sup>Pu thermal neutron fission and capture cross sections are higher still. Consequently, the neutron irradiation of <sup>237</sup>Np is kept short enough to prevent a build-up of undesired Pu isotopes and fission products.<sup>4</sup>

Irradiation creates a mixture of <sup>237</sup>Np, <sup>238</sup>Pu, and other radionuclides and the <sup>238</sup>Pu needs to be separated from this mixture to produce high purity <sup>238</sup>PuO<sub>2</sub> for the RTGs. The extractant tri-butyl phosphate (TBP) is currently used for purification.<sup>4</sup> The <sup>238</sup>Pu is first extracted from nitric acid as Pu(IV) into a TBP solution and then stripped from the TBP phase by reduction to poorly extracted Pu(III). During this

process the remaining <sup>237</sup>Np is also recovered separately to make more <sup>238</sup>Pu.

The intense alpha radioactivity of <sup>238</sup>Pu, which makes it desirable for RTGs, also degrades the TBP used to purify the Pu. Radiolytic degradation of TBP is well-known and is mitigated readily in less radioactive TBP-based separations such as the plutonium uranium redox extraction (PUREX) process. However, when used to purify the highly radioactive <sup>238</sup>Pu, the Pu and Np products become contaminated with significant amounts of phosphate, a TBP degradation product.<sup>2</sup> Additional, time-consuming separation steps are needed to reduce the phosphate contamination to acceptable levels.<sup>4</sup> Since other organophosphorus compounds will have similar issues, a phosphorous-free alternative for separating and purifying <sup>238</sup>Pu is desirable.

The *N,N*-dialkylamides are a class of phosphorus-free extractants that have been considered as TBP replacements for separating Pu from spent nuclear fuel. Studies of Np extraction by *N,N*-dialkylamides<sup>5</sup> suggest that *N,N*-dihexylhexanamide (DHHA), which can be thermally decomposed into gases after a separation,<sup>6</sup> may hold promise for separating <sup>238</sup>Pu and Np.

While there have been few studies of Pu extraction by DHHA, it shows promise for extracting Pu(IV) well.<sup>7, 8</sup> Unfortunately, recovering Pu from DHHA after reduction to Pu(III) is reported to be hampered at higher acidities when hydroxylamine nitrate (HAN) was used by itself.<sup>9</sup> (At higher acidities, ferrous sulfamate is a more effective reducing agent than HAN, but the ferrous sulfamate would contribute to the waste burden, whereas HAN is incinerable.<sup>4</sup>) Additionally, it was reported that at concentrations higher than 1 M nitric acid Pu(III) starts to be appreciably oxidized back to the extractable Pu(IV).<sup>10</sup>

To understand the potential of DHHA for Np/Pu separations, we have studied the extraction of <sup>239</sup>Pu from nitric acid solutions by 1 M DHHA. Even though previous reports indicate that Pu(VI) is not as well extracted as Pu(IV),<sup>11,12</sup> we considered the partitioning of Pu(III), Pu(IV), and Pu(VI) in this system to understand the utility of Pu(VI) in the purification of <sup>238</sup>Pu. Also, the extraction of Pu(III), Pu(IV), and Pu(VI) by DHHA were compared and contrasted with that of the baseline TBP system. Comparison with the literature values for TBP extraction indicate that extraction of Pu(IV) and Pu(VI) is comparable for the two different extractants, as are the patterns of Pu(III) extractability at low acidities.

## II. EXPERIMENTAL

DHHA, synthesized from dihexylamine and hexanoyl chloride as previously described,<sup>5</sup> was diluted with Exxsol D60 to 1 mol L<sup>-1</sup> (M) and then pre-equilibrated at the appropriate acidity. A fresh aqueous phase with an aliquot of <sup>239</sup>Pu tracer prepared in the desired oxidation state was vigorously contacted with an equal volume of the pre-equilibrated organic phase. The resulting mixture was centrifuged and the phases were separated for Pu determination by liquid scintillation counting. The following redox agents were added with the Pu to stabilize the intended Pu oxidation states: 3 % hydroxylamine hydrochloride for Pu(III), 2 mM sodium nitrite and 0.005 M ammonium metavanadate for Pu(IV), and 1 mM potassium bromate for Pu(VI). The oxidation states were checked using solvent extraction.<sup>13</sup>

## III. RESULTS AND DISCUSSION

The results of DHHA extraction of Pu(III), Pu(IV), and Pu(VI) across a range of equilibrium aqueous nitric acid concentrations are compared with available literature values in Figure 1. The distribution ratio,  $D_{Pu}$ , is the ratio of the Pu concentration in the organic phase to the Pu concentration in the aqueous phase. As can be seen in Figure 1, extraction of Pu(IV) and Pu(VI) is similar at aqueous nitric acid concentrations of 1 M or lower. However, the extraction preference at concentrations above 2 M nitric acid changes to Pu(IV) > Pu(VI) >> Pu(III).

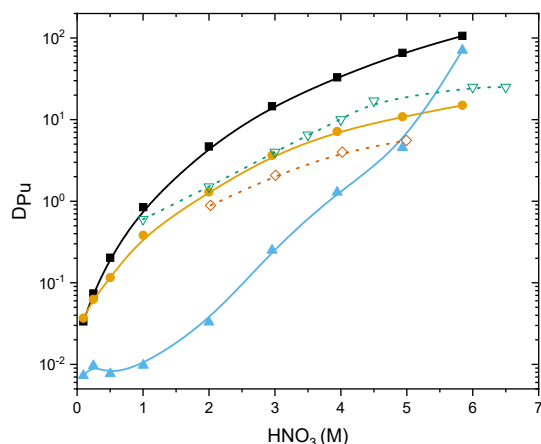


**Fig. 1.** Extraction of Pu in various oxidation states by DHHA. Experimental data: 1 M DHHA extracting Pu(III) (solid triangle), Pu(IV) (solid square), and Pu(VI) (solid circle). Literature data for 0.5 M DHHA extracting Pu(IV)<sup>8</sup> (open inverse triangle) and 1 M DHHA extracting Pu(VI)<sup>11</sup> (open diamond). The trendlines serve as visual aids.

Even though the distribution ratios for Pu(VI) are slightly higher than previously reported for DHHA, the literature values show the same trends as our experimental

results, suggesting that the concentrations of active extractant may have been different due to difference in the purity of the synthesized extractants. In addition, this experimental data extends the range of acidities where Pu(VI) distribution ratios have been studied to acidities below 2 M nitric acid,<sup>11</sup> a region of interest for Pu(VI) stripping. The present results show that while the Pu(VI) is poorly extracted in that acid range, Pu(VI) extraction is significantly higher than Pu(III) extraction.

Our experimental data for Pu(IV) extraction was indirectly compared to the literature as the data were collected with different DHHA concentrations. We measured an average DHHA:Pu(IV) stoichiometry of 2.35:1 at 1 and 4 M HNO<sub>3</sub>. Other *N,N*-diakylamide studies indicate that Pu(IV) is extracted as a mixture of plutonium-nitrate complexes containing 2 to 3 dialkylamide ligands. When 3 diamides are present, the third *N,N*-diakylamide is purported to bind in the outer coordination sphere of the extracted complex, especially at higher acidities.<sup>14, 15</sup> Taking the difference in DHHA concentration into account, that suggests the  $D_{Pu}$  values measured for Pu(IV) extraction by 1 M DHHA should be five times higher than the corresponding literature values measured for 0.5 M DHHA. Comparison of the data in Figure 1 show a four to five-fold difference in the two sets of Pu(IV) distribution ratios between 2 M and 6 M HNO<sub>3</sub>. With this correction, the trends in our experimental values and the literature data for Pu(IV) are similar between 2 and 4.5 M nitric acid. However, at lower and higher acidities the experimental results deviate from the literature data in a manner that again suggests the possible presence of impurities in the DHHA used for the literature experiments.

The extraction of Pu(III) shows a different trend. The steady climb in the extraction of Pu(III) with nitric acid concentration is most likely due to Pu(III) oxidizing to Pu(IV) because it has been shown elsewhere that TBP extracts Pu(III) poorly<sup>14</sup> and that the Pu(III)-Pu(IV) couple can be readily adjusted in either the aqueous or organic phase.<sup>10, 16</sup> Under the experimental conditions of this study, it is likely that oxidation of the Pu to Pu(IV) is nearly complete in 6 M HNO<sub>3</sub>, as the distribution ratios of the systems that initially contained Pu(III) or Pu(IV) are approximately the same. However, this may not be achieved under process conditions with higher concentrations of metal ions and substantially higher radiation fields. This study, using trace scale Pu(III), confirms that the holding reducing agent, 3% hydroxylamine, will be insufficient for maintaining Pu(III) at this acidity. Generally, the additional non-incinerable redox agent ferrous sulfamate is used to stabilize Pu(III). Unfortunately, there is no data to compare for using DHHA to extract Pu(III) under similar conditions. Regardless of what is occurring with the Pu(III), the DHHA extracts Pu(IV) well and Pu(VI) moderately well.

The extraction preference for Pu(IV) over Pu(VI) is also seen with TBP.<sup>17, 18</sup> Overall, DHHA seems to extract

Pu(VI) as well as TBP and extracts Pu(IV) better than TBP at higher acidities ( $> 4$  M) but not at the lower acidities. This indicates that the Pu(IV) could be more readily stripped from DHHA than TBP.

The goal of this work is to purify Pu from Np. Figure 2 compares the distribution ratios of Np and Pu in the tetravalent and hexavalent oxidation states as a function of acidity. The extraction preferences of DHHA below 3 M acid is  $\text{Pu(IV)} \sim \text{Np(VI)} > \text{Pu(VI)} > \text{Np(IV)}$ , but the extractabilities of Pu(VI) and Np(IV) reverse at 3 M nitric acid. Overall, at acidities above 4 M nitric acid DHHA extracts both oxidation states of Np and Pu well. Decreasing the acidity to 1 M shows that Np(IV) will be poorly extracted ( $D_{\text{Np}} \sim 0.1$ ) and Pu(VI) also will be stripped ( $D_{\text{Pu}} \sim 0.4$ ), while Np(VI) and Pu(IV) are still extracted.

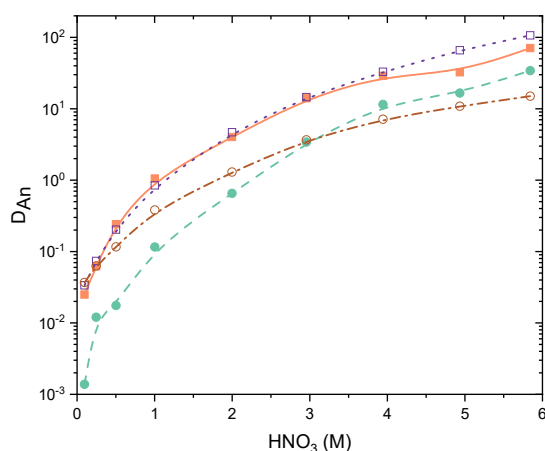


**Fig. 2.** Comparison of 1 M DHHA extracting Pu(IV) (open square), Pu(VI) (open circle), Np(IV) (solid circle), and Np(VI) (solid square). The trendlines serve as visual aids.

The metal ions best extracted by DHHA, Pu(IV) and Np(VI), show remarkably similar distribution ratios across the range of acidities studied, and are both efficiently stripped only in dilute nitric acid. Direct separation of these two species by varying the acidity would be difficult. However, either ion, Pu(IV) or Np(VI), could be selectively reduced to poorly extracted Pu(III) or Np(V) in order to be recovered at intermediate acidities. Above ca. 2.5 M  $\text{HNO}_3$  the solutions are sufficiently oxidizing that would be difficult to reduce the metals, as is seen for Pu in Figure 1. In this light, the preferred strategy for separating Np(VI) and Pu(IV) extracted by DHHA might be selective reduction of Np(VI) to Np(V) with nitrous acid. This one-electron, reversible reduction is fast, Np(V) is comparatively stable,<sup>19</sup> Pu(IV) is stabilized by nitrous acid, and substantial concentrations of nitrous acid are expected to be rapidly extracted by DHHA into the organic phase.

An additional stripping step would be required if the feed solution were to contain a mixture of the common oxidation states: Np (IV, V, VI) and Pu (III, IV, V, VI). In

this case, the tetravalent and hexavalent species of both actinides would be extracted significantly. With nitrous acid reduction, Np(VI) would be efficiently stripped as Np(V) but Np(IV) would remain in the organic phase. Reduction of both Pu(VI) and Pu(IV) to Pu(III) by ferrous sulfamate would still enable Pu stripping. However, this would leave residual Np(IV) in the organic phase. A low acid strip of Np(IV) would then be required to recover that Np and recycle the solvent.

## IV. CONCLUSIONS

The extractants TBP and DHHA show similar abilities to extract Pu(III), Pu(IV), and Pu(VI) from nitric acid. Pu(III) is poorly extracted by DHHA, however it is difficult to completely stabilize trivalent plutonium using only the incinerable redox agent hydroxylamine unless the aqueous acidity is maintained at 1 M  $\text{HNO}_3$  or lower. Although at these acidities, neither Np(IV) nor Np(VI) are strongly extracted. Consequently either other Pu reducing agents that are effective at higher acidity, less efficient Pu stripping at a higher acidity, less efficient Pu stripping at a higher acidity with more stripping stages, or selective reduction of Np(VI) to Np(V) in the presence of extractable Pu(IV) should be considered for the separation of Np and Pu using DHHA.

## ACKNOWLEDGMENTS

This work was supported by the U.S. DOE-NE/EM Radiochemistry Traineeship program.

## REFERENCES

1. N. FRISCHAUF, in *Compendium of Hydrogen Energy*, M. Ball, A. Basile, T. N. Veziroğlu, Eds. (Woodhead Publishing, Oxford, 2016), pp. 87-107.
2. D. W. DEPAOLI *et al.*, in *Nuclear and Emerging Technologies for Space*. (United States, 2019).
3. . (IAEA-Nuclear Data Section, 2019).
4. E. D. COLLINS *et al.*, "Status summary of chemical processing development in plutonium-238 supply program," (Oak Ridge National Lab, 2017).
5. J. GOGOLSKI, P. R. ZALUPSKI, T. S. GRIMES, M. P. JENSEN, Neptunium extraction by *N,N*-dialkylamides. *Radiochimica Acta*, (accepted for publication, 2020).
6. G. THIOLLET, C. MUSIKAS, Synthesis and uses of the amides extractants. *Solvent Extraction and Ion Exchange* **7**, 813-827 (1989).
7. P. N. PATHAK, D. R. PRABHU, V. K. MANCHANDA, Distribution behaviour of U(VI), Th(IV) and Pa(V) from nitric acid medium using linear and branched chain extractants. *Solvent Extraction and Ion Exchange* **18**, 821-840 (2000).

8. K. K. GUPTA, V. K. MANCHANDA, M. S. SUBRAMANIAN, R. K. SINGH, N,N-Dihexyl Hexanamide: A Promising Extractant for Nuclear Fuel Reprocessing. *Separation Science and Technology* **35**, 1603-1617 (2000).
9. S. L. YARBRO, S. B. SCHREIBER, E. M. ORTIZ, R. L. AMES, Reducing Pu(IV) to Pu(III) with hydroxylamine in nitric acid solutions. *Journal of radioanalytical and nuclear chemistry*. **235**, 21-25 (1998).
10. Y.-K. SZE, J. A. GOSSELIN, Oxidation of Pu(III) by nitric acid in tri-n-butyl phosphate solutions. Part II. Chemical methods for the suppression of oxidation to improve plutonium separation in contactor operation. *Nuclear Technology* **63**, 431-441 (1983).
11. K. MCCANN, S. I. SINKOV, G. J. LUMETTA, J. C. SHAFER, Inner versus outer sphere metal-monoamide complexation: ramifications for tetravalent & hexavalent actinide selectivity. *New Journal of Chemistry* **42**, 5415-5424 (2018).
12. K. MCCANN, B. J. MINCHER, N. C. SCHMITT, J. C. BRALEY, Hexavalent Actinide Extraction Using N,N-Dialkyl Amides. *Industrial & Engineering Chemistry Research* **56**, 6515-6519 (2017).
13. H. NITSCHKE, S. C. LEE, R. C. GATTI, Determination of plutonium oxidation states at trace levels pertinent to nuclear waste disposal. *Journal of Radioanalytical and Nuclear Chemistry, Articles* **124**, 171-185 (1988).
14. N. CONDAMINES, C. MUSIKAS, The extraction by N,N-dialkylamides. II. Extraction of actinide cations. *Solvent Extraction and Ion Exchange* **10**, 69-100 (1992).
15. E. ACHER *et al.*, Inner to outer-sphere coordination of plutonium(IV) with N,N-dialkyl amide: influence of nitric acid. *Dalton Transactions* **46**, 3812-3815 (2017).
16. V. SAGAR, K. V. CHETTY, D. D. SOOD, Extraction of plutonium(III) by TBP in presence of uranium. *Solvent Extraction and Ion Exchange* **18**, 307-317 (2000).
17. N. KUMARI, P. N. PATHAK, D. R. PRABHU, V. K. MANCHANDA, Comparison of extraction behavior of neptunium from nitric acid medium employing tri-n-butyl phosphate and N,N-dihexyl octanamide as extractants. *Separation Science and Technology* **47**, 1492-1497 (2012).
18. K. ALCOCK, G. F. BEST, E. HESFORD, H. A. C. MCKAY, Tri-n-butyl phosphate as an extracting solvent for inorganic nitrates—V: Further results for the tetra- and hexavalent actinide nitrates. *Journal of Inorganic and Nuclear Chemistry* **6**, 328-333 (1958).
19. M. PRECEK, A. PAULENOVA, Kinetics of reduction of hexavalent neptunium by nitrous acid in solutions of nitric acid. *Journal of Radioanalytical and Nuclear Chemistry, Articles* **286**, 771-776 (2010).

## DEVELOPMENT OF ENGINEERING QUALIFICATION MODEL OF A SMALL ETG FOR LAUNCH ENVIRONMENTAL TEST

Jintae Hong<sup>1</sup>, Kwang-Jae Son<sup>1</sup>, Jong-Bum Kim<sup>1</sup>, and Jin-Joo Kim<sup>1</sup>

<sup>1</sup>Neutron Radioisotope Utilization Technology Division, Korea Atomic Energy Research Institute, 989-111 Daedukdaero, Yuseong-gu, Daejeon 34057, Republic of Korea

Primary Author Contact Information: +82-42-868-4420, [jthong@kaeri.re.kr](mailto:jthong@kaeri.re.kr)

According to the development plan of the Korean launch vehicle, a performance verification satellite will be installed in the launch vehicle in 2021. In addition, three payloads, including a small electrically heated thermoelectric generator (ETG) will be developed and installed in the satellite. In particular, a small ETG was developed by the Korea Atomic Energy Research Institute (KAERI), and it is aimed at evaluating the characteristics of the ETG in the space environment prior to the development of a radioisotope thermoelectric generator (RTG) for lunar missions. In this study, shock and vibration tests were carried out to check whether the ETG endures the launch environment of the spacecraft. In addition, a thermal cycle test and thermal vacuum test were carried out to check whether the ETG maintains its performance, even at drastic temperature changes, which can be applied to the ETG in space. Finally, a periodic performance test was carried out to measure the degradation level of the small ETG.

### I. INTRODUCTION

In order to operate stably in space, the payload mounted on the space probe must be able to withstand the spacecraft's launch environment and the target environment. In addition to the goal of preventing the leakage of the radioisotope under extreme conditions, nuclear batteries should be designed to maintain stable performance against the spacecraft's launch vibration, shocks during pairing, and temperature changes in space as well as other payloads.

The Korea Atomic Energy Research Institute (KAERI) has developed a small electrically heated thermoelectric generator (ETG), one of the payloads of the artificial satellite, which is scheduled to be launched using a Korean launch vehicle in 2021 (Ref.1-3). According to the prototype development stage, the space component development process is divided into an engineering model (EM), an engineering qualification model (EQM) and a flight model (FM). In the EM stage, the basic performance of the developed component is tested. In the EQM stage, the reliability of the space environment with severe conditions must be assured. Finally, in the FM stage, the components should be fabricated for the actual spacecraft. After the basic

performance test and environment test, it will be installed on the spacecraft. KAERI has developed a small ETG and successfully completed the performance evaluation and reliability evaluation at the space environment. The Korea Aerospace Research Institute (KARI) has released the specifications of the spacecraft's launch environment and mission environment in space. In addition, the corresponding simulation tests were conducted to verify safety and reliability. This study will introduce the development status of the EQM for a small ETG and the progress of its reliability test.

### II. DESIGN EM AND EQM OF A SMALL ETG

At the EM stage, the feasibility study for the mechanical design of the payload and the target performance is carried out. Although the payload does not need to use the components with space heritage at this stage, it needs to satisfy the target performance. The performance of a small ETG will be tested while inducing 10 W<sub>th</sub> of thermal power from the satellite. Therefore, the basic performance and characteristics of the components that consist of the small ETG were analyzed using the first prototype, as shown in Figure 1.

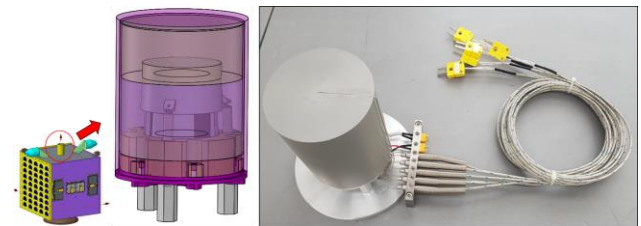


Fig. 1. The 1<sup>st</sup> prototype of a small ETG.

Then a preliminary review of the launch environment was conducted before fabricating the prototype for the EQM stage. A small ETG will be installed on the satellite and launched through the spacecraft, which will be parked at the Earth's low orbit. While launching the spacecraft, the small ETG could endure damage such as the launching impact, the launch vibration, and the thermal shock. According to the launch environment specifications issued by the Korea Space Launch Vehicle

(KSLV) development team, the maximum impact to be applied to the small ETG in various separation mechanisms of KSLV is 2000 g (Table I) and the launch vibration is 9.7grms (Table II). In addition, since the small ETG is located at the top exterior of the satellite, the temperature change of the small ETG experienced by orbiting the Earth's low orbit was calculated to range from -73 °C to 60 °C (Table III).

**TABLE I.** Shock response spectrum of the KSLV.

Description	Frequency (Hz)	Acceleration (g)
Spacecraft components	100	20
	1500	2000
	10000	2000

**TABLE II.** Random vibration level for satellite equipment.

Frequency (Hz)	Acceleration PSD (g <sup>2</sup> /Hz)
20	0.007
70	0.08
500	0.08
2000	0.02
Overall	9.7grms

**TABLE III.** Temperature limit of a small ETG.

Acceptance		Qualification		Survival	
Min	Max	Min	Max	Min	Max
-30°C	+45°C	-35°C	+50°C	-73°C	+60°C

Among the above environmental specifications, the most severe effect could be caused by the launch vibration due to the ceramic material used for the small ETG. Therefore, a random vibration test was performed with the first prototype that finished the performance test.

The results showed that the resonance frequencies did not match before and after the vibration test. As a result of the disassemble, all the legs of the thermoelectric module were damaged, as shown in Figure 2. To solve this problem, two options such as a seismic design structure and filling the empty space between the legs of the thermoelectric module with plastic material were considered. However, because the small ETG was too small to apply a seismic design, the latter option was selected as a solution (Figure 3).

Epoxy-filled thermoelectric modules were used to fabricate the EQM. In the first prototype, three springs with 3 kg of compressive force connect the case cover and the heat source module fixture to apply compression to the thermoelectric module. But in the EQM, the spring force was increased to 10kg so that approximately 30kg of compressive force was applied to the thermoelectric module.



**Fig. 2.** Failure of TE legs after a random vibration test.

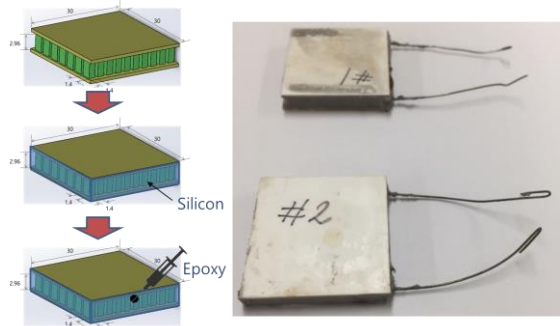


**Fig. 3.** TEM filled with epoxy bond.

The satellite design team requested to change the support structure of the case cover into an easy-to-assemble structure. In addition, four thermistors (PT-1000) with space heritage were applied from the EQM. The small ETG and the satellite will be connected with a 26 pin d-sub connector for the transmission of the temperature signals and the input / output power signals (Figure 4).

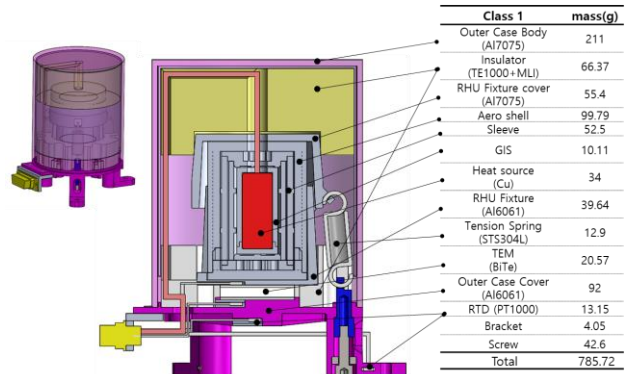


**Fig. 4.** Design of a small ETG for EQM.

### III. LAUNCH ENVIRONMENT TEST

The small ETG for EQM was fabricated as shown in Figure 5, and tested according to the test specification presented in the previous section.

The result of the performance test showed 91.3 mW (i.e., an output voltage of 0.37 V and a shunt resistance of  $1.5\Omega$ ) of electric output at an input voltage of 31.78 V, an input power of 9.51 W, and a vacuum of  $2.43E-3$  mbar. Although the first prototype of the small ETG showed 195 mW of electric output, more than 100 mW of electric output decreased in the small ETG for EQM. This was because the thermal conductivity of the epoxy filled in the thermoelectric module was  $0.58 \text{ W} / \text{m} \cdot \text{K}$ , which led to an increase in the amount of heat transfer compared to the thermoelectric module without epoxy, resulting in a smaller temperature difference across the thermoelectric module.



Fig. 5. Fabrication of a small ETG for EQM.

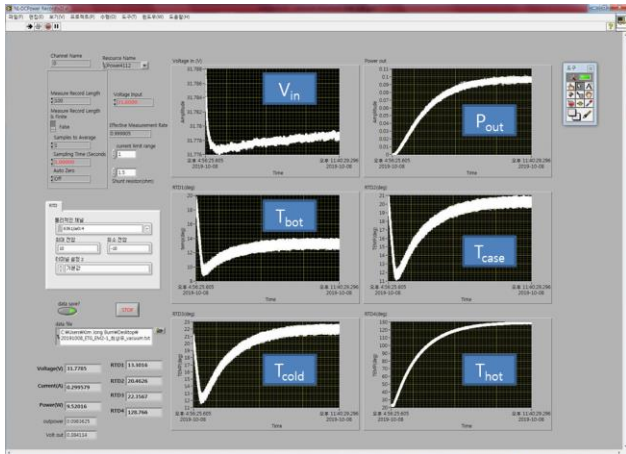
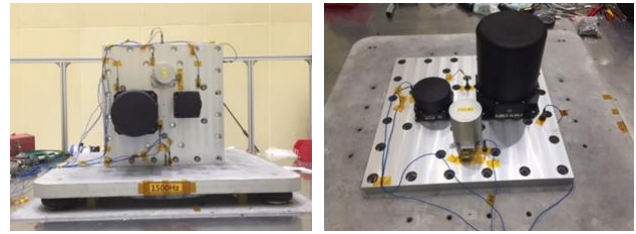


Fig. 6. Results of the performance test of a small ETG for EQM.

On the other hand, the launch impact test, the launch vibration test, the heat cycle test (6.5 cycles), and the thermal vacuum test (2.5 cycles) were carried out using the small ETG for EQM. There was no defect in the appearance, and its performance was stable without degradation. In addition, the performance of the small

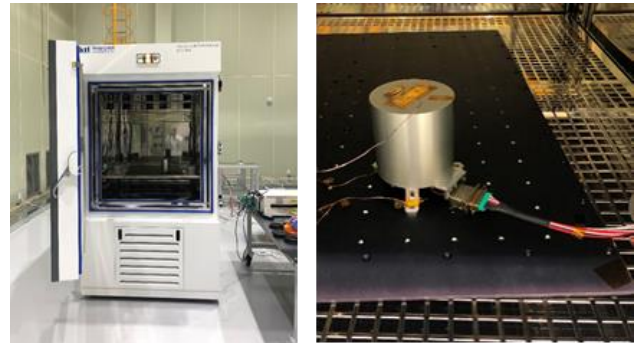
ETG for EQM showed little degradation up to 30 cycles of the performance test.



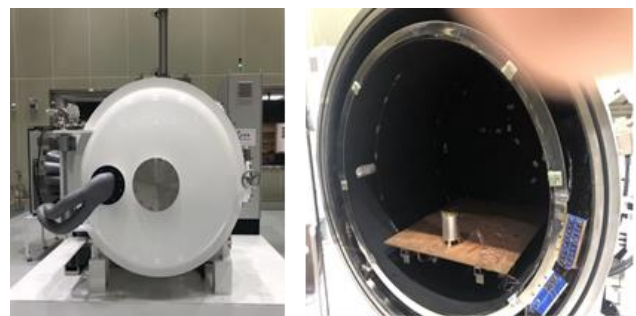
(a) Set up of shock test



(b) Set up of vibration test



(c) Set up of thermal cycle test



(d) Set up of thermal vacuum test

Fig. 7. Launch environmental test.

#### IV. CONCLUSIONS

In this study, a small ETG which will be installed on the satellite of Korean launch vehicles was developed and

tested. In the first prototype, 195 mW of electric output was generated, and it satisfied the target performance. However, failure occurred due to the breakage of the thermoelectric legs during the spacecraft's launch vibration test. To solve this problem, the space between the legs of the thermoelectric module was filled with epoxy, and the spring force for fixing the heat source module was increased more than three times. The support structure of the small ETG's case cover was modified to improve the workability. In addition, the temperature sensor, input voltage, and surface treatment were adjusted to meet the payload specifications released from KARI.

The performance test results of the small ETG for EQM showed that the output power is reduced due to the heat loss by epoxy. However, the small ETG endured all environmental tests such as the launching shock, launch vibration, and thermal shock. The small ETG for the EQM will be mounted on the prototype of the satellite system for further performance testing. For further study, a new epoxy material with low thermal conductivity will be tested to increase the performance of the small ETG.

## **ACKNOWLEDGMENTS**

This work was supported by the National Research Foundation of Korea government(MSIP) (No.2019M2D1A1059518).

## **REFERENCES**

1. J. T. HONG, K. J. SON, J. B. KIM, and J. J. KIM, "Design of ETG for low orbit test of the Korea launch vehicle," Proc. of Nuclear and Emerging Technologies for Space, Richland, USA, February, American Nuclear Society (2019).
2. J. T. HONG, K. J. SON, J. H. PARK, and J. J. KIM, "Study on the Design of Radioisotope Thermoelectric Generator for Earth Low Orbit Test," Transactions of the Korean Nuclear Society Autumn Meeting, Gyeongju, Korea, October (2017).
3. J. T. HONG, K. J. SON, J. H. PARK, J. J. KIM, and J. G. SON, "Development Status of the Radioisotope Battery for the Performance Evaluation Satellite of KSLV," Proc. of Korean Society of Precision Engineering, Spring meeting, Jeju, Korea, May (2019).

## RISK-INFORMED LIFE TEST MODELING FRAMEWORK – DEVELOPMENT OVERVIEW

Stephen Izon<sup>1</sup>, Steven Novack<sup>1</sup>, and Clayton Smith<sup>1</sup>

<sup>1</sup>Johns Hopkins Applied Physics Laboratory, 11000 Johns Hopkins Rd, Laurel, MD, 20740

Primary Author Contact Information: 240-228-7891 and [stephen.izon@jhuapl.edu](mailto:stephen.izon@jhuapl.edu)

Following up on lessons learned from previous Radioisotope Power System (RPS) technology programs, the Johns Hopkins University (JHU) Applied Physics Laboratory (APL), in support of the RPS program office at the NASA Glenn Research Center (GRC), started developing the Risk-informed Life Test modeling (RILT) framework. RILT integrates multi-level (material-, component-, subsystem-, and system-level) test data using physics-of-failure (PoF) models and Bayesian methods to characterize system-level reliability with uncertainty. RILT enables the identification of individual risk drivers within the system that prevent established target reliability and/or confidence goals from being met. This paper presents an overview of the RILT framework, how RILT has been applied to the dynamic power converters (DPCs) included in GRC's ongoing converter maturation efforts, as well as current and future RILT development activities.

### I. INTRODUCTION

Estimating long-life system reliability (e.g., >10 years) presents a unique set of challenges, since effective testing is expensive, time intensive, and often covers several levels of requirements and expectations. Typical testing schemes are developed to estimate the testing time to reach a reliability goal using standard statistical methods, with three such examples from Ref. 1 provided here. Applying sample theory and assuming an exponential distribution, 2.9 million hours of testing with no failures is needed to meet a reliability requirement of 0.90 at 15 years (130,000 hours) with 90% confidence. Following DoD MIL-HDBK-781, which provides test plan estimates for reliability demonstration, 1.1 million to 1.6 million hours of testing are needed depending on designated risk values. Applying Bayesian methods, such as the WeiBayes Zero-Failure formula, yields a similarly prohibitive test time of 1.2 million hours. If failures are considered, test times increase significantly.

A risk-informed goal-based testing process was developed to minimize resources (e.g., project budget and schedule) required to demonstrate lifetime of a new technology.<sup>1</sup> This led to the concept of RILT, a framework for implementing such a process through the combined use of PoF models and Bayesian inference techniques.<sup>2</sup> RILT addresses and identifies the underlying reliability drivers using physical degradation/failure models rather than focusing on how to demonstrate compliance with reliability requirements. Using physics models as the

framework allows the program to define tests that update and confirm the degradation/failure models and therefore the predicted reliability. RILT's Bayesian treatment allows for capturing uncertainty in the reliability analysis due to various sources such as sparsity of data, technology maturity, design maturity, concept of operations, and manufacturing process variability. While initial development is focused on application to DPCs, RILT's capabilities could be extended for application to other systems subject to time-dependent failure mechanisms.

### II. RILT OVERVIEW

RILT integrates system reliability models and test data at the material, component, subsystem, and system levels to characterize system risk using probabilistic PoF approaches and Bayesian updating techniques. Figure 1 shows the interaction of typical reliability analyses—failure mode effects analysis (FMEA), fault tree analysis (FTA), and probabilistic risk assessment (PRA)—with each other and with PoF models and testing. The FMEA identifies the failure modes and mechanisms of interest to be explored with physics models. The PoF model parameters are explored with testing and those results are flowed into a PRA to establish the reliability and its associated uncertainty.

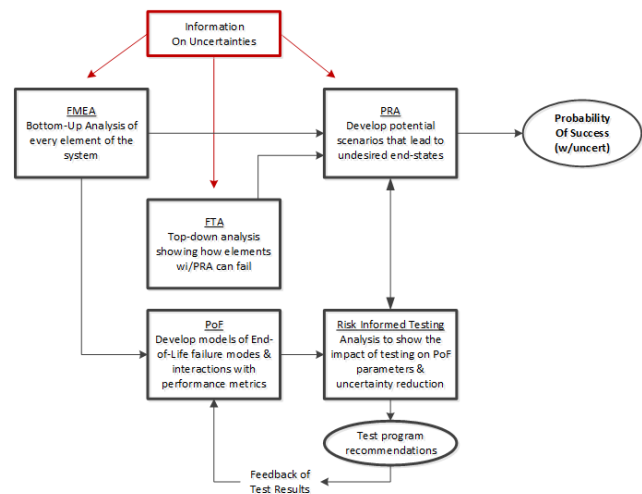


Fig. 1. RILT integrates with all reliability analyses

This risk characterization enables a more robust testing campaign providing confidence that the system will

deliver the required power at end-of-design-life (EODL). RILT also allows identification of the individual risk drivers within the system that prevent established target reliability and/or confidence goals from being met. In turn, trades on reliability and confidence for resources can be made to inform stakeholders of the potential options that can be pursued within resource constraints to better align predictions with goals.

RILT is comprised of three main elements: a physics-based failure/degradation modeling element, a probabilistic risk assessment element, and a decision optimization element. The following subsections describe each of these three elements in more detail.

## II.A. Physics-of-Failure Modeling

Physics-of-Failure is an approach that applies knowledge of physical failure or degradation mechanisms (e.g., from well-established parametric relationships, regression analysis of test data) to predict lifetime and hence reliability. As a departure from traditional regression analysis which yields point estimates of material constants, RILT employs Bayesian regression allowing for probabilistic estimates of material constants thereby capturing uncertainties such as measurement error and test specimen variability. Bayesian regression is based on the well-known Bayes theorem:

$$\pi_1(\Theta|D) = \frac{\mathcal{L}(D|\Theta) \times \pi_0(\Theta)}{\int_{\Theta} \mathcal{L}(D|\Theta) \times \pi_0(\Theta) d\Theta} \quad (1)$$

where  $\Theta$  is a vector of model parameters,  $D$  is the observed test data,  $\pi_1$  is the posterior distribution of  $\Theta$  given  $D$ ,  $\mathcal{L}$  is the likelihood of observing  $D$  given  $\Theta$ , and  $\pi_0$  is the prior distribution of  $\Theta$ . Using the posterior distribution of model parameters  $\Theta$ , probabilistic life predictions, and consequently reliability predictions with uncertainty, can be made:

$$R(t) = Pr(\pi_1(t_{fail}|\Theta, \Sigma_{use}) > t) \quad (2)$$

where  $R(t)$  is the reliability at time  $t$ ,  $\pi_1(t_{fail}|\Theta, \Sigma_{use})$  is the posterior distribution of the time to failure,  $t_{fail}$ , given model parameters  $\Theta$  and use conditions  $\Sigma_{use}$ .

The following subsections detail the PoF models either currently included in RILT or actively under development.

### II.A.1. Current Models

#### Creep

Creep is a credible failure mechanism for hot-end components and other components subjected to high operating temperatures and persistent stresses. The RILT Creep PoF model is built on the Arrhenius-based Sherby-Dorn time-temperature parameter,  $P_{SD}$ :

$$P_{SD} = \log(\theta_r) = \log(t_r) - \frac{0.217 \cdot Q}{T} \quad (3)$$

where  $\theta_r$  is the temperature-compensated time to rupture,  $t_r$  is the time to rupture,  $Q$  is the activation energy for creep,  $T$  is the absolute temperature, and  $\log$  is the base 10 logarithm.  $P_{SD}$  can be estimated by fitting a third-order polynomial to observed time-to-rupture and stress data at a given temperature, yielding:

$$\log(t_r) = \underbrace{a_1 + a_2 \cdot x + a_3 \cdot x^2 + a_4 \cdot x^3}_{\sim P_{SD}} + \frac{0.217 \cdot Q}{T} \quad (4)$$

where  $a_1$ ,  $a_2$ ,  $a_3$ , and  $a_4$  are regression coefficients and  $x = \log(\sigma)$  with  $\sigma$  being the stress.<sup>3</sup>

#### High Cycle Fatigue

Fatigue is a credible risk to moving components in dynamic systems due to the presence of cyclic stresses. The RILT high cycle fatigue (HCF) PoF model is built on the Basquin equation:

$$\sigma_a = A(N_f)^B \quad (5)$$

where  $\sigma_a$  is the stress amplitude,  $N_f$  is the cycles to failure, and  $A$  and  $B$  are material constants. Eq. (5) can be rearranged and linearized as follows:

$$\log(N_f) = \frac{1}{B} \cdot \log(\sigma_a) - \frac{1}{B} \cdot \log(A) \quad (6)$$

Given observations of  $N_f$  and  $\sigma_a$  from material fatigue life tests, the material constants  $A$  and  $B$  can be determined through regression analysis.<sup>2</sup>

#### Fracture

Pre-existing flaws in a component may propagate to component fracture under dynamic stress conditions. The RILT Fracture PoF model is built on the Paris Crack Law:

$$\frac{dA}{dN} = C(\Delta K)^m \quad (7)$$

where  $\frac{dA}{dN}$  is the crack growth rate,  $\Delta K$  is the stress intensity factor range, and  $C$  and  $m$  are material constants. Eq. (7) can be linearized by taking the logarithm of both sides:

$$\log\left(\frac{dA}{dN}\right) = m \cdot \log(\Delta K) + \log(C) \quad (8)$$

Given observations of  $\frac{dA}{dN}$  and  $\Delta K$  from material crack growth tests, the material constants  $m$  and  $C$  can be determined through regression analysis. Fracture response predictions can then be found by integration of Eq. (7):

$$N_{if} = \int_{a_i}^{a_f} \frac{da}{C(\Delta K)^m} \quad (9)$$

where  $a_i$  is the initial crack length,  $a_f$  is the final crack length, and  $N_{if}$  is the number of cycles required for crack growth from  $a_i$  to  $a_f$  Ref. (3).

#### Thermal Aging (Polymeric Materials)

Exposure of polymeric materials to heat can result in changes to their mechanical properties (e.g., lap shear

strength) and electrical properties (e.g., dielectric strength). The RILT thermal aging PoF model is built on an Arrhenius relation between life and temperature:

$$L = A \cdot e^{B/T} \quad (10)$$

where  $L$  is the life or time to a specified % reduction in the property of interest,  $T$  is the absolute temperature, and  $A$  and  $B$  are material constants. Eq. (10) can be linearized by taking the logarithm of both sides:

$$\log(L) = \log(e) \cdot \left(\frac{B}{T}\right) + \log(A) \quad (11)$$

Given observations of  $L$  and  $T$  from material thermal aging tests, the material constants  $A$  and  $B$  can be determined through regression analysis.<sup>4</sup>

### II.A.2. Models in Development

#### Very High Cycle Fatigue

The HCF PoF model currently implemented in RILT cannot be applied to the very high cycle fatigue (VHCF) regime ( $N_f \geq \sim 10^7$  cycles) where some materials such as ferrous metals and titanium exhibit a fatigue limit. A random fatigue-limit model (RFLM) can cover both the HCF and VHCF regimes therefore making it better suited for probabilistic fatigue life predictions for DPCs. The RFLM is based on the suggestion that each material specimen has its own individual fatigue limit and therefore treats the fatigue limit as a random variable:

$$\ln(N_f) = \beta_0 + \beta_1 \cdot \ln(\sigma_a - \gamma) \quad (12)$$

where  $\beta_0$  and  $\beta_1$  are material constants,  $\gamma$  is the fatigue limit, and  $\ln$  is the natural logarithm.<sup>5</sup>

#### Stress Relaxation

Where fasteners are used to maintain minimum clamping forces at bolted joint interfaces to prevent joint separation, loss of fastener preload due to stress relaxation should be considered. Various stress relaxation models presented in Ref. 6 accounting for temperature and initial strain are currently being evaluated, such as the Kohlrausch, Feltham, Tanh, Larson-Miller time-temperature parameter, and Wilshire models.

#### Demagnetization

Permanent magnets are susceptible to magnetic field strength degradation due to long-term exposure to elevated temperatures. This magnetic strength degradation should be characterized to ensure that output power will not fall below the minimum required EODL power threshold. Time-dependent demagnetization has been shown to follow a logarithmic law:

$$M = M_0 - S \cdot \ln\left(\frac{t}{t_0}\right) \quad (13)$$

where  $M$  is the magnetization at time  $t$ ,  $M_0$  is the initial magnetization,  $S$  is the magnetic viscosity, and  $t_0$  is a reference time.<sup>7</sup> While model development efforts are

expected to focus initially on temperature effects, other factors which could also degrade magnetic strength, such as external magnetic fields and ionizing radiation, will be considered for future models.

### II.A.3. Numerical Example

Exercising the Fracture PoF model using data from Ref. 8—generated from a constant amplitude crack growth test on a notched, pre-cracked arc shaped specimen of A723 (similar to AISI 4340) steel under a load ratio of  $R = 0.1$ —yields posterior values of model parameters  $C$  and  $m$  shown in Table I. Also included in Table I are the number of cycles,  $N_{if}$ , for a 1 mm initial crack in a notional A723 steel part to grow to 3 mm under a 100 MPa applied stress range,  $\Delta S$ . The resultant posterior distributions of the model parameters bound the point estimates obtained from simple linear regression. This is further illustrated in Figure 2 which compares simple linear regression against the Bayesian regression 50% and 95% confidence intervals fit from the same data. The Bayesian approach, unlike simple linear regression, allows for characterization of uncertainty which would be carried forward to  $N_{if}$  estimates and subsequent reliability predictions. A similar example using the HCF PoF model is presented in Ref. 2.

**TABLE I.** Summary statistics and point estimates of model coefficients and cycles-to-failure at 100 MPa

Parameter	Mean	SD	Point Estimate
$C$	4.32e-10	2.56e-10	3.76e-10
$m$	3.37e+00	1.23e-01	3.37e+00
$N_{if}$	4.36e+06	1.25e+06	4.2e+06

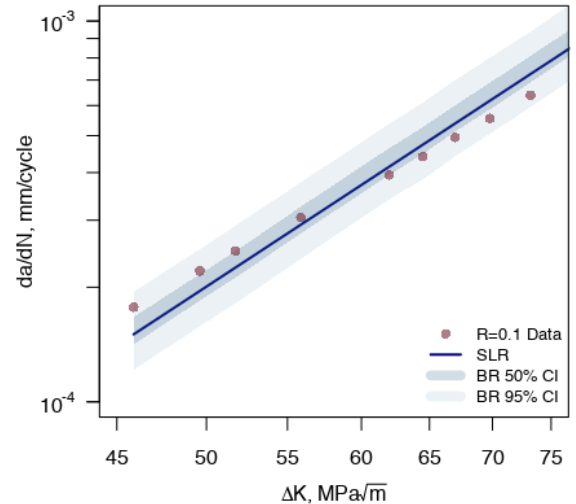


**Fig. 2.** Comparison of Bayesian regression (BR) confidence intervals and simple linear regression (SLR) from A723 steel crack growth data from Ref. 8

## II.B. System Probabilistic Risk Assessment

The system under evaluation is decomposed into a hierarchical nodal structure capturing the failure mechanisms applicable to each component, the components within each subsystem, and the subsystems within the overall system and establishing the system's failure logic. The lowest levels (e.g., failure mechanism level) are quantified via the PoF models while all other levels (component, subsystem, system) are combinations of their constituent elements. Assuming each component fails independently, a series system reliability expression can be applied:

$$R_{sys}(t) = \prod_{i=1}^N R_i(t) \quad (14)$$

where  $R_{sys}(t)$  is the system reliability at time  $t$ ,  $R_i(t)$  is the reliability of the  $i^{th}$  component or subsystem and  $N$  is the total number of components or subsystems. Alternatively, assuming components must fail concurrently for the system to fail, a parallel system reliability expression can be applied:

$$R_{sys}(t) = 1 - \prod_{i=1}^N (1 - R_i(t)) \quad (15)$$

The Weibull distribution, commonly used to model failure times of time-dependent failure mechanisms, was chosen as the time-to-failure distribution:

$$R_{sys}(t) = e^{-\left(\frac{t}{\alpha_{sys}}\right)^{\beta_{sys}}} \quad (16)$$

where  $\alpha_{sys}$  is the characteristic life of the system or subsystem and  $\beta_{sys}$  is the shape parameter of the system or subsystem. With  $R_{sys}(t)$  determined through the hierarchical nodal structure and the applicable reliability expressions Eq. (14) and Eq. (15),  $\alpha_{sys}$  and  $\beta_{sys}$  in Eq. (16) can then be determined. Consistent with failure/degradation mechanisms that have a wear-out influence,  $\beta_{sys}$  is constrained to values greater than 1.

When new test data becomes available (either from testing of the actual system/components, or from testing of heritage or equivalent systems/components), RILT can incorporate the data to provide updated predictions through Bayesian inference. If the new data reinforces the prior prediction, uncertainty is reduced (i.e., the data is considered confirmatory). If the new data is at odds with the prior prediction, a shift in the prediction occurs commensurate with strength of the data with respect to the strength of the prior.

## II.C. Test Plan Optimization

By introducing notional test data, a shift in the predicted reliability and a change in uncertainty around the estimate can be realized. Given reliability and confidence targets, an optimal combination of testing to achieve such targets can be determined, subject to constraints on testing schedule and cost. Considering that testing at lower levels

of assembly typically requires less resources and that the ability to accelerate testing at higher levels of assembly is limited due to operating constraints, a test plan optimization approach is key to identifying where testing resources would be best applied. The optimal test plan would specify what to test (e.g., components, subsystems, system), test stress levels, and test durations. While notional test data can currently be input into RILT to assess the impact on the reliability and uncertainty predictions on a case-by-case basis, a fully automated optimization approach is planned.

## III. APPLICATION TO DYNAMIC POWER CONVERTERS

Three DPCs are currently under NASA GRC's technology maturation effort: AMSC's Flexure Isotope Stirling Converter (FISC), Creare's Turbo Brayton Converter (TBC), and the Sunpower Robust Stirling Converter (SRSC). Throughout the maturation effort, RILT has been progressively developed and applied to provide risk characterizations for each DPC technology.

With the current development state of RILT, failure mechanism coverage for all three converter technologies is not yet comprehensive, and therefore risk characterizations are incomplete. While ranking of risks for currently modeled components and subsystems can provide some relative indication of their individual risk contributions, identification of any testing based on current rankings would be premature. Development and implementation of PoF models for the additional failure mechanisms will drive coverage to higher levels, at which point evaluation of risk drivers may be more appropriate.

## III. SUMMARY AND FUTURE WORK

An overview of the RILT framework was presented herein. A key feature of RILT is the ability to characterize system reliability with uncertainty by integrating multi-level test data using physics-of-failure models and Bayesian updating. While RILT currently provides modest coverage of the credible failure mechanisms identified for each of the DPCs under evaluation, more comprehensive coverage is expected with the PoF models currently in development. An optimization feature is planned for development capable of determining a multi-level accelerated test plan that enables meeting system reliability and confidence goals within test schedule and cost constraints.

As the DPC technologies mature, their respective risk characterizations will be updated with RILT. Further, RILT development is anticipated to continue beyond the converter maturation effort and into generator design and development. Risk characterizations at the generator level will need to address additional hardware such as heat source and heat rejection assemblies, controllers, and converters along with any redundancies, which will require

more complex system logic capabilities in RILT. While RILT was initially developed with DPCs in mind, RILT can be applied to other systems subject to time-dependent failure mechanisms (e.g., radioisotope thermoelectric generators) with some further development to address any system-specific failure mechanisms not currently modeled.

## REFERENCES

1. C. EVERLINE, C. SMITH, S. DISTEFANO, and N. GOLDIN, "Goal Based Testing: A Risk Informed Process," 12<sup>th</sup> International Energy Conversion Engineering Conference, July 28-30 (2014).
2. O. NDU and C. SMITH, "A Risk-Informed Life Test Modeling Framework for Uncertainty Characterization and Life Estimation," *Proceedings - Annual Reliability and Maintainability Symposium* (2018).
3. N. E. DOWLING, *Mechanical Behavior of Materials: Engineering Methods for Deformation, Fracture, and Fatigue*, Second Edition, Prentice Hall, Upper Saddle River, New Jersey (1999).
4. ASTM D2307-07a, "Standard Test Method for Thermal Endurance of Film-Insulated Round Magnet Wire," ASTM International (2013).
5. F. G. PASCUAL and W. Q. MEEKER, "Estimating Fatigue Curves with the Random Fatigue-Limit Model," *Technometrics*, 41, 4 (1999).
6. S. HOLMSTROM, R. POHJA, P. AUERKARI, V. FRIEDMANN, A. KLENK, B. LEIBING, P. BUHL, M. SPINDLER, and A. RIVA, "Long Term Stress Relaxation Modelling," *Proceedings of ECCO Conference on Creep & Fracture in High Temperature Components, Design & Life Assessment*, Rome, May 5-7 (2014).
7. M. HAAVISTO, S. TUOMINEN, H. KANKAANPÄÄ, and M. PAJU, "Estimation of Time-Dependent Polarization Losses in Sintered Nd-Fe-B Permanent Magnets," *IEEE Transactions on Magnetics*, 47, 1 (2011).
8. K. R. DENNIS and E. DOWLING, "Fatigue Crack Growth of Gun Tube Steel Under Spectrum Loading," MS Thesis, Virginia Polytechnic Institute and State University (1986).

## PRELIMINARY TESTING OF COMMERCIALY AVAILABLE SILICON GERMANIUM BASED THERMOELECTRIC MODULES

Daniel P. Kramer, Steven M. Goodrich, Mary L. Galaska, Chadwick D. Barklay,  
B. Allen Tolson, and Alexander B. Morgan

1700 Patterson Avenue, University of Dayton Research Institute (UDRI), Dayton, Ohio, 45469

937-229-1038; [daniel.kramer@udri.udayton.edu](mailto:daniel.kramer@udri.udayton.edu)

*Since the launch of Transit 4A in 1961 with the first space radioisotope thermoelectric generator (RTG), various thermoelectric materials have been employed in several generations of U.S. RTGs for converting the decay heat of plutonium-238 into electrical power. Silicon germanium (SiGe) based materials have been successfully utilized in Multi-Hundred Watt (MHW) and General Purpose Heat Source (GPHS) RTGs since the 1970s. SiGe thermoelectrics have a relatively high thermal to electrical conversion efficiency, and recently a manufacturer in Europe has initiated fabrication of SiGe modules for commercial waste heat recovery applications.*

*UDRI obtained several of the SiGe modules and performed preliminary testing to characterize the performance of the modules. Experiments employed a dual cone calorimeter, and a high-temperature furnace. This research has helped to determine various operating parameters of the modules as a function of cold side (~10 - 40°C) and hot side temperatures up to 1025°C.*

### I. INTRODUCTION

In 1954, Ken Jordan and John Birden at Mound Laboratories in Miamisburg, Ohio, invented RTG technology. Their first RTG (Battery #1) employed polonium-210 as the heat source and chromel-constantan thermocouples to convert the heat generated by the natural decay of polonium-210 into electrical power. Battery #1 had a thermal to electrical conversion efficiency of ~0.1%.<sup>1</sup>

Since the 1960s, spacecraft employing several different generations of RTGs have successfully provided the electrical power for a number of space missions tasked with the exploration of the solar system and beyond. As presented in Table 1, since the first application of a space RTG several different plutonium-238 fuel forms and thermoelectric materials have been employed in exploratory space missions.<sup>2</sup> One critical operating performance characteristic of an RTG is its electrical to thermal conversion efficiency. Table 1 shows that the SiGe based thermoelectrics employed in MHW and GPHS RTGs exhibit the highest conversion efficiency of all the thermoelectric materials flown to date. Unfortunately, U.S. space qualified SiGe thermoelectric couples for RTGs have not been manufactured since the late 1990s, when the production capability was discontinued.

Recently, UDRI obtained for characterization and testing several commercially available SiGe modules (Figure 1) fabricated by RGS Development BV (Langedijk, Netherlands).<sup>3</sup> The active SiGe dimensions of the modules are ~3.8 cm in width x ~9.84 cm in length, thus yielding a cross-sectional area of ~37.4 cm<sup>2</sup>. The material for these modules is produced using a novel ribbon-growth-on substrate (RGS) process. The RGS process is a cost effective, single step process for fabricating thermoelectric materials, which enables the design of specific material properties for the given application environment.<sup>4</sup> The ability to “tune” the material properties enables design flexibility for specific operating environments. In general, the RGS process produces near net-shape castings that result in thermoelectric module designs based upon a strip shaped leg. RGS Development is directly marketing their product for direct radiative industrial waste heat recovery applications consisting of a number of individual modules positioned together in removable panels, and not specifically for RTGs.



**Fig. 1.** Thermagy™ 20401-13 silicon germanium thermoelectric module obtained from RGS Development BV.<sup>5</sup> Total module dimensions including the substrate are ~4.8 cm by ~16 cm.

The manufacturer’s data sheet for the SiGe modules specifies a maximum operating temperature of 650°C, and a power output that is a function of the heat flux through the module. With a cold side temperature of 30°C and a heat flux of 38 kW/m<sup>2</sup>, the reported output for a module is up to ~9 W.<sup>6</sup> The modules are designed to operate via conduction and/or radiative coupling with a high-temperature heat source. Several of the SiGe based thermoelectric modules were purchased by UDRI, with the objective of determining their performance characteristics mainly focused on their potential in a RTG space application.

**TABLE I. Characteristics of selected RTGs employed in space exploration. Partially from Ref 2.**

RTG Type	Radioisotope Fuel	Thermoelectric Material	Beginning of Life Electrical to Thermal Conversion Efficiency	Approximate Launch Year(s)	Mission Examples
SNAP-3B	$^{238}\text{Pu}$ metal	PbTe	~5%	1961	Transit
SNAP-19	$^{238}\text{PuO}_2$ -Mo cermet	PbTe-TAGS	~4.5 – 6%	1972 - 1975	Pioneer/Viking
SNAP-27	$^{238}\text{PuO}_2$ microspheres	PbSnTe	~5%	1969 - 1972	Apollo
MHW	$^{238}\text{PuO}_2$ spheres	SiGe	~7%	1976 - 1977	Voyager
GPHS/RTG	$^{238}\text{PuO}_2$ pellets	SiGe	~7%	1989 - 2006	Galileo/Cassini New Horizons
MMRTG	$^{238}\text{PuO}_2$ pellets	PbTe/TAGS	~5.5%	2011 – scheduled 2020 scheduled 2026	MSL-Curiosity (MARS 2020) (Dragonfly)

## II. THERMOELECTRIC PERFORMANCE OF COMMERCIAL SiGe MODULES

UDRI has performed preliminary experiments on several 20401-13 Thermagy™ silicon germanium (SiGe) thermoelectric modules, which are similar to the module shown in Figure 1. The modules are designed to operate via radiative coupling with a high-temperature heat source. Operating characteristics of the SiGe modules were obtained using two different experimental setups employing as the thermal heat source; 1) a radiative dual cone calorimeter, and 2) a high-temperature resistance furnace. In both sets of experiments performed in air, a SiGe module was first firmly mounted on a water cooled aluminum cold plate to ensure excellent thermal transfer. Next, high-temperature ceramic insulation was machined to the cross-sectional dimensions of the active SiGe segment of the module, which was then positioned tightly in contact with it. Active cold side cooling and the use of ceramic insulation ensured a maximum hot side to cold side temperature gradient during the experiments. A SiGe module ready for testing is shown in Figure 2.



**Fig. 2.** Ceramic insulated SiGe module ready for testing.

## II.A. Radiative Dual Cone Calorimeter Experimental Set-up

A dual cone calorimeter (Figure 3) manufactured by FTT Instruments (East Grinstead, UK) was used to provide a calibrated thermal heat flux to a test module. Before testing, the cone calorimeter's thermal heat flux was carefully calibrated as a function of cone temperature and distance from the heating elements employing a calibrated (0-100 kW/m<sup>2</sup> range) Schmidt-Boelter (thermopile) type heat flux sensor. As the electrical input to the heaters is increased, the thermal flux (kW/m<sup>2</sup>) is measured. This allowed the development of a calibration chart for thermal fluxes up to 89 kW/m<sup>2</sup>, which was employed during the cone calorimeter experiments on SiGe modules.



**Fig. 3.** Cone Calorimeter experimental setup showing the location of the cone heater and a SiGe module.

A close-up of a typical test setup of a module with the cone calorimeter is shown in Figure 4. Prior to testing, the SiGe module is mounted onto an aluminum cooling block, and then carefully positioned within the high-temperature ceramic insulation to minimize thermal losses as shown in Figure 2. The separation between the top surface of the module and the cone calorimeter was carefully measured to be the exact distance as when the heat flux sensor was used to calibrate the cone calorimeter's thermal heat flux. This was accomplished by mounting the cold plate with the module on a small laboratory hand jack. Two Type K thermocouples were used to measure the hot side and cold side temperatures of the module during testing. A DC electronic load (Model 3710A, Circuit Specialists Inc., Tempe, AZ) was used to measure the output of the module under various experimental conditions, up to a maximum hot side temperature of 660°C. Since the manufacturer's data sheet for the SiGe modules states a maximum hot side temperature of 650°C, this temperature was only slightly exceeded during this set of experiments.<sup>6</sup> Cold side temperatures ranged from ~10 to 35°C via the application of an ice cooled circulating water bath, with higher cold side temperatures being measured at the higher experimental temperatures.

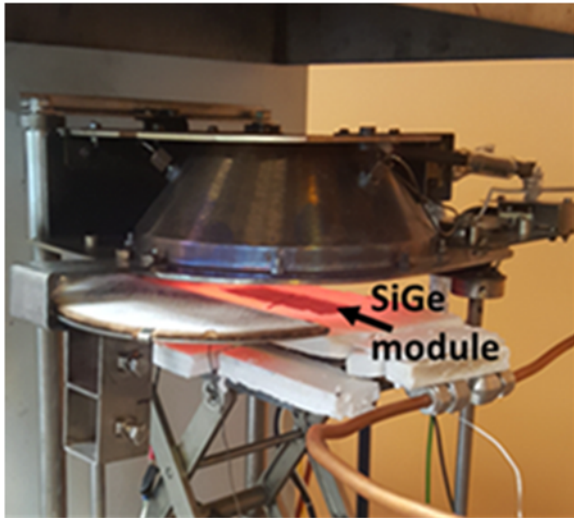


**Fig. 4.** A SiGe module during testing using the calibrated cone calorimeter.

*II.A.1. Dual Cone Calorimetry Experimental Results Obtained on SiGe Test Modules*

Figure 5 presents some of the experimental results obtained on a SiGe module employing the cone calorimeter. The figure shows the module's output power ( $W_e$ ) is a non-linear function of the module's hot side temperature. At a hot side temperature of 660°C, the module produced a maximum output power of 3.8 watts with a thermal flux of 89 kW/m<sup>2</sup> generated by the cone calorimeter.

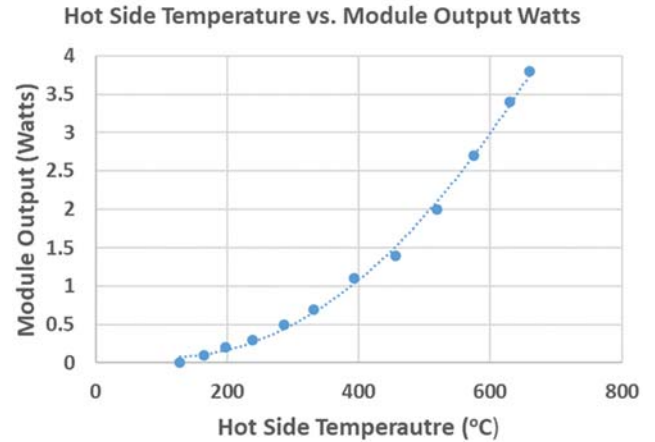


**Fig. 5.** SiGe module output ( $W_e$ ) as a function of hot side temperature experimental results.

In order to estimate the thermal to electrical conversion efficiency of the SiGe module under the described experimental conditions, the actual thermal flux exposed to the module was calculated. By measuring the actual surface area of a module, it was determined that the surface area is ~37.4 cm<sup>2</sup> or 0.00374 m<sup>2</sup>. Since the cone calorimeter flux is known as a function of the experimental parameters, this can be used to determine the actual amount of thermal flux being exposed to the entire top surface area of the module. In addition, since the module power output has also been measured during the experiments, it then becomes possible to estimate the thermal to electrical conversion efficiency of a module. Table 2 presents the results of this analysis showing that the conversion efficiency of the module peaked at ~1.14%.

**TABLE II.** Determining the thermal to electrical conversion efficiency of a SiGe module as a function of the dual cone calorimeter experimental parameters.

Cone Flux ( $W_{th}/m^2$ )	Module Flux ( $W_e$ per module surface area)	Module Output ( $W_e$ )	Conversion Efficiency (%)
9,800	36.6	0	0
13,100	49.0	0.1	0.20
17,000	63.6	0.2	0.31
21,500	80.4	0.3	0.37
27,000	101.0	0.5	0.50
33,200	124.2	0.7	0.56
40,500	151.5	1.1	0.73
49,200	184.0	1.4	0.76
58,600	219.2	2.0	0.91
69,700	260.7	2.7	1.04
82,200	307.4	3.4	1.11
89,000	332.9	3.8	1.14

## II.B. High-Temperature Furnace Experimental Set-up

Figure 5 suggests that the electrical output of a SiGe module is not a linear function of hot side temperature. As the hot side temperature increases, the electrical output of a module tends to increase at a faster rate. Summarily, Table II suggests that as the module's surface flux increases the thermal to electrical conversion efficiency also tends to increase.

In order to help determine the full potential of the SiGe modules, a module was tested to a maximum hot side temperature of 1025°C. This was performed utilizing the experimental setup shown in Figure 6.

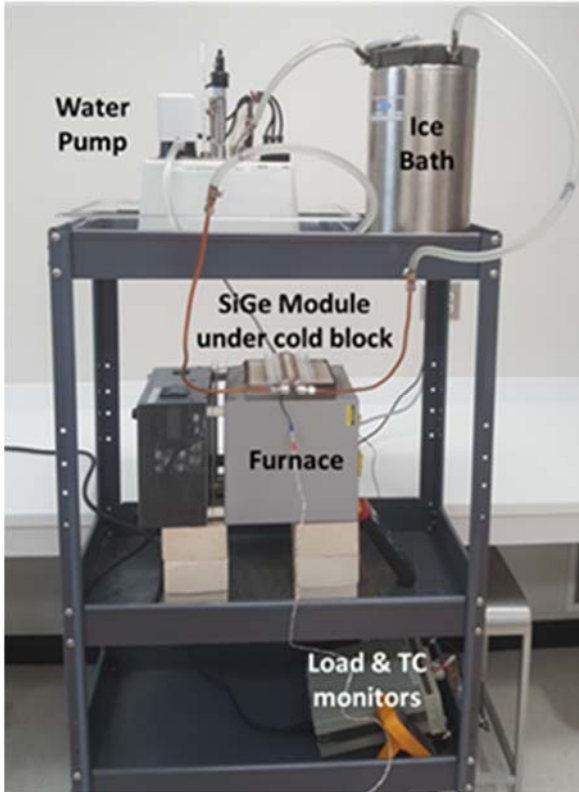


**Fig. 6.** High-temperature furnace experimental setup showing the location of various components.

The high-temperature experiment employed the same general test setup as the cone calorimeter experiments in terms of SiGe module ceramic insulation and hot and cold side Type K thermocouples for measuring the surface temperatures of the test module. The same electronic load that was previously discussed was also employed in these experiments to measure the output characteristics of a SiGe module as a function of temperature. Cold side temperatures ranged from ~10 to 45°C via the application of an ice cooled circulating water bath.

The main difference in these high-temperature experiments is that a resistance furnace was used to supply the radiant heat instead of the cone calorimeter. For the

experiments, the box furnace was placed on its back and the door was removed. The module was positioned in the “open” door slot and the ceramic insulation package was designed and cut to closely fit between the module and the door opening. This experimental setup allowed a maximum hot side module temperature of ~1025°C, compared to the 660°C maximum temperature measured during the cone calorimeter experiments. However, unlike the previously discussed cone calorimeter experiments, it was not feasible to determine the actual magnitude of the thermal flux during the high-temperature furnace experiments.

### II.B.1. High-Temperature Furnace Experimental Results Obtained on SiGe Test Modules

Figure 7 presents some of the experimental results obtained in the high-temperature furnace experiments. During the experiments, the SiGe test module was heated at a rate of ~5°C/min to a maximum temperature of 1025°C. Interestingly, the module continued to produce power significantly above the 650°C stated by the manufacturer as its maximum temperature. The power output of the module peaked at 7.7 W<sub>e</sub> at a temperature of ~950°C. However, at temperatures greater than 950°C, the power output of the module decreased. During the one hour soak at 1025°C the total decrease in power output was ~20%. All of the power decrease occurred during the first ~one-third of the soak, then leveled off for the remainder of the soak until the cooling ramp was initiated.



**Fig. 7.** SiGe module output power (W<sub>e</sub>) as a function of hot side temperature and time.

As shown in Figure 8, mixtures of Si-Ge form a continuous solid-solution phase diagram between Germanium's melting point of ~938°C and Silicon's melting point of 1412°C.<sup>7</sup> While the exact chemical composition of the materials employed in the manufacturing of the modules are not known to the authors, it is interesting that the maximum power output of the

module occurred at  $\sim 950^{\circ}\text{C}$ . As the temperature was increased to a maximum temperature of  $1025^{\circ}\text{C}$ , the output power of the module decreased. The phase diagram suggests that at the highest temperatures the solidus line may have been crossed into the liquid + solid phase field. Optical microscopy was performed on the top surfaces of both an as-received module and the module heated to the maximum temperature of  $1025^{\circ}\text{C}$ . Comparison of the surfaces of the two modules suggests that the surface of the module heated to  $1025^{\circ}\text{C}$  exhibited amorphous characteristics, suggesting the validity of the formation of a liquid phase hypothesis.

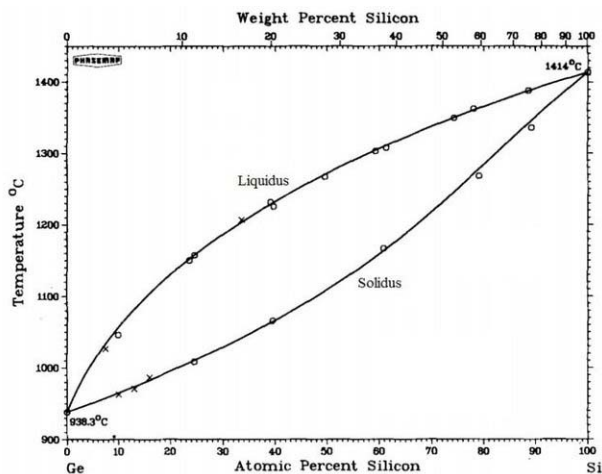


Fig. 8. Example of the Si-Ge phase diagram.<sup>7</sup>

### III. SUMMARY AND CONCLUSIONS

SiGe modules purchased for experiments centered on determining their operating characteristics at elevated temperatures. It needs to be acknowledged that these commercially available SiGe modules have been specifically marketed for industrial waste heat recovery applications, and not for nuclear space RTGs.

Two different high-temperature experiments were performed on several of the purchased SiGe modules. The cone calorimeter set of experiments exposed SiGe modules to a calibrated thermal heat flux. The maximum observed thermal to electrical conversion efficiency peaked at  $\sim 1.14\%$ , with a hot side temperature of  $660^{\circ}\text{C}$  and a cold side temperature of  $\sim 35^{\circ}\text{C}$ . The module produced a maximum output power of  $3.8 W_e$  with a thermal heat flux of  $332.9 W_{th}$  across the exposed surface area of the module.

A high-temperature furnace was employed in a second set of experiments to determine the operating characteristics of the modules at temperatures up to  $1025^{\circ}\text{C}$ . The maximum output power of the module peaked at  $7.7 W_e$  at a hot side temperature of  $950^{\circ}\text{C}$  and a cold side temperature of  $\sim 45^{\circ}\text{C}$ . A  $\sim 20\%$  reduction in output power was observed after the hot side temperature was increased from  $950^{\circ}\text{C}$  to  $1025^{\circ}\text{C}$ , though the output

power stabilized during the last two-thirds of the one hour soak at  $1025^{\circ}\text{C}$ . The high temperature results are interesting considering that several of the manufacturer's SiGe module related data sheets presents a maximum operating temperature of  $650^{\circ}\text{C}$ .

### ACKNOWLEDGMENTS

This research was performed using University of Dayton internal funding and funding from Battelle Energy Alliance contract 00184172, which the authors wish to acknowledge and thank for the continued support.

### REFERENCES

1. K. C. JORDAN and J. H. BIRDEN, "Thermal Batteries Using Polonium-210," MLM-984, Mound Laboratories, Miamisburg, Ohio (1954).
2. J. A. ANGELO JR. and D. BUDEN, *Space Nuclear Power*, pp. 133-157, Orbit Book Company, Inc., Malabar, Florida (1985).
3. RGS DEVELOPMENT BV, Bijlestaal 54-A, 1721 PW Broek op Langedijk, Netherlands (+31 226 332 950).
4. A. SCHAÖNECKER, B. KRAAIJVELD, A.E. VAN TIL, A.J. BÖTTGER, P. BRINKS, M. HUIJBEN, M. DEN HEIJER, "Cost Efficient Manufacturing of Silicide Thermoelectric Materials and Modules using RGS Technique," *Materials Today: Proceedings*, Vol. 2, Issue 2, pp. 538-547 (2015).
5. *Thermagy™ Power Module – Thermagy as a novel alternative for local electricity*, RGS Development BV Technical Data Sheet, Rev. no: 04, 2 pages, publish date: 09.04.2019.
6. *Thermagy™ Power module (15W)*, RGS Development BV Technical Data Sheet, Rev. no: 01, 7 pages, publish date 10.08.2018.
7. C. G. LITTLEJOHNS, F. Y. GARDES, M. NEDELJKOVIC, G. Z. MASHANOVICH, G. T. REED, "Silicon Diffusion Engineering in Rapid Melt Growth of Silicon-Germanium on Insulator," *ECS Trans.*, vol. 64, Issue 6, pp. 155-157 (2014).

## ICY AND OCEAN WORLD EXPLORATION ENABLED BY RADIOISOTOPE POWER SYSTEMS

Young H. Lee<sup>1</sup>, Brian Bairstow<sup>1</sup>, Sam Howell<sup>1</sup>, Benjamin Donitz<sup>1</sup>, Mathieu Choukroun<sup>1</sup>, and Scott Perl<sup>1</sup>

<sup>1</sup>*Jet Propulsion Laboratory, California Institute of Technology, 4800 Oak Grove Dr., Pasadena, CA, 91109  
818-354-13426, [young.h.lee@jpl.nasa.gov](mailto:young.h.lee@jpl.nasa.gov)*

*As the interest in exploring icy and ocean worlds gains increasing traction among scientists and mission communities, there are many potential icy and ocean world targets for in-situ lander missions. Potential targets include Europa, Enceladus, Titan, Triton, Ceres, Pluto, and more, which will allow the scientific community to address icy and ocean world related questions for understanding the distribution of life in the Solar System. Beyond Jupiter, solar power is infeasible for any landed missions and primary batteries are infeasible for long-duration missions. Radioisotope Power Systems (RPS) can be enabling for these long-duration in-situ missions. However, the interaction of RPS waste heat with icy world surfaces must be understood to assure the science and mission communities that RPS are a safe, enabling option to explore the surface of icy bodies.*

*This paper describes a study for the RPS Program that was conducted by the RPS Mission Analysis Team and JPL's Team X to investigate the system-level impact of a heat rejection system that would be required for RPS-enabled exploration of icy and ocean worlds.*

### I. INTRODUCTION

The extremely low temperature and pressure at the surface of most icy and ocean worlds could pose a challenge to surface exploration missions powered by RPS because these missions require management of RPS waste heat to prevent the ice from melting or sublimating. Thus, minimizing sublimation and melting of the top layers of ice at destinations like Europa or Enceladus is necessary for preserving science investigations and remaining compliant with planetary protection (PP) regulations.

When considering the use of RPS for icy surface explorations, RPS waste heat is of great concern to science and mission communities for two reasons: (1) waste heat impacts the viability of science measurements as it interacts with ice to evolve icy compositions and (2) waste heat must be compatible with NASA PP requirements (e.g., it must avoid creating a livable environment or enabling the delivery of organisms to a subsurface ocean). To address these concerns, the RPS Program's Mission Analysis Team and Jet Propulsion Laboratory's (JPL) Team X conducted a study to investigate the mission-level impact of a heat rejection system that would satisfy notional science and PP requirements for RPS-enabled exploration of icy and

ocean worlds. This study considered two representative Icy World destinations, Europa and Enceladus, because they occupy end-members in thermal conductivity given their different porosities and non-ice compositions. The objectives of the study were to find the heat flux at the surface under which: (1) surface liquid water does not form, and (2) surface sublimation is within the limits determined by notional science requirements, considering surface temperature, pressure, and porosity. In addition, the scope of the study included estimation of the mass and volume of a heat shield sufficient to reject enough RPS waste heat to remain within the calculated maximum surface flux, governed by the surface characteristics of the target body.

### II. STUDY PLAN

#### II.A. Study Assumptions

To develop the science requirements for the study, the study team used notional values derived from science community consensus on the most scientifically valuable measurement types and required performance capabilities, leveraging the published Europa Lander Science Definition Team (SDT) report<sup>1</sup>. The RPS study team also used the current NASA and Committee on Space Research (COSPAR) standards for PP (Ref. 2). For icy world environmental requirements, the team used values derived from a 23-target set of missions, categorizing them with similar environmental requirements based on surface temperatures, surface topography, and composition. The study assumed a representative 6-year flight time and 2-year surface mission time. Three notional RPS were studied: two Next Generation Radioisotope Thermoelectric Generator (Next-Gen RTG) variants (2-GPHS and 16-GPHS), and a Dynamic Radioisotope Power System (DRPS) (6-GPHS) (Ref. 3). Waste heat, dimensions, nominal operating temperature, and maximum fin-root temperature were identified as relevant characteristics to the study. The study treated the lander as a black box, and assumed a generic lander body similar to Europa lander in the shape of a 1 m x 1 m x 0.5 m rectangular prism. The RPS was studied both in a vertical and a horizontal configuration (telecom coverage, RPS integration, and EDL were not considered in RPS placement).

#### II.B. Approaches

The study team first characterized 23 icy and ocean world target surfaces according to their range of expected thermal conductivities, the key environmental parameter controlling the dissipation of waste heat in the surface, and therefore controlling the rate of sublimation and melting. Thermal conductivity was treated as a function of the targets' ice purity, surface porosity, and surface temperature to define a maximum allowable surface heat

flux for each target body. Note that worlds with atmospheres, like Titan, were considered out of scope for the remainder of this study. The driving requirement for the heat flux was that surface sublimation shall not exceed 10 cm over 2 years, which was derived from Europa Lander, which would conduct science operations at a depth of 10 cm to avoid environmental radiation effects.

The study team then focused on two bodies of interest, Europa and Enceladus, which act as bounding cases in the space of icy and ocean worlds. The study team found that Enceladus, which has an extremely cold surface and thus is harder to warm, could tolerate up to 100 W/m<sup>2</sup> heat surface flux to remain compliant and that Europa, which has a relatively warmer surface, could only tolerate up to 10 W/m<sup>2</sup>.

Thermal engineers modeled the effects of placing a variety of RPS on the surface of both these worlds and varied the waste heat rejected by the system, the height of the system off the surface, and the orientation of the system with respect to the surface (i.e. vertical or horizontal). The engineers proceeded to design a heat shield for each case that would prevent the heat flux from exceeding the sublimation requirement and also prevent the RPS from overheating. In total, 18 cases were investigated. Mechanical engineers, along with the thermal engineers, determined the mass and size of the notional heat shields required to create PP compliant, RPS-enabled icy and ocean world landers.

### III. Ocean World Science

The 2013-2022 Decadal Survey in Planetary Science establishes Ocean Worlds as one of the highest priority targets for understanding the emergence of life and the distribution of volatiles in the solar system. Six bodies have been identified as putative ocean worlds, including Earth, and ~10 more candidates have been proposed. Lander concepts have already been proposed to Europa, Enceladus, Titan, and Ceres (Figure 1.)

The surfaces of Ocean Worlds record evidence of interior processes, chemical potential, habitability, and potentially life within the interior. The largest science risk when using an RPS on an Ocean Worlds lander is altering, losing, or destroying traces of volatile compounds and biosignatures preserved in these ancient, low-temperature environments.

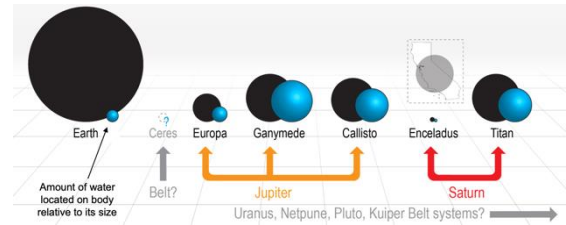


**Fig. 1.** Six Known Ocean World and Their Estimated Relative Amount of Water

## IV. Analysis for RPS Impact on Science and PP

### IV.A Surface Conductivity Model

When considering radiative heating of the surface of an icy body, with conduction of heat into the subsurface and phase change, heat transfer deeper into the ice is controlled by ice thermal conductivity. Thermal conductivity of ice is strongly dependent on temperature, porosity, and impurities. Higher thermal conductivity (solid ice) means the thermal wave will travel deeper into the ice and farther away from the RPS over a set mission duration, potentially causing sublimation or melting, but also potentially dispersing the heat harmlessly. The different Ocean World environments, including H<sub>2</sub>O versus exotic ices, compacted ice versus regolith, pure ice versus salty ice, etc., simplify down to each Ocean World occupying a range of thermal conductivities. Thus, a study over the anticipated extrema in thermal conductivity provides results applicable to all Ocean Worlds. Each individual Ocean World can be fully described as a range in surface thermal conductivity. Figure 2 shows three target bodies described in this space.

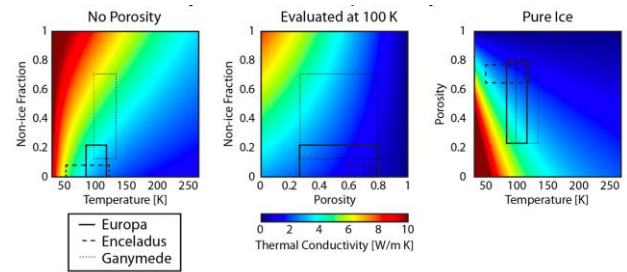


**Fig. 2.** Surface Conductivity Model

### IV.B RPS Impact on Science Considerations

Melting H<sub>2</sub>O ice at the surface of an airless body is extremely difficult, requiring a radiative heat flux of > 2 MW/m<sup>2</sup>. Instead, ice sublimates away faster than it can be heated, keeping the vapor pressure too low to reach the triple point of water (Figure 3a). On exotic bodies like Triton and Pluto, thin atmospheres prevent reaching the triple point of N<sub>2</sub> (Figure 3b). In essence, the RPS would have to sublimate enough nitrogen to raise the atmospheric pressure > 5 orders of magnitude; thus, the atmosphere works as a buffer against melting.

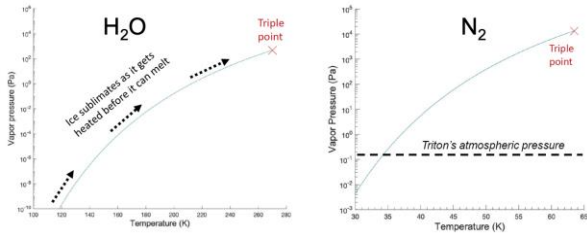


**Fig. 3a.** Airless Body and **Fig. 3b.** Thin Air Body

Because porous ice (regolith) is insulating, thermal waves will propagate faster through solid ice (Figure 4a). More thermal energy will be contained in a smaller area for more porous ice, causing the temperature of the ice to increase more quickly where the porosity is greatest and thermal conductivity is lowest. Because sublimation rate increases logarithmically with increasing temperature (Figure 4b), regolith will erode to greater depths than pure ice over the same timescale and heat flux. Thus, to avoid > 10 cm erosion over the mission duration (the baseline sampling depth for the Europa Lander), the end-member case of warmer European regolith (warm, easy to warm) can receive a flux of no more than 10 W/m<sup>2</sup>, while the end-member colder Enceladus pure ice (cold, harder to warm) cannot exceed 100 W/m<sup>2</sup>.

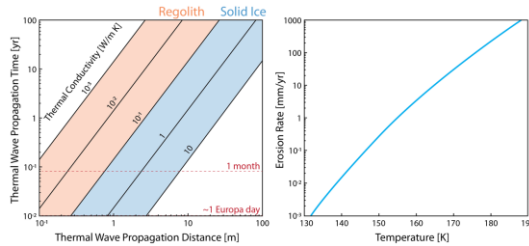


**Fig. 4a.** Thermal Waves and **Fig. 4b.** Temperature

#### IV.C RPS Impacts on PP Considerations

An additional consideration arises from PP requirements, which classifies worlds by their potential to host life. Europa and Enceladus are Class IV, requiring that the most stringent PP criteria be met. Missions must demonstrate a low chance of off-nominal impact and <1/10,000 chance of introducing one or more viable organisms into any long-lived body of liquid water. Because Europa and Enceladus have geologically young surfaces, long-lived heat sources might create warm oases for terrestrial life that would allow continued growth of any organisms. Europa Lander is considering a Terminal Sterilization System that would achieve a 12-log reduction on bioburden by heating to 500 C for 0.5 s. Any RPS mission would have to have a PP implementation that can show sterility, or sterilization of outer surface and robustness of enclosure for 1,000 years.

### V. Thermal Analysis

#### V.A Thermal Analysis Assumptions

A boundary condition at 80 K was modeled because the difference between 50 K, 80 K, or 100 K for the target body ground has negligible effect on anticipated spacecraft thermal system design due to the small difference between (T<sub>rps</sub><sup>4</sup> - T<sub>ground</sub><sup>4</sup>) when T<sub>rps</sub> is relatively high (420-473 K). The absorptivity (and emissivity) of the target body surface and the RPS surfaces were assumed as 0.9. The absorptivity (and emissivity) of the external shield structure (when used) in the IR band was assumed as 0.02, and the shield consisted of multi-layer insulation (MLI) with an effective emittance of 0.03.

#### V.B Thermal Analysis Approaches

A numerical simulation propagated the thermal environment using the body surface as a boundary condition. A shield was designed to reduce heat flux at the surface to below the limit of either 100 W/m<sup>2</sup> or 10 W/m<sup>2</sup>, depending on the target body. Analyses were run for a variety of RPS waste heat magnitude, heights, configurations, and shield cases. Each run was an independent numerical simulation with its own inputs. The independent variables were identified as: RPS waste heat, RPS distance above surface (defined as the absolute distance from the lowest part of the RPS to the surface, ignoring any lander or shield in the way), horizontal/vertical configuration, and shield dimensions and mass.

#### V.C Thermal Analysis Results

Thermal analyses were conducted for 18 scenarios using 3 RPS options with < 10 W/m<sup>2</sup> flux and < 100 W/m<sup>2</sup> flux requirements. Some of the studied scenarios warranted shielding between the RPS and target body surfaces, while others did not. See Figure 5, Thermal Analysis Summary, for details.

Thermal Shields for RPS on Ocean Worlds Surface							
RPS Waste Heat after Assumed Transit Time (W)	RPS Power at Arrival after Transit Time (W)	RPS System	Target Body and Surface Flux Constraint	Vertical Orientation		Horizontal Orientation	
				Distance between RPS and Surface (m)	Thermal Shield Description	Distance between RPS and Surface (m)	Thermal Shield Description
				Distance			
446	31	2-GPHS Next-Gen	Europa Ice (< 10 W/m <sup>2</sup> flux to surface)	0.50	1 m diameter disc (lander can likely act as a shield if diameter > 1 m)	0.40	1.5 kg, 1 m diameter disc
			Enceladus Ice (< 100 W/m <sup>2</sup> flux to surface)	1.30	No surfaces between RPS and Europa ice surface required	1.30	No surfaces between RPS and Europa ice surface required
1153	277	DRPS (6-GPHS)	Europa Ice (< 10 W/m <sup>2</sup> flux to surface)	0.80	1 m diameter disc (lander can likely act as a shield if diameter > 1 m)	1.00	1.5 kg, 1 m diameter disc
			Enceladus Ice (< 100 W/m <sup>2</sup> flux to surface)	1.70	No surfaces between RPS and Europa ice surface required	2.40	No surfaces between RPS and Europa ice surface required
3458	357	16-GPHS Next-Gen	Europa Ice (< 10 W/m <sup>2</sup> flux to surface)	1.00	5 kg, 2 m top diameter x 1 m bottom diameter x 0.2 m depth	1.50	11 kg, 1.4 m long x 0.5 m radius cylinder portion spanning 120 deg
			Enceladus Ice (< 100 W/m <sup>2</sup> flux to surface)	0.75	No surfaces between RPS and Enceladus ice surface required	0.75	No surfaces between RPS and Enceladus ice surface required
			Enceladus Ice (< 100 W/m <sup>2</sup> flux to surface)	0.30	1 m diameter disc (lander can likely act as a shield if diameter > 1 m)	0.50	1.5 kg, 1 m diameter disc

**Fig. 5.** Thermal Analysis Summary

### VI. STUDY FINDINGS

#### VI.A Largest Studied RPS

A maximum of 100 W/m<sup>2</sup> RPS waste heat flux to the icy surfaces could be maintained with **no shielding** as long as the distance between the surface and the RPS is at least 0.75 m. Reducing the maximum allowable surface flux to 10 W/m<sup>2</sup> requires a shield.

In a vertically-mounted configuration, the shield is shaped like a cone with the smallest cone diameter at the interface between the RPS root and the lander. The minimum cone angle is driven by the maximum allowable fin-root temperature and packing considerations. A 1-m bottom x 2-m top x 0.2-m depth shield is the most conformal design assuming 1 m separation between the RPS and the surface. This shield has a mass of ~5 kg (Figure 6a).

In a horizontally-mounted configuration, assuming 1.5 m separation, the shield is cylindrical at 1.4-m long, a 0.5-m radius, and spanning 120 degrees. The end caps span 150 degrees. This shield has a mass of ~11 kg (Figure 6b). Careful design is required to keep the RPS below its maximum fin-root temperature of 473 K, taking into account fin view factors.



**Fig. 6a.** Vertical Cone Shield and **Fig. 6b.** Horizontally Cylindrical Shield

### VI.B Smallest Studied RPS

A maximum of 10 W/m<sup>2</sup> RPS waste heat flux to the icy surfaces could be maintained for the smallest RPS with a 1-m simple disc shield as long as the distance between the surface and the RPS is at least 0.5 m or with no shielding at 1.3 m. For the vertically mounted configuration, the lander itself will likely act as a sufficient shield at 0.5 m. A maximum of 100 W/m<sup>2</sup> could be maintained for the smallest RPS with no shielding as long as the RPS is at least 0.25 m above the surface.

### VI.C Finless Configuration

Another approach to thermal management could be to replace the RPS fins with active cooling fluid loops. To stay under 100 W/m<sup>2</sup> surface flux at a height of 1.5 m would require a system with mass greater than 25 kg, based on Mars Science Laboratory<sup>4</sup>. Due to added mass and complexity of active cooling, it is not recommended for thermal management on Icy Worlds in most scenarios.

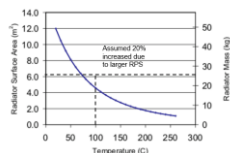


**Fig. 7.** Active Cooling Radiator Mass Estimate

## VII. CONCLUSIONS

Based on thermal analysis, RPS are a feasible, enabling power system option for missions to icy and ocean worlds with only marginal mass allocated to spacecraft thermal accommodations (Figure 8 and 9). Even in the most driving case, the lander can remain compliant with PP and science investigation requirements with a shield mass of 11 kg at only 0.5 m above the surface.

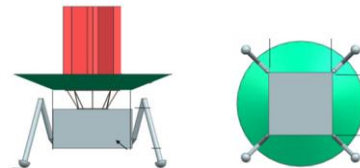


**Fig. 8.** 16-GPHS RPS Vertically Mounted (5 kg shield mass)



**Fig. 9.** 16-GPHS RPS Horizontally Mounted (11 kg shield mass)

## ACKNOWLEDGMENTS

This work was performed at the Jet Propulsion Laboratory, California Institute of Technology, under a contract with the National Aeronautics and Space Administration. The authors would like to acknowledge the valuable contributions from members of Team X at Jet Propulsion Laboratory. This study was funded by the Radioisotope Power System Program at Glenn Research Center. The information presented about potential future mission concepts is pre-decisional and is provided for planning and discussion purposes only.

## REFERENCES

1. Europa Lander website, <https://www.jpl.nasa.gov/missions/europa-lander/>
2. NASA Planetary Protection website, <https://sma.nasa.gov/sma-disciplines/planetary-protection>
3. J. ZAKRAJSEK, “RPS Decadal Planning Information,” NSPIRES Planetary Mission Concept Studies Solicitation NNH18ZDA001N-PMCS
4. A. D. PARIS, P. BHANDARI, and G. C. BIRUR, “High Temperature Mechanically Pumped Fluid Loop for Space Applications – Working Fluid Selection,” *Journal of Aerospace*, **113**, , 1 (2004) <https://www.jstor.org/stable/44737951?seq=1>

## A FACILE POLYMERIC TEMPLATING ROUTE TOWARDS FABRICATING RTG AND RHU VENT HOLE FILTERS

R. Mesalam<sup>1</sup>, G. Sheppard<sup>2</sup>, K. Tassenberg<sup>2</sup>, R. M. Ambrosi<sup>1</sup>, E. J. Watkinson<sup>1</sup>, A. Barco<sup>1</sup>, T. Crawford<sup>1</sup>, K. Stephenson<sup>3</sup>

<sup>1</sup>University of Leicester, School of Physics and Astronomy, Space Research Centre, University Rd, Leicester, LE1 7RH, UK

<sup>2</sup>University of Leicester, School of Engineering, University Rd, Leicester, LE1 7RH, UK

<sup>3</sup>European Space Agency, ESTEC TEC-EP, Keplerlaan 1, 2201AZ Noordwijk, The Netherlands.

Primary Author Contact Information: +44(0)116252 5850, [rm467@le.ac.uk](mailto:rm467@le.ac.uk)

Filtered vent holes are typically included in radioisotope fuel clads to accommodate radiogenic outgassing and potential oxygen release. Historically, pressed and sintered metal powder in the form of a porous disc (frit) has been employed as a particulate filter to prevent contamination. However, their small size and thinness mean they can be non-trivial to manufacture with high reproducibility. Not to mention, variability in the characteristics of the starting powder will likely have a critical influence on the final properties of the frit. This paper describes a powder-free method for fabricating porous platinum discs that can potentially be integrated into radioisotope fuel clads. A European clad design incorporating these platinum discs is illustrated. Initial permeability testing of this design concept is reported and compared to a pressed and sintered metal powder frit design.

### I. INTRODUCTION

Both radioisotope thermoelectric generators (RTG) and heater units (RHU) make use of radioisotope heat sources. The first containment layer in a radioisotope heat source typically consists of a welded cladding structure made from a compatible metallic alloy. The design is driven by safety principles, with the most important being retention of the radioisotope fuel within the clad in the event of all foreseeable launch accidents. One possible mechanism that could cause the clad to breach is the generation of gaseous species pressuring the clad from within (Ref. 1). These gases are typically generated from oxygen release at elevated temperatures and helium build up over time from the radiogenic alpha decay of the fuel (Ref. 2). To avoid clad pressurisation, a vent hole covered by a porous medium is designed into the clad in order to allow for controlled gas release while preventing contamination.

Historically, the porous medium covering the vent hole consists of a pressed and sintered metal powder disc known as a frit (Ref. 1). For compatibility reasons, precious metal powders, such as pure platinum, are typically used in the making of frits (Ref. 1 and 3). The size of a single frit can be a few millimeters in diameter and much less than 1 millimeter in thickness (Ref. 1) and

2). Their small size and thinness mean they can be non-trivial to manufacture with high reproducibility. Not to mention, variability in the characteristics of the starting powder will likely have a critical influence on the final properties of the frit. To the best knowledge of the authors, frits made of pure platinum are currently not commercially available in Europe (Ref. 4). Therefore, for European RTG and RHU systems, porous platinum discs are currently being developed by the University of Leicester as highlighted in this paper.

To circumvent some of the challenges associated with a powder metallurgy process, a powder-free method for fabricating porous platinum discs has instead been explored. The powder-free method primarily is comprised of a facile polymeric templating route in which a sacrificial polymer is loaded with an aqueous platinum salt solution, dried and calcined in air (Ref. 5). Using a small handheld hollow punch, circular discs are then removed from the porous platinum sheet that remains.

A European clad design incorporating these platinum discs is illustrated in figure 1. The design makes use of a machined recess and press fit cover disc to tightly encase a stack of porous platinum discs over the vent hole. The cover disc would be welded in place using a Tungsten Inert Gas (TIG) welding technique.

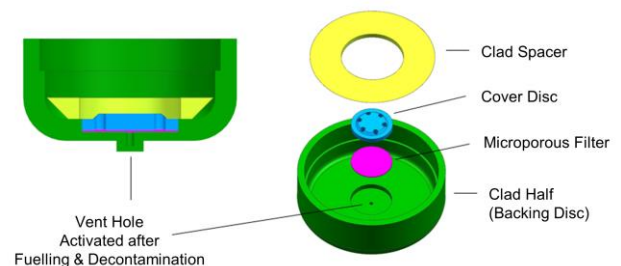


**Fig. 1.** CAD model illustrating a potential European RTG/RHU filtered vent hole design.

In this paper, surface porosity of the platinum discs is characterised and initial permeability testing of this design concept is reported. For comparison, these initial results are compared to a more typical pressed and sintered metal powder frit design.

## II. METHODS AND PROCEDURES

### II.A. Polymeric Templating Route

Table 1 describes the stepwise procedure used to produce porous platinum discs through the polymeric templating route. For this study, the polymeric template used consisted of high purity alpha cellulose (ash content  $\leq 0.06\%$ ) filter paper. The filter paper template had a nominal thickness of around 0.4 mm.

**TABLE I.** Processing sequence.

1. A 0.1-0.6 Molar aqueous platinum salt solution is first prepared.
2. The polymer template is soaked in the aqueous platinum salt solution under mild agitation.
3. The loaded template is removed from solution and dehydrated in air at ambient temperature.
4. The loaded template is placed between two meshed sheets, calcined in air for 5-10 minutes at 800-950 K and left to naturally air cool.
5. The free-standing porous platinum sheet is removed from the meshed sheets and placed back into the furnace for a further 10-15 minutes at 1200-1350 K and left to naturally air cool
6. Circular discs are removed from the porous platinum sheet using a hollow punch.

Figure 2 shows an example of the final circular discs produced using the processing sequence described above. The discs had a nominal diameter and thickness of 9 mm and 0.2 mm, respectively.



**Fig. 2.** Three porous platinum discs fabricated using the polymeric templating route.

For comparison, cold pressed and sintered metal powder frits were also produced in this study. The frits were manufactured to a similar diameter and had a nominal thickness of around 1 mm.

### II.B. Porosity Characterisation

To characterise the surface porosity of each sample, scanning electron microscopy (FEGSEM, FEI Quanta 600, Oregon, USA) images of the sample's surface (80 mm<sup>2</sup>) were first collected and stitched together using FEI MAPS software (Version 2.1, FEI, Oregon, USA). The large format high-resolution image was then processed and characterised by proprietary software developed by the University of Leicester. The porosity data collected was subsequently represented as a frequency histogram showing pore size distribution.

### II.C. Permeability Testing

Permeability testing was performed using the experimental setup illustrated in figure 3. The experimental setup consists of a high-pressure helium source, sample chamber, sample holder, differential pressure sensor, flow rate meter and a needle valve to regulate the input pressure. Before use, the setup was initially leak tested using thin aluminium blanking discs in place of the porous platinum discs.

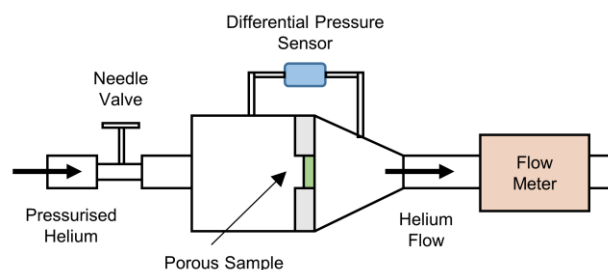


**Fig. 3.** Schematic of the setup used for measuring helium permeability.

To more closely represent the permeability of the design concept illustrated in figure 1, the sample holder was designed with a similar input and output vent hole configuration. Figure 4 illustrates the sample holder configuration used in this study. Multiple porous platinum discs were stacked and encased within a single holder.

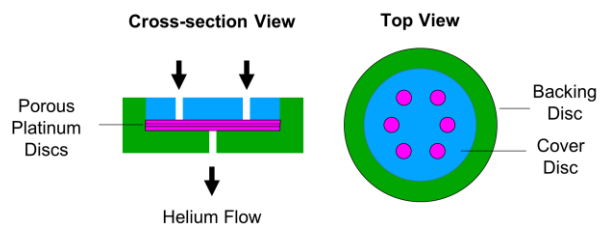


**Fig. 4.** Schematic of the sample holder design.

The cold pressed and sintered frit discs were tested using the same backing disc, illustrated in figure 4, but without the use of a cover disc. This provided a frit vent configuration similar to that of the light weight radioisotope heat unit (LWRHU) (Ref. 1).

### III. RESULTS AND DISCUSSION

#### III.A. Porosity

The surface morphology of both the cold pressed and sintered frit and templated porous platinum discs can be seen below in figure 5. From figure 5a it is shown that the porous platinum discs have a fibrous morphology similar to their starting cellulose paper template. More so, the resulting porosity can be described as hierarchical. Since the crossing of fibres leads to one type of pore structure, while each fibre itself contains a multitude of smaller pores. In contrast, figure 5b shows the cold pressed and sintered frit to be relatively non-hierarchical, with only one type of pore structure being formed from a lack of sintering between two or more adjacent particles.

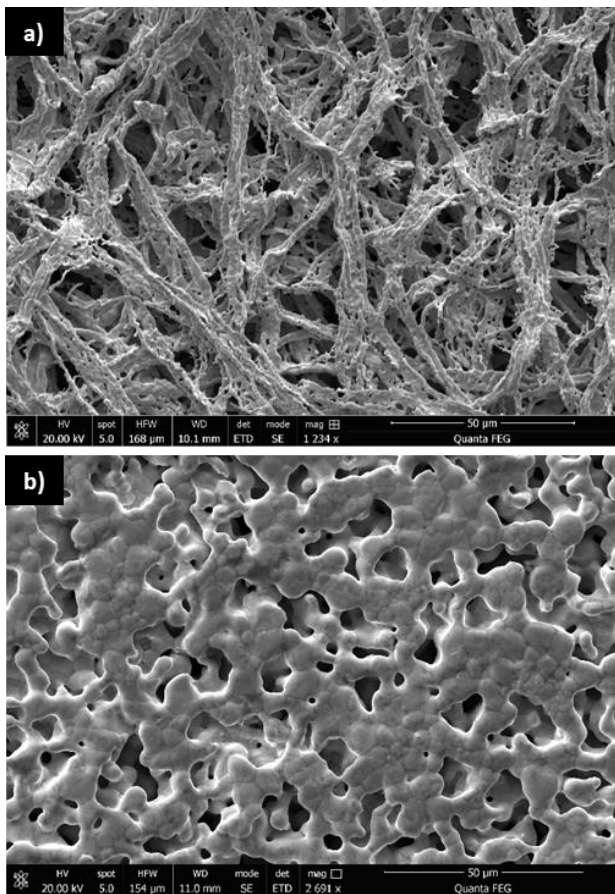


**Fig. 5.** Scanning electron microscopy images of (a) a templated porous platinum disc and (b) a cold pressed and sintered frit disc.

Figure 6 illustrates the relative distribution of surface pore size for both samples highlighted in figure 5. Based on the cumulative frequency, it is shown that over 90% of all pores were found to be below 10 μm for both sample types. However, the templated porous platinum disc was found to have an average pore size of 2 μm, which is smaller than that of the cold pressed and sintered frit at 6 μm. This is primarily due the large majority of smaller pores distributed along each single fibre. The smaller average pore size would likely prove beneficial for filtering out radiogenic particulates if a subsequent reduction in permeability is avoided.

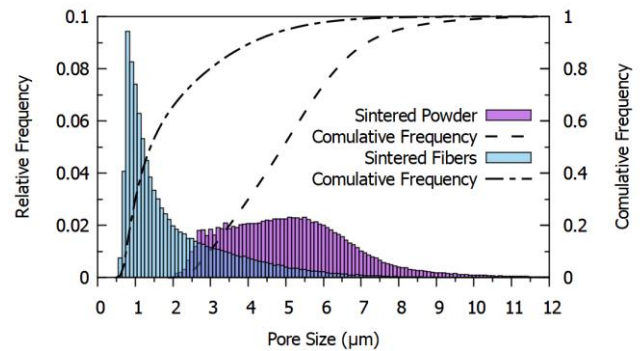


**Fig. 6.** Surface pore size distribution determined from large format high-resolution FEGSEM images of the samples highlighted in figure 5.

#### III.B. Permeability

Helium permeability measurements for both filtered vent configurations are shown in figure 7. For perspective, the average helium permeability of the multi-mission RTG (MMRTG) frit vent system at ~70 mbar (Ref. 2) has also been included as a single point of reference.

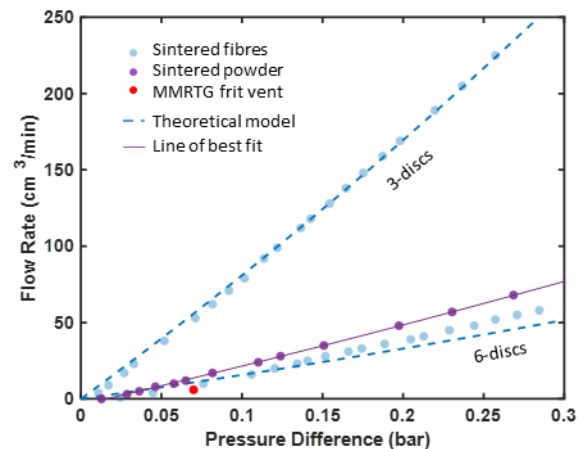


**Fig. 7.** Permeability testing in the form of flow rate measurements as a function of differential pressure.

Advantageously, by varying the number of porous platinum discs stacked within a single holder (see figure 4), the permeability of the vent system can be readily tuned. This is demonstrated in figure 7 where a 6-disc stack provides roughly 4 times less flow rate in comparison to a 3-disc stack. In fact, the permeability of the 6-disc stack can be seen to roughly coincide with both the MMRTG frit vent system and this study's cold pressed and sintered frit at ~70 mbar.

In future studies, the porosity of the starting template could be varied to further tune the permeability of the filtered vent system. Although, theoretical modelling is first needed to understand what level of permeability is desirable for a European RHU and RTG system. Not to mention the high reproducibility of the templating approach is still to be demonstrated. Furthermore, an experimental campaign is also required to examine the particulate filtration efficiency of such a configuration.

#### IV. CONCLUSIONS

In this study a powder-free method for fabricating porous platinum discs for European RHU and RTG vent systems was explored. The powder-free method comprised of a facile polymeric templating route in which a sacrificial polymer sheet was loaded with an aqueous platinum salt solution, dried, calcined in air and then punched into small circular discs. The surface porosity of the discs was analysed and compared to a cold pressed and sintered frit disc.

Furthermore, the permeability of a filtered vent system incorporating the porous platinum discs was examined. By varying the number of discs within the vent system, it was shown that the permeability could be readily tuned. Using 6 porous platinum discs in a single stack, the permeability of the vent system was lowered to a value which was shown to be similar to that of the MMRTG frit vent system at ~70 mbar. However, further study is needed to identify what level of permeability is desirable for a European RHU and RTG system.

#### ACKNOWLEDGMENTS

The University of Leicester is funded by the European Space Agency. The authors would like to thank the UK Space Agency and acknowledge the ongoing collaboration with National Nuclear Laboratory (UK) Ariane Group (France) and Thales Alenia Space UK.

#### REFERENCES

1. R. E. Tate, *The Light Weight Radioisotope Heater Unit (LWRHU): A Technical Description of the*

*Reference Design*, Los Alamos National Laboratory, **LA-9078-MS** (1982).

2. G. B. Ulrich, *Examination of Frit Vent from Sixty Watt Heat Source Simulant Fueled Clad Vent Sent*, Oak Ridge Y-12 Plant, **Y/DV-1393** (1995).

3. G. B. Ulrich, *The Metallurgical Integrity of the Frit Vent Assembly Diffusion Bond*, Oak Ridge Y-12 Plant, **Y/DV-1321** (1994).

4. R. M. Ambrosi, H. Williams, E. J. Watkinson, et al., *European Radioisotope Thermoelectric Generators (RTGs) and Radioisotope Heater Units (RHUs) for Space Science and Exploration*, *Space Science Reviews*, **215:55** (2019)  
<https://doi.org/10.1007/s11214-019-0623-9>.

5. Christodouleas, D., Simeone, F., Tayi, A., et al., *Fabrication of Paper-Templated Structures of Noble Metals*, *Advanced Materials Technologies*, **2:1600229** (2017).  
<https://doi.org/10.1002/admt.201600229>.

## MEASUREMENT OF THE INTEGRAL CAPTURE AND FISSION CROSS SECTION OF $^{238}\text{Np}$

Catherine Romano, David Glasgow, Ben Roach, Ram Venkataraman

Oak Ridge National Laboratory, Oak Ridge, TN 37830

Primary Author Contact Information: (865) 574-1617, [romanoce@ornl.gov](mailto:romanoce@ornl.gov)

The  $^{238}\text{Np}$  capture and fission cross sections are important for the accurate modeling and simulation of  $^{238}\text{Pu}$  production in a reactor. Uncertainties in these cross sections can impact the ability to predict and optimize the target design and loading for the  $^{238}\text{Pu}$  production targets in High Flux Isotope Reactor (HFIR) at Oak Ridge National Laboratory. The half-life of  $^{238}\text{Np}$  is 2.099 days, making the cross section very difficult to measure using traditional means. This paper describes the uncertainties in the cross sections and details of the planned experiments at the HFIR. This paper describes the preliminary experimental results.

### I. INTRODUCTION

Detailed neutronics calculations are required to plan the  $^{237}\text{Np}$  target irradiations for the production of  $^{238}\text{Pu}$  in HFIR. Even small uncertainties in the cross sections will significantly impact the accuracy of the calculations over several irradiation cycles (Ref. #1). Using a  $^{238}\text{Np}$  fission cross section that is too high results in overpredicting  $^{238}\text{Np}$  fission and overpredicting the operating temperature of the target. Overpredicting the operating temperature of the target results in constraining how much neptunium can be loaded in a target.

It is believed that the  $^{238}\text{Np}$  fission cross section has a high uncertainty and the greatest impact to the  $^{238}\text{Pu}$  production simulations. The  $^{238}\text{Np}$  fission cross section was measured in 1996 at Rensselaer Polytechnic Institute in the lead slowing-down spectrometer (LSDS) (Ref. #2). As shown in Figure 1, a large resonance was measured at about 1 eV and the thermal fission cross section was found to be larger than previous values. ENDF/B-VIII.0 reflects the large resonance from the 1996 measurement, but it is still below the measured cross section at thermal energies. The JEFF-3.3 cross section is lower still, and the 1 eV resonance is missing.

In an effort to reduce uncertainty in the fission rate and  $^{238}\text{Pu}$  production within the targets, measurement of the  $^{238}\text{Np}$  capture and fission cross section was proposed. This paper describes the planned experiment.

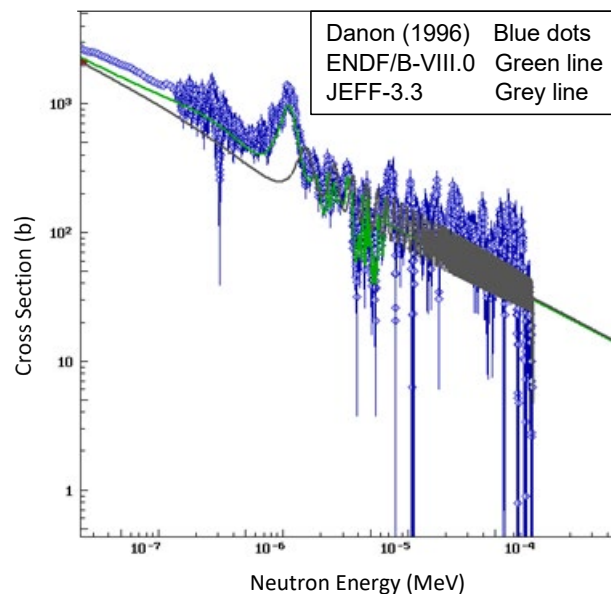


**Fig 1.** Comparison of  $^{238}\text{Np}$  fission cross section measurement with ENDF/B-VIII.0 and JEFF 3.3 libraries.<sup>2</sup>

### II. THE CROSS SECTION AND FISSION YIELD MEASUREMENTS

The  $^{238}\text{Np}$  energy integral measurements will be conducted in the pneumatic tubes located in the Neutron Activation Analysis (NAA) laboratory at HFIR. The measurements will provide the data necessary to calculate thermal and resonance integral capture and fission cross sections (Ref. #3). The irradiated targets will be analyzed using gamma spectroscopy and mass spectrometry.

#### II.A. The Neutron Activation Analysis Laboratory

The HFIR NAA laboratory pneumatic transfer systems have in-line decay stations in the reactor pool (shown in Figure 2) for the reduction of short-lived radioactivity. The short-lived fission products produced in the  $^{237}\text{Np}$  targets and the activation products produced in the Cd thermal absorber will be safely handled using the decay station design feature.

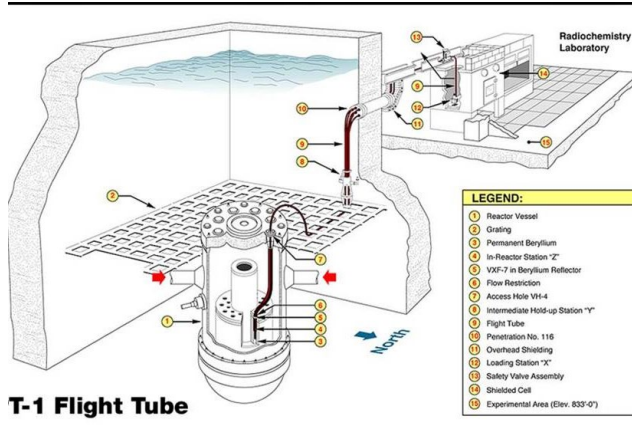


**Fig. 2.** The HFIR, the NAA laboratory, and the pneumatic tubes connecting the two facilities.

The targets will be irradiated in Pneumatic Tube 1 (PT-1) and Pneumatic Tube 2 (PT-2). The magnitude of the flux in each irradiation location is shown in TABLE I.

**TABLE I.** Flux in the irradiation locations.

Location	Thermal Flux	Thermal-to-Resonance Ratio
PT-1	$4 \times 10^{14}$ n/cm <sup>2</sup> s	35
PT-2	$4 \times 10^{13}$ n/cm <sup>2</sup> s	250

In a previous experiment, a precise measurement of the flux spectrum was made in each irradiation location and compared to the modeling results. The flux measurement in the PT-1 and PT-2 reactor irradiation locations consisted of one cadmium-covered and one bare set of flux wires in each location. The cadmium filter is designed to absorb the thermal neutrons so that the target interacts with the fast neutron flux. Cadmium-filtered monitors were irradiated in the PT-2 at 100% reactor power and in the PT-1 at 10% reactor power. The monitors in the shielded package were wires of Al, Al(0.1% Au), Al(0.116% Co), Al(1.08% Ag), Cu, Fe, Nb, Ni, Ti, and W. The unperturbed thermal flux was measured by irradiation of Al (0.0879% Mn) and Al (0.116% Co) wires, with Al (0.1% Au) serving as an epithermal flux monitor. The activities of the individual monitors were measured on HPGe detectors and formed the basis for spectrum unfolding using the STAYSL-PNNL dosimetry code. The results of the unperturbed spectra in PT-1 and PT-2 calculated with the STAYSL-PNNL code are shown in Figure 3 (Ref. #4).

Because the spectrum in each irradiation location can change based on the target loading in HFIR, cycle-specific models are used to account for the perturbations in the spectrum from those targets. The calculations will be confirmed through flux monitor irradiations immediately before and after the <sup>237</sup>Np target irradiations.

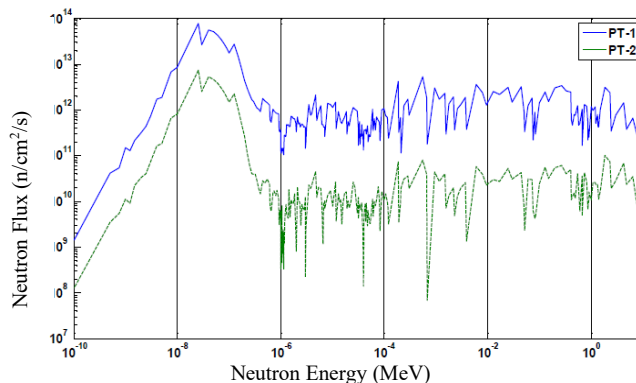


**Fig 3.** The STAYSL-PNNL unfolded neutron spectra in the PT-1 and PT-2 irradiation locations in HFIR.<sup>4</sup>

The monitor dosimetry package is selected such that the response of the nuclear reactions induced in the dosimeters span the entire energy spectrum of the neutrons—thermal, resonance, and fast energies. The reaction rate per target atom of the dosimetry reactions is determined based on measured saturated activities of monitors using gamma spectrometry.

The neutron energy spectrum that is consistent with the measured reaction rates of neutron dosimeters is then unfolded using the STAYSL-PNNL code.<sup>4</sup> The inputs to the STAYSL-PNNL codes are the reaction rate per target atom for the appropriate flux wire reactions and an initial estimated neutron energy spectrum at the irradiation location. The microscopic reaction cross sections used in the spectral unfolding are from IRDFF-II (International Reactor Dosimetry and Fusion File -II) (Ref. #5). The IRDFF-II cross-section file was released in January 2020 and represents the latest international reference in neutron metrology for multiple applications.

## II.B. <sup>237</sup>Np Target Design

The cross section targets will consist of tens of micrograms of 99.9999+% pure <sup>237</sup>Np deposited on thin titanium or carbon foils. The foils are rolled into an annulus to avoid overlapping of the <sup>237</sup>Np material to minimize self-shielding. The foils are then placed into a quartz vial, which is placed in a graphite capsule. For irradiations with a cadmium filter, 1 mm thick cadmium tubing with end caps will be fit between the quartz vial and the graphite irradiation capsules, as illustrated in Figure 4. To reduce the uncertainties introduced by the overlap of the cadmium layer, two separate single-layer cadmium pieces will be wrapped around the vial and the ends pressed together, with the seams of each layer located on opposite sides.



**Fig 4.** Graphite irradiation capsule and cadmium filter (left) and a target contained in a quartz ampule (right).

### II.C. Target Irradiations

The planned  $^{237}\text{Np}$  target irradiations include three series of measurements, as described in TABLE II. The irradiated target isotopics were calculated using ORIGEN depletion code which is part of the SCALE code package developed at ORNL. The irradiation times were selected to optimize specific parameters of either isotopic mass content or post-irradiation activities of specific isotopes (Ref. #6).

Targets 1 through 3 are intended to provide a baseline  $^{237}\text{Np}$  capture cross section within the PT-1 and PT-2 irradiation locations in order to reduce uncertainties in the  $^{238}\text{Np}$  cross section calculations. The targets will be irradiated for 600 or 6000 seconds, and the 984.45 keV and 1028.53 keV gamma lines from  $^{238}\text{Np}$  decay will be measured to determine the amount of  $^{238}\text{Np}$  in the irradiated target. It may also be possible, although unlikely, to measure the 277.6 and 228.2 keV gamma lines from  $^{239}\text{Np}$  decay.

**TABLE II.** Description of the target irradiations.

Target Number	Mass $^{237}\text{Np}$	Location	Time	Thermal Filter
1	10 ng	PT-1	600 sec	
2	10 ng	PT-2	6000 sec	2 mm Cd
3	10 ng	PT-2	6000 sec	
4	50 $\mu\text{g}$	PT-1	25 hrs	
5	50 $\mu\text{g}$	PT-2	135 hrs	2 mm Cd
6	50 $\mu\text{g}$	PT-2	135 hrs	
7	10 ng	PT-1	25 hrs	
8	10 ng	PT-2	135 hrs	2 mm Cd
9	10 ng	PT-2	135 hrs	

Targets 4 through 5 will be irradiated and sent to the Nuclear Analytical Chemical & Isotopics Lab (NACIL) Service Center for mass spectrometry analysis. The

irradiation times are selected to ensure at least  $10^{-10}$  grams of  $^{238,239}\text{Np}$ ,  $^{238,239}\text{Pu}$ , and  $^{148}\text{Nd}$  are created in the target to reduce the uncertainties in the analysis. Because it is a stable isotope with a low cross section,  $^{148}\text{Nd}$  will be used to determine the number of fissions in the target.

Targets 7 through 9 will be irradiated with the goal of measuring the gamma emission from the fission products specifically to improve decay heat calculations. The irradiation time of 25 hours in PT-1 and 135 hours in PT-2 will result in 98% of the total fissions in  $^{238}\text{Np}$ .

### II.D. Post-Irradiation Measurements and Analysis

After the irradiations, the targets will be analyzed via destructive and nondestructive techniques.

#### II.D.1. Gamma Spectroscopy

The irradiated targets will be placed in a HPGe well counter with Compton suppression where the decay of  $^{238}\text{Np}$  and, potentially,  $^{239}\text{Np}$  will be recorded in order to determine the amount of each isotope that was produced during the irradiation. Figure 5 is an example of a gamma-ray spectrum of an irradiated  $^{237}\text{Np}$  target showing the decay of  $^{238}\text{Np}$  (Ref #7). These data will be used to determine the number of captures and fissions in the targets.

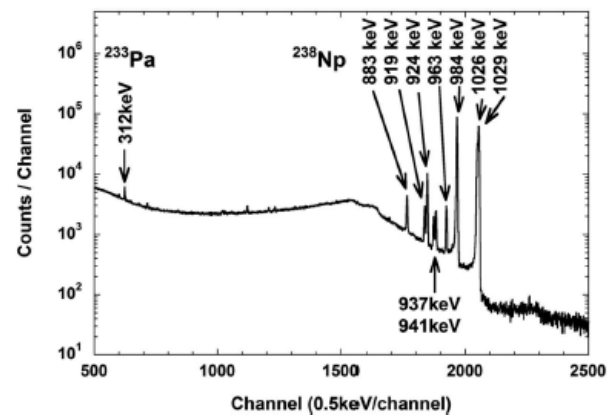


**Fig. 5.** Example of  $^{238}\text{Np}$  and  $^{233}\text{Pa}$  gamma-ray spectrum of an irradiated  $^{237}\text{Np}$  target (Ref #7).

#### II.D.2. Mass Spectrometry

The irradiated targets will be allowed to decay and then will be transferred to the NACIL Service Center. Each target will be analyzed for both actinide and fission content, with the plutonium isotopes and key fission indicators, such as  $^{148}\text{Nd}$  and  $^{137}\text{Cs}$ , being analyzed by isotope dilution mass spectrometry and yielding a total combined uncertainty of 0.5–1.0% at a 95% confidence level. High-pressure ion chromatographic separation will be employed to elementally isolate key analytes, which will be analyzed using a Thermo Scientific Neptune multicollector–inductively coupled plasma mass

spectrometer (MC-ICPMS). The  $^{237}\text{Np}$  and  $^{238}\text{Np}$  content will be determined by mass via a standard addition approach using a NIST-certified standard, yielding a combined uncertainty of <3% at a 95% confidence level. The analytical uncertainties will be calculated according to the principles of GUM. Figure 6 shows an high-pressure ion chromatogram of the dissolver solution (irradiated  $^{237}\text{Np}$  targets) from the 2019  $^{238}\text{Pu}$  production campaign. Clear elemental isolation from the bulk  $^{237}\text{Np}/^{238}\text{Pu}$  solution and isobaric interferences allows high-precision measurement of the neodymium isotopes, in particular  $^{148}\text{Nd}$ .

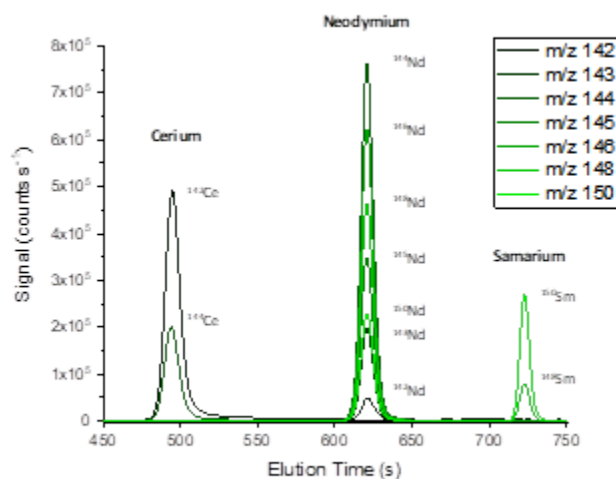


**Fig. 6.** Example high-pressure ion chromatogram of irradiated  $^{237}\text{Np}$  targets, as detected by ICPMS, showing elemental isolation of the neodymium fission isotopes from the cerium and samarium isobaric interferences.

### III. CONCLUSIONS

A cross section and fission yield experiment is planned to measure the  $^{238}\text{Np}$  capture and fission cross sections and fission yields in the HFIR pneumatic tubes. The irradiation facility at HFIR and the planned target irradiations are described in this paper. The subsequent presentation will provide the preliminary experimental results. The results of these measurements are expected to inform the production target neutronics models to improve their predictive capabilities.

### ACKNOWLEDGMENTS

Research sponsored by the Laboratory Directed Research and Development Program of Oak Ridge National Laboratory, managed by UT-Battelle, LLC, for the US Department of Energy.

### REFERENCES

1. C. R. DAILY and J. L. McDUFFEE, “Design Studies for the Optimization of  $^{238}\text{Pu}$  Production in  $\text{NpO}_2$  Targets Irradiated at the High Flux

Isotope Reactor,” *Nuclear Technology* (2019) DOI: 10.1080/00295450.2019.1674594

2. Y. DANON, M. S. MOORE, P. E. KOEHLER, P. E. LITTLETON, G. G. MILLER, M. A. OTT, L. J. ROWTON, W. A. TAYLOR, J. B. WILHELMY, M. A. YATES, A. D. CARLSON, N. W. HILL, R. HARPER, and R. HILKO, “Fission Cross-Section Measurements of the Odd-Odd Isotopes  $^{232}\text{Pa}$ ,  $^{238}\text{Np}$ , and  $^{236}\text{Np}$ ,” *Nuclear Science and Engineering*, **124**(3), 482–491 (1996), DOI: 10.13182/NSE96-A17926
3. B. PRITYCHENKO and S.F. MUGHABGHAB, *Nuclear Data Sheets*, **113**(12), 3120–3144 (2012), ISSN 0090-3752, DOI: 10.1016/j.nds.2012.11.007
4. L. R. GREENWOOD and C. D. JOHNSON, *User Guide for the STAYSL PNNL Suite of Software Tools*, PNNL-22253, Pacific Northwest National Laboratory, Washington (2013).
5. A. TRKOV, P.J. GRIFFIN, S.P. SIMAKOV, L.R. GREENWOOD, K.I. ZOLOTAREV, R. CAPOTE, D.L. ALDAMA, V. CHECHEV, C. DESTOUCHES, A.C. KAHLER, C. KONNO, M. KOSTAL, M. MAJERLE, E. MALAMBU, M. OHTA, V.G. PRONYAEV, V. RADULOVIC, S. SATO, M. SCHULC, E. SIMECKOVA, I. VAVTAR, J. WAGEMANS, M. WHITE, and H. YASHIMA, “IRDF-II: A New Neutron Metrology Library,” special issue of *Nuclear Data Sheets*, **163**, 1–108 (2020). Also available as arXiv 1909.03336 (2019).
6. SCALE Code System, ORNL/TM-2005/39, Version 6.2.3 (March 2018).
7. S. NAKAMURA, F. KITATANI, A. KIMURA, A. UEHARA, and T. FUJII, “Measurements of thermal-neutron capture cross-section and resonance integral of neptunium-237,” *Journal of Nuclear Science and Technology*, **56**(6), 493–502 (2019), DOI: 10.1080/00223131.2019.1598304

## SPECTROSCOPIC AND MULTIVARIATE ANALYSIS DEVELOPMENT IN SUPPORT OF THE PLUTONIUM-238 SUPPLY PROGRAM

Luke R. Sadergaski<sup>1</sup>, Kristian G. Myhre<sup>1</sup>, Lætitia H. Delmau<sup>1</sup>, Dennis E. Benker<sup>1</sup>, David W. DePaoli<sup>1</sup>,  
and Robert M. Wham<sup>1</sup>

<sup>1</sup>*Oak Ridge National Laboratory, P.O. Box 2008, Oak Ridge, TN, 37831-6234, 865-874-1167, sadergaskilr@ornl.gov*

*Neptunium-containing targets are being irradiated at Oak Ridge National Laboratory's (ORNL) High Flux Isotope Reactor to produce plutonium-238 for NASA. After irradiation, the targets are processed through a series of radiochemical separations at the ORNL Radiochemical Engineering Development Center (REDC). ORNL is developing capabilities to meet the projected needs of NASA (1.5 kg of plutonium oxide per year on average) by the mid-2020s. Monitoring radiochemical processing streams with optical spectroscopy and multivariate analysis is being evaluated for real-time, remote analytical measurements within the hot cells at REDC.*

### I. INTRODUCTION

Plutonium-238 (<sup>238</sup>Pu) is the preferred radioisotope heat source for radioisotope thermoelectric generators in the United States for space applications. Heat produced by the alpha decay of <sup>238</sup>Pu is converted to electricity by thermoelectric generators to power NASA spacecraft for deep space missions. Radioisotope thermoelectric generators are key to enabling the exploration of planets such as Mars and deep-space probe missions because they provide reliable power for many years without the sun. Plutonium-238 was produced at Savannah River National Laboratory until the late 1980s. Since then, the supply has declined, and without a new supply of <sup>238</sup>Pu, future NASA space missions will be jeopardized. Thus, a joint effort between the Department of Energy and NASA was initiated in 2011 to re-establish the capability to produce this valuable radioisotope in the United States. Efforts to restore this domestic production have been successful, and new <sup>238</sup>Pu was produced at Oak Ridge National Laboratory (ORNL) in 2015 for the first time since U.S. production ceased 30 years ago.

In the <sup>238</sup>Pu supply process, targets containing <sup>237</sup>Np are irradiated at the High Flux Isotope Reactor at ORNL. The <sup>238</sup>Pu is extracted from these targets through a series of chemical processes at the Radiochemical Engineering Development Center to produce pure plutonium dioxide. This material is shipped to Los Alamos National Laboratory (LANL) for conversion to heat source pellets. The pellets are stored at LANL and shipped, as needed, to Idaho National Laboratory for incorporation into radioisotope power systems. In fact, a portion of the new

<sup>238</sup>Pu produced at ORNL has been blended with material from the existing inventory and used in the Multi-Mission Radioisotope Thermoelectric Generator, which will power a rover in the upcoming Mars 2020 mission.

The process flow sheet at ORNL is comprised of numerous steps, including the preparation of NpO<sub>2</sub> feedstock for target fabrication, dissolution of irradiated aluminum-neptunium oxide cermet pellets, solvent extraction removal of fission products and separation of Np and Pu, ion exchange for the purification of Np and Pu and conversion of each product to their oxide form.<sup>1</sup> Each step is conducted in hot cells that provide shielding to eliminate the exposure of personnel to radiation.

Chemical processing of highly radioactive materials in shielded hot cell environments challenges the timely quantification of processing samples via traditional approaches, such as inductively coupled plasma mass spectrometry (ICP-MS) and acid/base titrations. The need for timely analytical methods is being addressed by the development of optical spectroscopy and multivariate, or chemometric, analysis capabilities. Process monitoring of aqueous solutions with optical spectroscopy (e.g., Raman spectroscopy) and multivariate regression analysis (e.g., partial least squares) has been used in a variety of processing environments from micro- to industrial-scale operations.<sup>2</sup>

Partial least-squares regression (PLSR) is one of the most common techniques to generate predictive models used to quantify concentration from spectroscopic data.<sup>3</sup> This mathematical approach is useful for systems with confounding and/or covarying effects of analytes on spectral signatures. Sets of well-known calibration standards are required to build high-quality PLSR models.<sup>4</sup> Traditional approaches to building training sets that capture the full range of expected solution conditions generally require many samples and may improperly balance fitting and prediction abilities by overemphasizing the fitting aspect.<sup>5</sup> Thus, experimental designs (e.g., optimal designs) are often used to build sets of calibration standards when the number of factors is relatively high ( $\geq 3$ ) and a minimum number of runs is desired.<sup>6</sup>

These approaches are being used to monitor <sup>238</sup>Pu-related processing materials *in situ* at ORNL. The ability to

This manuscript has been authored by UT-Battelle, LLC, under contract DE-AC05-00OR22725 with the US Department of Energy (DOE). The US government retains and the publisher, by accepting the article for publication, acknowledges that the US government retains a nonexclusive, paid-up, irrevocable, worldwide license to publish or reproduce the published form of this manuscript, or allow others to do so, for US government purposes. DOE will provide public access to these results of federally sponsored research in accordance with the DOE Public Access Plan (<http://energy.gov/downloads/doe-public-access-plan>).

obtain quantitative process information using nondestructive techniques that are free from sample preparation will enable timely processing and lower resource consumption. This paper provides examples from a recent  $^{238}\text{Pu}$  supply demonstration campaign, Campaign 4, of spectroscopic and chemometric development, for the monitoring and remote characterization of processing streams, in support of the  $^{238}\text{Pu}$  Supply Program at ORNL.

## II. EXPERIMENTAL

Stokes Raman spectra were collected using a Czerny–Turner type iHR-320 imaging spectrometer (Horiba Scientific), outfitted with a Sincerity CCD camera. A 532 nm laser source (Cobalt Samba 150 laser) was passed through a cuvette holder (CVH100, Thorlabs) containing samples in a borosilicate glass screw-thread vial (VWR Scientific, 66009-882). A protective windowpane, made of KTP acrylic material with an OD of 5+ @ 532 nm, was placed over the hot cell window for safety. An Ocean Optics spectrophotometer (QE Pro) was used for UV-Vis measurements with the associated SpectraSuite software. A 1 cm pathlength cuvette and process probes (by Hellma Analytics) of varying pathlengths (2–20 mm) were used. Laser and scattered light ( $180^\circ$  scattering geometry) and the incoherent halogen light (HL-2000 by Ocean Optics) and transmitted signals were directed into and out of the hot cell through approximately 20 m of ThorLabs multimode SMA fiber patch cables (FG550LEC-Custom).

The Unscrambler X (version 10.4) software package was used to build PLSR models that correlate spectral features to the concentration of each component for quantitative prediction. D-optimal designs were generated using a Design of Experiments toolkit within the Unscrambler software package by Camo Analytics (version: 11.0.5.0). Several preprocessing treatments were tested including standard normal variate analysis, detrending, derivatives using the Savitsky–Golay method, and baseline corrections. All chemicals were commercially obtained (ACS grade) and used as received. Calibration samples (standards) were prepared by dissolving solid reagents in volumetric glassware using deionized water ( $18.2\text{ M}\Omega\text{ cm}$  at  $25^\circ\text{C}$ ).

## III. ALUMINUM CLADDING DISSOLUTION

Processing of irradiated pellets begins with the dissolution of the outer aluminum cladding (alloy Al-6061) and aluminum in the cermet pellets (alloy X8001) in a strong caustic and sodium nitrate solution. This process has been used for decades at the Radiochemical Engineering Development Center for the dissolution of targets used to produce transuranium elements.<sup>7</sup> A capability is being developed to monitor the dissolution of aluminum in real-time to inform technicians when the dissolution is complete.

Raman spectroscopy and PLSR were used to quantify each analyte of interest including aluminate ( $\text{Al}(\text{OH})_4^-$ ), nitrate ( $\text{NO}_3^-$ ) and hydroxide ( $\text{OH}^-$ ). Raman spectroscopy is sensitive to each analyte and measurements on samples within the hot cell can be collected remotely from the control room through fiber-optic cables.<sup>8,9</sup> Training sets were generated using a “standard” approach, which consisted of 125 samples, and an optimal design approach. Concentrations in the set of 125 samples were calculated based on 0, 5, 25, and 50% of the highest concentration in the expected concentration range for each analyte including sodium aluminate (0–1.25 M), sodium nitrate (0–2 M), sodium hydroxide (0–6 M). The training set generated using experimental design resulted in a total of 15 samples.

PLSR models were generated using the set of 125 samples and 15 sample approaches. Several metrics were used to determine the quality of each regression model including R-squared ( $R^2$ ), slope, offset, and root mean square error of the calibration and validation set.  $R^2$  is a metric describing how well the model will fit future predictions with values closest to one reflecting the best correlation values. Regressions with slopes closest to one and offsets closest to zero represent data that are better modeled. Root mean square errors represent the expected prediction error in the same units as the response variable Y (concentration). Each metric was better with the regression generated from the design of experiments-based samples than the more traditional approach. This finding is particularly noteworthy because operations in hot cell environments are acutely challenging because of the need to handle samples with a manipulator, conflicts with ongoing process operations, and waste generation.

The concentrations of aluminate, hydroxide, and nitrate were quantified using Raman spectroscopy and PLSR. Data for aluminum and hydroxide were compared with routinely used analytical techniques (i.e., ICP-MS and acid/base titrations). The concentration of nitrate was determined based on material balance and consideration of the dissolution stoichiometry previously reported.<sup>10</sup> Values determined by Raman spectroscopy and PLSR were in good agreement with the more traditional techniques and were of the desired quality. This demonstrated the ability to be quantitative and laid the groundwork for optical spectroscopy and multivariate analytical methods in different processing stages and future campaigns.

## III. SOLVENT EXTRACTION

Solvent extraction is used to separate plutonium and neptunium from fission products and separate plutonium from neptunium. Plutonium is recovered during the extraction step, further purified by anion exchange, and converted to oxide. Separated neptunium is further purified and recycled for fabrication into targets. Real-time

spectroscopic measurements are being used during solvent extraction runs to ensure that Np and Pu are being extracted into and/or stripped from the organic phase before exiting with the aqueous raffinate and unloaded organic solvent. This capability benefits the program by providing online feedback with information needed to make real-time process adjustments during the extraction.

In one example, UV-Vis was used to monitor the concentration of Pu(III) to ensure  $^{238}\text{Pu}$  product was being stripped from the loaded solvent and recovered in the aqueous phase (see Fig. 1). A dip probe was placed in the settlers of multiple stages of the mixer-settler bank to obtain UV-Vis spectra of the process solutions (see Fig. 1). This example demonstrates that UV-Vis is a useful tool for monitoring the concentration profiles during a solvent extraction run. The concentrations of Pu(III) and Np(V) were approximated using Beer's law and molar extinction coefficients from the published literature.<sup>11</sup> These values were in good agreement with alpha spectroscopy and ICP-MS results for grab samples. The concentration profile was significantly different than the profile predicted based on a modified version of the SEPHIS model.<sup>12</sup> This highlights the need for a monitoring tool that provides real-time process information. In addition, there is opportunity for studies to determine which elements of the process model contribute to the disagreement (e.g., redox reactions, kinetics, back mixing, mass transfer, etc.).

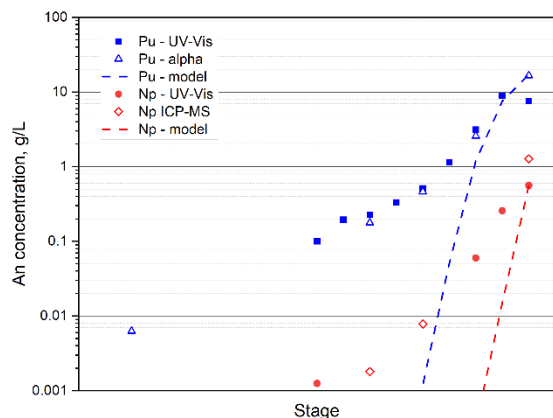


**Fig. 1.** Concentration profiles of the actinides (An) Pu(III) and Np(V) in a bank of mixer-settlers used for stripping during a solvent extraction run. UV-Vis determinations (solid squares and circles, respectively) are compared to predictions of a modified SEPHIS model (dashed lines), Pu concentrations measured by alpha spectroscopy (open triangles), and Np concentrations measured by ICP-MS (open diamonds).

Raman spectroscopy is sensitive to hydroxylammonium (HA) nitrate and nitric acid (see

Fig. 2). The O–H stretching region was used to determine the concentration of  $\text{H}_3\text{O}^+$  in solution and is also sensitive to the concentration of HA and nitrate. The responses at  $1,006\text{ cm}^{-1}$  and  $1,047\text{ cm}^{-1}$  were used to quantify HA and nitrate ions respectively. Thus, the quantification of these analytes at concentrations utilized during the solvent extraction was tested. PLSR models were developed and used for the accurate quantification of HAN at concentrations  $> 0.1\text{ M}$ . It was challenging to measure HAN in process samples due to the detection limits of our current set-up. We are currently exploring techniques, such as UV resonance Raman spectroscopy<sup>13</sup>, which will improve our detection limits such that HAN concentrations, relevant to the solvent extraction process, will be quantifiable.

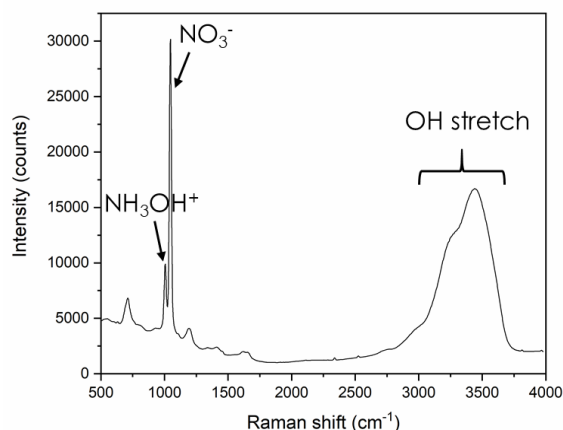


**Fig. 2.** Raman spectrum of 2.8 M hydroxyl ammonium nitrate (HAN). The peak at  $1,047\text{ cm}^{-1}$  is attributed to the nitrate symmetric stretching mode. The peak at  $1,006\text{ cm}^{-1}$  is attributed to hydroxylammonium ion. And the broad band between  $2,700$  and  $3,800\text{ cm}^{-1}$  is attributed to the O–H stretching region.

#### IV. PLUTONIUM ANION EXCHANGE (AXPu)

The goal of each plutonium anion exchange (AXPu) run is to purify  $^{238}\text{Pu}$  product by removing phosphate, thorium, fission products, and most of the neptunium. The actinides are converted to anionic complexes in strong nitric acid, loaded onto an anion exchange column, then eluted with lower-concentration acid. The development and use of a tool that can convert convoluted absorbance spectra into process data useful for system control, in real-time, would improve the efficiency and of anion exchange column runs. For example, it could advise technicians when to make processing decisions associated with redirecting column effluent to specific collection tanks. Key analysis points include the adjustment of Pu in the feed to Pu(IV), identification of Pu(VI) in the effluent, identification of Np(V) and Np(IV) in the effluent, and identification of an appropriate time to collect  $^{238}\text{Pu}$

product. The cut for  $^{238}\text{Pu}$  product is primarily based on two parameters: (1) maximize the yield of purified  $^{238}\text{Pu}$  per run and (2) minimize the concentration of Np in the product toward the goal of meeting the specification of <0.5 wt%.

UV-Vis spectroscopy was used to monitor for Pu(III), Pu(IV), Pu(VI), Np(IV), Np(V), and nitric acid in the effluent during AXPu column runs. Actinides have unique spectral signatures that are sensitive to oxidation state, complexation, ionic strength, and temperature. However, portions of each signature overlap with other species (see Fig. 3).

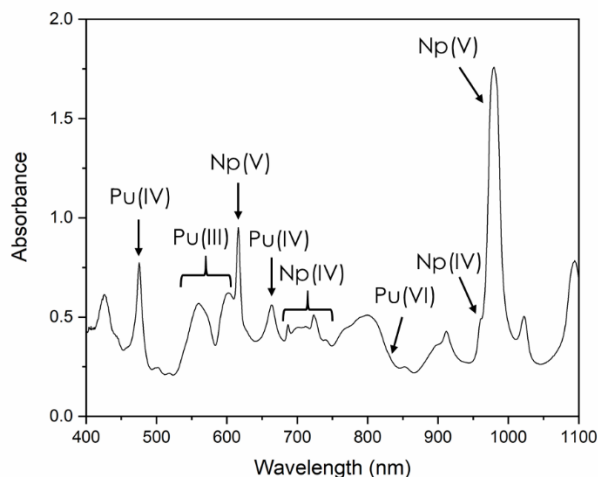


**Fig. 3.** Example effluent absorbance spectrum acquired during an AXPu column run. A subset of major peaks from each of the Np and Pu species are denoted.

Arguably the most important decision is the optimal point to start collecting Pu product. Determining the appropriate time to collect the product is challenging for several reasons: (1) Np and Pu coexist in solution and absorption bands significantly overlap, (2) high concentrations of actinides fall outside dynamic range of instrumentation, and (3) building effective training sets will be challenging because of complex redox behavior.<sup>11</sup> UV-Vis data was collected throughout each process run on the eluent using a 0.5 cm process cell, and the concentration of each analyte was approximated using a univariate (Beer–Lambert) approach. This approach failed to distinguish between several species with confounding peaks (e.g., Pu(IV) and Np(IV)). These data are not shown here. Multivariate approaches were tested on historical AXPu data and assessed to determine whether such an approach would provide a functional tool that meets the desired requirements of the  $^{238}\text{Pu}$  supply program. Historical data from AXPu anion exchange column runs were analyzed with multivariate regression approaches to develop predictive models.

A subset of spectra, with absorption bands that were relatively free from significant overlap, were deconvoluted to determine the concentration of Np and Pu in their respective valences. The concentrations were approximated using the Beer–Lambert law and respective extinction coefficients from the literature.<sup>11,14</sup> PLSR models were built using this subset of data as a set of calibration “standards.” Each figure of merit used to evaluate the quality of the regression models suggested that the species were adequately modeled. This model was used to predict the concentrations of Pu(III), Pu(IV), Pu(VI), Np(IV), and Np(V) in the effluent during the dilute nitric acid eluent in several column runs. Predicted Np and Pu concentrations were compared with grab samples analyzed with ICP-MS by analytical and were in good agreement. In addition, the predictive PLSR model was able to estimate concentration profiles that were consistent with each of the three AXPu column runs. Although the concentrations generated using this approach were not independently quantitative, the trends in the predictions were consistent with the spectra and clearly differentiated between the Np and Pu elution fronts. These results suggest that historical data combined with multivariate approaches may be useful for informing processing decisions. Raman spectroscopy will be used to improve the predictions of nitric acid concentration.

Raman measurements were collected in transmission mode during the AXPu column runs to predict acid concentration in the effluent. When the wavelength of scattered light coincides with the absorption spectrum of an actinide species in solution, a phenomenon known as self-absorption likely occurs. When scattered Raman signal coincides with a samples absorption wavelength the scattered light is absorbed and changes the signal-to-noise ratio (i.e., decreases the Raman signal intensity). This effect was evident during the elution of the Np and Pu fronts where the Raman signal intensity was completely lost. Future experiments will use a process probe with a short focal length to minimize the impact of the translucent solutions on Raman signal intensity. Acid profiles will be quantifiable during the entire column run by combining Raman and UV-Vis data.

Building calibration sets with traditional approaches that span the set of conditions found in AXPu column runs will be incredibly challenging. Experimental design will help reduce the number of calibration standards required to model this complex factor space.<sup>6</sup> Standards will be generated using electrochemistry and measured using spectroelectrochemical methods.<sup>14,15</sup> The overall range of solution conditions found in the anion exchange runs will likely be divided into subregions that are matched to local models. This will improve the quantification of analytes in the effluent that are present at concentrations that vary over several orders of magnitude.

## V. CONCLUSIONS

Optical spectroscopy was performed remotely on processing samples within a shielded hot cell environment. Experimental design can be used to generate sets of calibration standards that provide more information for multivariate modeling from fewer training samples. Remote characterization capabilities are expected to decrease the time required to characterize processing streams. Quantitative, real-time measurements will allow for rapid process information feedback and operational benefits that help the  $^{238}\text{Pu}$  supply program meet the production goals of NASA.

## ACKNOWLEDGMENTS

Funding for this program was provided by the Science Mission Directorate of the National Aeronautics and Space Administration and administered by the US Department of Energy, Office of Nuclear Energy, under contract DEAC05-00OR22725. This work used resources at the High Flux Isotope Reactor, a Department of Energy Office of Science User Facility operated by Oak Ridge National Laboratory.

The authors wish to thank Nonreactor Nuclear Facilities Division technicians for assistance with hot cell operations and Chris Wightman for ICP-MS data.

## REFERENCES

1. DePaoli, D. W.; Benker, D. E.; Delmau, L. H.; Collins, E. D.; Wham, R. M. "Progress in Chemical Processing for Production of Plutonium-238 from Irradiated Neptunium Oxide Cermet Targets," *ANS NETS* (2018).
2. Assirelli, M.; Xu, W.; Chem, W. "Reactor Kinetics Studies via Process Raman Spectroscopy, Multivariate Chemometrics, and Kinetics Modeling," *Org. Process Res. Dev.* **15**, 610–621 (2011). DOI:10.1002/jrs.4886
3. Beebe, K. R.; Pell, R. J.; Seasholtz, M. B. *Chemometrics: A Practical Guide*. John Wiley and Sons: New York (1998).
4. Faber, N. M. "A Closer Look at the Bias-Variance Trade-Off in Multivariate Calibration," *J. Chemometr.* **13**, 185–192 (1999). DOI:10.1002/(SICI)1099-128X(199903/04)13:2,185::AID-CEM538.3.0.CO;2-N.
5. Green, R. L.; Kalivas, J. H. "Graphical Diagnostics for Regression Model Determination with Consideration of the Bias/Variance Trade-Off," *Chemom. Intell. Lab. Syst.* **60**, 173–188 (2002). DOI:10.1016/S0169-7439(01)00194-0.
6. Eriksson, L. Johansson, E.; Kettaneh-Wold, N. Wikstrom, C.; Wold, S. *Design of Experiments: Principles and Applications*, pp. 217–230, 3rd ed. Umetrics, Umea, Sweden (2008).
7. Felker, L. K.; Benker, D. E.; Chatten, F. R.; Stacy, R. G. "Separation of Americium, Curium, and Plutonium from Irradiated Targets." *Sep. Sci. Technol.* **30**, 1769–1778 (1995). DOI:10.1080/01496399508010375.
7. McFarlane, J.; DePaoli, D. W.; Mattus, C. H. "Reaction Rate and Prediction of Thermal Instability During Aluminum Alloy 6061 Dissolution," *Sep. Sci. Technol.* **53**, 1894–1905 (2018). DOI:10.1080/01496395.2017.1377245.
8. Casella, A. J.; Levitskaia, T. G.; Peterson, J. M.; Bryan, S. M. "Water O–H Stretching Raman Signature for Strong Acid Monitoring via Multivariate Analysis," *Anal. Chem.* **85**, 4120–4128, (2013). DOI:10.1021/ac4001628.
9. Johnston, C. T.; Agnew, S. F.; Schoonover, J. R.; Kenney, J. W.; Page, B.; Osborn, J.; Corbin, R. "Raman Study of Aluminum Speciation in Simulated Alkaline Nuclear Waste," *Environ. Sci. Technol.* **36**, 2451–2458, (2002). DOI:10.1021/es011226k.
10. Ferguson, D. E.; Brown, K. B.; Wymer, R. G.; Blanco, R. E.; Whatley, M. E.; Goeller, H. E.; Brooksbank, R. E. *Chemical Technology Division Annual Progress Report*. ORNL-4272; Oak Ridge National Laboratory: Oak Ridge, TN (1968).
11. Lee, M. H.; Park, Y. J.; Kim, W. H. "Absorption Spectroscopic Properties for Pu(III, IV and VI) in Nitric and Hydrochloric Acid Media," *J. Radioanal. Nucl. Chem.* **273**, 375–382 (2007). DOI:10.1007/s10967-007-6848-1.
12. Mitchell, A. D. "Use of the SEPHIS-MOD4 Program for Modeling the Purex and Thorex Solvent Extraction Processes," *Sep. Sci. Technol.* **16**, 1299–1319 (1981). DOI:10.1080/01496398108058303.
13. Ianoul, A.; Coleman, T.; Asher, S. A. "UV Resonance Raman Spectroscopic Detection of Nitrate and Nitrite in Wastewater Treatment Processes," *Anal. Chem.* **74**, 1458–1461 (2002). DOI:10.1021/ac010863q
14. Chatterjee, S.; Bryan, S. A.; Casella, A. J.; Peterson, J. A.; Levitskaia, T. G. "Mechanisms of Neptunium Redox Reactions in Nitric Acid Solutions," *Inorg. Chem. Front.* **4**, 581–594 (2017). DOI:10.1039/C6QI00550K.
15. Branch, S. D.; Lines, A. M.; Lynch, J.; Bello, J. M.; Heineman, W. R.; Bryan, S. A. "Optically Transparent Thin-Film Electrode Chip for Spectroelectrochemical Sensing," *Anal. Chem.* **89**, 7324–7332 (2017). DOI: 10.1021/acs.analchem.7b00258.

**STIRLING CONVERTOR EXTENDED TESTING IN SUPPORT OF DYNAMIC RPS MATURATION**

Nicholas A. Schifer<sup>1</sup> and Daniel D. Goodell<sup>1</sup>

<sup>1</sup>NASA Glenn Research Center, Cleveland, Ohio, 44135, 216-433-5824, [nicholas.a.schifer@nasa.gov](mailto:nicholas.a.schifer@nasa.gov)

The Thermal Energy Conversion branch at the NASA Glenn Research Center (GRC) has been developing free-piston Stirling conversion technology for space electrical power for decades. Free-piston Stirling conversion technology is attractive for Radioisotope Power Systems (RPS) because it offers thermal-to-electric conversion efficiency of greater than 20 percent at the system level, which is three to four times greater than state-of-the-art thermoelectric conversion and greater end-of-life performance. Previous Stirling RPS development efforts include two flight projects; the 110 W Stirling Radioisotope Generator (SRG110) project and the Advanced Stirling Radioisotope Generator (ASRG) project. The reformulated Dynamic Radioisotope Power Systems (DRPS) project seeks to mature dynamic power conversion technology to flight readiness. Convertors currently operating at GRC represent two manufacturers and their unique convertor designs, each the result of the two flight projects. Under the SRG110 project from 2001 to 2006, the Infinia Corporation, now known as American Superconductor (AMSC), produced 16 Technology Demonstration Convertors (TDC) which utilize flexure bearings to enable wear-free operation. Under the ASRG project from 2007-2013, Sunpower Incorporated developed and delivered numerous prototypes and engineering models, which utilized gas bearings to enable wear-free operation. Continued extended operation of these highly valued assets at NASA GRC demonstrates long-life designs for future potential science and exploration missions.

**I. STIRLING CONVERTOR TESTING AT GRC**

A total of 9 flexure-bearing convertors and 39 gas-bearing convertors have been operated at GRC in support of dynamic energy conversion for a radioisotope power system, with a cumulative runtime exceeding 1,100,000 hours (125.5 years). A limited number of convertors continue to operate at GRC due to the limited number of test stations, as well as, the need to prepare new stations for testing of the next generation convertors. Over the years, some convertors have failed to maintain performance requirements and have been disassembled and inspected for non-obvious failure mechanisms and develop improvements in the technology. Other units are used for tactical testing based on need. GRC is currently maintaining 24/7 operation of 4 flexure bearing convertors and 4 gas bearing convertors, for which the cumulative runtime exceeds 454,500 hours (51.8 years). A summary of the ongoing tests is shown in Table I. The Technology Demonstration Convertors (TDCs) and the

SRG110 Engineering Unit Stirling Convertor Assembly (SES) are flexure-bearing convertors designed by Infinia, while the Advanced Stirling Convertors (ASCs) are gas-bearing convertors designed by Sunpower. Both of these companies are also developing new and improved versions of these convertors under NASA contracts, managed by the DRPS project, with an emphasis on robustness and reliability, while relaxing efficiency requirements. The Sunpower Robust Stirling Convertor (SRSC) and AMSC’s Flexure Isotope Stirling Convertor (FISC) will be delivered to NASA GRC this year for environmental testing and extended operation to verify reliability.

**Table I. Summary of on-going Stirling convertor operation at NASA GRC as of February 2020.**

Convertors	Power & Temp (We, Hot/Cold °C)	Start	Runtime (hours / years)
TDC #13	65, 650/80	Jun 2003	122,300 / 13.9
TDC #15	62, 645/80	Mar 2005	116,200 / 13.2
TDC #16	59, 645/80	Mar 2005	116,200 / 13.2
SES #2	62, 640/75	Apr 2017	15,000 / 1.7
ASC-0 #3	76, 650/90	Aug 2007	87,500 / 9.9
ASC-L	75, 750/28	Jul 2011	50,200 / 5.7
ASC-E3 #4	81, 760/38	Aug 2013	41,400 / 4.7
ASC-E3 #9	75, 760/38	Feb 2016	27,500 / 3.1

**I.A. GRC Testing Role**

The key roles of testing at GRC are to provide government verification and validation of convertor performance to design specifications and to build a performance database to support life and reliability estimates. These roles have traditionally been fulfilled through 24/7 unattended operation of convertors and testing performed in relevant environments aimed to simulate the expected mission lifecycle a Stirling convertor would experience in a radioisotope power system. All testing performed at GRC is electrically heated instead of using heat from a general purpose heat source (GPHS), as would be the case in a space application.

Unattended 24/7 operation is enabled through dedicated test racks which provide software with user controls, data acquisition, automated fault detection and shutdown capability, and hard-wired protections in case the automated functions fail. These systems are continuously being improved to provide better data and increased protection to the hardware and data retention. One example of improvement is the increase in quantity and rate of data archiving. In the past, a database kept a 72 hour buffer of data collected at ½ Hz, which would

have to be manually downloaded and saved if there were a desire to keep the data long term. The current LabVIEW data acquisition software samples thermocouples at a 90 Hz rate and dynamic signals, such as alternator voltage and current and piston position, at a 7 kHz rate. All parameters and calculations are averaged every 2-seconds to create a data point, which is stored in the local database and referred to as 2-second data. The database stores a buffer of 96 hours of 2-second data, which is automatically downloaded and saved daily to a remote, backed up data center. This data is also reviewed regularly through automated plotting routines that enable engineers to quickly assess the performance of the convertor and any factors contributing to a change in the performance. In addition, the dynamic signals sampled at a 7 kHz rate are also automatically saved to the data center, and can be used to help investigate data further as needed.

The required life time of a radioisotope power system is 17 years, consisting of Earth ground operation for up to three years prior to launch, launch, optional spin stabilization, cruise to an exploration destination, and optional entry, decent, and landing onto a planetary surface. GRC tests simulate mission lifecycle conditions in a representative sequence using relevant laboratory environments, and when possible through relevant flight-like interfaces and convertor controllers. The harshest conditions for the convertor, launch and landing, are simulated through vibration testing on a shaker table and static acceleration testing in a centrifuge, respectively.

### **I.B. Environmental Testing and Extended Operation**

At this time, eight Stirling convertors remain in extended operation at GRC based on available facilities and project priorities. Table II provides some information for those units, including hermeticity and exposure to the random vibration and static acceleration environments. Figures 1 and 2 show plots of the performance of these convertors throughout their entire operational history at GRC. Adjustments have been made to maintain steady operating conditions. In some cases, these convertors are used to conduct short term tactical tests based on project need, which causes short term power variation seen in the performance plots. The four Infinia convertors (TDCs & SES) are non-hermetic units that require periodic pressure adjustments, which also contributes to the variation observable in the plots. The four Sunpower ASC units are hermetic and do not require such adjustments. It is important to keep in mind that these convertors represent two different sets of project requirements and represent different stages in the developmental history of the units for each manufacturer. Convertors found in Tables I and II are listed in order of oldest to newest in the production sequence.

The following sections for each convertor are not intended to be an exhaustive list of tests each convertor has undergone, but rather to highlight the significance of key tests and unit performance. Of particular note are units that have demonstrated performance after exposure to the harsh environments of vibration and static acceleration, which is critical to demonstrating robustness and reliability.

**Table II. Summary of on-going Stirling convertor hermeticity, vibration test, and centrifuge test status.**

<b>Convertors</b>	<b>Hermetic</b>	<b>Random Vibration</b>	<b>Static Acceleration</b>
TDC #13	No	No	No
TDC #15	No	No	No
TDC #16	No	No	No
SES #2	No	Flight Acceptance	5 g axial 20 g radial
ASC-0 #3	Yes	Flight Acceptance	No
ASC-L	Yes	Flight Acceptance	No
ASC-E3 #4	Yes	Flight Acceptance	No
ASC-E3 #9	Yes	No	No

#### *I.B.1. TDC #13*

TDC #13 is the world record holder for longest-running heat engine with 122,300 hours (13.9 years) of operation. The TDC was designed to produce approximately 65 W<sub>e</sub> at operating temperatures of 650 °C on the hot-end and 80 °C on the cold-end. This unit was developed under the Infinia Quality Assurance program and was, therefore, considered a flight prototype (Ref. 1). This unit has not been exposed to vibration or static acceleration environments and had been paired with TDC #14 in a dual-opposed configuration through 105,616 hours of operation. At that time, despite TDC #13 & #14 not showing any unexplainable degradation in performance, a programmatic decision was made to disassemble TDC #14 and inspect the internal components for internal signs of degradation. Prior to stopping operation of TDC #14, an effort was made to adjust the operating conditions as closely as possible to early operation for a direct performance comparison. During this effort, it was discovered that the coolant passages of the cold end cooling jackets had formed deposits on the internal surfaces of the heat exchanger, believed to come from the crystallization of corrosion inhibitors in Ethylene Glycol. This was a significant finding because the cold end temperature is a calculation based on the coolant temperature, flowrate, and heat transfer properties; rather than a direct measurement. These deposits fouled the heat transfer surfaces and increased the thermal resistance, effectively elevating the cold end temperature and degrading the heat exchanger performance without any change in the calculated value for cold end temperature. A borescope was used to inspect these surfaces and CLR® was used to remove the deposits. After cleaning these surfaces and matching early

test conditions as closely as possible (noted in Fig. 1 by notation 3), performance of TDC #13 & #14 both matched early performance data within the measurement uncertainty, demonstrating the long-life design. Since disassembly of TDC #14, TDC #13 has continued to steadily operate with no observable degradation in performance, as can be seen in the long term trends of Figure 1. The temporary drops in power output, noted by notations 1, 2, and 4, are explained by intentional changes in the set point.

**I.B.2. TDC #15 & #16**

TDC #15 & #16 continue to operate as a dual-opposed pair and follow close behind the leader with 116,200 hours (13.2 years) of operation. These units were also developed under the Infinia Quality Assurance program and are identical to TDCs #13 & #14. For this reason, they also were susceptible to the fouling issue on the cold end heat exchanger and underwent borescope inspection and CLR® cleaning at roughly 105,000 hours of operation. A corresponding increase in performance can be seen at this time in Fig 1 as notation 8. Similar to the previous TDCs, these units were not exposed to the vibration or static acceleration environments. A low power operating point was used prior to having laser weld flanges sealed at around 5,000 hours (shown as notation 5). A slight decrease in performance from 5,000 to 15,000 hours was previously attributed to variations in cold-end temperature control, yet different from the fouling issue previously described (Ref. 1). The temporary changes in power output, noted by notations 6 and 7 are explained by intentional changes in the set point. Since maintaining the operating point established around 20,000 hours, no unexplainable degradation in performance has been observed on TDC 15 & 16.

**I.B.3. SES #2**

SES #2 is an engineering-unit version of the TDC that was in process when the SRG110 project ended. It contains design elements tailored for spaceflight application, including a cold side adapter flange and heat collector. SES #2 was placed into storage in 2006 and put into service in 2016 due to a renewed interest in flexure-based convertors. This unit was exposed to launch acceptance and launch simulation level vibration tests (10.2 g<sub>rms</sub>) in May 2017. After operating approximately 1,800 hours, a performance mapping test was completed in March 2018. After accumulating 2,600 more hours of operation, a static acceleration test was completed in April 2018, exposing the convertor to 5 g<sub>rms</sub> in two axial orientations and 20 g<sub>rms</sub> in two lateral orientations. At the time this convertor was fabricated, there was no specification that required this convertor be designed to endure these static acceleration conditions. Based on analysis completed prior to static acceleration testing, it was expected that the piston would begin to rub on the

cylinder at 5 g<sub>rms</sub> and the displacer rod would rub at 19 g<sub>rms</sub>. A risk in loss of performance was knowingly accepted prior to testing, as there was value in assessing the robustness against conditions that were expected to cause contact between moving and stationary components. A comparison of pre and post static acceleration test results indicates a permanent power loss of 2.5 W<sub>e</sub> due to the exposure, likely the result of slight increases in the piston seal during lateral rubbing. SES #2 has now accumulated 15,000 hours (1.7 years) of operation and maintains 62 W<sub>e</sub> at operating temperatures of 640 °C hot-end and 75 °C cold end. No further degradation in performance has been observed, as shown in Figure 1, demonstrating a robust design.

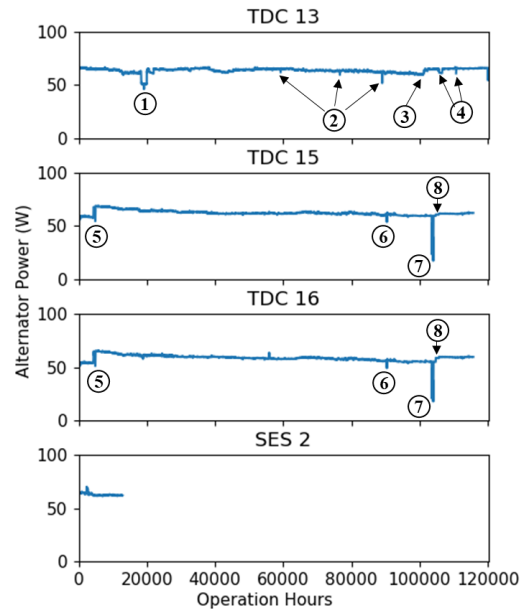


**Fig. 1.** Performance plots of on-going flexure-bearing Stirling convertor tests.

**I.B.4. ASC-0 #3**

ASC-0 #3 represents the earliest ASC design on test and is on 24/7 extended operation at GRC. It is the longest running ASC with more than 87,500 hours (9.9 years) of operation. Designed to produce approximately 75 W<sub>e</sub> at operating temperatures of 650 °C on the hot-end and 90 °C on the cold-end. This unit was subjected to flight acceptance vibration levels (8.7 g<sub>rms</sub>) at approximately 7,500 hours of operation in three orthogonal axes. The unit is hermetically sealed but has not been exposed to static acceleration conditions. No degradation in performance has been observed over the long-term operation of ASC-0 #3, as shown in Figure 2. Performance has been especially stable since 25,000 hours, after improvements were made to the test rack power path connections.

### I.B.5. ASC-L

ASC-L is the second longest running ASC with 50,200 hours (5.7 years) of operation. However, the unit is the longest running convertor under the control of a fault-tolerant controller. Designed to operate at a nominal hot end temperature of 850 °C and a cold end temperature range of 47 to 147 °C, a new lower temperature operating condition of 74  $W_e$  at operating temperatures of 750 °C hot-end and 25 °C cold-end was established near 4,000 hours (notation 9 in Fig. 2) to extend heat source life and match desired generator hot-end temperatures derived from the ASRG flight project. The Single Convertor Controller (SCC) is an engineering model controller designed by John Hopkins University/Applied Physics Laboratory. The SCC was used to control the ASC-L during flight acceptance-level vibration testing within the first 500 hours of operation at GRC. ASC-L is hermetically sealed but has not been exposed to static acceleration testing. The integrated testing of the SCC and ASC-L has including SCC fault tolerance and mapping of performance over a range of expected operating conditions, including variations in cold-end temperature and piston amplitude (Ref. 2). ASC-L has demonstrated steady performance when operating conditions have been maintained, and has not shown any signs of degraded performance, as shown in Figure 2.

### I.B.6. ASC-E3 #4

ASC-E3 #4 represents the longest running third generation engineering unit from Sunpower with more than 41,400 hours (4.7 years) of operation. The ASC-E3s were built using the flight design with the intent to pathfind the fabrication process that was to be used for the ASRG flight units. While capable of operating at 850 °C on the hot end, the ASC-E3 units were designed to produce approximately 80  $W_e$  at operating temperatures of 760 °C on the hot end and 38 °C on the cold end. ASC-E3 #4 is hermetically sealed and was exposed to flight acceptance vibration levels at 2,200 hours before continuing extended operating. Several intentional setpoint changes were made during the first 10,000 hours of operation for characterization testing (notation 10 in Fig. 2). A slight test condition change was made when ASC-E3 #4 was paired with E3 #9 at 25,000 hours (notation 11 in Fig 2), and a characterization test performed near 35,000 hours (notation 12 in Fig. 2). Performance of E3 #4 has demonstrated steady performance when conditions have been maintained.

### I.B.9. ASC-E3 #9

ASC-E3 #9 was the last ASC delivered to GRC and incorporates all design improvements learned from operation of earlier units. This unit has accumulated more than 27,500 hours (3.1 years) of operation. Because of programmatic direction changes at the time ASC-E3 #9 was delivered, this unit has not been exposed to vibration

or static acceleration tests. The temporary drop in power output, noted by notation 13, is explained by intentional changes in the set point for characterization tests. A slight test condition change was made when the convertor was paired with E3 #4 at 10,000 hours (notation 11 in Fig. 2), and a characterization test performed near 18,000 hours (notation 12 in Fig. 2). ASC-E3 #9 has demonstrated steady performance when conditions have been maintained.

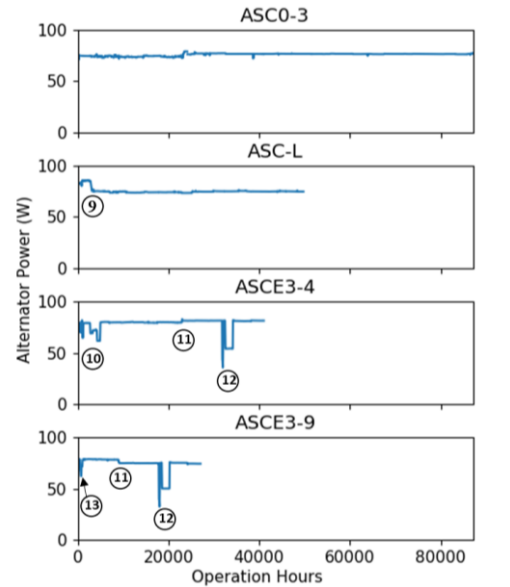


**Fig. 2.** Performance plots of on-going gas-bearing Stirling convertor tests.

## II. CONCLUSIONS

GRC has established facilities for environmental testing and reliable long-term unattended operation of free-piston Stirling convertors to demonstrate steady performance and long life designs. Extended operation of relevant flexure-bearing and gas-bearing Stirling designs enables development of the life and reliability data needed for future missions. Thus far, the longest running flexure-bearing machine is approaching 14 years while the longest running gas-bearing machine is approaching 10 years.

## REFERENCES

1. N. SCHIFER, S. ORITI, "Summary of Stirling Convertor Testing at NASA Glenn Research Center in Support of Stirling Radioisotope Power System Development," NETS 2013, Albuquerque, New Mexico, Feb 25-28, 2013.
2. G. DUGALA, M. BELL, S. ORITI, M. FRAEMAN, D. FRANKFORD, and D. DUVEN, "Small Radioisotope Power System Testing at NASA Glenn Research Center," 11th IECEC, San Jose, California, July 14-17, 2013.

## DEVELOPMENT OF A NOVEL MINIATURE POWER CONVERTER FOR LOW-POWER RADIOISOTOPE HEAT SOURCES: NUMERICAL AND EXPERIMENTAL RESULTS

Francisco I. Valentin<sup>1</sup>, Gregory Daines<sup>1</sup>, and Mark Zagarola<sup>1</sup>

<sup>1</sup>Creare, Hanover, NH, 03748, 603-643-3800

Primary Author Contact Information: 603-640-2354 and [fiv@creare.com](mailto:fiv@creare.com)

*Creare is developing a miniature, low power, free-piston energy conversion system. Our converter is designed to transform thermal energy from Radioisotope Heater Units into on-demand electricity essential to space exploration probes, unmanned surface rovers, small landers, small satellites, and similar small-scale systems operating in darkness. We have achieved a simple system design with a single moving part, requiring no recuperators, no regenerators, or valves. Our converter technology promises a high-efficiency system in an extremely compact enclosure. This work describes preliminary numerical and experimental work. We fabricated a laboratory-scale prototype and acquired experimental data at prototypical temperatures to validate our performance models. Our numerical model was able to accurately predict converter losses. These results have been used to guide subsequent converter design modifications.*

### I. BACKGROUND

Producing electric power for space applications is challenging. Although short-term missions can use batteries or fuel cells, these techniques are impractical for durations longer than about one month. Photovoltaic (PV) systems are typically used for long-term missions near Earth, where solar radiation is significant. However, PVs become less attractive as the distance from the sun increases, and they are ineffective in sun shadowed environments and in atmospheres that limit solar penetration. For these types of missions, thermal-to-electric converters can produce electric power from nuclear heat sources. Conventional converter technologies include thermoelectric, Stirling, Brayton, thermophotovoltaic (TPV), and Alkali Metal Thermal to Electric Conversion (AMTEC) (Ref. 1 - Ref. 4). The currently designated heat source for long-term missions with power levels less than about 10 kWe is radioisotope (Pu-238) decay. The scarcity and high cost of Pu-238 leads one to pursue higher conversion efficiency. Dynamic conversion can offer up to 40% thermal to electric efficiency, compared to the 6% efficiency provided by thermoelectric conversion. (Ref. 5)

Although Stirling converters are a fairly mature option for future space power systems, certain future missions require miniature converters (1-10 We) to provide the vital electricity to maintain operations while

in darkness (Ref. 6). Examples of such applications include probes, landers, rovers, or communication repeaters. NASA's Glenn Research Center (GRC) Thermal Energy Conversion Branch is developing a Stirling converter low power dynamic radioisotope power system (RPS). This system is being designed to accept heat from Light Weight Radioisotope Heater Units (LWRHUs) and fractional General Purpose Heat Sources (GPHS), and generate at least 1 We, with at least 12% system efficiency. The design system mass is 3 kg (Ref. 6). The need for further converter system miniaturization while maintaining requirements of high efficiency, for the aforementioned reasons, opens the doors for innovative dynamic converter concepts at these scales.

### II. DESCRIPTION OF WORK

Creare is developing a Modified Stirling free-piston Converter (MSC) that promises high-efficiency, and simple to manufacture system in an extremely compact enclosure. The primary challenge of the proposed project is the design and fabrication of high-efficiency converters of extremely small size. For miniaturized systems, defining the fractional contribution of frictional losses, leakage, parasitic heat losses, and potential dead volumes, becomes increasingly important to a system's power density as its design volume is reduced.

This work describes our preliminary design and testing efforts. An unsteady model was developed to predict the integral system performance and to guide the design of each system component. We designed, fabricated, and assembled a laboratory-scale prototype to acquire preliminary performance data and validate our performance model.

#### II.A. Proposed System and Thermodynamic Cycle

The Creare MSC generates power through the closed loop compression and expansion of Xenon—a high molecular mass, low-thermal conductivity gas. A linear alternator and power-conditioning electronics convert the piston's motion into continuous DC electricity with very low ripple. Gas flow is maintained through the generation of high and low pressure zones by a displacer. Our system's single moving part acts as both the compressor and a displacer, replacing hot gases in the hot-side heat exchanger (HX) with fresh cold gas during each cycle. Figure 1 presents a schematic of the proposed converter, outlining the primary system components. We predict a

thermal-to-electric conversion efficiency of approximately 20.0% using a 650°C heat source and with heat rejected at 27°C (approximately 30% of Carnot).

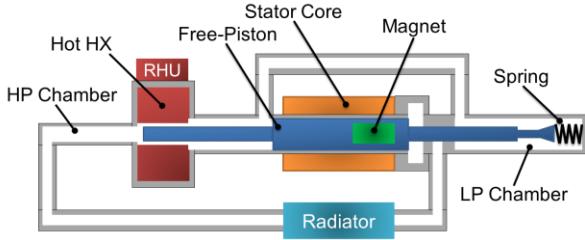


**Fig. 1.** SPOC System Schematic Diagram.

The MSC’s ideal thermodynamic cycle consists of three phases. First, the cold gases undergo isentropic compression up to the hot-side temperature. Second, the hot gases are expanded isothermally. Third, the hot gases are exhausted and replaced with fresh cold gas during isochoric heat rejection. In this manner, the ideal MSC thermodynamic cycle is similar to cutting the Stirling cycle in half using an isentropic compression, as best shown on the PV and TS diagrams shown in Fig. 2.

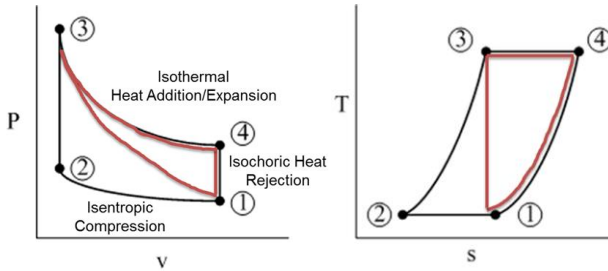


**Fig. 2.** Ideal MSC Cycle (Red) Compared to Ideal Stirling Cycle (Black).

### III. POWER CYCLE MODELING

To determine the predicted efficiency of our dynamic power converter, we constructed a transient-based model that captures key details of the system, including all inefficiency sources: non-ideal heat addition, pumping losses, leakage, heat losses, and friction; which result in deviations from the ideal cycle behavior. At the core of the model are two control volumes: one volume represents the gases within the hot HX and the other volume represents the gases inside of the cylinder (see Fig. 3). For each timestep, mass and energy balance equations are solved through an iterative process. Gas charges and temperatures are determined for each control volume to satisfy both energy and mass balance under the constraint that both control volumes share the same pressure. The calculated gas pressure is then used to determine the pressure force acting on the piston.

The piston’s change in momentum during each timestep is determined from a force balance which takes into account the spring force, pressure force, friction

force, and the total drag force (due to pumping losses and the electrical power output) acting on the piston. As an example, Fig. 4 shows the temperature and pressure of the gasses inside the cylinder volume one complete cycle.

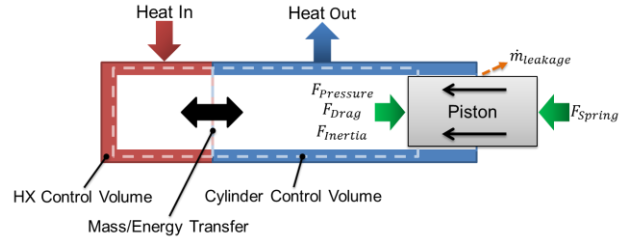


**Fig. 3.** Diagrammatic Representation of Thermodynamic Model

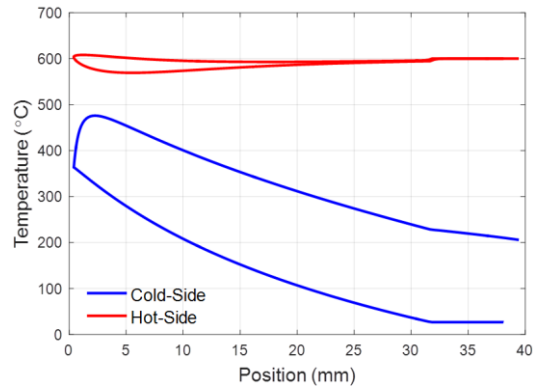


**Fig. 4.** Piston Temperature and Pressure as Functions of its Position Inside the Cylinder.

The predictive model includes and models the following sources of inefficiencies:

**Non-ideal heat input.** The heat source is always active, thus heat is continuously added to the working fluid even during the compression phase.

**Gas pressure leakage.** Because we do not plan to implement piston seals, gas leakage from the high-to-low side of the piston is inevitable.

**Frictional losses.** Tight clearances could also lead to increased viscous drag losses.

**Pumping losses.** To facilitate proper gas flow through our system our displacer pumps gas in and out of the cylinder, which results in parasitic pumping losses.

### IV. CONCEPTUAL DESIGN OF FLIGHT UNIT

Figure 5 shows a conceptual design of an MSC flight unit. Specifically, MSC employs hydrostatic bearings, which in combination with tight clearances between the piston and the cylinder’s inner walls (2.54 μm) provide the required fluid lubrication, and clearance seals. This guarantees long-life by eliminating piston wear and reducing internal gas leakage. High-performance multi-layered insulation (MLI) reduces heat leakage to the

environment. Our engine also operates at relatively low-speed speed ( $< 100$  Hz) to lessen engineering and fabrication challenges while maintaining competitive power density (estimated system mass of 80 g excluding power conversion and control electronics, tubes to or from the radiator, the radiator mass, and the fuel mass). Our predicted end-to-end thermal-to-electric conversion efficiency approximates 20% when using a  $650^{\circ}\text{C}$  heat source with heat rejected at  $27^{\circ}\text{C}$ . These estimates take into account insulation, stator, and power conditioning electronics efficiencies of 95%, 92%, and 95% respectively.

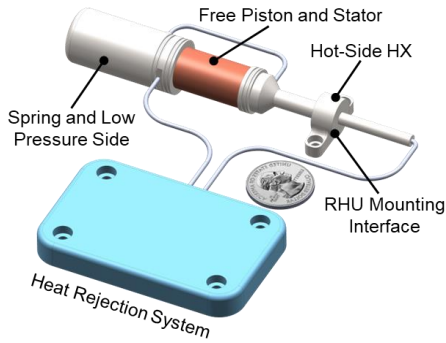


**Fig. 5.** Conceptual Design of MSC Flight Unit.

#### IV. EXPERIMENTAL SETUP

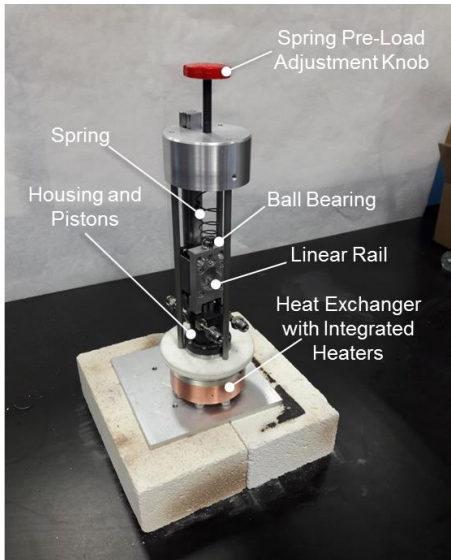


**Fig. 6.** Completed Phase I Prototype Converter Assembly

To validate our performance models we completed the design, fabrication and assembly of a preliminary prototype converter (Fig. 6). The prototype converter consists of a high-surface-area heater, a parallel-piston housing design, and a conical spring. A ball bearing-supported linear motion carriage is used to support the reciprocating assembly. For the laboratory prototype instead of the proposed gas bearing for the flight unit, we utilized ball bearings at the interface between the carriage

and the pistons to minimize side loads applied to the pistons by the motion carriage. The hot-side is thermally isolated from the rest of the system using a small-diameter, thin-walled stainless steel tube. Details of primary component dimensions are shown in Table 1.

**TABLE I.** Primary Converter Parameters.

Parameter	Value
Piston Diameter	6.35 mm
Piston Stroke	38.10 mm
Piston-Cylinder Diameter Clearance	$5.08 \mu\text{m}$
Spring Constant	462 N/m
Cycle Frequency	15 Hz
Compression Ratio	3
Hot HX Temperature	873 K
Hot HX Surface Area	$53 \text{ cm}^2$
Heat Rejection Temperature	300 K
Working Fluid	Argon
Charge Pressure	101.3 kPa

## V. RESULTS AND DISCUSSION

### V.A. Separate Effects Testing

We conducted separate effects tests on the individual components to assess how closely their performance matches the predicted performance in our model. This work documents two principal areas of interest: the frictional losses in the reciprocating assembly, and the frictional and pressure losses in the pistons.

#### V.A.1. Pressure Leakage

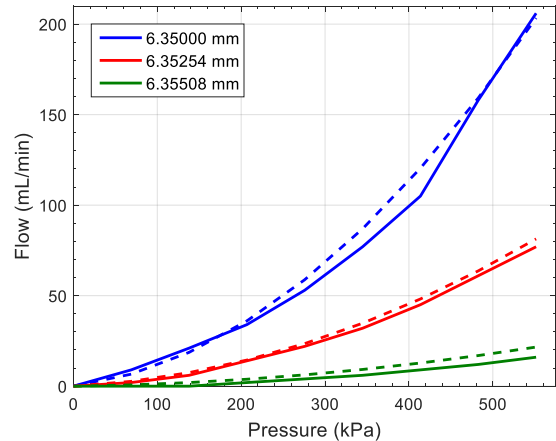


**Fig. 7.** Measured (Solid) vs. Calculated (Dashed) Leakage Flowrates for Various Piston Diameters. Assumed cylinder bore diameter of 6.36016 mm (0.2504").

To quantify the gas leakage and calibrate our model, we measured the leakage as a function of cylinder pressure for various piston diameters. Although our nominal piston diameter is 6.35000 mm (0.2500"), we could also fit 6.35254 mm (0.2501") and 6.35508 mm (0.2502") pistons into the cylinders. We measured the leakage flowrate vs. pressure up to 552 kPa for each

piston diameter, and then iterated on our leakage model to determine the actual bore diameter of the cylinders. Leakage through the piston clearance is calculated using the Darcy-Weisbach equation, in conjunction with a laminar friction factor ( $64/\text{Reynolds}$ ). We determined that using a true cylinder bore diameter of 6.36016 mm (0.2504") resulted in very good agreement between the measured and calculated leakage flowrates (Fig. 7).

#### V.A.2. Frictional Losses

The friction of the piston inside the cylinder was measured by determining what pressure was required to overcome friction and move the pistons located inside the cylinders. We could then estimate the frictional loss of the pistons based on the piston stroke and converter operating speed. The friction when using the 6.35000 mm (0.2500"), 6.35254 mm (0.2501"), and 6.35508 mm (0.2502") pistons resulted in 0.3 W, 0.5 W, and 7.5 W of frictional loss respectively. Because the friction increased substantially between the 6.35254 mm and 6.35508 mm pistons, we believe that the surface roughness of the cylinder bore results in asperities on the order of 2.54  $\mu\text{m}$  (0.0001") tall, causing substantial sliding friction when the radial gap is below 2.54  $\mu\text{m}$  (0.0001"). These frictional loss values were incorporated to further refine our performance model.

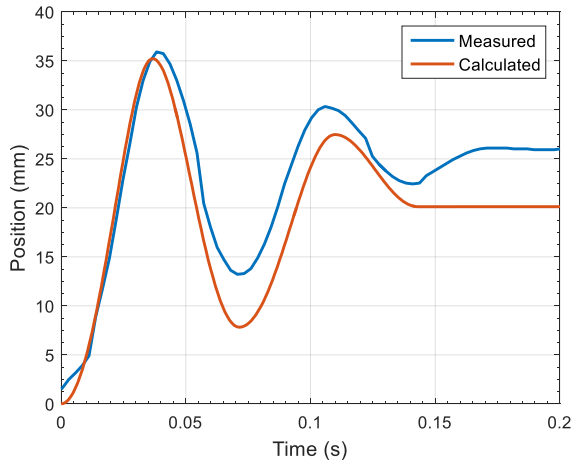


**Fig. 8.** Comparison of Measured and Calculated Oscillation Behavior

Furthermore, we captured the oscillatory behavior of the converter with hot-side temperatures up to 600°C. We processed high speed camera videos to determine the position vs. time behavior of the reciprocating assembly and frictional losses. Combining the known spring constant and spring deflection we calculated the spring's potential energy as a function of time. This was used to determine the decay of the internal energy of the system over time. The spring potential energy decayed by approximately 30% of the oscillation amplitude over each subsequent cycle, which would result in 1.5 W of frictional loss for our converter running at 15 Hz. The

oscillation decay died slower as more heat was added to the system suggesting that the temperature was resulting in useful work being done on the system. A comparison of our model's predicted oscillation behavior vs. the measured oscillation behavior at 600°C, incorporating the piston leakage and frictional losses (1.8 W total), is shown in Fig. 8.

## II. CONCLUSIONS

Creare is developing a Modified Stirling free-piston Converter. It is an extremely compact, high thermal-to-electric efficiency system, with target power output in the 1-5 W range. This work describes a preliminary laboratory-scale prototype developed to validate and further refine our performance model which will guide the design of subsequent full-scale prototype systems.

## ACKNOWLEDGMENTS

This work was completed under NASA contract 80NSSC19C0315. The support from NASA is gratefully acknowledged.

## REFERENCES

1. Kaszeta, R.W., "Developments in Radioisotope Thermophotovoltaic Power Systems," Presented at: TPV Conference & IEC Standards Workshop (International Conference on Solar Concentrators for the Generation of Electricity ICSC-5), Palm Desert, CA, 20 Nov 2008.
2. Mason, L. S., "Realistic Specific Power Expectations for Advanced Radioisotope Power Systems," 4th International Energy Conversion Engineering Conference and Exhibit (IECEC), Paper AIAA 2006-4193, San Diego, CA, 26–29 June 2006.
3. Shaltens, R. K., "Future Opportunities for Dynamic Power Systems for NASA Missions," NASA/TM 2007-214707, Aug 2007.
4. Oriti, S. M. and Wilson, S. D., "Dynamic Power Converter Development for Radioisotope Power Systems at NASA Glenn Research Center," 2018 International Energy Conversion Engineering Conference, AIAA Propulsion and Energy Forum, AIAA 2018-4498.
5. Wong, W. A., et al., "Advanced Stirling Converter (ASC) Technology Maturation," 13th International Energy Conversion Engineering Conference, AIAA Propulsion and Energy Forum, (AIAA 2015-3806), 2016.
6. Wilson, S., et al., "NASA Low Power Stirling Converter for Small Landers, Probes, and Rovers Operating in Darkness." Presented at: AIAA Propulsion and Energy (P&E) Forum and Exposition, International Energy Conversion and Engineering Conference (IECEC), Cincinnati, OH, 9 July 2018.

## BIPOLAR COUPLE ASSEMBLED MODULE (BCAM) DESIGN FOR SCALABLE AND RUGGED ARCHITECTURE FOR TEG APPLICATIONS

Rama Venkatasubramanian<sup>#</sup>, Jonathan Pierce, Meiyong Himmtann and Geza Dezsi

*The Johns Hopkins University Applied Physics Laboratory (JHU-APL), Laurel, MD*

<sup>#</sup> [rama.venkatasubramanian@jhuapl.edu](mailto:rama.venkatasubramanian@jhuapl.edu)

*While considerable research in thermoelectric materials, particularly in enhancing the figure of merit (ZT), is progressing in the US and in other countries, the focus in transitioning the ZT of the materials to p-n couple efficiency (in cooling or power generation) has been limited. The research and success in the scalability of device performance from p-n couples to modules is even more limited. In contrast, most of the DARPA funded R&D at JHU-APL has emphasized both materials research for ZT advancement and translating the materials progress to module results. We will describe our unique approach to this endeavor with our Bipolar Couple Assembled Module (BCAM) technology and describe the advantages of the BCAM architecture, based on thermo-mechanical modeling in stress reduction. This has enabled us to build and test scalable modules in a broad spectrum of materials from thin-film to bulk materials and also achieve robust data under extreme conditions of test. We believe the BCAM architecture is essential to scale-up and ruggedization and could lead to successful RTG designs in the future. The relevancy of the BCAM modeling to SiGe modules for RTG missions are discussed in some detail.*

### I. Introduction

Outer-planetary missions rely on radioisotope heat to electric conversion as the sunlight is too weak to provide power for scientific missions. Radioisotope Thermoelectric Generators (RTGs) offer modest heat-to-electric conversion efficiency, but have no moving parts and offer the reliability needed for decade or multi-decade long flight-plus-scientific observation missions. A major challenge in reducing the cost and timeline of fabrication of RTGs is the ability to fabricate TEG converters in a modular fashion as well as using standard semiconductor device fabrication tools. These methodologies are employed today in the production of photovoltaic (PV) arrays used in space systems as well as in several commercial semiconductor products like light-emitting diodes for displays; the scalability and ruggedness are improved with manufacturable semiconductor methodologies as well. The cost of space missions can be potentially reduced and issues such as pressure-sensitive couples in a modular array can be minimized for reliability during long flights.

### II. Results, Discussions and Summary of Developments

**BCAM architecture:** We have developed thermoelectric devices with a variety of materials configured in a BCAM structure. [Figure 1](#) illustrates the difference between the BCAM device architecture and the conventional TE device modules where a hard-bonded top header is used on the hot-side. In the traditional compact (SP-100) module (Ref. 1), a glass bond acts as an encapsulating layer to bring the TE element legs together and also to provide encapsulation against sublimation. In the traditional non-compact module, a common sub-header connects all of the element legs on both sides. In the BCAM (Bipolar Couple Assembled Module), a split sub-header separates adjacent couples on the hot-side but still shares one common header on the cold-side. [Figure 2](#) further delineates the differences between the traditional compact versus the BCAM architecture. Although encapsulation is not shown in BCAM, it can be employed as well for protection against sublimation purposes (Ref. 2). We will show, by both modeling and experimental results, that glass-bonding layer and significant compliance pads are unnecessary in the BCAM device fabrication and assembly. Validation of the BCAM advantage, and comparison against a traditional compact, was performed using ANSYS finite element modeling. A lot of initial modeling comparison was made with SP-100 design, so as to confirm our baseline modeling, before validating the BCAM architecture. Such BCAM concepts are applicable for flexible TEG modules as well.

**BCAM Modeling:** It is worth considering the various stressors in a TE module. We considered various sources of stress in TE elements and in a TE module, as shown in [Figure 3](#), including self-stress from pellet thermal expansion, stress due to hot and cold plate thermal expansion mismatch with TE element's thermal expansion, and stress due to interaction between the dielectric encapsulation material and the TE pellet. Note that in the compact structure, the dielectric and TE element may have a CTE mismatch, thus the dielectric and TE element are affected by expansion of hot and cold plate differently, exacerbated by the common hot-side header.

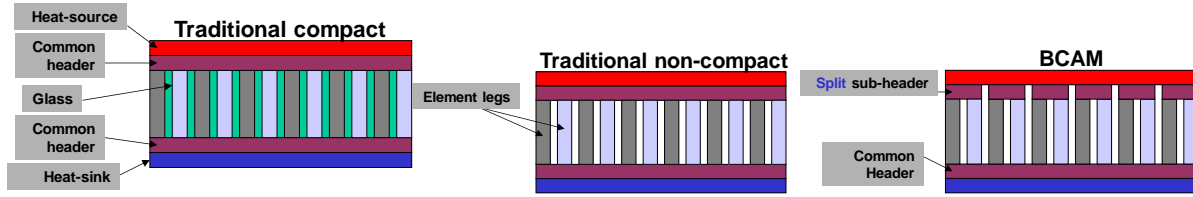


**Fig. 1** Traditional compact structure (left); Traditional non-compact structure (middle) and BCAM architecture (right). For clarity, various metal layers are not shown. Note: a common heat collector or source is applied across all the couples with individual sub-headers without a hard-bond; the thermal interface resistance between the common heat source header and the individual sub-headers is reduced through the use of liquid metal such as GaSn that can offer extremely low thermal resistance ( $\sim 0.02$  to  $0.05$  K/W-cm<sup>2</sup>).

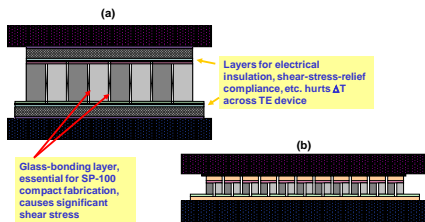


**Fig. 2** (a) Traditional compact versus (b) BCAM approach to module assembly. Note: the sizes of TE elements in BCAM can actually be made smaller, leading to higher electric power density as well as reduced material usage, compared to a traditional compact. The ability to reduce the size of TE element thickness in BCAM architecture directly comes from the reduced stress discussed below

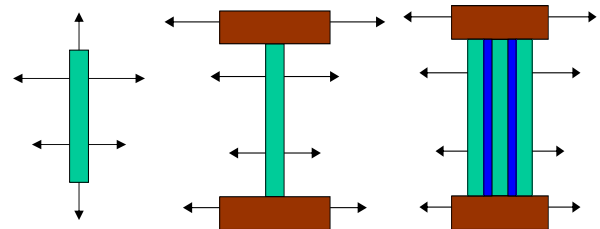


**Fig. 3** Various sources of mechanical stress in TE pellets in module include (from left to right): self-stress, stress due to hot and cold plate thermal expansion mismatch with TE element’s thermal expansion and stress due to interaction between dielectric material and TE pellet

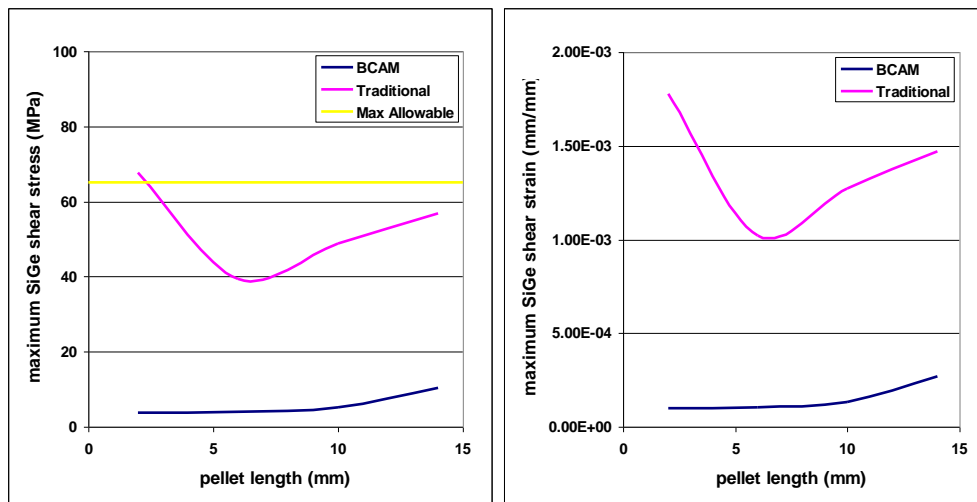


**Fig. 4** Comparison of maximum shear stress and strain in the SiGe pellets, for the traditional versus BCAM, as a function of thickness or length or height of element. Note that with BCAM architecture, the shear stress slightly increases as a function of thickness or length of TE pellet and the choice of optimal pellet thickness is based on electrical contact quality – where with thicker elements, electrical contact losses become a smaller fraction of total loss. In any case, the shear stress with BCAM is smaller than in conventional modules for all relevant thicknesses. Note in the chart above, pellet or element length or thickness are used interchangeably.

Our thermo-mechanical model verified the SP-100 conclusion that  $\sim 6$  mm is the ideal pellet length for reducing SiGe shear stress in the traditional compact approach, as shown in Figure 4. This gave us the confidence in the baseline model. Also shown in Figure 4 is the clear advantage of the BCAM design over the compact in terms of reducing shear stress in the SiGe element with respect to the top and bottom contact interfaces. The BCAM structure offers exceptional ruggedness by minimizing the shear stress on TE elements as illustrated in Figure 5. Finite element analysis showed that elements in the traditional TE device structure can undergo shear stresses on the order of  $\pm 35$ MPa while the BCAM architecture limits shear stresses to the order of  $\pm 2.25$ MPa. In addition to this modeling data and experimental data discussed next, the robustness of our device structure has been confirmed by random vibration testing ahead of flight qualification, where the BCAM device survived 16 Grms forces (Ref. 2).

Impact of BCAM on device efficiency: The lower stress allows BCAM approach to employ minimal thickness of compliance pads and hence obtain a larger fraction of the total system  $\Delta T$  across the active TE elements thereby reducing parasitic thermal drops; this is shown in the case of SiGe modules in Figure 6. The larger  $\Delta T$  translates to higher Carnot efficiencies and hence higher heat-to-electric conversion efficiencies, for the same external  $\Delta T$  – i.e., between the GPHS fuel cladding and the radiator heat-sink. The impact of reduced shear-stress with BCAM architecture is especially advantageous for thin-substrate or thin-film devices, needed for high electric power density ( $> 5\text{W}/\text{cm}^2$ ). The BCAM architecture has been a factor in demonstrating scalable modules in a range of materials including thin-film (in both cooling and power generation) and bulk materials in power generation with substantial  $\Delta T$ . These are summarized in the next section.

Demonstrated device module results with BCAM architecture: In Figure 7, we show large modular arrays with thin-film materials for both large-area cooling and power generation. Similarly, we show near-ideal scalability of power achievable at module level with devices made using half-Heusler (HH) materials, with hot-side approaching  $\sim 780^\circ\text{C}$  and cold-side  $\sim 180^\circ\text{C}$ . These materials and modules are robust at high-

temperatures and have shown reliable performance in extreme test conditions (Ref. 3, 4). These results on scale-up exemplify the advantages offered by the BCAM architecture in combination with the improvements in materials, device contacts and GaSn thermal interfaces at key locations for minimizing thermal losses. Recently at APL, we have also successfully incorporated thermal insulation (Ref. 5) like aerogel materials with modules incorporating a BCAM architecture.

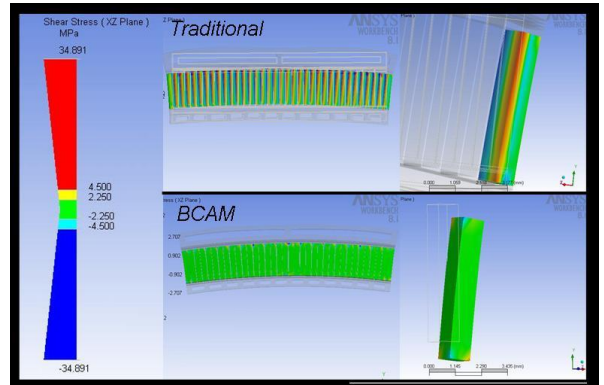


**Fig. 5** Shear stress comparison between traditional and BCAM, showing a factor  $\sim 15$  reduction in shear stress for comparable  $\Delta T$  and device element thickness.

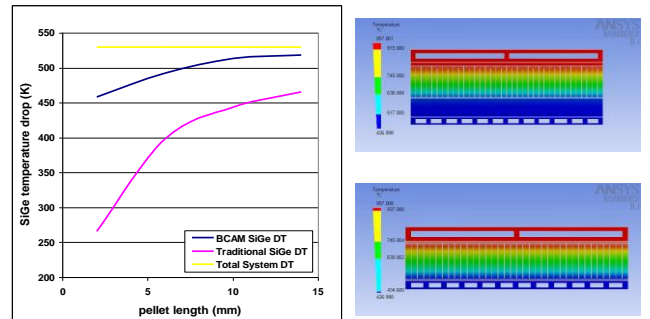


**Fig. 6** Impact of BCAM architecture, versus conventional module, on efficiently translating the external system  $\Delta T$  to active power producing  $\Delta T$  across the TE legs.

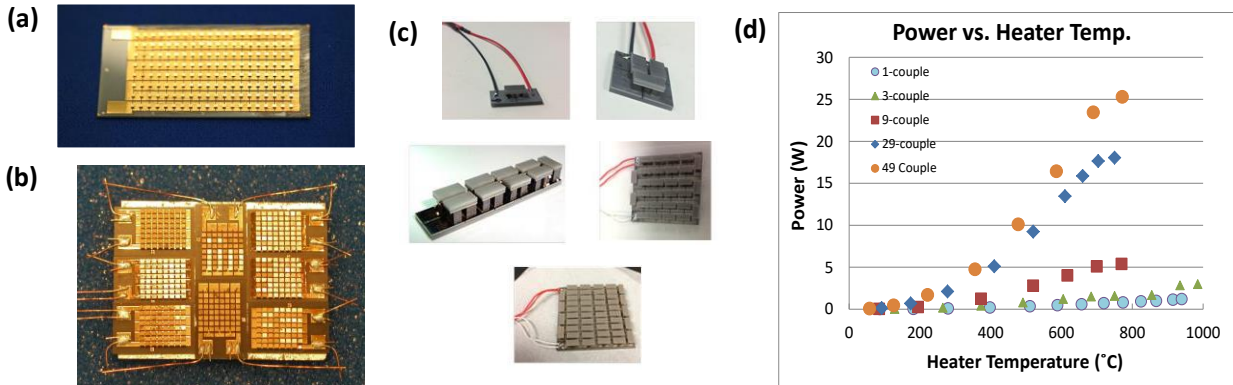


**Fig. 7** (a) An array of thin-film modules employing BCAM concept, consisting of 160 couples for IR-FPA cooling (Ref. 3); (b) a 528-couple multi-module-array of several BCAM thin-film modules for power generation (Ref. 4); progression from 1-couple to 49-couple bulk HH module that produced >25W electric power while sustaining a  $\Delta T \sim 600^\circ\text{C}$  with only a 2-mm thick TE elements; thinner elements allow for increased electric power density.

In summary we have described the BCAM device module approach, driven by extensive modeling, that has been reduced to successful demonstrations for scalability, compactness and long-term reliability for new generations of highly efficient RTG systems into the next decade.

#### ACKNOWLEDGMENTS

The authors acknowledge longstanding DARPA support for device development, staff at RTI International who worked with Dr. Venkatasubramanian in the thermo-mechanical modeling, JHU-APL internal R&D support and NASA-RPS program support for writing the technical paper on these developments of interest to the RTG community.

#### REFERENCES

1. Demuth S., SP100 Space Reactor Design, *Progress in Nuclear Energy* 42, 323-359 (2003).
2. Venkatasubramanian R., Reddy A., Pierce J., Dezsi G. et al., BCAM architecture for scalable and rugged thermoelectric module technology (Unpublished).
3. Bulman G., Siivola E., Wiitala R., Venkatasubramanian R., Acree M. and Ritz N., *Journal of Electronic Materials* 38, Issue7 (2009).
4. Venkatasubramanian R., Watkins C., Stokes D., Posthill J., and Caylor C., *Proc. of the International Electron Devices Meeting (IEDM)*, Washington, D.C., 367-370 (2007).
5. Venkatasubramanian R., Pierce J., Himmtann M., Ostdiek P., Singh R., Poon J., SiGe BCAM Devices, NASA-sponsored RPS Project, (2020).

## ADVANCEMENTS IN LOW-TEMPERATURE, MID-TEMPERATURE AND HIGH-TEMPERATURE HEAT-TO-ELECTRIC CONVERSION DEVICES

Rama Venkatasubramanian<sup>1#</sup>, Jonathan Pierce<sup>1</sup>, Meiyong Himmtann<sup>1</sup>, Geza Dezsi<sup>1</sup>, Jeff Snyder<sup>2</sup>, and Joseph Poon<sup>3</sup>

<sup>1</sup>The Johns Hopkins University Applied Physics Laboratory, Laurel, MD; <sup>2</sup>Northwestern University, Evanston, IL; <sup>3</sup>University of Virginia, Charlottesville, VA

# [rama.venkatasubramanian@jhuapl.edu](mailto:rama.venkatasubramanian@jhuapl.edu)

*Current single-stage heat-to-electric energy converters are at best 6 to 8% efficient. In order to develop a paradigm-changing 20 to 25% efficient converters, based on a 3-stage cascade design that utilizes optimum thermoelectric materials for each temperature range rather than a single material covering the full temperature range, it is important to develop advanced low-temperature, mid-temperature and high-temperature heat-to-electric conversion devices. In this paper, we discuss the development of heat-to-electric conversion devices using nano-engineered thin-film Bi<sub>2</sub>Te<sub>3</sub>-based devices for the low-temperature (~250°C), nano-engineered bulk PbTe-based devices for mid-temperature (~500°C) and high-performance half Heusler (HH) based devices for high-temperature (~800°C). We believe these developments will allow us to develop >20% cascade heat-to-electric converters which will lead to efficient RTGs and novel mission capabilities.*

### I. Introduction and Summary of Developments

Outer-planetary missions rely on radioisotope heat to electric conversion as the sunlight is too weak to provide power for scientific missions. Advanced Stirling Radioisotope Generators (ASRG) and Dynamic Radioisotope Power System (DRPS) offer ~25% heat-to-electric conversion efficiency, while have shown long life in lab tests, have moving parts and are not likely to offer the reliability needed for decade or multi-decade long flight-plus-scientific observation missions. In contrast, solid state thermoelectric converters have a legacy of reliability over many decades (eg: Voyager to New Horizons) as there are no moving parts but suffer from 6 to 8% conversion efficiency, requiring a larger Pu-source for a fixed mission electric power. Developing ~20 to 25% efficient thermal-to-electric converters using a 3-stage cascade design, that utilizes the optimum thermoelectric materials for each temperature range, will be game changing. In essence, the development of 20% to 25% TE converters will lead to significantly reduced quantity of radio-isotope with enhanced mission safety and reduced cost, lighter weight system than ASRG and DRPS, enabling more missions and novel fly-by trajectories. These will greatly expand our exploration of the solar system. This means, we can utilize about 1/3rd to 1/4<sup>th</sup> of radio-isotope materials that were used in

Voyager or Cassini or New Horizons Mission, for about the same electric power respectively, thereby significantly enhancing mission safety. Novel mission fly-by trajectories can be considered, with less concerns for gravity assist from earth, due to significantly lower nuclear materials. The cost of space missions can be significantly reduced due to the reduced need for nuclear radioisotopes and associated reduction in safety engineering costs.

Cascade TEG concept has been considered by Cook, Poon and Venkatasubramanian (Ref. 1) with an initial demonstration of lab-scale device using nano-Bi<sub>2</sub>Te<sub>3</sub> bulk alloys for low-temperature stage, advanced PbTe and enhanced-TAGS materials for mid-stage and HH materials for top stage with an actual measured efficiency of ~20% based on total heat flow and summation of the electric power from all three stages measured simultaneously. Further validation and improvement in efficiencies of such cascade devices, with recent advances in material for each stage, as well as scale-up for larger powers are needed and the work presented here is a step in that direction.

In order to build 3-stage cascade devices, with the top-stage operating between ~800°C and ~500°C, mid-stage between ~500°C and ~250°C and the bottom-stage between 250°C and 100°C, we need to develop high-performance single-stage devices with materials suitable for these stages. In this paper, we will first present the development of heat-to-electric conversion devices using nano-engineered thin-film Bi<sub>2</sub>Te<sub>3</sub>-based devices for the low-temperature (~200°C). At APL, we have built on past work on thin-film superlattice materials (Ref. 2) and device developments (Ref. 3), and have developed advanced thin-film TE materials and validated with device performance. Specifically, we have obtained (i) module-level figure-of-merit (ZT) approaching ~1.4, that is about 70% better than commercial state-of-the-art COTS bulk Bi<sub>2</sub>Te<sub>3</sub>-alloy materials; (ii) heat-to-electric conversion efficiencies that are 65% better than COTS in the temperature range of 32°C-200°C. We believe these are unprecedented results with thin-film thermoelectric materials and devices which have been achieved through addressing the critical gaps in materials and devices, setting the stage for exciting opportunities in the low-temperature stage of multi-stage cascade devices for RTG

applications. Next, we will present the device heat-to-electric conversion efficiencies achieved with nano-engineered bulk PbTe-based materials applicable for the mid-temperature range ( $<500^{\circ}\text{C}$ ). The nano-engineered n-type PbTe materials (Ref. 4) and p-type PbTe materials (Ref. 5) have been developed by Snyder et al. Although there has been innumerable reported work on higher ZT in bulk materials, to our knowledge there have been minimal to no reported translation of materials' ZT to heat-to-electric conversion efficiencies. We will describe our progress in this critical area that is directly relevant to their use in RTG applications. Finally, we will present the device heat-to-electric conversion efficiencies achieved with nano-engineered bulk half-Heusler (HH) high-performance materials (Ref. 6) applicable for the high-temperature range ( $\sim 800^{\circ}\text{C}$ ).

## II. Results, Discussions and Summary of Developments

Low-temperature nano-engineered thin-film materials and devices: On a DARPA funded program, we at JHU-APL have developed nano-engineered thin-film thermoelectric materials (Ref. 7) to improve the ZT of both P- type and N-type materials, to values approaching  $\sim 3$  and  $\sim 2$  at 300K, respectively. In addition, the device level p-n couple ZT with these materials have been improved to  $\sim 1.5$  at 300K. The value of these materials for RTG applications has been evaluated with thermal to electric power conversion devices. The thin-film devices, consisting a  $1 \times 4$  p-n couple array, were tested with a thermally managed heat-sink and calibrated heat source shown in Figure 1. The power output from the 4-couple array was about 50 mW, with a  $\Delta T$  of only  $\sim 150\text{K}$ . The effective device ZT (from efficiency measurements) and the efficiency versus temperature differential ( $\Delta T$ ) across the thin-film device are shown in Figure 2. The data of best COTS bulk  $\text{Bi}_2\text{Te}_3$ -alloy based devices are also overlaid in this figure. We note that these efficiencies are measured from actual heat flow and electric power produced and not computed from material ZT values. Hence electrical and thermal losses are included in the measurement; hence these are significant device advancements.

We observe that the module-level device ZT approaching  $\sim 1.4$  is about 70% better than state-of-the-art COTS bulk  $\text{Bi}_2\text{Te}_3$ -alloy materials. Also, heat-to-electric conversion efficiencies are 65% better than COTS in the temperature range of  $32\text{-}200^{\circ}\text{C}$ . We believe these are exciting results with thin-film thermoelectric materials and devices. Such high efficiencies can add onto the high-temperature and mid-temperature portions of a 3-stage cascade. If the total efficiencies of heat-to-electric conversion is higher, then for a fixed electric power, less heat needs to be rejected at the heat-sink/radiator and so lower cold-side temperatures can be tolerated, further improving the efficiencies.

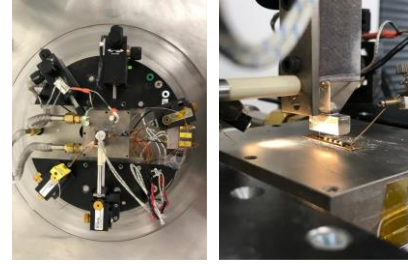


**Fig. 1.** Experimental set up for testing thin-film devices (left) where a calibrated heat source is placed on top of an array of  $1 \times 4$  couples on a heat-sink (right)

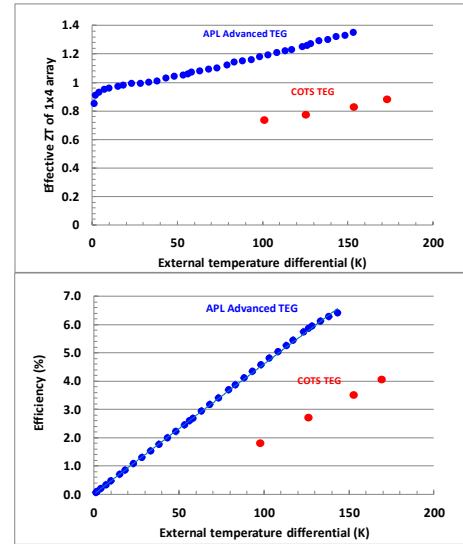


**Fig. 2.** Effective ZT of the thin-film device modules (top); Impact of higher ZT on heat-to-electric conversion efficiencies as a function of temperature differential applied to the thin-film devices (bottom)

Mid-temperature nano-engineered PbTe materials and devices: For mid-temperature applications, we have evaluated devices based on breakthrough nano-engineered bulk n-type PbTe materials with Ag inclusions (Ref. 4) and p-type PbTe-PbSe bandgap-engineered materials (Ref. 5). The material ZT as a function of temperature for these materials are shown in Figure 3. The impact of higher ZT of materials on device heat-to-electric conversion efficiency is shown in Figure 4; we observe that p-n couples made from nano-engineered PbTe materials offer significantly better efficiencies than standard N-PbTe - p-TAGS devices. However, we note that PbTe-TAGS offer superior efficiencies to all-PbTe devices. The device couples like shown in Figure. 4 were carefully evaluated with calibrated q-meter/heat-flow meter for efficiency measurements. Again, we note that these efficiencies are measured from actual heat flow and electric power produced and not computed from material ZT values.

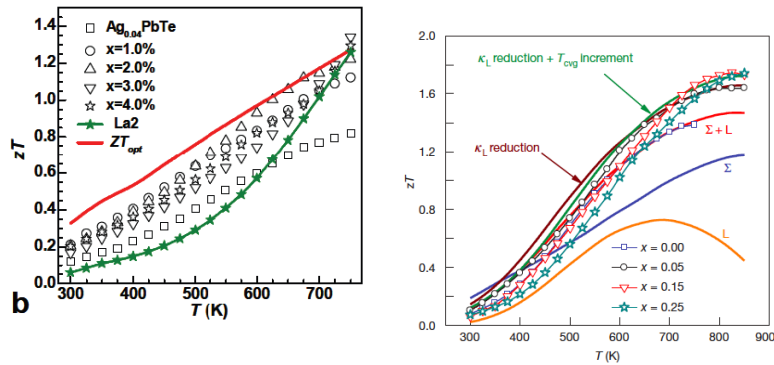


**Fig. 3.** ZT of nano-engineered PbTe materials with Ag inclusions for N-type leg (left); ZT of nano/multi-valley (L,  $\Sigma$ , L+ $\Sigma$ ) bandgap engineered PbTe-PbSe materials for P-type leg (right)

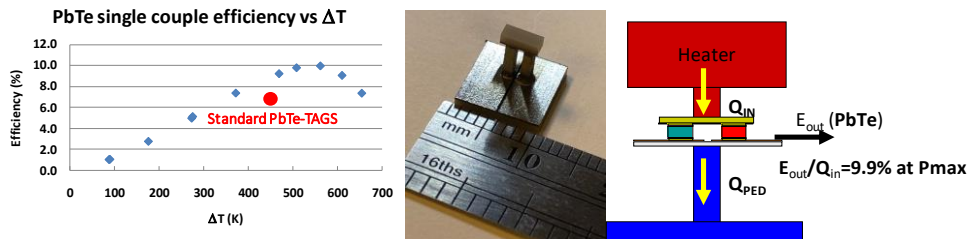


**Fig. 4.** (Left) Efficiency of nano-engineered PbTe devices approach  $\sim 10\%$ , significantly better than  $\sim 6\%$  attainable from conventional PbTe p-n couples and  $\sim 7\%$  attainable from standard PbTe-TAGS couples; (middle) typical p-n couple; (right) schematic of efficiency measurement set-up. *These are actual measured efficiencies and not computed values from materials ZT.*

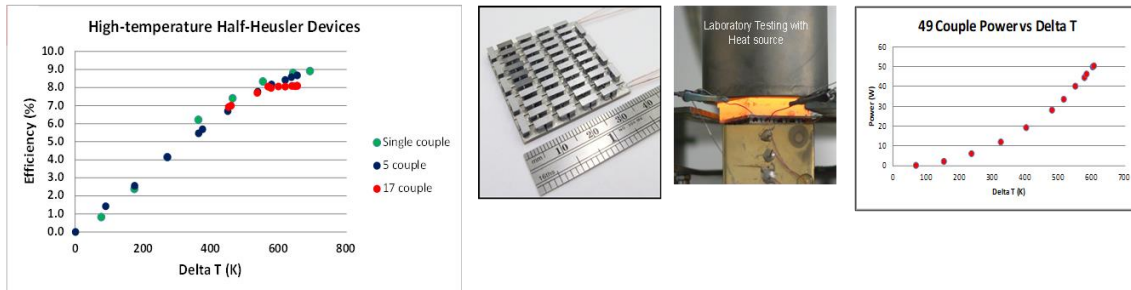


**Fig. 5.** (left to right); efficiency of HH device module (single, 5-couple, 17-couple module) as a function of  $\Delta T$ ; a 3.5 cm x 3.5 cm HH-module consisting of a 49-couple array; power testing of a HH module with a heat source and a calibrated heat-sink attached with thermocouples to monitor heat flow; power output from the 49-couple HH module as a function of temperature differential ( $\Delta T$ ) showing electric power output levels of  $\sim 50$ -plus Watts.

High-temperature half-Heusler (HH) Materials and Devices: Half-Heusler n- and p-type alloys with a nominal composition of  $\text{Hf}_{0.6}\text{Zr}_{0.4}\text{NiSn}_{1-x}\text{Sb}_x$  ( $x=0.005, 0.01, 0.02$ ) and  $\text{Hf}_{0.3}\text{Zr}_{0.7}\text{CoSn}_{0.3}\text{Sb}_{0.7}$ , respectively, were synthesized by arc melting and grinding the resulting ingots into 10 to 30 micron powders which were subsequently consolidated by spark plasma synthesis (SPS). Thermal diffusivities and specific heat values of the samples were measured on a Netzsch (LFA-457) micro-flash system and DSC-404C Pegasus system, respectively. Through doping of the alloy

host as well as constituting bulk nanoparticles-in-matrix composite, the n-type and p-type HH alloys were shown to exhibit  $ZT = 1.05$  and  $0.8$  near  $600\text{--}750^\circ\text{C}$ , respectively. Details of the synthesis and characterization of the materials are given elsewhere (Ref. 6). The focus of this work is on heat-to-electric device performance achieved with these improved materials. In Figure 5, we show that  $\sim 9\%$  efficiencies are achievable at module level with HH devices, with hot-side approaching  $\sim 780^\circ\text{C}$  and cold-side  $\sim 180^\circ\text{C}$ . These materials and modules are robust

at high-temperatures and show the ability to be scaled up from single couple to a multi-couple module. Again, we note that these efficiencies are measured from actual heat flow and electric power produced and not computed from material ZT values.

In summary, we believe, we have device components for the low-temperature, mid-temperature and high-temperature stages of a 3-stage cascade, based on recent advances in materials, that will allow us to develop 3-stage cascade efficiencies in excess of 20%, and with further material and device optimizations, allow us to move towards 25% conversion efficiencies. Such an advancement would be a significant breakthrough and place solid state thermoelectric technology on an exciting pathway towards efficient heat-to-electric conversion along with no moving parts, scalability, compactness and long-term reliability, for new generations of highly efficient RTG systems for the next decade.

#### ACKNOWLEDGMENTS

The authors acknowledge longstanding DARPA support for thin-film materials and device development, JHU-APL IRAD support for thin-film heat-to-electric device development and for HH device development and

ruggedization studies, and NASA-RPS program support for writing the technical paper on these developments of interest to the RTG community.

#### REFERENCES

1. B. Cook, T. Chan, G.Dezsi, P. Thomas, C. Koch, J. Poon, T. Tritt, and R. Venkatasubramanian, High-Performance Three-Stage Cascade Thermoelectric Devices with 20% Efficiency, *Journal of Electronic Materials*, DOI: 10.1007/s11664-014-3600-9 (2015)
2. Venkatasubramanian R., Siivola E., Colpitts T., O'Quinn B., *Nature* 413, 597 (2001)
3. Choudhry, I., Prasher, R., Koester D., Venkatasubramanian R., *Nature Nanotech.* 4, (2009)
4. Pei Y., May F., Snyder J., *Adv. Energy Mater.* (2011)
5. Pei. Y., Shi. X, LaLonde A, Wang. H, Chen. L & Snyder J., *Nature* 473 (2011)
6. Poon, J., Wu., Tritt, T., Thomas, P., Venkatasubramanian, R., *J. Materials Res.* 26 (2011).
7. Venkatasubramanian, R., Pierce J., Himmtann, M., Dezsi, G., Maranchi, J., Manuscript in preparation; To be submitted for publication (2020)

## AMERICIUM-BASED OXIDE AND PT-RH ALLOYS COMPATIBILITY/INTERACTION TESTS IN THE CONTEXT OF EUROPEAN SPACE RADIOISOTOPE POWER SYSTEMS

E. J. Watkinson<sup>1</sup>, B. Cremer<sup>2</sup>, P. Lajarge<sup>2</sup>, S. Gardeur<sup>2</sup>, J.-F. Vigier<sup>2</sup>, C. Berkmann<sup>2</sup>, M. Ernstberger<sup>2</sup>, T. Wiss<sup>2</sup>, D. Freis<sup>2</sup>, T. Crawford<sup>1</sup>, S. Pfirrmann<sup>2</sup>, R. Ambrosi<sup>2</sup>, R. Konings<sup>2</sup>, K. Stephenson<sup>3</sup>

<sup>1</sup>University of Leicester, University Road, Leicester, LE1 7RH, United Kingdom

<sup>2</sup>European Commission Joint Research Centre Karlsruhe, Germany

<sup>3</sup>European Space Agency, ESTEC TEC-EP, Keplerlaan 1, Noordwijk, 2201AZ, The Netherlands

Primary Author Contact Information: +44116 223 1033 and [ejw38@le.ac.uk](mailto:ejw38@le.ac.uk)

The European Space Agency is funding the development of European radioisotope power systems (RPSs) for space, namely, radioisotope heater units (RHUs), radioisotope thermoelectric generators (RTGs) and Stirling generators. The University of Leicester is leading the design and manufacture of the RHU, and of the heat source that will be common to the RTG and Stirling generator. All RPSs will incorporate Pt-Rh clad americium based oxide fuel.

In this study, we present an interaction/compatibility test between an americium based oxide disc, namely, an Am-U oxide, and Pt-20%Rh and Pt-30%Rh alloy discs. The number of samples available was extremely limited, i.e., only a single ‘fuel’ disc was available. This had a direct influence on the procedure required for the test. We summarise the procedure for this study that is underway and the many challenges involved when working with a limited number of samples. Scanning electron microscopy coupled with energy dispersive spectroscopy is used to analyse the discs’ surfaces. Initial results are presented. Temperatures relevant to RHU and RTG standard operation are targeted as well as extreme high temperatures. Tests are conducted in argon and air.

### I. INTRODUCTION

European radioisotope power systems (RPSs) for space will utilise an americium (<sup>241</sup>Am) based oxide fuel as its heat source. The University of Leicester is leading the design and development of the following technologies for the European Space Agency (ESA): the radioisotope heater unit (RHU), the radioisotope thermoelectric generator (RTG) and the heat source that will supply the necessary heat for the RTGs and the Stirling generators.<sup>1</sup> All systems will have a platinum rhodium clad as the primary containment layer for the fuel.<sup>1</sup> Previous designs focussed on the use of Pt-30%Rh clads and initial cladding structures were made.<sup>2</sup> This was consistent with the US Light Weight Radioisotope Heater Unit (LW-RHU). Designs now focus on Pt-20%Rh. This is due to a number of reasons as outlined by Barco et al.<sup>2</sup> and Ambrosi et al.<sup>1</sup>, e.g., it has improved ductility. The final Pt-Rh alloy choice is still to be decided and will be the

focus of a future study by the University of Leicester. An advantage of Pt-Rh alloys is they are chemically unreactive with several materials. However, previous studies have suggested evidence for different reactions between platinum and americium when heated in hydrogen atmospheres at 1200 °C and 1400 °C for 40 and 60 hours, respectively.<sup>3,4</sup> Reactions between rhodium and americium were also noted e.g., at 1550 °C in hydrogen.<sup>3</sup>

As part of current research and development activities, a number of fuel options have been considered conceptually in RTG and RHU designs including AmO<sub>2</sub>, Am<sub>2</sub>O<sub>3</sub> and Am-U oxide fuel.<sup>1,5,6</sup> The latter was presented by Vigier et al.<sup>7</sup> as a promising fuel option following experimental sintering trials that confirmed that integral discs and pellets can be created.<sup>7</sup>

An RPS fuel and its cladding need to be chemically compatible. The compatibility of fuel and cladding options will need to be tested and verified (if literature exists) under a range of temperatures and atmospheric conditions that are relevant to operational and accident scenarios.

In this study, we present an investigation to test the chemical interaction/compatibility between an Am-U oxide and Pt-Rh alloys (Pt-20%Rh and Pt-30%Rh) at operational RHU and RTG fuel temperatures, and at more extreme temperatures. Argon atmospheres and air atmospheres are used. The RTG is designed to operate under argon as well as vacuum. This paper presents the initial results of this study. Although RPS clad designs have moved to Pt-20%Rh and away from Pt-30%Rh, the procedure of this investigation provided the opportunity to collect data for both alloys. It is key to highlight that the materials available were extremely limited. The following were available:

- a single Am-U oxide disc (around 4 mm in diameter by around 1 mm in thickness). This was produced by the previous JRC study using in-house material.<sup>7</sup> Material composition details are outlined in the paper by Vigier et al.<sup>7</sup>
- sufficient material to make a single Pt-30%Rh disc of similar dimensions to the fuel. This material was provided by JRC.

- material to make two Pt-20%Rh discs of similar dimensions to the fuel disc and one that was slightly thicker (2 mm). Although the Am-U oxide disc is invaluable, the Pt-Rh alloy materials are also expensive per gram. Additionally, it was not going to be possible to decontaminate the platinum rhodium materials used in this study and so they could not be recovered. This material was prepared by the University of Leicester (see Acknowledgements for further details).

## II. METHOD

### II.A. Limitations

The limited mass of materials had a direct influence on the experimental method of this study. Destructive preparation and/or analysis techniques of the discs needed to be avoided to ensure multiple investigations could be conducted on the same samples via successive treatments and analyses under different conditions (see Table I). The argon tests are conducted first to avoid changing the sintered fuel's oxygen-to-metal ratio. By characterising the surface in significant detail before the first test and after each subsequent test, an assessment of whether an interaction has occurred for each test condition can be made. The extent of the interaction can be assessed and a decision to continue with the test matrix (Table I) can then be made. This provides the potential for a single fuel disc to be used for multiple tests, particularly as the test matrix proceeds with successively higher temperatures for the argon tests. It is assumed that an interaction may be more likely as the temperature is increased.

A final test in air is targeted as the fuel will likely change stoichiometry.

#### II. A.1 A Key Planning Principle

The ability to distinguish between the two faces of the fuel disc was key to make it possible to distinguish between the side that would be in contact with the Pt-20%Rh disc and the side that would be in contact with the Pt-30%Rh disc. This way, should any evidence of interaction arise, it would be clear which alloy was involved. The fuel disc and each of the Pt-Rh discs were marked with a scratch.

A given fuel face would only ever be in contact with one of the Pt-Rh alloys and not both. To aid this, a test procedure was written to ensure that the samples tested in a given atmosphere would always be arranged in the same manner within the test fixture. The argon atmosphere environment tests are conducted first. This also had the added benefit that there was a 'fresh' side of the Pt-Rh alloys' surfaces not used in the argon interaction tests (see Table I in section II.C) that could be used for the air tests; the Pt-Rh alloy discs would simply be flipped.

A schematic illustrating the arrangement of the discs for the argon tests with the marks shown on their surfaces (depicted as red lines) is shown in Figure 1.

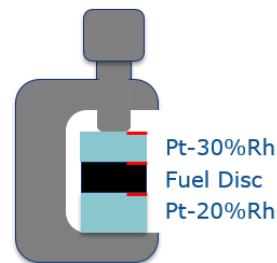


**Fig. 1.** A schematic (not to scale) illustrating an example of the disc stacking. This is the argon test configuration.

### II.B. Preparation

#### II.B.1. Pt-Rh discs Preparation and Characterisation

It was assumed that polished sample surfaces would aid optical identification of new features (if present). Additionally, it was assumed that it would improve physical contact between the discs to enhance any potential reactions during the compatibility tests.

The Pt-20%Rh alloy (80 wt.% Pt and 20 wt.% Rh; Johnson-Matthey UK) discs were machined from the threaded ends of Pt-20%Rh rod specimens at the University of Leicester. The first disc used in this study was around 4.5 mm  $\phi$  and around 2 mm in thickness. Both sides of the disc were ground and polished by hand without a polishing wheel. A 1200 grit sized SiC paper was initially used and the 1  $\mu$ m diamond paste (RS Components) was used to polish the sample.

Previous experience at University of Leicester found that Pt-20% Rh can be readily marked during grinding and polishing as the material is soft.<sup>9</sup> Energy dispersive X-ray spectroscopy (EDX) analysis was therefore conducted to verify if the sample had been cross-contaminated with Si or C. Note that this is always coupled with scanning electron microscopy (SEM). A secondary electron image of an area on one of the disc's surfaces is shown in Figure 2. The darker region shown evidenced Si and C contamination in addition to Pt and Rh. Other darker regions only evidenced C and some Ca was highlighted after a water wash.

The Pt-30%Rh discs (70 wt.% Pt and 30 wt.% Rh; Wieland Edelmetalle GmbH) were machined to create a single disc at JRC. The sample was polished using an alternative procedure.

The Pt-20%Rh and the Pt-30%Rh discs were cleaned at JRC in alcohol using an ultrasonic bath. SEM and EDX analysis highlighted that contamination was present with Si and C as the most prevalent contaminants.

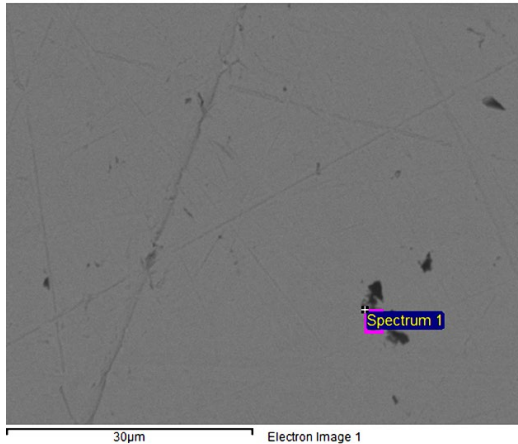


**Fig. 2.** A secondary electron image of a polished Pt-20%Rh disc face (20 keV). The scratch marks arise from SiC grinding.

### II. B.3. Preparing the Am-U oxide disc and its Characterisation

The Am-U oxide disc was mounted to an aluminium holder with a glue. A device within a shielded glovebox clamped the holder and ground the sample with SiC paper. The sample was then polished using successive cloths: diamond solution from 9 µm down to 1 µm was used. The grinding/polishing procedure was automated. The procedure was then repeated for the opposite face of the fuel disc. The disc was heated to ~80 °C to heat and remove the glue from the sample's surfaces. Acetone was used to remove the remaining glue. The sample was placed in an alcohol filled ultrasonic bath for 30 minutes to clean it. Nonetheless, it was considered possible that Si, C and Al could be elemental contaminants identified during EDX (elements expected from the grinding/polishing procedure). The Am disc was cleaned via an ultrasonic bath also. A mark was made one side of the disc.

The disc was inspected by SEM. The high activity of the americium sample prevented EDX analysis to check the disc for elemental contamination.

### II. B.2. Designing sample test fixtures for different atmospheres and a storage container

Two types of test fixtures were designed and manufactured in order to test the samples under different atmospheres (argon and air). The test fixtures were required to 1) be expansion-compatible with the Pt-Rh alloys and Am-U oxide and 2) remain chemically stable with respect to argon up to 1650 °C and air up to 1000 °C. These temperatures were essentially the maximum temperatures achievable in the relevant furnaces that could be used to heat americium samples. A molybdenum test fixture was designed for the argon tests (see Figure 3). A ceramic (Macor®) test fixture was designed for the

tests in air (see Figure 4). Each fixture included a screw and thread to enable the Pt-20%Rh to Am-U oxide to Pt-30%Rh stack to be clamped together during the heating procedure for improved contact. The designs and photographs of the fixtures are shown together with the assembled Pt-Rh discs and the fuel disc (see Figures 3 and 4). The fixtures were manufactured by the workshop at JRC. For reference, the standing height of each fixture with the assembled discs is around 2 cm.

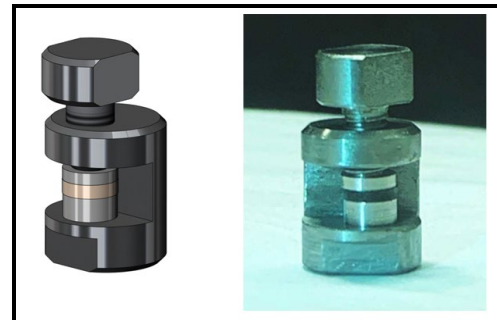


**Fig. 3.** Left) The CAD drawing of the Mo test fixture for the compatibility tests in argon. Right) The manufactured fixture with the discs assembled.

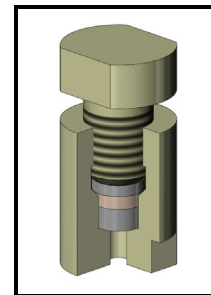


**Fig. 4.** The CAD drawing of the Macor® test fixture for the compatibility tests in air.

A stainless steel sample container was also designed and manufactured to house each of the discs to aid their identification when working in a glovebox environment. It was designed to house four different sizes of disc (Two different sizes of Pt-20%Rh were prepared.). The storage container, the tests fixtures was also cleaned prior to use.

## II. C Procedure and Experimental Matrix

The minimum number of investigations that were proposed are outlined in Table I. The overall procedure for each test was to assemble the samples according to Figure 1, heat-treat the entire assembled fixture in a furnace based on the heat treatment outlined in Table 1, analyse the surfaces extensively by SEM to inspect the microstructure of the discs, and use EDX for the Pt-Rh discs to assess if there were differences in elemental concentrations compared to the previous test condition. If

the Am and U concentration had increased significantly and there was no evidence of powder contamination then this could indicate a chemical interaction, particularly if the microstructure had changed.

The temperatures targeted for test 1 and 2 shown in Table I are based on RHU and RTG operating fuel temperatures.<sup>9</sup> At the time of writing test 1 has been completed and test 2 is soon to be underway.

**TABLE I.** The minimal experimental matrix. Test no. 4 is the maximum readily achievable temperature in the minor actinide laboratory's furnace.

Test no.	Atmos.	Ramp/Cooling Profile (°C/hour)	Dwell temperature (°C) /time (hrs)
1	Ar	100	200/50
2	Ar	100	650/50
3	Ar	100	1000/50
4	Ar	100	1650/50
5	Air	100	1000/50

The Test 1 assembled samples were heated in a furnace. For example, those heated in argon are heated in the shielded glovebox in the minor actinide laboratory at JRC, Karlsruhe (see Figure 5). Note that only the manipulator interface is shown in Figure 5. The glove interface is out of view.

The scanning electron microscopy and EDX analysis were conducted in a different glovebox.



**Fig. 5.** The shielded gloveboxes with installed manipulators for in the minor actinides laboratory at JRC Karlsruhe.<sup>8</sup>

### III. RESULTS AT 200 °C IN ARGON

#### III.A Pt-20%Rh

A secondary electron image map of the inspected locations of the Pt-20%Rh disc is shown in Figure 6. The marked region is shown in 'picture 11011'. Several features with differing shades were presented that were

not noted during the initial SEM inspection. Any variations from the 'standard/average grey' background were inspected further by EDX. This was also the case for the Pt-30%Rh disc. As an example, Figure 7 illustrates the variation present in the 11001 region of Figure 6. Despite noticeable visual variation from the background e.g., 19071463-61, 19071463-62 and 19071463-63 looked different, the atomic and weight % of all identified species were quite similar (see Table II).

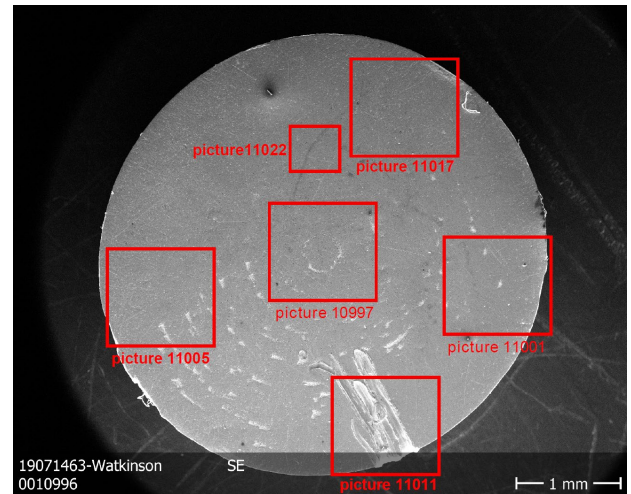


**Fig. 6.** The inspected regions of the marked Pt-20%Rh that was in contact with the fuel disc.

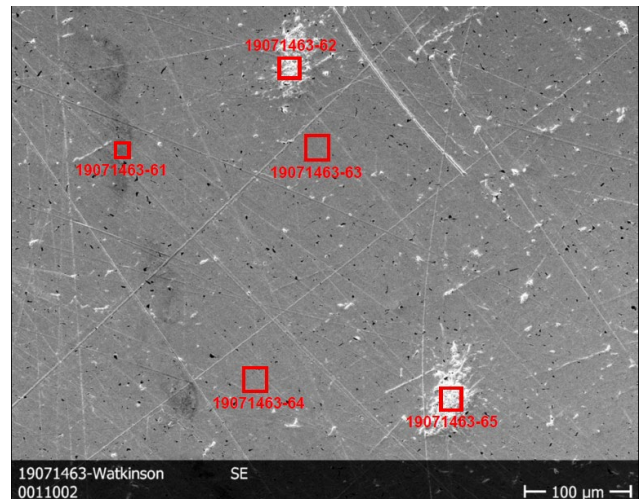


**Fig. 7.** A secondary electron image of the 11001 region of Figure 6 inspected by secondary inspected regions of the Pt-20%Rh that was in contact with the fuel disc.

**Table II.** Examples of the EDX results for three different regions of Figure 7. Rounded to the nearest integer.

El. /Line	Weight %/ Atomic %		
	19071463-61	19071463-62	19071463-63
Si/Ka	3/16	3/18	3/17
Rh/La	15/21	14/20	14/21
Pt/La	82/63	83/62	82/62
U/Ma	0/0	0/0	0/0

### III.B Pt-30%

Figure 8 illustrates a secondary electron image map of the locations inspected on the Pt-30%Rh disc. Once again, there were several examples of variations in shade that suggested potential features as shown in Figure 9 (the 11035 region of Figure 8). However, except for the lightest and darkest of regions (19071463-128 and 19071463-129, respectively), EDX analysis (see Table III) once again highlighted similar elemental abundances with the exception for Pt and Rh as it is a different alloy.

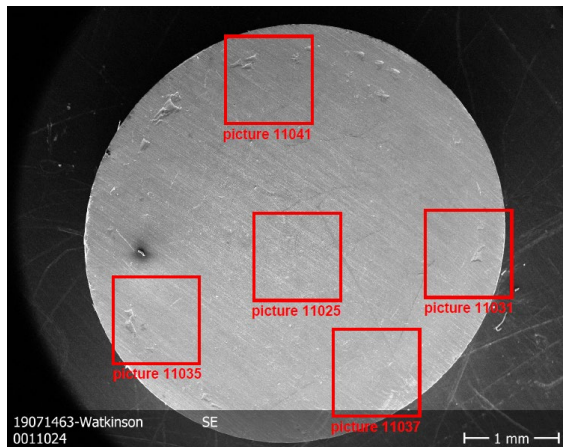


**Fig. 8.** The inspected regions of the unmarked Pt-30%Rh that was in contact with the fuel disc.

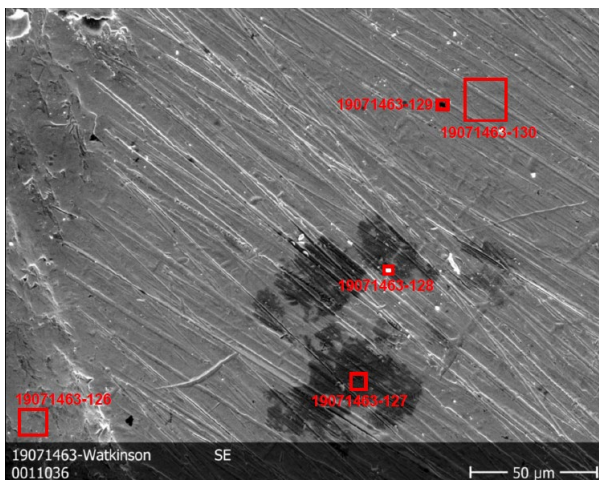


**Fig. 9.** A secondary electron image region 11035 in Fig.8.

The light region was primarily uranium, with a smaller fraction of plutonium. Although Np was detected this may be below the detection limit of the detector. These results are omitted from Table III. As the light region's composition by percentage differed significantly from the Am-U oxide fuel and because it contained no americium, it was believed to be a mixed actinide contaminant from other investigations conducted in the same facilities. Particles were found randomly across the disc (on both faces) but their compositions and percentage compositions differed. None were consistent with the Am-U oxide fuel. Actinide oxide contaminants were found on the Pt-20%Rh discs but there were fewer examples.

The very dark region contained a very high amount of Si. As the peak was so large, it is thought that the quantification of Pt and Rh based on their much smaller peaks was affected. The elemental quantification of the EDX spectrum will need be repeated again in the future with the Si peak excluded. This should produce a result more consistent with Pt-30% Rh.

**Table III.** Examples of the EDX results for four different regions of Figure 9. Rounded to the nearest integer. No data are provided for the Np abundance for 19071463-128 as the result may have been below the detection limit.

El. /Line	Weight %/ Atomic %			
	19071463-126	19071463-127	19071463-128	19071463-129
Si/Ka	3/15	3/15	3/21	46/84
Rh/La	23/32	25/33	8/14	6/3
Pt/La	74/53	72/52	20/17	48/13
U/Ma	0/0	0/0	61/43	0/0
Np/Ma	0/0	0/0	N/A	0/0
Pu/Ma	0/0	0/0	7/5	0/0

### IV. CONCLUSIONS TO DATE

Analysis of the Pt-20%Rh and Pt-30%Rh indicates no evidence of a chemical reaction of the fuel with the material at 200 °C based on EDX analysis. Although EDX analysis evidences some U or Pu, and even Np, the lack of Am and the appearance of powder suggests that this was contamination from other sources in the glovebox. Despite different shades across the sample, other element abundances remained similar suggesting no chemical changes. All Pt-Rh disc surfaces were thoroughly analysed (around 88 images and 200 spectra were taken for the 200 °C test) to ensure a thorough 'background' data set had been collected for future higher temperature tests. Future investigations will proceed to higher temperatures that will be relevant to an RTG operation temperature and even higher temperatures. It is

possible that significantly longer duration tests (by orders of magnitude) may need to be conducted in the future.

## ACKNOWLEDGMENTS

This project has been enabled by an unpaid visiting scientist (Emily Jane Watkinson) agreement between the University of Leicester and the European Commission Joint Research Centre Karlsruhe. The University of Leicester (UL) wishes to acknowledge the funding provided by the European Space Agency via the National Nuclear Laboratory to enable the travel for this research. UL also wishes to thank and acknowledge ESA for allowing them to prepare and use the Pt-20%Rh disc samples for this study. The material is owned by ESA. We wish to acknowledge helpful discussions with colleagues R. Mesalam and A. Barco during these studies.

The authors wish to thank the reviewers for their helpful comments and feedback.

## REFERENCES

1. R. M. AMBROSI et al., “, *Space Sci Rev*, **215**: 55 (2019) DOI: 10.1007/s11214-019-0623-9
2. A. BARCO et al., 2019 IEEE Aerospace Conference, Big Sky, MT, USA, (2019), pp. 1-11. DOI: 10.1109/AERO.2019.8741786
3. W. W. SCHULZ, The Chemistry of Americium. ERDA Critical Review Series (1976). <https://www.osti.gov/servlets/purl/7232133>, accessed 19<sup>th</sup> February 2019
4. B. ERDMANN and C. KELLER, *Inorg. Nucl. Chem. Letters*, **7** (1971) pp. 675-683.
5. M. SARFIELD et al., E3S Web Conf. 16, 05003 (2017). DOI: 10.1051/e3sconf/20171605003
6. M. SARFIELD, et al., *Prog. Nucl. Energy* **106**, 396–416 (2018). DOI: 10.1016/j.pnucene.2018.02.008
7. J-F. VIGIER et al., *Inorg. Chem.* **578**, 4317–4327 (2018). DOI: 10.1021/acs.inorgchem.7b03148
8. K. HESKETH et al., Min. Actinide Burning in Therm. Reactors. A Report by the Working Party on Scientific Issues of Reactor Systems. No. NEA--6997. Organ. for Econ. Co-Op. and Develop., 2013.
9. R. MESALAM and E. J. WATKINSON (2018), an in house investigation of how to grind and polish Pt-20%Rh samples for microscopy (not published but presented to ESA).

## PROPOSED STANDARD FOR EXTRAPOLATING LIMITED RTG PERFORMANCE DATA TO ESTABLISH BEHAVIOR TRENDS AND A LIFETIME PERFORMANCE PREDICTION

Christofer E. Whiting

University of Dayton, Dayton, OH, 45469

Primary Author Contact Information: (937) 229-2570; [chris.whiting@udri.udayton.edu](mailto:chris.whiting@udri.udayton.edu)

*Current performance predictions for radioisotope thermoelectric generators (RTG) tend to rely on either simple mathematical techniques that are founded in faulty assumptions, or advanced mathematical models that require extensive empirical data libraries. When extensive data libraries do not exist, such as with the Multi-Mission RTG or the Next Gen RTG, these advanced methods may produce a high degree of error. Kinetic rate law equations have been used for centuries to study rates of change, and have been adapted for use with RTGs. This rate law method was used recently to provide a high-quality analysis and prediction of MMRTG degradation. A detailed description of this method, and how to use it, is presented here. This rate law method allows users to produce an in situ prediction of performance with a minimal amount of empirical data. It will no longer be necessary to collect performance data for an arbitrary period of time (e.g. 10,000 hours) and assume it is sufficient for analysis. The rate law method will inherently allow the user to determine if there is enough data to perform a high-quality prediction, or if more data is needed. Finally, the user will be able to analyze system performance, determine if unexpected changes are occurring, and evaluate the impact of those changes. Given the utility, and relatively small quantity of data needed, it is recommended that the rate law method is adopted as a standard for analyzing RTG data and performing in situ power predictions.*

### I. INTRODUCTION

Power predictions for multi-mission radioisotope thermoelectric generators (MMRTG) are important for NASA mission planning purposes. Power predictions are also important when evaluating systems that are under development, such as the Next Gen RTG. Unfortunately, some power predictions used over the past decade have used relatively simple mathematical techniques that are founded in flawed assumptions. Accurate power predictions and analytical methods for MMRTG users and Next Gen RTG system developers are needed to aid in NASA mission planning.

Some advanced models have been developed that can predict RTG power, such as the Advanced Thermoelectric Performance Model (ATPM)<sup>1,2</sup> and the Life Performance Prediction Model (LPPM),<sup>3</sup> which is a modern evolution

of the DEGRA model used with SiGe based RTGs.<sup>4</sup> These models are powerful *a priori* prediction techniques that are capable of simulating RTG performance, including statistical variations between individual units. Building these models, however, requires a considerable amount of empirical data, implying that they are prone to error with limited available data. These are just some of the inherent strengths and weaknesses of a simulation-based model compared to an empirical analysis method.

Thus, there is value in establishing a standard method for evaluating and extrapolating RTG degradation directly from performance data. This *in situ* method would provide a tool that compliments *a priori* simulations, and would improve our ability to understand RTG behavior.

This *in situ* analysis method will need to be able to analyze RTG performance from a limited set of empirical data. It will also need to be able to determine when the RTG is experiencing changes in the dominant degradation mechanism. This will allow users to determine if the RTG is experiencing an unexpected change in performance, and attempt to evaluate that change in a timely manner. Finally, this method should be based on proven techniques for analyzing rates of change.

Recently, a rate law based analysis was performed on telemetry from the first MMRTG flight unit (F1), which is currently powering the Mars Curiosity rover.<sup>5</sup> Results from this analysis indicated that after 17 years, F1 will be producing 25% more power than previously predicted. In addition, the analysis produced a degradation curve that agreed with F1 telemetry to within  $\pm 0.3 W_e$  at all points, which was a significant improvement over the curves that were previously published.<sup>5</sup>

This technique was then applied to the MMRTG Engineering Unit (EU) and Qualification Unit (QU). Results from the EU indicate excellent agreement with F1 telemetry,<sup>6</sup> while QU results suggest that operating an MMRTG with a lower thermal inventory could result in more power at the end of design life.<sup>7</sup> While the accuracy of this technique cannot be fully assessed until after F1 has its 17<sup>th</sup> birthday in 2025, these results provide high confidence in the accuracy and precision of the prediction.

A detailed walkthrough of the technique used to analyze F1, EU, and QU data is provided in this report. In addition, this technique will allow users to identify if their

system is operating under a constant degradation mechanism, which will allow users to have confidence in future performance of the RTG.

## II. METHODOLOGY

Techniques applied here are adaptations of the techniques used to study chemical reaction kinetics. The fundamental principles governing kinetic equations can be found in any Physical Chemistry textbook, with an example provided here as Ref #8.

This Section will provide a theoretical description of the methodology. Section III will provide examples of how the methodology can be applied to real data.

### II.A. Integrated Rate Law Equations

The key to an analysis based on kinetics is fitting the degradation data to a rate law equation and converting that into an integrated rate equation. The classical rate law, when applied to power degradation, is:

$$\text{Rate} = k P^x \quad (1)$$

Mathematically speaking, Rate is the instantaneous slope in the power curve at a given point in time. Obtaining an instantaneous slope from real data can be challenging, so a common approximation can be obtained from:

$$\text{Rate} = \frac{-dP}{dt} \approx \frac{-\Delta P}{\Delta t} \quad (1.1)$$

Where  $\Delta P$  is the change in power over a given time interval,  $\Delta t$ . Accuracy of the Equation 1.1 approximation increases as  $\Delta t$  gets smaller.

In order to obtain the integrated rate equation, Equation 1.1 must first be rearranged, and then integrated from time  $t_1$  to  $t_2$ .

$$-P^{-x} dP = k dt \quad (2.1)$$

$$\int_{t_1}^{t_2} -P^{-x} dP = \int_{t_1}^{t_2} k dt \quad (2.2)$$

$$\frac{-1}{(-x+1)} P_{t_2}^{(-x+1)} - \frac{-1}{(-x+1)} P_{t_1}^{(-x+1)} = kt_2 - kt_1 \quad (2.3)$$

Where  $x$  is the order of the reaction,  $k$  is the rate constant,  $t_n$  is time at point  $n$ ,  $P_{t_n}$  is the power at the corresponding time. This equation can be rearranged:

$$\frac{-1}{(-x+1)} P_{t_2}^{(-x+1)} = k(t_2 - t_1) + \frac{-1}{(-x+1)} P_{t_1}^{(-x+1)} \quad (2.4)$$

And then simplified:

$$P_{t_2}^{(-x+1)} = k'(t_2 - t_1) + P_{t_1}^{(-x+1)} \quad (2.5)$$

Where  $k'$  includes all of the constants in Equation 2.4.

In order to use Equation 2.5, it is necessary to determine the order of reaction and rate constant. It is important to note that Equation 2.5 will only be accurate if the degradation rate is dominated by a consistent mechanism. Subsections II.B and II.C provide methods to identify when the degradation mechanism is changing.

### II.B. Determining the Order of Reaction

Order of reaction is determined using one of two methods. The preferred method is direct analysis of data with a log-log plot. Unfortunately, sometimes RTG data does not meet the requirements necessary for direct analysis. In that case, a trendline is obtained from the data, and a log-log analysis is performed on the trendline.

Requirements, advantages, and disadvantages of these two techniques are discussed below.

#### II.B.1. Theoretical Basis of the Log-Log Plot

Applying a logarithmic function to both sides of Equation 1 produces the following

$$\ln \text{Rate}_t = \ln(k P_t^x) \quad (3.1)$$

$$\ln \text{Rate}_t = x \ln P_t + \ln k \quad (3.2)$$

Where  $\text{Rate}_t$  is the instantaneous rate of change at time  $t$ , and  $P_t$  is the power at that point. A plot of  $\ln \text{Rate}_t$  versus  $\ln P_t$  will have a linear slope equal to the order of reaction (i.e.  $x$ ). Once the log-log analysis has determined  $x$ , it can be inserted into the integrated rate equation (Equation 2.5).

When utilizing a log-log plot, it is important to remember that the log of a negative number is undefined. This means that a log-log analysis of RTG power requires that every data point is smaller than the previous data point (i.e.  $\text{Rate}_t$  must always be positive).

#### II.B.2. Direct Log-Log Analysis of RTG Data

Direct conversion of RTG data into a log-log plot via Equation 3.2 is the preferred method for deriving  $x$ . Direct conversion minimizes subjective treatment of the data and provides the truest representation of degradation.

RTG data tends to be noisy, however, with F1 showing power swings that were sometimes as large as 10  $W_e$  over the course of a single day.<sup>5</sup> This noise interferes with the log-log analysis, but it can be dealt with by averaging the power before analysis. These averages can cover significant periods of time, with the F1 analysis requiring 30 day power averages.

While there is no upper limit to the size of the average, the quality of analysis tends to improve as the size of the average decreases. Reasons for this include: improved accuracy and precision in the integrated rate equation with more data; improved accuracy of the  $\text{Rate}_t$  assumption as the time interval decreases (Equation 1.1); and additional data helps to assure that the log-log plot is linear over the analyzed range (c.f. Section II.B.4). If averaging produces an unacceptably small number of data points, then it may be necessary to perform a trendline analysis of the data, as described in Section II.B.3.

#### II.B.3. Analysis of Trendlines Derived from RTG Data

Noise in RTG data can sometimes be significant enough that the requirement of decreasing data points

cannot be met without using excessively large averages. In these cases, an analyst can fit the data to a trendline, and use the trendline to generate data for the log-log plot. Logarithmic trendlines tend to fit RTG data very well, and were used when analyzing data from both the EU and QU.

This method is not preferred because it introduces additional subjectivity into the analysis. The analyst must select a type of trendline that is a “good fit” and still meets the constantly decreasing data requirement. If data does not fit the trendline well, the analyst must determine if the difficulty is due to the selection of a bad trendline, or if some data may be operating via different degradation mechanisms. Data from different mechanisms must be analyzed with different trendlines (c.f. Section II.B.4). Finally, most trendlines do not describe RTG behavior well during early life, meaning some subjectively determined early life data may need to be deleted before the trendline can be drawn.

Fortunately, later stages of the rate law method can “self-check” the analysis. This self-check may also help an analyst select a new region of data that will provide more accurate results. See Section II.C. for more details.

#### *II.B.4. Linear Versus Curved Log-Log Plots*

Log-log analysis is also valuable because it allows the analyst to determine if the dominant degradation mechanism is changing. When the log-log data is linear, the rate is controlled by a single degradation mechanism. An integrated rate equation obtained from linear log-log data is very likely to provide an accurate extrapolation of performance.

If the log-log data is curved, that is an indication that the dominant degradation mechanism is changing. For the sake of simplicity, this report will define “curvature” as data that does not show any clear linear trends. Results obtained from curved data should not be used. Instead, data should continue to be collected until the log-log plot is linear, and a sufficient quantity of linear data is available to produce a high-confidence integrated rate equation.

A change in the dominant degradation mechanism is expected during the early life of an RTG. Most thermoelectric materials experience a short lived, high degradation period during the first several months of operation. This is referred to as “burn-in.” After burn-in has completed, the RTG is expected to settle into a slower mechanism that will likely control degradation for the remainder of the design life. A log-log plot, therefore, can determine when burn-in has completed, and when long-term RTG degradation has begun. Long-term degradation data can then be used to obtain an integrated rate equation.

A common question that occurs when new thermoelectric materials are tested is, “How much test data is needed to produce a high confidence life prediction?” One advantage of the log-log analysis is that it provides the

evidence needed to have confidence in the prediction. If the data is curved, the analyst knows that the mechanisms are changing and an extrapolation will not produce accurate results. If the data is linear, the analyst can have confidence in predictions made from the data.

It should be noted, that the goal of the mathematical transformations presented throughout this method is to produce linear trends. As a result, standard linear regression statistical techniques can be used to assist an analyst in assessing the quality of the data, estimating error, and identifying curvature. Additional analyses that could prove useful include a regression analysis to evaluate confidence intervals and an analysis of residuals.

#### **II.C. Determining the Rate Constant**

After completing the log-log analysis, a rate constant plot of  $P_t^{(-x+1)}$  versus  $t$  should be generated. The slope of this plot will be equal to  $k'$  (c.f. Equation 2.5). It is important to assure that data used to create this plot is operating under the same mechanism. In other words, the log-log analysis needs to show that the data is linear and that  $x$  is constant over the range being analyzed.

If the value of  $x$  is incorrect, the rate constant plot will be curved. If the dominant degradation mechanism is changing, then the rate constant plot will be linear where the mechanism associated with  $x$  is dominant, but it will curve as the mechanism changes.

In this way, linearity of the rate constant plot can check the quality of the log-log analysis. In addition, localized curvature identifies changes in the degradation mechanism. The character of the curvature can also help determine the nature of the change. Decreasing degradation rates cause a downward curve in the plot, while increasing degradation rates curve upward.

Thus, the rate constant plot provides additional value as both a final “self-check” of quality, as well as an early indicator of changes in degradation behavior.

#### **II.D. Lifetime Power Predictions**

Before a prediction/extrapolation can be performed, it is necessary to assure that the most recent RTG data is operating under a constant degradation mechanism. Both the log-log analysis and rate plot should produce results that are linear through to the end of the available data. In addition, it is important to assure that there is enough linear data to have confidence in a regression analysis. While this is somewhat subjective, more linear data generally improves confidence. Unfortunately, a guideline on the amount of data needed cannot be provided because it depends on the noise in the data being analyzed.

Once all of the conditions described throughout this report are met, a high-quality power prediction can be performed using the integrated rate equation.

Of course, predictions made using the integrated rate equation assume that the dominant degradation mechanism is not going to change in the future. Fortunately, preliminary analysis indicates that the MMRTG trends do not experience changes in mechanism after the early life burn-in has completed. This suggests that as long as the burn-in data is removed, accurate power predictions can be obtained from the rest of the data. While other RTGs are expected to experience similar behavior, their performance should be analyzed to verify this general conclusion.

### III. EXAMPLE APPLICATIONS

The methodology described in this report has been applied to MMRTG F1, EU, and QU. Brief examples of how this was performed are presented here.

#### III.A. Log-Log Analysis

##### III.A.1. Log-Log Using Data Averages

Power data from F1 on Mars is very noisy, which is primarily due to the Martian diurnal cycle and weather.<sup>5</sup> It was necessary to perform monthly power averages on F1 to meet the constantly decreasing data requirement.

Rates were then obtained for each month (30 Earth days) using Equation 1.1. The log-log analysis of this data is presented in Figure 1, and it shows that  $x = 3.273$ . Figure 1 contains telemetry obtained from the beginning Martian operations on August 2012 through August 2018.

Figure 1 does not present any evidence of curvature. This suggests that the rate law analysis should produce a high-quality prediction. In addition, it suggests that F1 has experienced the same dominant degradation mechanism for the entirety of its 6+ years of operations on Mars.

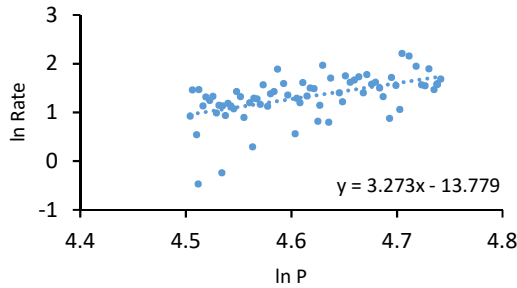


**Fig. 1.** Example of log-log analysis obtained from F1 monthly average power data on Mars.

An analyst must not confuse noise in the log-log analysis with curvature. F1 data is very noisy, but does not show evidence of curvature. If the analyst cannot clearly differentiate between noise and curvature, more data is required and a power prediction should not be performed.

##### III.A.2. Log-Log Analysis from a Trendline

A trendline analysis was required when evaluating MMRTG EU data. This is because some noise was

observed due to minor fluctuations in the heater power supply and the test facility climate. In addition, the EU was operated at a constant thermal input of 2000 W<sub>th</sub>. F1, on the other hand, had a constant decrease in thermal input due to the <sup>238</sup>Pu fuel decay, which helped meet the constantly decreasing data requirement. Without the <sup>238</sup>Pu thermal decay, noise in the EU was large enough that multi-month averages would have been required. A trendline analysis was therefore used in order to maintain confidence in the EU analysis.

Figure 2 presents a logarithmic trendline and subsequent log-log plot obtained from the EU data. This analysis shows that  $x = 10.832$ . Data prior to 554 days was not used due to burn-in and power supply issues causing inconsistencies in the data.<sup>6</sup>

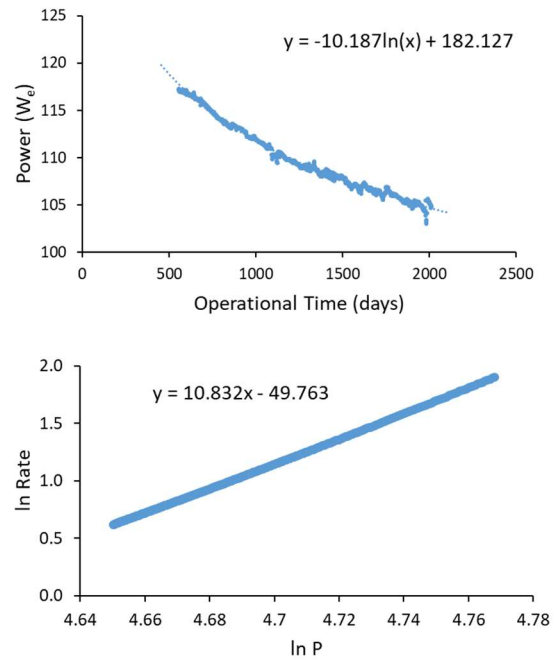


**Fig. 2.** (top) Example of a trendline applied to MMRTG EU data and (bottom) log-log analysis of the Rate

Since the trendline used here was logarithmic, by definition the log-log analysis was linear. In cases like this, the rate constant plot will be more instrumental in evaluating the quality of the analysis.

This analysis also highlights the difference between the *in situ* rate law method, and an *a priori* method. An *in situ* method is not able to predict differences in  $x$ , like the differences observed between F1 and EU. A well-developed *a priori* method, on the other hand, would show that differences like this are possible.

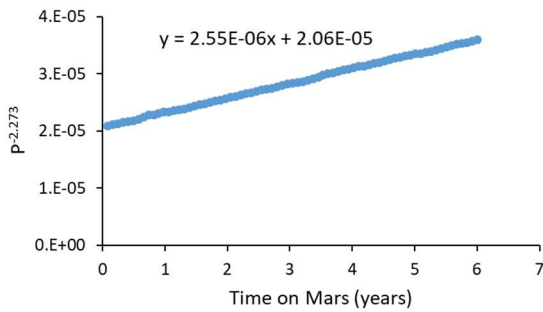
#### III.B. Rate Constant Plots

Figure 3 presents the rate constant plot obtained from F1 telemetry. Despite the significant noise observed in Figure 1, the rate constant plot shows a very tight, linear

trend. This is a strong indication that the log-log analysis was accurate, and that the integrated rate equation can produce an accurate and precise prediction of power.

### III.C. Analysis of Curved Data

Figure 4 presents an example of a log-log analysis obtained over the first 554 days of EU operations. In this example, degradation is dominated by the burn-in mechanism for the first ~120 days. After burn-in, the dominant mechanism transitions to a slow failure of the heater power supply. When burn-in dominates the degradation, the log-log plot shows a linear trend. When the power supply failure is dominant, the log-log plot shows a different linear trend. Data obtained during the transition between these two mechanisms does not show linear behavior. While this transition data may not be clearly “curved,” it is clear that this data has no consistent trend and should be ignored.



**Fig. 3.** Example rate constant plot obtained from F1 telemetry using  $x$  determined from the log-log analysis.

Figure 4 also provides an example of how a log-log analysis can help an analyst evaluate abnormalities in RTG behavior. The power supply failure produces a negative slope, indicating that the rate of degradation is increasing. This is not normal behavior for the MMRTG, and is a clear indication that something unusual is occurring.

### III.D. Power Predictions

Upon completing the log-log and rate plot analysis, performing a power prediction is a relatively simple application of Equation 2.5. Using the F1 telemetry as an example,  $x = 3.273$  and  $k' = 2.55 \times 10^{-6}$ . This results in an integrated rate equation of:

$$P_{t_2}^{-2.273} = 2.55 \times 10^{-6}(t_2 - t_1) + P_{t_1}^{-2.273} \quad (4)$$

Equation 4 can predict the power at any future point in time using a single, known power measurement. Of course, Equation 4 can be drawn as a graph for a more comprehensive power prediction, as shown in Figure 5.

## IV. ADVANCED MODLING TECHNIQUES

The rate law method described here is an *in situ* technique, meaning it is useful in evaluating and predicting the performance from an individual RTG that is currently

in operation. Extending these rate law predictions to other units should be performed with caution. Applying an *in situ* rate law result obtained on one unit (e.g. F1) and attempting to apply it to a different unit (e.g. F2), is likely to produce a result that is in the right ballpark, but advanced modeling techniques, like ATPM and LPPM, are required for a true *a priori* prediction. These advanced techniques include many additional considerations, including, but not limited to: different operating conditions, known differences in construction, and statistical variance between units. Once a unit enters operation, however, performance analysis should be passed off to a rate law based method to assure that unexpected deviations can be detected and evaluated in a timely manner.

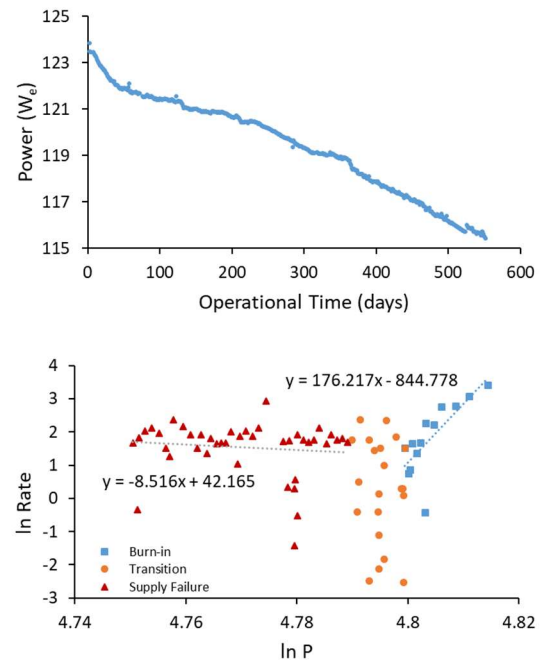


**Fig. 4.** Example analysis of EU data with two dominant degradation mechanisms: (top) raw data and (bottom) log-log plot. Linear behavior is observed when only one mechanism dominates, and a lack of linearity (i.e. “curvature”) is observed in the transition.

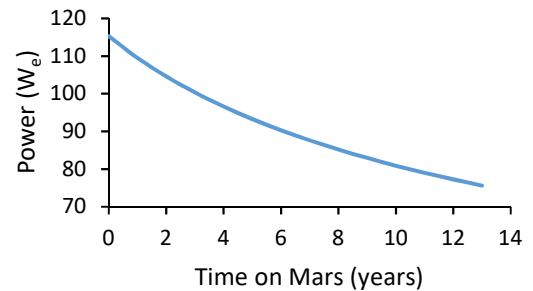


**Fig. 5.** Power prediction for F1 using the rate law method.

## V. FUTURE WORK

The method described here is a powerful *in situ* tool for evaluating RTG performance from a limited amount of empirical data. To date, this method has only been used to analyze MMRTG data. Future work should include analysis of other RTG units for generic trends in RTG behavior. This analysis should include data from at least the Multi-Hundred Watt RTG and GPHS-RTG. This in depth mining of historical data could help improve our understanding of RTG performance in general.

This technique should also be applied to the analysis of RTG systems under development, such as the Next Gen RTG. Application of the rate law method to Next Gen RTG will allow developers to make power predictions with a minimum amount of data. In addition, the rate law method will allow developers to assure that their systems are behaving as expected, which will improve the confidence in any performance predictions.

## VI. CONCLUSIONS

A new method for analyzing *in situ* RTG degradation rates is presented. This rate law method is based on well-established rate law equations, and provides analysts with a powerful, self-checking tool for evaluating the quality of their prediction. The method can also help users determine if the RTG is producing unexpected behavior, and allow evaluation of this behavior in a timely manner.

The rate law method also allows the analyst to confidently predict the future performance of an RTG with empirical data. Common questions regarding the amount of data needed for a confident prediction are no longer necessary because the rate law method produces results that support the validity of its predictions. As a result, the rate law method presented here will produce high quality power predictions without requiring complete and extensive life test data.

This *in situ* method is not intended to replace advanced *a priori* models, such as ATPM or LPPM. Each technique has a place in predicting and evaluating RTG performance. They should be used in concert to provide a comprehensive understanding of RTG performance and degradation.

## ACKNOWLEDGMENTS

The author would like to acknowledge Dr. Chadwick Barklay and Dr. Daniel Kramer at the University of Dayton; Thomas Hammel and Dr. Joseph VanderVeer at Teledyne Energy Systems; David Woerner and Dr. Jean-Pierre Fleurial for their support, general discussions regarding RTG performance, and general discussions of advanced RTG modeling techniques. This work was funded by Battelle Energy Alliance contract 00184172.

## REFERENCES

1. T. HAMMEL, *et al.*, *Proc. NETS 2015*, Albuquerque, NM, February 2015, 5107, American Nuclear Society (2015).
2. J. R. VANDERVEER, *Proc. TFEC2017*, Las Vegas, NV, April 2017, TFEC-IWHT2017-17687 (2017).
3. E. G. WOOD, *et al.*, *Proc. NETS 2016*, Huntsville, AL, February 2016, 6024, American Nuclear Society (2016).
4. G. STAPFER, *DOE/ET/33003-T4*, Jet Propulsion Laboratory. California Institute of Technology, Pasadena California (1976).
5. C. E. WHITING, *et al.*, *Proc. NETS 2019*, Richland, WA, February 2019, 51, American Nuclear Society (2020)
6. C. E. WHITING, *Proc. IEEE: Aero. 2020*, Big Sky, MT, March 2020, 2060, IEEE Publications (2020)
7. C. E. WHITING, *Proc. NETS 2020*, Knoxville, TN, April 2020, Oak Ridge National Laboratory (2020).
8. G. W. CASTELLAN, *Physical Chemistry, 3<sup>rd</sup> Ed.*, pp 799-912, The Benjamin/Cummings Publishing Company, Inc., Menlo Park, CA (1983).

## EMPIRICAL ANALYSIS OF THE MMRTG QUALIFICATION UNIT OPERATED AT A LOW THERMAL INVENTORY

Christofer E. Whiting

University of Dayton, 300 College Park, Dayton, OH, 45469-7532

Phone: 937-229-2570; email: [chris.whiting@udri.udayton.edu](mailto:chris.whiting@udri.udayton.edu)

*Performance predictions for the MMRTG were recently reported for the first flight unit and the Engineering Unit. Both units were produced and operated/tested within specifications. In an attempt to study the effect of a mid-life, deep space cruise on the MMRTG, the Qualification Unit (QU) was placed on life test with a below-specification thermal inventory of 1904  $W_{th}$ . Analysis indicates that loading an MMRTG with a lower thermal inventory may result in less power at the beginning-of-life, but more power at the end-of-design-life (EODL). The lower thermal inventory in the QU produces a lower operating temperature, which appears to cause a significant reduction in the degradation rate of the thermoelectric couples. Preliminary calculations indicate that a thermal inventory of 1904  $W_{th}$  could result in a 9  $W_e$  power boost at EODL (i.e. 84  $W_e$ ), which is a 12% improvement over F1/EU predictions. Preliminary degradation analysis suggests that a 1904  $W_{th}$  unit will begin to produce more power than a 2027  $W_{th}$  unit approximately 4 years after fueling. This suggests that missions with a primary power requirement more than 4 years after fueling would benefit from a lower thermal inventory. In addition, using a lower thermal inventory has significant benefits for  $^{238}\text{Pu}$  stockpile management, and may allow for additional MMRTGs to be fueled from our current reserves. Conclusions and hypotheses presented here should be considered preliminary because the QU data set is very small, and there are some uncertainties regarding how early life QU data will translate into later life performance. More QU testing at a thermal inventory of 1904  $W_{th}$  is needed to prove that the preliminary conclusions presented here are valid.*

### I. INTRODUCTION

The Multi-Mission Radioisotope Thermoelectric Generator (MMRTG) is a relatively recent design that uses heritage TAGS/PbTe thermoelectric technology. Despite a long and successful history using TAGS/PbTe,<sup>1,2</sup> the performance and degradation characteristics of the MMRTG have not been evaluated until recently.<sup>3,4</sup> Understanding how the MMRTG will perform at EODL (End-of-Design-Life – 17 years after fueling) is very important for NASA mission planning.

Analysis of telemetry from the first MMRTG flight unit (F1) indicates that the monthly average power at EODL will be  $75.2 \pm 0.3 W_e$ .<sup>3</sup> Life test data from the

MMRTG Engineering Unit (EU) indicates that, after adjusting for differences in operational conditions, the monthly average power at EODL will be  $75.2 \pm 0.4 W_e$ .<sup>4</sup> The similarity between these results significantly improves our confidence in the F1 predictions as a leading indicator for MMRTG flight unit performance.

Life test data from the Qualification Unit (QU) may also improve our understanding of MMRTG performance and degradation. This report will analyze the QU life test data using the same methods used to analyze EU and F1. While the QU has less time on test, the preliminary results suggest that EODL power may be improved by operating the MMRTG with a slightly lower thermal inventory. Additional life testing will be necessary to determine if this hypothesis is correct.

### II. METHODS

#### II.A. Data Analysis

A detailed description of the method used to analyze F1 and EU data is described in several other places.<sup>3-6</sup> These methods will be used to analyze the QU data. A very brief summary of the method is provided here.

Once a clear trend in the data has been identified, the rate of change in the data is established and used to create an integrated rate law equation. This equation is then used to predict future performance.

#### II.B. Outliers

It is important to remove outliers so that trends in the data can be analyzed. Data that does not appear to be part of the QU trends were considered outliers and removed before analysis. The following rules were used to identify outliers:

- Data obtained during changes in test conditions\*
- Temporary deviations exceeding 2 °C or 0.5  $W_e$  from the average values from a week before or after

Data obtained during the thermoelectric burn-in period should not be considered during analysis.<sup>4</sup> During EU testing, burn-in occurred over the first 120 operational days. Based on this result, the first 120 operational days of the QU will not be analyzed.

---

\* For example, QU test conditions were altered to support a test for the Mars 2020 mission. See Section II.D for more information.

### II.C. Operational Time

For the purposes of this paper, an operational day for the QU will be defined as a day when the average hot junction temperature ( $T_{hj}$ )  $\geq 457$  °C. This is the same definition used in the EU analysis, and a detailed justification can be found elsewhere.<sup>4</sup>

Based on this definition, the QU has experienced a total of 804 operational days. After removing data from outliers, burn-in, and Mars 2020 support, only 480 data points are available for analysis.

### II.D. Life Test Conditions

QU life test conditions were selected to simulate a deep space cruise approximately halfway to Europa. This resulted in a nominal thermal inventory of 1904  $W_{th}$ , an average fin root temperature ( $T_{fr}$ ) of 154 °C, and a load voltage of 28 V.

Between 347 and 483 operational days, the QU was not under nominal life test conditions because of routine parametric testing and a simulation designed to support the Mars 2020 mission. Data during this period of time will not be analyzed.

EU life test conditions were a nominal thermal inventory of 2000  $W_{th}$ ,  $T_{fr} = 182$  °C, and a load voltage of 28 V. F1 operational conditions were a BOL thermal inventory of 2027  $W_{th}$ , average  $T_{fr} = 165$  °C, and a load voltage of 32 V. A detailed description of these operational conditions and their implications is provided elsewhere.<sup>4</sup>

### III. HOT JUNCTION TEMPERATURE ANALYSIS

Figure 1 presents the  $T_{hj}$  for the QU and EU over the first 750 operational days. A higher  $T_{hj}$  for the EU was expected because the thermal inventory (2000  $W_{th}$ ) was higher than the QU thermal inventory (1904  $W_{th}$ ).

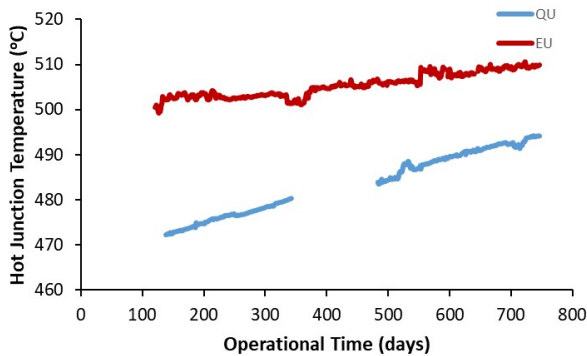


**Fig 1.** Hot junction temperature ( $T_{hj}$ ) for the EU and QU from 120 to 750 operational days.

Figure 1 shows that  $T_{hj}$  for the EU appears to be

increasing linearly. Previous reports indicate that this linear trend continues to at least 1800 operational days.<sup>4</sup>

Meanwhile,  $T_{hj}$  for the QU is increasing more quickly, but the data does not appear to be linear. A series of regression analyses indicate that the slope produced over 120-220 days (0.044 °C per day) is almost 2x larger than the slope obtained from 650-750 days (0.027 °C per day).

One hypothesis that could explain this curvature is that the lower thermal inventory led to lower  $T_{hj}$ , which led to a delay in the thermoelectric burn-in. If this hypothesis is correct, the burn-in will eventually become complete. At that point, the  $T_{hj}$  slope should become linear, and most likely similar to the EU data. More test data is needed to determine if this hypothesis is correct.

### III. POWER DEGRADATION ANALYSIS

Figure 2 presents the QU power data after outliers have been removed. EU data acquired during the same timeframe are presented for comparison. Unfortunately, EU data before 554 days is not viable for analysis due to inadequacies in the initial power supply.<sup>4</sup>

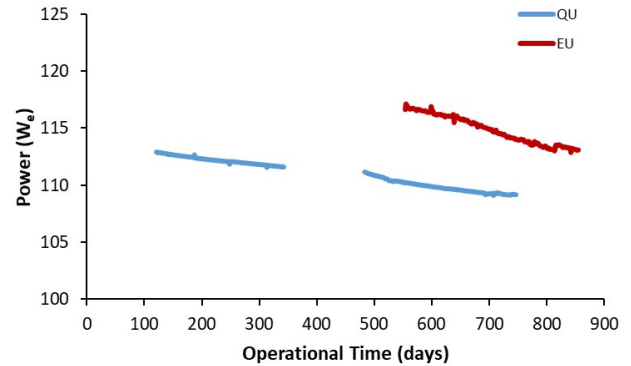


**Fig 2.** Power produced by the EU and QU.

It is extremely important to note that strong conclusions cannot be drawn from Figure 2 due to the very small size (480 days) of the data set. In addition to the small data set,  $T_{hj}$  analysis suggests that burn-in may still be occurring in this data set. By comparison, high confidence EU data was analyzed using 1460 day and 1189 day data sets, and both were obtained hundreds of days after burn-in completion was observed. Thus, any results obtained from the QU analysis should be considered a hypothesis, and more QU testing is needed to prove the validity of those hypotheses.

Figure 2 appears to indicate that EU power is degrading faster than QU power. This result is not surprising. Degradation rates are expected to be strongly tied to  $T_{hj}$ , and Figure 1 shows that  $T_{hj}$  for the QU is between 15-30 °C lower than the EU.

QU data was then converted into an integrated rate law equation using the standard techniques described elsewhere.<sup>3-6</sup> Results cannot be directly compared to EU or F1 because all 3 systems were operated under different conditions. Fortunately, these operational differences can be accounted for with simple mathematical adjustments. The basis for these adjustments are described in previous reports<sup>4</sup> and/or the MMRTG User's Guide.<sup>7</sup> These adjustments were applied to the EU and QU results so they are comparable to the operational conditions experienced by F1. These adjustments are:

- Increase BOL power to account for F1 thermal load of 2027  $W_{th}$  – 1.35% for EU and 6.5% for QU
- Apply a 1.2% per year first-order degradation to account for fuel decay and Carnot efficiency losses
- Adjust the power for a  $T_{fr} = 165$  °C
- Adjust the power for a 32 V load

### III.A. EU Performance and Degradation Analysis

Figure 3 presents the results from the integrated rate law equations obtained from F1, EU, and QU. EU and QU results have been adjusted as described previously.

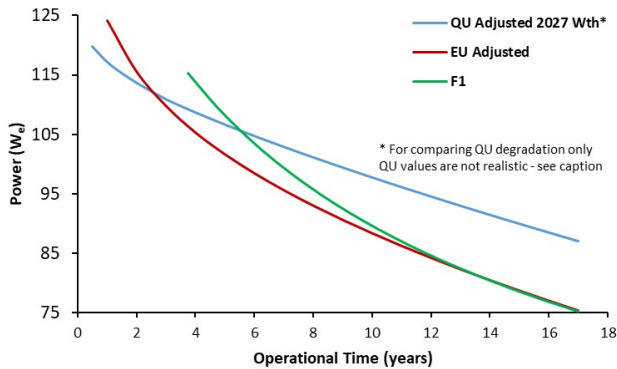


**Fig 3.** Comparison of degradation rates for F1, EU, and QU. QU power values are not representative of a real unit because it shows the degradation of a low thermal inventory unit with the initial power of a high thermal inventory unit.

Figure 3 shows that F1 produces more power at the beginning-of-mission (BOM), but F1 and EU produce the same power at EODL. This is due to a complex relationship between operating conditions and degradation mechanisms that will be discussed below. The conclusion that can be drawn from this, however, is that operating units under broadly similar conditions should produce similar EODL power.

F1 starts life on Mars (3.75 years after fueling) with more power than the EU or QU. This is because F1 spent most of its pre-mission operational time in storage under active cooling, or on a 9 month cruise to Mars. Under

both of these conditions,  $T_{fr}$  and  $T_{hj}$  were lower, which caused F1 to have a lower degradation rate.

Degradation for F1 is higher at the beginning of operations on Mars because some of the degradation mechanisms were suppressed due to storage under active cooling. As these mechanisms approach completion, the degradation rate slows down and F1 power values asymptotically approach EU power. By the time EODL is reached, the degradation rates and total degradation experienced by both EU and F1 are very similar.

This phenomenon was explained in a previous study using temporary degradation mechanisms.<sup>4</sup> A temporary degradation mechanism is a reaction with a rate that has a strong dependence on temperature. This mechanism will eventually reach completion and stop contributing to degradation. If temperatures are lower, it will take longer for the temporary degradation mechanisms to reach completion. Once these mechanisms are complete, however, the total amount of degradation will be the same as a system operated at a slightly different temperature.

This concept of temporary degradation mechanisms appears to be playing out in Figure 3 with F1 and EU. EU was operated at a higher temperature, so the degradation rate was faster during early life. As the unit aged, the degradation rate appears to flatten out and become more consistent. F1 had higher power and degradation at BOM because it was under cooler conditions for nearly 4 years, but the total degradation is expected to eventually catch up with EU. According to Figure 3, this will most likely occur after ~13 years of operational time.

The integrated rate law equation for the EU indicates that the monthly average power at EODL will be  $75.2 \pm 0.4 W_e$ . Deviation values are the 99% confidence interval obtained from an analysis of residuals. This result is very similar to the  $75.2 \pm 0.3 W_e$  predicted for F1, and significantly improves our confidence in the F1 power predictions.<sup>3</sup> In addition, these results indicate that EU and F1 are following the expected trends for an MMRTG, despite operation under slightly different conditions.

### III.B. QU Performance and Degradation Analysis

Figure 3 suggests that the lower thermal inventory has lowered critical temperatures within the QU enough to significantly decrease degradation. In fact, the degradation rate is so low that these preliminary predictions indicate that the QU will eventually produce more power than F1 or EU.

This further suggests that the lower thermal inventory has decreased the rate of some temporary degradation mechanisms enough that they have a reduced impact on total degradation. It is very likely that those temporary degradation mechanisms are still occurring, but the time needed to reach completion is longer than the design life of the unit. Thus, these preliminary results suggest that

operating at a lower thermal inventory could result in a significant boost in EODL power.

It is very important to note here that Figure 3 is an unrealistic analysis of how an MMRTG would perform with lower thermal inventory. QU results in Figure 3 have the degradation rate of 1904  $W_{th}$ , but the total power output of 2027  $W_{th}$ . As a result, Figure 3 should not be used to compare QU power to other units. The real value of Figure 3 is that it allows for a visual comparison of the power degradation rate for each of the different units.

Figure 4 provides a more realistic comparison of the power predicted by the QU preliminary results because the data was not adjusted to have a higher BOL thermal inventory. These results show that an MMRTG loaded with a lower thermal inventory would produce approximately 10  $W_e$  less at BOL. At EODL, however, Figure 4 predicts that the QU would produce 81.7  $W_e$ , which is 6.5  $W_e$  (9%) more than EU and F1.

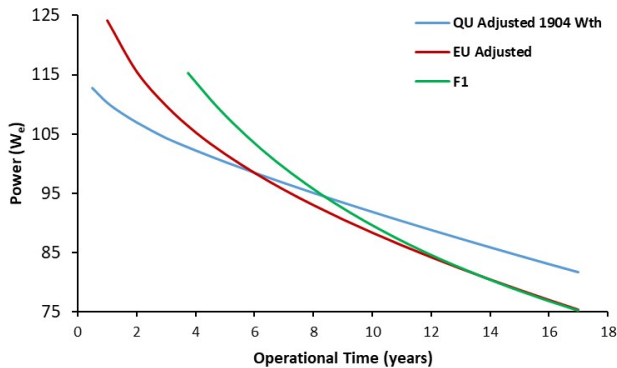


**Fig 4.** Comparison of preliminary power predictions for the QU with units that have a 2027  $W_{th}$  thermal inventory. QU data is not adjusted for the 4  $W_e$  deviation observed in the BOL power analysis.

A BOL power analysis indicated that the QU started life producing approximately 4  $W_e$  less than the EU. This deviation is most likely due to unit-to-unit differences in MMRTG construction. This implies that the EODL boost generated by lower thermal inventory is greater than what is shown in Figure 4. Power degradation is expected to cause this 4  $W_e$  to shrink to ~2.7  $W_e$  at EODL. Therefore, this preliminary analysis indicates that fueling a generic MMRTG with 1904  $W_{th}$ , instead of 2027  $W_{th}$ , should cause a total power boost of ~9.2  $W_e$  (12%) at EODL.

This suggests that if the EU had been operated with a thermal inventory of 1904  $W_{th}$ , the predicted EODL power for that unit would be ~84  $W_e$ .

Figure 5 provides a more direct comparison of how a single MMRTG would perform with different thermal inventories. One data set presents the EU results after adjusting for F1 operational conditions and BOL thermal inventory. The other data set presents the QU results

after adjusting for F1 operational conditions and the 4  $W_e$  lower BOL unit performance, but the QU thermal inventory is maintained. In other words, the second data set is a prediction of how the EU would have performed and degraded if it had the lower QU thermal inventory.

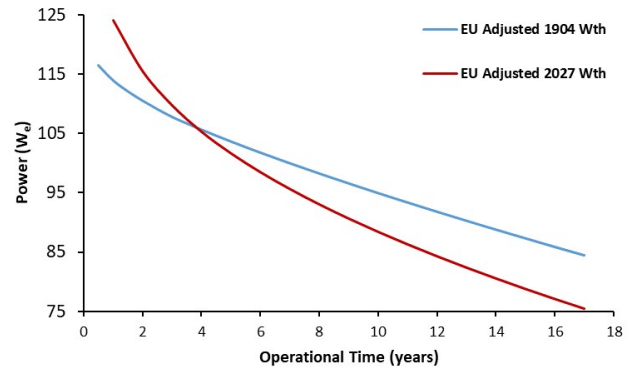


**Fig 5.** Prediction of EU behavior if it had been loaded with 1904  $W_{th}$  based on QU test results after adjusting for F1 operational conditions and the 4  $W_e$  difference between units.

It is interesting to note that the two power predictions cross at ~4 years. This suggests that it only takes 4 years for an MMRTG with a thermal inventory of 1904  $W_{th}$  to start outperforming a unit loaded with 2027  $W_{th}$ .

An analysis of the F1 and QU crossover is not made here because of the extended time F1 spent under active cooling prior to launch. Previous reports indicate that the active cooling resulted in a suppression of power degradation.<sup>4</sup> Since this effect is not understood on a quantitative level, it is not possible to make a fair comparison of the early life behavior of F1 vs. QU.

It is important to reiterate that the results based on QU data are preliminary. The QU data set is small, and there are still some open questions regarding how this early life data will correlate to long term life predictions. Additional testing of the QU under the low thermal inventory conditions will be needed to determine if these preliminary conclusions and hypotheses are correct.

#### IV. IMPLICATIONS

These preliminary results suggest that an MMRTG mission with a primary power need 4 or more years after fueling may benefit from using a lower thermal inventory. This would include missions to Titan (e.g. Dragonfly), the icy moons, or any of the outer planets. Missions with a primary power need less than 4 years after fueling (e.g. Martian missions), would benefit more from the current specification BOL thermal inventory.

In addition to potentially supplying long duration missions with more power, using a thermal inventory of ~1900  $W_{th}$  has other significant advantages. Current

stockpiles of in-specification  $^{238}\text{Pu}$  fuel are limited. However, if MMRTG units can be loaded below the current thermal specification, then a significant quantity of below-specification fuel can also be used. A detailed blend plan would be required to determine how much additional fuel would be made available, but it is possible this could enable the fueling of one or more additional MMRTGs with our current stockpile.

## V. CONCLUSIONS

Preliminary evaluation of QU data suggests that operating an MMRTG with a below-specification thermal inventory of 1904  $W_{\text{th}}$  may result in a significant reduction in degradation rates. Analysis indicates that this could result in a  $\sim 9 W_e$  boost in power at EODL, which would be a 12% boost over F1/EU performance.

QU results suggest that a low thermal inventory of 1904  $W_{\text{th}}$  will produce less power at BOL, but after  $\sim 4$  years the unit will begin to produce more power. Thus, missions with a primary power need more than 4 years after fueling would benefit more from a lower thermal inventory. Missions with a primary power need of less than 4 years would benefit more from an in-specification thermal inventory.

Operating with below-specification thermal inventory may also have significant benefits for  $^{238}\text{Pu}$  stockpile management. Using below-specification fuel might help extend our  $^{238}\text{Pu}$  fuel supply, and allow additional generators to be fueled with our current stockpile.

BOL analysis indicates that the QU was producing about  $4 W_e$  less than the EU under similar conditions. This is the first report of unit-to-unit power variation for MMRTG. This is a simple comparison of two units, and not a statistically derived variance.

Finally, it is important to note that any results or hypotheses obtained from QU life test data should be considered preliminary. The amount of QU data available for analysis is small, and there are still some open questions about how the early life data will translate into later life performance. Additional QU testing at the low thermal inventory condition will be needed to determine if these conclusions/hypotheses are valid.

## ACKNOWLEDGMENTS

The author would like to acknowledge William Otting and other team members at Aerojet Rocketdyne for maintaining the MMRTG performance database and for performing the EU simulated thermal vacuum life test. Thomas Hammel at Teledyne Energy Systems, Inc. for discussions on interpretation of MMRTG data. David Woerner at the Jet Propulsion Laboratory for discussions regarding MMRTG testing conditions. Dr. Chadwick Barklay, B Allen Tolson, and Carl Sjöblom at the University of Dayton for performing the EU diurnal cycle

life testing and the QU life testing. The author would also like to thank Eric Clarke and Dr. Stephen Johnson at Idaho National Lab for advice regarding the analysis of MMRTG data and production of this manuscript. The work was funded by Battelle Energy Alliance contract 00184172.

## REFERENCES

1. ANONYMOUS, *Atomic Power in Space*, DOE/NE/32117-H1, U.S. Department of Energy, Washington, DC (1987).
2. ANONYMOUS, *Atomic Power in Space II*, INL/EXT-15-34409, Idaho National Laboratory, Idaho Falls, ID (2015).
3. C. E. WHITING, D. P. KRAMER, and C. D. BARKLAY, "Empirical Power Prediction for MMRTG F1" *NETS 2019*, Richland, WA, February, Paper #51 (2019).
4. C. E. WHITING, "Empirical Performance Analysis of MMRTG Power Production and Decay," *IEEE: Aerospace 2020*, Big Sky, MT, March, Paper #2060 (2020).
5. C. E. WHITING, "Proposed Standard for Extrapolating Limited RTG Performance Data to Establish Behavior Trends and a Lifetime Performance Prediction" *NETS 2020*, Knoxville, TN, April, *ibid.* (2020).
6. G. W. CASTELLAN, *Physical Chemistry*, 3<sup>rd</sup> Ed., pp. 799-846. The Benjamin/Cummings Publishing Company, Inc., Menlo Park, CA (1983).
7. J. WERNER and W. OTTING, *Multi-Mission Radioisotope Thermoelectric Generator User's Guide*, INL/LTD-16-38850, Idaho National Laboratory, Idaho Falls, ID (2016).

## CONVERTOR DEVELOPMENT FOR DYNAMIC RADIOISOTOPE POWER SYSTEMS

Scott Wilson<sup>1</sup>, Sal Oriti<sup>1</sup>

<sup>1</sup>NASA Glenn Research Center, Cleveland, OH, 44135, 216.433.6681, [Scott.D.Wilson@nasa.gov](mailto:Scott.D.Wilson@nasa.gov)

*Dynamic power conversion technologies are being developed for future space science and exploration missions by NASA's Radioisotope Power Systems (RPS) Program, in collaboration with the U.S. Department of Energy (DOE). The Dynamic Radioisotope Power Systems (DRPS) Project is working to mature dynamic power convertors and controllers for infusion into potential future flight generators. Maturation of power conversion technologies is being executed by the DRPS Project and the Thermal Energy Conversion Branch, located at NASA's Glenn Research Center (GRC), and includes convertor technology development contracts and in-house controller development. Three convertor technology development contractor teams are tasked to design and fabricate prototypes, and complete performance testing before the units are delivered to GRC for independent assessment. All contractors have completed convertor designs and are fabricating convertors to enable performance testing, while one has demonstrated initial performance of their design. The contractors also have provided generator conceptual designs, which utilize their respective convertor technologies being developed.*

### I. BACKGROUND

Past development efforts provided Stirling convertor demonstration units and engineering models for performance verification and life and reliability testing (Ref. 1 & 2). These legacy units utilized temperature resistant materials and non-contacting bearings to demonstrate wear-free, long-life operation and were validated against performance specifications before undergoing extended operation testing. A total of eight Stirling convertors currently remain on test at GRC in extended operation, based on available test stations which have been reduced to make room for the incoming prototypes. Flexure-bearing Stirling convertors were delivered between 2003-2005 and have accumulated over 14 years of operation on a single unit. Gas-bearing Stirling convertors were delivered between 2007-2015 and have accumulated over 10 years of operation on a single unit. Many legacy units are used to support ongoing controller or generator concept development while some were taken offline due to failure and investigated to improve future designs and increase robustness. The current DRPS technology development effort builds on past lessons-learned and incorporates new requirements focused on demonstrating convertor robustness to critical environments. These contracts were enabled through the

2016 Research Opportunities in Space and Earth Sciences (ROSES-16, element C.22) solicitation program and are intended to gather data on candidate dynamic conversion technologies to fill knowledge gaps, support assessments of prototype dynamic power convertors (DPC), and elicit generator requirements (Ref. 3).

### II. TECHNOLOGY DEVELOPMENT CONTRACTS

The contracts included three phases that cover design, fabrication, and support during government verification and validation (V&V) testing. The fabrication phase is in progress and prototypes will be delivered to GRC throughout 2020. DPC prototypes are shown in Fig. 1.

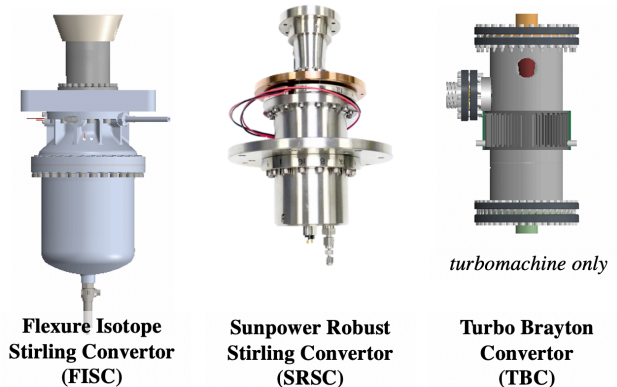


**Fig. 1.** Dynamic Power Convertor Prototypes.

The design life and power requirements enable a long-life, 100-500 We generator, which would be populated by multiple convertors operating at a derated power level to enable redundancy, thus increasing generator reliability. New and noteworthy requirements introduced in this development effort include an increased rejection temperature of 175 °C, the ability to survive new conditions without permanent degradation, namely a temporary loss of electrical load and a constant acceleration load of 5g in 3 orthogonal axis for an extended period. The rejection temperature was increased to account for a variety of higher temperature environments, such as a potential planetary protection process and the Lunar equator. The requirement to survive a temporary loss of electrical load was added to safeguard convertors from potential ground test errors or controller malfunction and provide margin for harsh mission conditions. If successfully met, these requirements will ensure future DRPS meet performance, life, and reliability requirements

while decreasing risk through implementation of robust designs.

Each Stirling contractor will deliver two convertor prototypes for testing at GRC while the Brayton contract will deliver a single convertor prototype. As prototypes arrive this year, they will undergo V&V testing according to government assessment plans that compare prototype performance to contract requirements.

### **II.A. Flexure Isotope Stirling Convertor (FISC)**

The FISC prototype concept was developed by American Superconductor (AMSC) of Richland, WA. The FISC prototype used the Technology Demonstration Convertor (TDC) from the 110W Stirling Radioisotope Generator (SRG-110) flight development project as a point of departure. It includes changes that improve performance, reduce mass, and ease manufacturability, compared to the TDC. A total of 16 TDC prototypes and two engineering units were produced during the flight contract, between 2000-2006. The four longest running TDC have accumulated over 52 years of operation and TDC #13 is currently the longest running heat engine in the world with over 14 years of operation. Its paired convertor, TDC #14, was disassembled and inspected after 12 years of error-free operation and no unanticipated observations were made, successfully demonstrating a long life design. Other TDCs are still used for tactical testing based on need.

While the TDC and FISC designs use flexure bearings to maintain non-contacting running clearances needed for wear-free operation, some aspects were changed to improve upon the TDC design. The FISC employs a moving-magnet alternator instead of the previous moving-iron design and the engine contains new alignment features that help streamline assembly. The prototype design is non-hermetic to permit disassembly and inspection during the government assessments. To meet the temporary loss of electrical load requirement, the FISC contains organic material bumpers that are designed to absorb energy during collisions between the moving components and stationary gas manifold without permanent degradation or compromising life or reliability.

The FISC prototypes are currently being fabricated. They are expected to produce 70  $W_{AC}$  electrical power output at 31% conversion efficiency while at 650 °C on the hot end and 100 °C on the cold end. The prototype will operate across the specified power levels and temperatures, including half heat input and the high rejection temperature of 175 °C. The loss of load test is planned for later in government assessment testing.

Each contract was modified to deliver a conceptual system design. The FISC generator concept, shown in Fig. 2, was developed by Teledyne Energy Systems, Inc. with support from AMSC. The concept contains a centrally located stack of four General Purpose Heat Sources

(GPHS) modules, surrounded by radiatively-coupled convertors with. There are six convertors installed and four required for full power operation, making two convertors redundant. Each pair of convertors are electrically synchronized for dynamic balancing so a single convertor failure would require a pair of convertors to be shut down in order to avoid excessive exported vibration from the surviving convertor. With a focus on modularity, the FISC generator concept could utilize 2, 3, or 4 GPHS step-2 modules, providing a beginning of life power output of 107, 176, and 237 W, respectively. The heat rejection exchanger is integral to the generator housing radiator surface, improving heat rejection while requiring separate engine and alternator attachment during integration into the housing. To protect from a micrometeoroid environment, a Whipple shield or hypervelocity impact shielding could be used to protect exposed portions of the convertors. Finally, the generator contains a sealed internal gas volume and would be filled with xenon or argon to protect hot components from oxidation. The FISC DRPS concept performance parameters are shown in Table I.

### **II.B. Sunpower Robust Stirling Convertor (SRSC)**

The SRSC prototype is being developed by Sunpower Inc. of Athens, OH. The SRSC prototype used the Advanced Stirling Convertor (ASC) from the Advanced Stirling Radioisotope Generator (ASRG) flight development project as a point of departure. It includes changes that improve robustness and ease startup, compared to the ASC. A total of 17 ASC prototypes and 20 engineering units were produced between 2007-2015. Two flight units were in production when the ASRG contract was canceled and remain preserved. Based on available supporting facilities, four ASC continue to operate in extended operation and have accumulated over 23 years of operation. Other ASCs are used for tactical testing based on need. ASC-0 #3 is currently the longest running ASC with over 10 years of operation and ASC-L has accumulated over 5.9 years of operation while under control of the Single Convertor Controller (SCC), developed by the Applied Physics Laboratory. Some early ASC units degraded due to imperfections caused by improper controls during production while other units were damaged due to overtest conditions experienced during ground testing. Disassembly and inspection helped identify design revisions that improve thermal stability of running clearances and robustness to overtest conditions, should they arise.

While the ASC and SRSC designs use gas bearings to maintain non-contacting running clearances needed for wear-free operation, changes were made to increase the stiffness of the bearings and improve robustness. The gas bearing system now employs more gas pads, a check valve filter, and a redundant check valve. It also has incorporated the passive ability to prevent collisions in case of

temporary loss of electrical load by dissipating thermodynamic cycle energy for a portion of the cycle where the moving components exceed a threshold amplitude. This patented Loss of Load Tolerance (LLT) function could prevent damage during ground test errors or piston excursions caused by the random vibration environment. Sunpower has incorporated the loss of load test into production processes to enable LLT verification on all units. As a backup to the LLT, the design also includes bumpers that could be removed later if so desired.

Sunpower has assembled and tested the first prototype, shown in Fig. 1. To enable inspection, the prototype design contains bolted joints that are not present in the flight design. The first SRSC prototype produced 64  $W_{AC}$  of electrical power output while at 700 °C on the hot end and 100 °C on the cold end. The conversion efficiency has not been measured yet but is expected to be 30%. The prototype has operated across the specified temperatures, having accumulated 9 hours at a rejection temperature between 170 °C and 175 °C. The loss of load test has been successfully demonstrated without indication of contact between moving and stationary components, based on inspection of data and internal parts.

As previously noted, each contract was modified to deliver a conceptual system design. The SRSC generator concept, shown in Fig. 2, was developed by Aerojet Rocketdyne with support from Sunpower. Similar to the FISC concept, the generator contains a centrally located stack of four GPHS modules surrounded by radiatively-coupled convertors. Again, there are six convertors installed and four required for full power, making two convertors redundant and requiring pairs to be shut down in the case of a failure due to the synchronization approach. The convertor heat rejection flange is bolted to the generator housing fin assembly, making assembly straight forward. The generator contains a vented internal volume instead of a sealed volume. The SRSC DRPS concept performance parameters are shown in Table I.

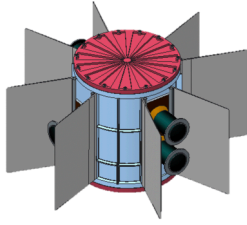
### **II.C. Turbo-Brayton Convertor (TBC)**

The TBC prototype design was developed by Creare Inc. of Hanover, NH. The TBC prototype design's point of departure is a flight cryocooler that successfully served on Hubble's Near Infrared Camera and Multi-Object Spectrometer (NICMOS) instrument. It includes changes necessary for power production as well as changes that improve bearing performance and increase temperature tolerance to accommodate DRPS requirements. GRC ground testing successfully demonstrated Brayton technology for space power conversion applications in the 1990's. The convertor provided by AlliedSignal Aerospace was considerably different than the TBC, containing foil bearings and producing nearly 6 times more output power. The 2 kW Solar Dynamic System measured a gross

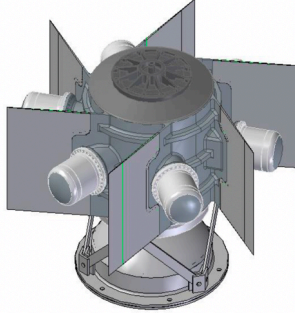
efficiency of 17% and accumulated over 780 hours of power production.

The TBC prototype uses hydrodynamic journal bearings and thrust bearings to maintain non-contacting running clearances needed for wear-free operation. The turbo machine consists of a single rotating shaft with turbine and compressor impellers located at each end. The shaft contains a rare-earth magnet which rotates inside a stationary coil and iron of the rotary alternator. The conversion process is enabled by unidirectional gas flow through the turbomachine assembly, recuperator, and heat exchangers. The counter-flow recuperator enables high thermodynamic efficiency by pre-warming gas before it flows into the heat source assembly. To meet the temporary loss of electrical load requirement, the TBC doesn't contain any special features to prevent collisions like Stirling convertors, but was simply designed to sustain stable operation during loss of electrical load without compromising life or reliability. The cycle thermodynamic energy is dissipated through drag losses without reaching the resonant bending frequency, safeguarding the convertor from damage during potential ground test errors. The prototype is expected to produce 337  $W_{AC}$  of electrical power output at 25% conversion efficiency while at 730 °C on the hot end and 100 °C on the cold end. The prototype will operate across the specified power levels and temperatures, including half heat input and the high rejection temperature of 175 °C. Similar to the FISC, the loss of load test is planned during government assessment testing.

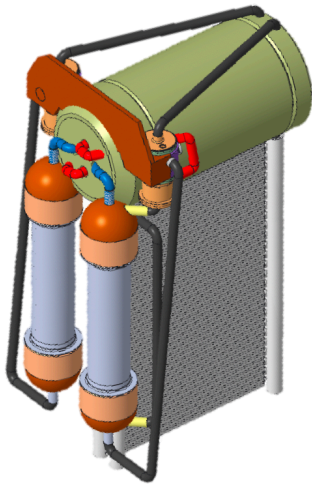
The TBC generator concept, shown in Fig. 2, was developed by Aerojet Rocketdyne and Creare with support from West Coast Solutions. The TBC generator concept contains two convertors to provide 100% redundancy and enable counter-rotating turbo-alternators so no net angular momentum is imparted into the space vehicle with both convertors operating. A stall or restart of one convertor would induce a transient torque and permanent shutdown of one convertor would result in a net angular momentum. While both convertors share the heat source assembly, each convertor contains a turbomachine, recuperator, and a radiator with a high surface area. Similar to the other generator designs, Whipple shielding could be used to mitigate the risk of damage due to the micrometeoroid environment. The heat source assembly uses six GPHS step-2 modules inside an evacuated multi-layer insulation to maximize insulation efficiency and protect the GPHS modules from oxidizing environments. The sealed assembly contains a vent to allow excess helium, a natural biproduct from the decay of plutonium-238, to escape during the mission. Two separate gas flow channels are located in the heat source assembly to enable heat input to each convertor. The TBC DRPS concept performance parameters are shown in Table I.



**ARD/Sunpower Generator  
containing 6x SRSC**  
Diameter = 69 cm  
Height = 39 cm



**TESI/AMSC Generator  
containing 6x FISC**  
Diameter = 82 cm  
Height (DRPS only) = 45 cm  
Height (with mount) = 63 cm



**ARD/Creare Generator  
containing 2x TBC**  
Diameter\* = 78 cm  
Height\* = 100 cm

\*estimated

**Fig. 2. DRPS Generator Concepts.**

**TABLE I. DRPS Concept Performance.**

Parameter	Units	FISC	SRSC	TBC
# of GPHS	#	4	4	6
# of convertors	#	6	6	2
Heat from fuel	$W_t$	1000	1000	1500
Ref. BOL power	$W_{dc}$	237	238	319 <sup>a</sup>
Ref. sys. eff.	%	24	24	21
Lunar BOL power	$W_{dc}$	198	210	184
Lunar sys. eff.	%	20	21	12
Ref. EODL power	$W_{dc}$	203	208	265 <sup>b</sup>
1 string failed	$W_{dc}$	218	214	319
Generator mass <sup>c</sup>	kg	66	49	128
Specific power <sup>c</sup>	$W_{dc}/kg$	3.6	4.9	2.4

*BOL*: beginning of life, *EODL*: end of design life, *dc*: direct current, *t*: thermal, <sup>a</sup>95% controller efficiency, <sup>b</sup>0.8% fuel decay rate over 17 years, <sup>c</sup>controller mass not included

### III. VERIFICATION AND VALIDATION TESTING

Independent government assessment of prototypes will be carried out upon delivery of each unit. The independent assessment serves multiple purposes, including ensuring initial quality, verifying contractor measurements, and validating requirements and durability. The V&V activities, shown in Table II, will be carried out through a combination of inspections, analysis, and testing to demonstrate a high technology readiness level.

**TABLE II. Verification and Validation Effort.**

Activity	Purpose
Receipt & Acceptance	Perform key characterization measurements
Performance Mapping	Verify requirements
Random Vibration Test	Simulate launch environment
Constant Acceleration Test	Simulate spin stabilization and entry, descent, and landing
Inspection	Document running surfaces
Thermal Cycling	Verify integrity of running clearances
10-sec loss of electrical load	Verify robustness
Extended Operation	Verify reliability

### IV. CONCLUSIONS

Dynamic Radioisotope Power Systems are being developed by NASA's RPS Program in collaboration with the DOE because they are roughly four times more efficient compared to thermoelectrics. Two Stirling technologies and a Brayton technology were designed and are being fabricated and tested prior to delivery for government V&V testing. Generator concepts were also delivered under these contracts to help fill knowledge gaps and inform requirements development for a potential DOE flight generator development effort. If successful, one or more of the power conversion technologies being developed will be determined ready for flight development in 2021.

### ACKNOWLEDGMENTS

This work has been funded by the Science Mission Directorate of NASA, through the RPS Program Office.

### REFERENCES

1. S. ORITI, S. WILSON, "Dynamic Power Converter Development for Radioisotope Power Systems at NASA Glenn Research Center", *AIAA 2018-4498*.
2. G. DUGALA, "Stirling Converter Controller Development at NASA Glenn Research Center", *NASA/TM-2018-219963*.
3. S. WILSON, S. ORITI, "Maturation of Dynamic Power Convertors for Radioisotope Power Systems", *GRC-E-DAA-TN63191*.